

UNIVERSITY OF BIRMINGHAM

Functional colloids from a lignin-rich bioresidue and their application

by

Alex Christopher Gerrow

A thesis submitted to
the University of Birmingham
for the degree of
DOCTOR OF PHILOSOPHY

School of Chemical Engineering
College of Engineering and Physical Sciences
University of Birmingham
20th December 2023

UNIVERSITY OF
BIRMINGHAM

University of Birmingham Research Archive

e-theses repository

This unpublished thesis/dissertation is copyright of the author and/or third parties. The intellectual property rights of the author or third parties in respect of this work are as defined by The Copyright Designs and Patents Act 1988 or as modified by any successor legislation.

Any use made of information contained in this thesis/dissertation must be in accordance with that legislation and must be properly acknowledged. Further distribution or reproduction in any format is prohibited without the permission of the copyright holder.

Abstract

This thesis details the extraction and characterisation of a lignin-rich bioresidue from cocoa bean shell (CBS), the formation of particles using antisolvent precipitation, and applications in emulsions and microfluidics. A co-product of the food industry, there is an estimated 600 kt of CBS produced annually. Lignin, an aromatic component of CBS, is of interest to researchers aiming to develop analogues to current consumer goods from sustainable feedstocks, and as a natural source of aromatics has properties of interest such as hydrophobicity and anti-microbial effects. Lignin liberation from biomass typically involves depolymerisation by processes such as bleaching, often produced as a by-product of commercial processes such as the Kraft paper pulping process termed Kraft lignin, however, this research uses mild acid assisted ethanol extraction. The bioresidue characteristics and co-products were characterised using analysis techniques such as FTIR and GCMS, identifying the presence of molecular surfactant, termed lipid. The extracted bioresidue which contained the lipid fraction (CBS-LC) was processed further to remove molecular surfactant, generating a second 'lipid removed' extract (CBS-LR).

It was found that hydrodynamic flow-focusing microfluidics was unsuitable for a proposed desorption approach to antisolvent precipitation in water. An alternative continuous process for colloidal lignin-rich particle (CLP) production was generated by setting up a coaxial jet mixing device (CJM). By varying processing conditions to explore the effect of Reynolds number and volumetric flow rate ratio, non-aggregating particles were precipitated with average diameters between 150 and 600 nm. The aqueous dispersions were stable with respect to particle size for at least 14 days, for both types of extract.

The impact of both lipid and co-extractives from the crude bioresidue was assessed by use of CLPs as Pickering particles in emulsion studies. It was found that the emulsions containing crude CLPs were less efficient at stabilising a 1 in 10 sunflower oil-in-water emulsion than Kraft lignin analogues. This was theorised to be the result of the presence of co-extracted molecular surfactant, which may have had a competitive adsorption effect with the CLPs at the oil and water interface. The lipid fraction of the CBS extract was removed, and the resultant change in measured contact angle offered an indication that the CLP surface properties varied from hydrophobic to hydrophilic. It was also found that lignin-rich CLPs could be transferred from aqueous to non-aqueous dispersion in the presence of a molecular surfactant.

The application of the aqueous and non-aqueous CLP dispersions as a particle dispersion for ghost particle velocimetry (GPV) was explored, motivated by the fact that non-aqueous tracer particle systems for GPV have not yet been reported. GPV is a technique for flow field imaging introduced in the last 10 years, allowing development of real-time quantification of flow fields in the focal plane and different cross-sections of a microfluidic channel using particles with a diameter of < 200 nm. This is currently achieved using a polystyrene based particle dispersion in the aqueous phase, and by demonstrating that lignin-rich CLPs can equally quantify flow fields, there potential to substitute these, which is an example of waste valorisation and environmentally sustainable substitution of a material. Application examples of this novel particle system were found not only to agree with theoretical flow velocity values but were able to quantify flow simultaneously in static and dynamic flow systems in both aqueous and non-aqueous phases. Whilst this thesis has demonstrated the ability to visualise and quantify flow fields using CLPs, the systems presented contain molecular surfactant in each instance.

This thesis contributes to the understanding of extraction and utilisation of lignin-rich bioresidue from CBS, highlighting its potential for use as a source of colloidal particles. Combining the spectroscopic techniques with characterisations such as contact angle offer insights into how particle behaviour is impacted by composition, paving the way for future advancements in creating dispersed particle systems with potential applicability in flow field imaging. Additionally, the first example of non-aggregating colloidal tracer particles in a non-aqueous system offers great potential for imaging not only the velocity of non-aqueous systems in confined channels, but formation of droplets; an area of significant interest in chemical micro-reactor systems.

To advance research in this area, it is recommended that initial work on the interactions between lignin and co-extracted surfactants are developed with respect to non-aqueous phase dispersions. Furthermore, there is an opportunity to explore the variation of the wetting characteristics of CLPs by employing novel solvent-antisolvent pairings. This would enable greater variation in the polarity of solvents in which CLPs can be dispersed. . In combining modified wettability with the adjustable particle diameter in a CJM, CLPs tailorable in both diameter and wettability may be produced, which could substitute a variety of current food-grade Pickering stabilisers.

Table of Contents

Abstract ..... *ii*

Table of Contents ..... *v*

Acknowledgements ..... *xi*

Publications and conference contributions ..... *xiii*

List of Figures ..... *xiv*

List of Tables ..... *xxvi*

List of abbreviations and symbols ..... *xxviii*

1. Introduction *1*

1.1. Lignin **1**

1.1.1. Introduction **1**

1.1.2. Sources of lignin **3**

1.1.3. Lignin-rich bioresidues and their extraction **5**

1.1.4. Quantifying physical-chemical characteristics of lignin extracts **7**

1.1.4.1. Infrared spectroscopy 7

1.1.4.2. Gas chromatography and mass spectrometry 10

1.2. Microparticle production **12**

1.2.1. Antisolvent precipitation **12**

1.3. Continuous processes for particle production **14**

1.3.1. Hydrodynamic flow-focusing devices **14**

1.3.2. Coaxial Jet Mixing **17**

1.4. Emulsions **20**

1.4.1. Emulsion stabilisation **20**

1.4.2. Pickering stabilisation 22

1.5. Wetting properties of colloidal particles 23

1.5.1. Contact angle 23

1.6. Flow field analysis in confined flow systems 26

1.6.1. Flow in confined channels 27

1.6.2. Quantifying flow in micromixers 28

1.6.3. Flow field evaluation in segmented flows 29

1.7. Summary of the literature review 30

1.8. Research objectives 31

1.9. Thesis structure 33

2. Materials and Methods *34*

2.1. Materials 34

2.1.1. Cocoa bean shell 34

2.1.2. Reagents and solvents 34

2.1.3. Materials for hydrodynamic flow-focusing device fabrication 36

2.2. Lignin-rich cocoa bean shell extract: Preparation, characterisation, and manipulation methods 36

2.2.1. Organosolv extraction of a lignin-rich bioresidue from cocoa bean shell 36

2.2.2. Lipid extraction 37

2.2.3. Quantification of extraction yield 38

2.2.4. Quantification of lignin in extract 38

2.2.5. Solvent solubility of lignin-rich bioresidue 40

2.2.6. Identification of bioresidue lipid fraction 41

2.2.7. Fourier-transformed infrared spectroscopy for lignin component identification 42

2.2.8. Ancillary bioresidue analysis methods 42

2.2.8.1. Viscosity 42

2.2.8.2. Density 43
2.2.8.3. Refractive index 43
2.2.9. Lignin bioresidue solution preparation 44
2.3. Flow-focusing method for precipitation of lignin-rich microparticles 45
2.3.1. Flow-focusing device manufacture 45
2.3.2. Device surface treatments 46
2.3.2.1. PVA treatment 46
2.3.2.2. Polyelectrolyte treatment 47
2.3.3. Colloidal particle production set-up 47
2.4. Coaxial jet mixing method for precipitation of lignin-rich microparticles 48
2.4.1. Coaxial jet mixing device manufacture 48
2.4.2. Colloidal particle production conditions 49
2.5. Methods for assessing surface characteristics of lignin-rich extracts 50
2.5.1. Treated sunflower oil preparation method 50
2.5.2. Preparation of emulsions 50
2.5.3. Surface tension of particle suspensions 51
2.5.4. Contact angle measurement method 51
2.6. Characterisation methods applied to precipitated lignin-rich particles....53
2.6.1. Dynamic light scattering 53
2.6.2. Electrophoretic mobility 54
2.6.3. Optical microscopy 54
2.7. Methods for flow field analysis using CLPs for Ghost Particle Velocimetry 55
2.7.1. Channel construction for flow field visualisation 55
2.7.2. Preparation of particle dispersions for flow field visualisation 56
2.7.3. Quantification of flow fields by cross-correlation 57

2.8. Statistical analysis 58

3. Characteristics and extraction efficiency of a lignin -rich bioresidue of cocoa bean shell 59

3.1. Physical extract properties 60

3.1.1. Extraction yield 60

3.1.2. Refractive index 61

3.1.3. Density 61

3.2. Chemical profile 61

3.2.1. Lignin content 61

3.2.2. Chemical composition analysis of CBS bioresidue using FTIR spectroscopy 63

3.2.3. Quantification of the lipid fraction of CBS using GC-MS spectrometry 66

3.3. Selected physical properties of bioresidue solutions 73

3.3.1. Solubility 73

3.3.2. Viscosity 74

3.3.3. Density 75

3.4. Conclusions 76

4. Hydrodynamic flow-focusing for microfluidic droplet formation 77

4.1. Optimisation of conditions for droplet formation in a HFF device 78

4.1.1. Droplet formation for antisolvent precipitation 78

4.2. Fouling behaviour caused by interactions between PDMS and lignin 79

4.3. Surface treatment of a PDMS microchannel to mitigate fouling in the microchannel 81

4.3.1. PDMS surface treatment methods 81

4.3.2. Interactions between lignin and device 82

4.4. Conclusions 85

5. Coaxial jet mixing for colloidal particle formation from crude extracts of cocoa bean shell 86

5.1. Application of a coaxial jet mixer for antisolvent particle precipitation ... 87

5.1.1. Definition of processing parameters 87

5.1.2. Validation of coaxial jet mixer setup 89

5.1.2.1. Effect of dilution of colloidal particle dispersions on particle diameter of dispersions 93

5.2. Impact of Re and flow ratio (R) on diameter of lignin-rich particle dispersions 94

5.2.1. Profile of particle diameter distributions 94

5.2.2. Influence of R and Re on average size and span of colloidal particle distributions . 97

5.2.3. Span of colloidal particle distributions 101

5.2.4. Multivariable analysis of particle dispersions 104

5.3. Characterisation of particle dispersions 107

5.3.1. Effect of lipids on particles 108

5.3.2. Stability of particle dispersions 111

5.4. Conclusions 116

6. Assessing the wetting properties of CBS lignin extracted, and the influence of the lipid fraction on their ability to stabilise emulsions 118

6.1. Application of CLPs as a Pickering particle for emulsion stabilisation .. 119

6.1.1. Validation of emulsion stabilising performance of CLPs 119

6.1.2. Impact of emulsion processing conditions on emulsion stability 122

6.2. Interfacial properties of lignin-containing system 125

6.3. Influence of lipids on the wetting properties of precipitated lignin 127

6.4. Role of the lipid in stabilising CLPs 129

6.5. Conclusions 133

7. Water and oil dispersible colloidal particles for Ghost Particle Velocimetry imaging.....134

7.1. Formation of colloidal particle dispersions of suitable diameter for GPV 135

7.2. Quantifying flow fields in GPV.....137

7.2.1. Determination of flow rates and camera speed suitable for GPV.....137

7.2.2. Precision of vectors in GPV conducted using CLPs.....139

7.2.3. Reproducibility and accuracy of flow fields determined by CLPs.....142

7.2.4. GPV using CLPs to visualise complex single-phase flows.....146

7.3. Imaging segmented flow fields in GPV.....148

7.3.1. Vector validation in segmented flows.....148

7.3.2. Flow fields in a segmented flow.....155

7.4. Effect of surfactant on GPV.....161

7.4.1. Effect of surfactant on the dispersibility of CBS-LC CLPs for GPV analysis.....161

7.4.2. Effect of surfactant inherent in the CBS-LC CLP system on droplets for segmented GPV analysis.....162

7.5. Conclusions.....165

8. Overall conclusions and future work.....166

References.....173

Appendix A – Statistical analysis of particle dispersions.....188

Acknowledgements

Writing a thesis has been possibly the most difficult thing in my professional career. I'm beyond thankful for those who have helped me, who I will now thank in a mixture of past and present tense which seems to haunt me and my writing.

Firstly, I'd like to thank my fiancée Eden, without whom I'd never have had the confidence to attempt a research degree, much less actually produce (and finish) a thesis. The support you have offered is unbelievable; from encouraging me to apply and giving me a pre-interview pep talk, to getting through covid, to 120-mile commutes, 5 am starts, 2 am finishes, and Saturday thesis-writing trips to what feels like every coffee shop in the West Midlands – I really couldn't manage without you! And I hereby promise in writing that I specifically won't do another PhD ***ever***, and that I am now satisfied that this is enough education! If I ever say otherwise, show me this!

Secondly, I would like to thank Prof. Bettina Wolf, who has given me all the help I could possibly offer. Whilst there are far too many examples of your help and encouragement to detail here, one specific example which I will always remember was in Autumn 2020, when I was under pressure, and feeling like I would never be able to complete this PhD. You took an hour after a meeting to remind me of the positive steps my work had taken to date and told me 'failure is not an option'. It's something which has stuck with me, and I won't ever forget, thank you!

I'd like to thank Dr. Nina Kovalchuk, who has perhaps unexpectedly found herself involved with this research project. In what started as general scientific conversation and use of a fume hood, to 'hang on, I think my colloids might work in GPV', to checking presentations before I presented my research chapter at multiple conferences, your calm

but incredibly well considered advice has been invaluable in getting this research project over the line!

I'd like to thank Dr. Daniele Vigolo, and Dr. Fotis Spyropoulos, who have always helped (often at short notice!) with questions, and preparation for conferences, documents, and presentations.

I'd like to thank my fellow researchers in the Microstructure and Microfluidics groups, who have been encouraging and offered very sympathetic ears to complain about research.

I'd like to thank my family, who I have forced into scientific discussions at every single function we have had over the past four years, and have humoured me every time. It has probably felt like 10 years. Hopefully we can talk about cats etc. now!

Lastly, can I publish an emoji? 😊

Publications and conference contributions

Publications

Mao, Y., Gerrow, A., Ray, E., Perez, N.D., Edler, K., Wolf, B. and Binner, E. (2023) 'Lignin recovery from cocoa bean shell using microwave-assisted extraction and deep eutectic solvents', *Bioresource Technology*, 372, available: http://dx.doi.org/10.1016/j.biortech.2023.128680.

Presentations

The Institute of Physics. 'Designed assembly of colloids at interfaces: Assembly to applications' 14th – 16th June 2021, poster, online.

13th European Congress of Chemical Engineering and 6th European Congress of Applied Biotechnology 20th – 23rd September 2021, poster, online.

2nd Edible Soft Matter Conference, 9-13 July 2022, poster, Wageningen University & Research, Wageningen, The Netherlands.

UK Colloids (2023), 17th – 19th July 2023, oral presentation, ACC Liverpool, Liverpool, United Kingdom.

Micro and Nano Flows Conference, 18th – 20th September 2023, oral presentation, University of Padova, Padova, Italy.

List of Figures

FIGURE 1: SKELETAL FORMULA OF KEY MONOMERIC COMPONENTS OF THE BIOMOLECULE LIGNIN. SHOWN ARE P-COUMARYL (H, LEFT), GUAIACYL (G, CENTRE), AND SINAPYL (S, RIGHT) ALCOHOLS. 2

FIGURE 2: PARTIAL IDEALISED STRUCTURE OF LIGNIN, SHOWING THE COMMON SUB-UNITS; GUAIACYL (1), SYRINGYL (2) AND COUMARYL (3) ALCOHOLS. REDRAWN AND ADAPTED FROM (HOLLADAY ET AL. 2007). 3

FIGURE 3: REPRESENTATION OF THE ARRANGEMENT OF CHARGES AROUND A PARTICLE IN AN AQUEOUS SYSTEM. THE CHARGES IN WATER REARRANGE TO REDUCE ELECTROSTATIC REPULSION. 14

FIGURE 4: SCHEMATIC OF A FLOW-FOCUSING DEVICE. CONTINUOUS PHASE QC FORMS A CHANNEL TO ENVELOP THE DISPERSED PHASE Q_D FROM EITHER SIDE. 15

FIGURE 5: SCHEMATIC DIAGRAM OF ANTISOLVENT PRECIPITATION. SOLUTE CONTAINING PHASE Q_D JET IS FED INTO A CONTINUOUS PHASE Q_C, IN WHICH THE SOLVENT IS MISCIBLE, BUT THE SOLUTE IS INSOLUBLE. THIS RESULTS IN PRECIPITATION. 19

FIGURE 6: IDEALISED VIEW OF A PICKERING STABILISED EMULSION. AN OIL PHASE (YELLOW) IS EMULSIFIED IN AN AQUEOUS CONTINUOUS PHASE (BLUE) USING PARTICLES WHICH ARE KINETICALLY STUCK AT AN INTERFACE (BROWN). 22

FIGURE 7: BOUNDARIES BETWEEN MATERIALS FOR A DROPLET OF LIQUID ON A SURFACE, WITH INTERFACES BETWEEN THE SOLID, LIQUID, AND GAS DEMARKED. 25

FIGURE 8: A PARABOLIC FLOW PROFILE DEMONSTRATING THE VELOCITY PROFILE OF A FLUID BETWEEN TWO SURFACES IN A STRAIGHT CHANNEL. 27

FIGURE 9: SETUP OF THE SOXHLET EXTRACTION OF LIGNIN FROM COCOA SHELL. A 250 ML ROUND-BOTTOM FLASK WAS FITTED WITH A SOXHLET CONTAINING A CBS FILLED THIMBLE, AND A CONDENSING COLUMN. 37

FIGURE 10: CALIBRATION CURVE OF SAMPLES TO DETERMINE THE ABSORPTIVITY CONSTANT OF LIGNIN USING A COMMERCIALLY AVAILABLE KRAFT LIGNIN AT 280 NM, AND CONCENTRATIONS BETWEEN 0 (REPRESENTED BY A SOLVENT BLANK) AND 400 MG L^{-1}. MARKERS SHOW THE MEAN VALUES,

AND ERROR BARS REPRESENT ± 1 S.D. THE GRADIENT OF THE RESULTING LINEAR TRENDLINE OF 0.0024 L MG^{-1}. (R^2 VALUE OF 0.9864) WAS USED IN THE BEER-LAMBERT LAW TO DETERMINE THE ABSORPTIVITY CONSTANT FOR LIGNIN.....40

FIGURE 11:REFRACTIVE INDEX OF A SERIES OF CONCENTRATIONS OF CBS-LC LIGNIN, IN ETHANOL, YIELDING AN APPROXIMATION OF THE REFRACTIVE INDEX AT 100 WT%. 44

FIGURE 12: SETUP OF FLOW-FOCUSING MICROFLUIDIC DEVICE. Q_C DENOTES INLETS FOR THE CONTINUOUS PHASE, AND Q_D DENOTES THE INLET FOR THE DISPERSED PHASE. THE CHANNEL WAS RECTANGULAR WITH THE FOLLOWING DIMENSIONS; W_A WAS 200 MM, W_B WAS 600 MM, AND CHANNEL HEIGHT WAS 150 MM. 46

FIGURE 13: SCHEMATIC OF THE CJM DEVICE, CONSISTING OF A CONCENTRIC INTERNAL GLASS TUBE WITH AN OUTER FLOW PHASE. THE SOLVENT STREAM (Q_{SOL}) WAS PASSED THROUGH A COAXIAL CHANNEL OF INNER DIAMETER 200 ΜM AND MIXED WITH THE ANTISOLVENT STREAM PASSING THROUGH THE CHANNEL OF INNER DIAMETER 2,000 ΜM AT A GIVEN FLOW RATE ($Q_{A\text{-}S}$). 48

FIGURE 14: (LEFT): CJM DEVICE FOR ANTISOLVENT PRECIPITATION IS SHOWN IN THREE PARTS; A) THE SOLVATED LIGNIN WAS INJECTED THROUGH A CAPILLARY, B) THE ANTISOLVENT WAS INJECTED AROUND THE CAPILLARY, C) THE PRECIPITATED CLP WAS COLLECTED. (RIGHT) A CLOSE VIEW OFF (LEFT) PART A, SHOWING THE GLASS CAPILLARY INSERTED INTO THE FERRULE TO GENERATE A WATER-TIGHT CONCENTRIC CAPILLARY FOR CJM. 49

FIGURE 15: IMAGE OF AN INTERFACE BETWEEN AN OIL DROPLET (20 ML) AND A BOROSILICATE GLASS SLIDE (22 X 22 MM). 52

FIGURE 16: A) SCHEMATIC DIAGRAM OF A 3-D PRINTED STAND TO ALLOW COVERSLIPS TO BE BALANCED FOR CONTACT ANGLE MEASUREMENT, CONSTRUCTED FROM POLY (LACTIC ACID). B) A DROPLET OF SUNFLOWER OIL INTRODUCED TO A GLASS COVERSLIP SUPPORTED BY THE 3-D PRINTED STAND IN A DISTILLED WATER. 53

FIGURE 17: PDMS CAST HYDRODYNAMIC FLOW-FOCUSING DEVICE WITH A CHANNEL WIDTH OF 600 ΜM, SHOWING DROPLET FORMATION. DROPLETS ARE FORMED OF A DISPERSED PHASE (Q_D) IN A CONTINUOUS PHASE (Q_C) APPLIED USING SYRINGES. CHANNEL HEIGHT WAS 150 ΜM. 56

FIGURE 18: STEPS FOR FLOW FIELD VISUALISATION USING CROSS-CORRELATION IMAGING OF FLUIDS CONTAINING DISPERSED COLLOIDS. A) FLUID WITH DISPERSED POLY(STYRENE) PARTICLES PASSING THROUGH A MICROFLUIDIC CHANNEL. B) THE CHANNEL ROTATED TO VERTICAL AND THE MEAN INTENSITY OF EACH PIXELS ACROSS THE IMAGE CORRESPONDING TO ANY STATIC FEATURES WAS SUBTRACTED LEAVING A SPECKLE PATTERN CAUSED BY PARTICLE LIGHT SCATTERING. C) CROSS-CORRELATION PLOT SHOWING VECTORS DUE TO MOTION OF SPECKLE PATTERN (GREEN) AND REMOVED VECTORS DUE TO BROWNIAN MOTION (ORANGE). D) A FLOW FIELD MADE OF AN AVERAGE OF 400 CROSS-CORRELATION IMAGES. WHITE ARROWS INDICATE DIRECTION OF FLOW, AND SCALE BAR IS ACCURATE FOR ALL IMAGES IN THE FIGURE.....58

FIGURE 19: LIGNIN-RICH ORGANOSOLV BIORESIDUE PREPARED FROM CBS BEFORE (LEFT) AND AFTER (RIGHT) REMOVAL OF THE LIPID FRACTION. 60

FIGURE 20: FTIR ABSORBANCE SPECTRA (4,000 – 800 CM^{-1}) OF CBS-LC(RED/TOP DATA TRACE) AND COMMERCIALLY AVAILABLE KRAFT LIGNIN (BLACK/BOTTOM DATA TRACE) AS REFERENCE. THE DATA TRACES WERE SHIFTED VERTICALLY TO FACILITATE COMPARISON.....64

FIGURE 21: FTIR ABSORBANCE SPECTRUM OF AN ORGANOSOLV EXTRACTED RESIDUE OF CBS. CBS-LC (BLACK, CENTRAL) SPECTRA ARE COMPARED TO THE SPECTRA OF A HEXANE WASH. INDICATED ARE THE SOLUBLE (GREY, SOLID) AND INSOLUBLE (BLACK, TOP) FRACTIONS OF A HEXANE WASH. 65

FIGURE 22: FTIR ABSORBANCE SPECTRUM OF A HEXANE-SOLUBLE LIPID FRACTION OF A BIORESIDUE OF COCOA BEAN SHELL. 66

FIGURE 23: MASS SPECTRUM OF ISOPROPYL MYRISTATE ON A NORMAL PHASE MASS SPECTRUM. LIPID WAS SEPARATED FROM A CRUDE BIORESIDUE OF COCOA SHELL ON A RXI SIL-MS COLUMN IN GRADIENT MODE BETWEEN 120 AND 300 °C AT A RAMP OF 10 °C PER MINUTE. THE MASS SPECTRUM WAS OBTAINED BY ELECTROSPRAY IONISATION AT 70 MV, WITH AN INTERFACE TEMPERATURE OF 250 °C. KEY FRAGMENT ASSIGNMENT OF THE MOLECULE (TOP RIGHT). PEAKS WITH AN ASTERISK (*) DENOTE REARRANGEMENTS OF FRAGMENTS. SPECTRUM WAS COMPARED TO THE NIST DATABASE TO AID IDENTIFICATION. 68

FIGURE 24: MASS SPECTRUM OF OCTADECENOIC ACID ETHYL ESTER ON A NORMAL PHASE MASS SPECTRUM. LIPID WAS SEPARATED FROM A CRUDE BIORESIDUE OF COCOA SHELL ON A RXI SIL-MS COLUMN IN GRADIENT MODE BETWEEN 120 AND 300 °C AT A RAMP OF 10 °C PER MINUTE. THE MASS SPECTRUM WAS OBTAINED BY ELECTROSPRAY IONISATION AT 70 MV, WITH AN INTERFACE TEMPERATURE OF 250 °C. KEY FRAGMENT ASSIGNMENT OF THE MOLECULE (TOP RIGHT). PEAKS WITH AN ASTERISK (*) DENOTE REARRANGEMENTS OF FRAGMENTS. SPECTRUM WAS COMPARED TO THE NIST DATABASE TO AID IDENTIFICATION. 69
FIGURE 25: MASS SPECTRUM OF TETRADECENOIC ACID TRIMETHYLSILYL ESTER ON A NORMAL PHASE MASS SPECTRUM. LIPID WAS SEPARATED FROM A CRUDE BIORESIDUE OF COCOA SHELL, HYDROLYSED, AND REACTED WITH A DONOR OF TRIMETHYLSILANE FOR 60 MINUTES AT 60 °C, BEFORE SEPARATION ON A RXI SIL-MS COLUMN IN GRADIENT MODE BETWEEN 120 AND 300 °C AT A RAMP OF 10 °C PER MINUTE. THE MASS SPECTRUM WAS OBTAINED BY ELECTROSPRAY IONISATION AT 70 MV, WITH AN INTERFACE TEMPERATURE OF 250 °C. KEY FRAGMENT ASSIGNMENT OF THE MOLECULE (TOP RIGHT). PEAKS WITH AN ASTERISK (*) DENOTE REARRANGEMENTS OF FRAGMENTS. SPECTRUM WAS COMPARED TO THE NIST DATABASE TO AID IDENTIFICATION. 70
FIGURE 26: MASS SPECTRUM OF ETHYL HEXADECANOATE ON A NORMAL PHASE MASS SPECTRUM. LIPID WAS SEPARATED FROM A CRUDE BIORESIDUE OF COCOA SHELL ON A RXI SIL-MS COLUMN IN GRADIENT MODE BETWEEN 120 AND 300 °C AT A RAMP OF 10 °C PER MINUTE. THE MASS SPECTRUM WAS OBTAINED BY ELECTROSPRAY IONISATION AT 70 MV, WITH AN INTERFACE TEMPERATURE OF 250 °C. KEY FRAGMENT ASSIGNMENT OF THE MOLECULE (TOP RIGHT). PEAKS WITH AN ASTERISK (*) DENOTE REARRANGEMENTS OF FRAGMENTS. SPECTRUM WAS COMPARED TO THE NIST DATABASE TO AID IDENTIFICATION. 71
FIGURE 27: MASS SPECTRUM OF ETHYL OLEATE ON A NORMAL PHASE MASS SPECTRUM. LIPID WAS SEPARATED FROM A CRUDE BIORESIDUE OF COCOA SHELL ON A RXI SIL-MS COLUMN IN GRADIENT MODE BETWEEN 120 AND 300 °C AT A RAMP OF 10 °C PER MINUTE. THE MASS SPECTRUM WAS OBTAINED BY ELECTROSPRAY IONISATION AT 70 MV, WITH AN INTERFACE TEMPERATURE OF 250 °C. KEY FRAGMENT ASSIGNMENT OF THE MOLECULE (TOP RIGHT). PEAKS

WITH AN ASTERISK (*) DENOTE REARRANGEMENTS OF FRAGMENTS. SPECTRUM WAS COMPARED TO THE NIST DATABASE TO AID IDENTIFICATION. 72
FIGURE 28: SOLUBILITY BY SOLIDS CONTENT OF LIGNIN-RICH CBS BIORESIDUE IN A SELECTED RANGE OF COMMON SOLVENTS. ERROR BARS INDICATE ± 1 STANDARD DEVIATION. 74
FIGURE 29: DROPLET FORMATION CONDITIONS AND IMPACT OF AN ETHANOL:WATER MIXTURE DISPERSED IN AN OIL PHASE WITH FLOW CONDITIONS OF 10 ML MIN^{-1} (INTERNAL) AND 40 ML MIN^{-1} (EXTERNAL). 78
FIGURE 30: CBS ANTISOLVENT PRECIPITATION IN A WATER CONTINUOUS PHASE (D = 5 ML MIN-1, C = 15 ML MIN^{-1}, DEMONSTRATING PRECIPITATION OF PARTICLES FROM DISPERSION. TIME AS FOLLOWS AT 10 X MAGNIFICATION: (A), T = 0.00 S, (B), T = 0.05 S. 80
FIGURE 31: CONTACT ANGLE OF PDMS CONTAINING SEVERAL TREATMENT METHODS IMMEDIATELY AFTER TREATMENT, AND 24 H AFTER TREATMENT. SAMPLES ARE THE RESULTS OF 10 REPEATS, AND ERROR BARS ARE ± 2 STANDARD DEVIATIONS. 82
FIGURE 32: EXAMPLE OF A POLYELECTROLYTE TREATED HFF DEVICE AT 10 X MAGNIFICATION. IN (A) CBS (5 MG ML^{-1}) IN ETHANOL DISPERSED PHASE (5 ML MIN^{-1}) IS PASSED THROUGH THE DEVICE IN A WATER CONTINUOUS PHASE (30 ML MIN^{-1}), IN (B), A HYDROPHOBIC DOMAIN INHIBITING DROPLET FORMATION WITHIN THE DEVICE. 83
FIGURE 33: SCHEMATIC OF A T-JUNCTION DERIVED CJM DEVICE, CONSISTING OF A CONCENTRIC INTERNAL GLASS TUBE WITH AN OUTER FLOW PHASE. A PHASE CONTAINING THE SOLVENT STREAM (Q_{SOL}) IS PASSED THROUGH A COAXIAL CHANNEL OF INTERNAL DIAMETER 200 ΜM AND EXTERNAL DIAMETER 2,000 ΜM. 87
FIGURE 34: PARTICLE DIAMETER INTENSITY DISTRIBUTIONS OF PARTICLE DISPERSIONS FORMED IN TWO INDEPENDENTLY ASSEMBLED CJM DEVICES, RIG 1 (BLUE) AND RIG 2 (RED). DISPERSED LIGNIN IN ETHANOL (5 MG ML^{-1}) WAS FIXED AT A VOLUMETRIC FLOW RATE OF 50 ML MIN^{-1}, WITH A CONTINUOUS PHASE OF WATER FIXED AT 300 ΜL MIN^{-1}, RESULTING IN A *RE* VALUE OF 100. RECORDED AS TRIPLICATED REPEATS OF EACH SYSTEM USING TWO SEPARATELY PREPARED CJM DEVICES. ERROR BARS DENOTE ± 1 STANDARD DEVIATION. 90

FIGURE 35: PARTICLE DIAMETER INTENSITY DISTRIBUTIONS OF PARTICLE DISPERSIONS FORMED IN CJM RIG 1 & 2. DISPERSED LIGNIN IN ETHANOL (5 MG ML^{-1}) WAS FIXED AT 50 ML MIN^{-1}, WITH A CONTINUOUS PHASE OF WATER FIXED AT 1,100 ML MIN^{-1}, CORRESPONDING TO A *RE* VALUE OF 329. DISTRIBUTIONS WERE COLLECTED AS TRIPLICATED REPEATS OF TWO SEPARATE SAMPLES. ERROR BARS DENOTE ± 1 STANDARD DEVIATION. 92

FIGURE 36: INFLUENCE OF DILUTION ON COLLOIDAL PARTICLE DISPERSIONS. A STOCK SOLUTION (5 MG ML^{-1}) OF AQUEOUS CLPS FORMED VIA ANTISOLVENT PRECIPITATION (R = 0.5, RE = 573) (BLUE) WERE DILUTED 1 IN 10 IN DISTILLED WATER (RED). ERROR BARS DENOTE ± 2 STANDARD DEVIATIONS 93

FIGURE 37: PARTICLE DIAMETER INTENSITY DISTRIBUTIONS OF PARTICLE DISPERSIONS FORMED IN THE CJM DEVICE. DISPERSED LIGNIN IN ETHANOL (5 MG ML^{-1}) WAS FIXED AT 50 ML MIN^{-1}, WITH A CONTINUOUS PHASE OF WATER VARIED, GENERATING REYNOLDS VALUES OF 129, 186, AND 358. DISTRIBUTIONS WERE COLLECTED AS TRIPLICATED REPEATS OF TWO SEPARATE SAMPLES. ERROR BARS DENOTE ± 1 STANDARD DEVIATION. 96

FIGURE 38: REPRESENTATION OF THE EFFECT OF *RE* ON THE FEATURES OF A PARTICLE DIAMETER DISTRIBUTION MEASURED BY DLS USING TWO FEATURES OF THE DISTRIBUTION; AVERAGE PARTICLE DIAMETER (LEFT), AND PARTICLE DISTRIBUTION SPAN (RIGHT). ERROR BARS DENOTE ± 1 STANDARD DEVIATION. 97

FIGURE 39: A) IMPACT OF *RE* VALUE ON (CUMULANTS) AVERAGE PARTICLE DIAMETER OF CLPS MEASURED BY DLS. PARTICLES WERE FORMED BY THE CJM AT A SERIES OF *R* VALUES. ERROR BARS DENOTE ± 1 STANDARD DEVIATION. B) IMPACT OF *R* (0.1, 0.5, 1) ON (CUMULANTS) AVERAGE PARTICLE DIAMETER OF COLLOIDAL PARTICLE DISPERSIONS AS DETERMINED BY DLS AT A SERIES OF *RE* VALUES BETWEEN 50 AND 500. ERROR BARS INDICATE ± 1 STANDARD DEVIATION. 100

FIGURE 40: (A) IMPACT OF *RE* ON SPAN AVERAGE PARTICLE DIAMETER OF CLPS MEASURED BY DLS. PARTICLES WERE FORMED BY A CJM AT A SERIES OF *R* VALUES. ERROR BARS DENOTE ± 1 S.D. (B) IMPACT OF *R* (0.1, 0.5, 1) ON (SPAN OF PARTICLE DISPERSIONS AS DETERMINED BY DLS AT A SERIES OF *RE* VALUES BETWEEN 50 AND 500. ERROR BARS INDICATE ± 1 STANDARD DEVIATION. 103

FIGURE 41: A SURFACE PLOT SHOWING THE INFLUENCE OF TWO PROCESSING PARAMETERS *RE* AND *R,* ON AVERAGE PARTICLE DIAMETER IN NM. THE PARTICLE DISPERSION IS FORMED IN A CJM DEVICE VIA ANTISOLVENT PRECIPITATION OF AN EXTRACT OF CBS IN WATER. OVERLAID ON THE SURFACE PLOT (RED) ARE OTHER DATA NOT USED IN GAINING THE PLOT, TO ASSESS THE PREDICTIVE ABILITY OF THE SURFACE PLOT. 105

FIGURE 42: PARTICLE DIAMETER INTENSITY DISTRIBUTIONS OF PARTICLE DISPERSIONS FORMED IN A CJM DEVICE. DISPERSED LIPID-REMOVED LIGNIN IN ETHANOL (5 MG ML^{-1}) WAS FIXED AT 50 ML MIN^{-1}, WITH A CONTINUOUS PHASE OF WATER FIXED AT 1,100 ML MIN^{-1}, CORRESPONDING TO A *RE* VALUE OF 329. DISTRIBUTIONS WERE COLLECTED AS TRIPLICATED REPEATS OF TWO SEPARATE SAMPLES. ERROR BARS DENOTE ± 1 STANDARD DEVIATION. 109

FIGURE 43: PARTICLE DIAMETER INTENSITY DISTRIBUTIONS OF PARTICLE DISPERSIONS FORMED IN A CJM DEVICE. DISPERSED LIPID-REMOVED LIGNIN BIORESIDUE IN ETHANOL (5 MG ML^{-1}) WAS FIXED AT 50 ML MIN^{-1}, WITH A CONTINUOUS PHASE OF WATER VARIED, GENERATING REYNOLDS VALUES OF 129, 186, AND 358. DISTRIBUTIONS WERE COLLECTED AS TRIPLICATED REPEATS OF TWO SEPARATE SAMPLES. ERROR BARS DENOTE ± 1 STANDARD DEVIATION. 111

FIGURE 44: REPRESENTATION OF THE EFFECT OF *RE* ON THE FEATURES OF A PARTICLE DIAMETER DISTRIBUTION MEASURED BY DLS USING TWO FEATURES OF THE DISTRIBUTION; AVERAGE PARTICLE DIAMETER (LEFT), AND PARTICLE DISTRIBUTION SPAN (RIGHT). THE DATA DEMONSTRATE THE DIFFERENCE BETWEEN LIPID-CONTAINING (RED) AND LIPID REMOVED (BLUE) LIGNIN SOLUTIONS. ERROR BARS DENOTE ± 1 STANDARD DEVIATION. 111

FIGURE 45: ZETA POTENTIAL OF CLPS IN A SUSPENSION FORMED AT A *RE* VALUE OF 100 IN A CJM WITH A HYDRODYNAMIC RADIUS OF 235 NM. THE PH RANGE WAS ADJUSTED USING SODIUM HYDROXIDE AND HYDROCHLORIC ACID. ERROR BARS DENOTE ± 1 STANDARD DEVIATION. 113

FIGURE 46: MICROSCOPY IMAGES OF COLLOIDAL PARTICLE SUSPENSIONS (INITIAL AVERAGE DIAMETER OF 600 NM) PRECIPITATED FROM ETHANOL-DISSOLVED COCOA BEAN SHELL EXTRACT (5 MG ML^{-1}) IN DISTILLED WATER AT *RE* OF 29, *R* = 0.5) AND STORED AT 20 °C FOR 30 DAYS WITH PERIODIC MICROSCOPY OF 10 ML ALIQUOTS AT PH 4.3. 115

FIGURE 47: DROPLET DIAMETER OF OIL IN WATER EMULSION (1:9 W/W) WITH CBS-LC CLPS (220 NM, 0.5 WT%) FORMED VIA HIGH SHEAR MIXING AT 9,000 RPM FOR 2 MINUTES. OIL PHASE IS SUNFLOWER OIL, AND AQUEOUS PHASE IS DISTILLED WATER. SAMPLES WERE STORED AT 4 °C, AND DIAMETER OF DROPLETS WERE MEASURED AT 0 H (BLACK) ,24 H (GREY, LONG DASH) AND 5 DAYS (GREY, SHORT DASH). 120
FIGURE 48: DROPLET DIAMETER DISTRIBUTION OF DISPERSIONS OF AN OIL IN WATER EMULSION (1:9 W/W) WITH CBS-LC CLPS (220 NM) DISPERSED AT 0.5 WT% (LEFT) AND 1 WT% (RIGHT).EMULSIONS WERE FORMED VIA HIGH SHEAR MIXING AT 14,000 RPM FOR 5 MINUTES. OIL PHASE IS SUNFLOWER OIL, AND AQUEOUS PHASE IS DISTILLED WATER. SAMPLES WERE STORED AT 4 °C, AND DIAMETER WAS MEASURED AT 0 H (BLACK) AND 24 H (BLUE). 121
FIGURE 49: DROPLET DIAMETER DISTRIBUTION OF DISPERSIONS OF AN OIL IN WATER EMULSION (1:9 W/W) WITH CBS-LC CLPS (220 NM) DISPERSED AT 0.5 WT%. EMULSIONS WERE FORMED VIA HIGH SHEAR MIXING AT 9,000 RPM FOR TWO MINUTES (BLACK), 14,000 RPM FOR 5 MINUTES (RED), AND VIA SONICATION AT 750 W FOR 25 SECONDS, CONSISTING OF 5 X 5 S PULSES, WITH A 5 SECOND REST PERIOD. OIL PHASE IS SUNFLOWER OIL, AND AQUEOUS PHASE IS DISTILLED WATER. SAMPLES WERE STORED AT 4 °C, AND DIAMETER WAS MEASURED AT 0 H (LEFT), 5 DAYS (CENTRE), AND 10 DAYS (RIGHT). 124
FIGURE 50: SURFACE TENSION OF AN AQUEOUS ETHANOL AND WATER (50:50 V/V) DROPLET CONTAINING A 3.5 MG ML^{-1} CBS-LC CLP DISPERSION IN THE PRESENCE OF CLPS (GREEN) AND WITH THEM REMOVED BY FILTRATION (RED). 126
FIGURE 51: CONTACT ANGLE MEASUREMENTS OF A DROPLET OF SUNFLOWER OIL ON A SERIES CBS-LC EXTRACT SURFACES, WITH PRECIPITATION CONDITIONS ALTERED TO REPLICATE PRECIPITATION OF LIGNIN USING ANTISOLVENT PRECIPITATION. 129
FIGURE 52: A PICTORIAL REPRESENTATION OF THE HYPOTHESISED POSITION OF LIPIDS, REPRESENTED BY A POLAR HEAD GROUP (RED) AND A HYDROPHILIC TAIL GROUP (BLACK) RELATIVE TO A PRECIPITATED COLLOIDAL LININ-RICH PARTICLE (BROWN) IN AQUEOUS DISPERSION. 130
FIGURE 53: PARTICLE INTENSITY DISTRIBUTIONS OF COLLOIDAL PARTICLE DISPERSIONS FORMED IN A COAXIAL JET MIXER. THE DISPERSED PHASE CONTAINING 5 MG ML^{-1} LIPID-REMOVED LIGNIN IN

ETHANOL WAS FIXED AT 50 ML MIN^{-1}, AND WATER VARIED CORRESPONDING TO A REYNOLDS NUMBER RANGE OF 500. FOLLOWING THE EVAPORATION OF THE SOLVENT, 5 ML OF AQUEOUS DISPERSION WAS ADDED TO 5 ML OF SUNFLOWER OIL, AND THE WATER WAS REMOVED BY HEATING. THE SOLUTION WAS FILTERED WITH A 1 MM SYRINGE FILTER. THE ERROR BARS DENOTE ± 1 STANDARD DEVIATION.....131

FIGURE 54: A PICTORIAL REPRESENTATION OF THE HYPOTHESISED POSITION OF LIPIDS, REPRESENTED BY A POLAR HEAD GROUP (RED) AND A HYDROPHILIC TAIL GROUP (BLACK) RELATIVE TO A PRECIPITATED COLLOIDAL LININ-RICH PARTICLE (BROWN) IN A SUNFLOWER OIL DISPERSION....132

FIGURE 55: DYNAMIC LIGHT SCATTERING DIAMETER INTENSITY DISTRIBUTIONS OF DISPERSIONS OF POLYSTYRENE NANOPARTICLES; A STANDARD TRACER PARTICLE FOR GPV SHOWING A DIAMETER OF 220 NM (BLACK). FOR COMPARISON, CLPS FORMED USING ANTISOLVENT PRECIPITATION AND DISPERSED IN AQUEOUS (RED), AND NON-AQUEOUS (SUNFLOWER OIL, BLUE) PHASES ARE SHOWN. 136

FIGURE 56: LINE PROFILE MATRIX SHOWING THE DISTRIBUTION OF MAGNITUDE OF VELOCITY VECTORS ACROSS THE WIDTH OF A 600 MM CHANNEL WITH 3.5 MG ML^{-1} CBS-LC CLPS OF AVERAGE DIAMETER 220 NM IN AQUEOUS DISPERSION FLOWING AT 10 AND 50 ML MIN^{-1}, WITH FRAME RATES OF 2000 AND 10,000 FPS. LINE PROFILES TAKEN FROM A CROSS-CORRELATION PLOT MEAN AVERAGE OF 400 FRAMES. 139

FIGURE 57: A SERIES OF SCATTER PLOTS, SHOWING VELOCITY MAGNITUDES OF VECTORS IN A MEAN CROSS-CORRELATION PLOT AT 50 AND 400 FRAMES, CREATED BY GPV. THREE SYSTEMS; AQUEOUS DISPERSED CBS-LC DERIVED CLPS, SUNFLOWER OIL DISPERSED CBS-LC DERIVED CLPS, AND POLYSTYRENE DERIVED PARTICLES ARE SHOWN. 141

FIGURE 58: A FLOW FIELD FORMED BY DISPERSING CLPS AT 3.5 WT% IN DISTILLED WATER AND PASSING THE FLUID THROUGH A PDMS CHANNEL WITH A WIDTH OF 600 MM AND A HEIGHT OF 150 MM, AND A FLOW RATE OF 50 ML MIN^{-1}. IMAGE AN AVERAGE PROFILE OF 200 FRAMES. 143

FIGURE 59: A FLOW FIELD FORMED BY DISPERSING CLPS AT 3.5 WT% IN SUNFLOWER OIL AND PASSING THE FLUID THROUGH A PDMS CHANNEL WITH A WIDTH OF 600 MM AND A HEIGHT OF 150 MM AND A FLOW RATE OF 50 ML MIN^{-1}. IMAGE AN AVERAGE PROFILE OF 200 FRAMES. 144

FIGURE 60: A FLOW FIELD FORMED BY DISPERSING CLPS AT 3.5 WT% IN SUNFLOWER OIL AND PASSING THE FLUID THROUGH A PDMS CHANNEL WITH A DIAMETER OF 600 MM AND A HEIGHT OF 150 MM AND A FLOW RATE OF 50 ML MIN^{-1}. IMAGE AN AVERAGE PROFILE OF 200 FRAMES. 147
FIGURE 61: SCHEMATIC DIAGRAM SHOWING THE IMAGE ANALYSIS METHOD BY CROSS-CORRELATION FOR MAPPING THE FLOW FIELD OF A DROPLET MOVING IN A CHANNEL, BY MOVING LATER FRAMES OF THE SAME DROPLET TO A CONSISTENT PART OF THE FIELD OF VIEW.....149
FIGURE 62: SCHEMATIC DIAGRAM SHOWING THE IMAGE ANALYSIS METHOD BY CROSS-CORRELATION FOR MAPPING THE FLOW FIELD OF A DROPLET MOVING IN A CHANNEL BY AVERAGING SUCCESSIVE DROPLETS PASSING THE SAME AREA IN SPACE.....149
FIGURE 63: DISTRIBUTION PLOT OF THE VECTOR MAGNITUDE AND DIRECTION GENERATED BY CROSS-CORRELATION OF A SCATTERING PATTERN INDIRECTLY CAUSED BY A COLLOIDAL PARTICLE DISPERSION. THE PARTICLES ARE SIMULTANEOUSLY DISPERSED IN A DROPLET AND A CONTINUOUS PHASE IN A MICROCHANNEL. FOR EACH DROPLET, ONE IMAGE IS TAKEN AS IT REACHES A SET POINT IN A FIELD OF VIEW. 150
FIGURE 64: DISTRIBUTION PLOT OF THE VECTOR MAGNITUDE AND DIRECTION GENERATED BY CROSS-CORRELATION OF A SCATTERING PATTERN INDIRECTLY CAUSED BY A COLLOIDAL PARTICLE DISPERSION. THE PARTICLES ARE SIMULTANEOUSLY DISPERSED IN A DROPLET AND A CONTINUOUS PHASE IN A MICROCHANNEL. FOR EACH DROPLET, TWO SUCCESSIVE IMAGES ARE TAKEN AS IT REACHES A SET POINT IN A FIELD OF VIEW.....151
FIGURE 65: DISTRIBUTION PLOT OF THE VECTOR MAGNITUDE AND DIRECTION GENERATED BY CROSS-CORRELATION OF A SCATTERING PATTERN INDIRECTLY CAUSED BY A COLLOIDAL PARTICLE DISPERSION. THE DISPERSION IS SIMULTANEOUSLY DISPERSED IN A DROPLET AND A CONTINUOUS PHASE IN A MICROCHANNEL. FOR EACH DROPLET, FOUR SUCCESSIVE IMAGES ARE TAKEN AS IT REACHES A SET POINT IN A FIELD OF VIEW. 152
FIGURE 66: A SERIES OF IMAGES SHOWING A DROPLET OF WATER DISPERSED IN OIL CAPTURED AS 1 FRAME (LEFT), AND THE MEAN OF TWO FRAMES (CENTRE) AND FOUR FRAMES (RIGHT). 154
FIGURE 67: AN AVERAGE FLOW FIELD PROFILE OF 100 DROPLETS OF WATER IN A SUNFLOWER OIL CONTINUOUS PHASE IN A MICROCHANNEL. EACH VECTOR IS GENERATED FROM TWO PAIRS OF

TWO SUCCESSIVE (FOUR IN TOTAL) IMAGES BY CROSS-CORRELATION PER DROPLET. THE FLOW RATE OF THE DISPERSED PHASE IS 8 ML MIN^{-1}, AND THE CONTINUOUS PHASE IS 42 ML MIN^{-1}. THE AQUEOUS CONTAINS 3.5 WT%. LIPID CONTAINING (LC) COLLOIDAL LIGNIN PARTICLES OF AVERAGE DIAMETER 220 NM. THE EXTERNAL PHASE OF SUNFLOWER OIL CONTAINS THE SAME TRACER PARTICLES AT A CONCENTRATION OF 3.5 WT%. 156

FIGURE 68: LINE PROFILE MATRIX SHOWING THE DISTRIBUTION OF MAGNITUDE OF VELOCITY VECTORS ACROSS THE WIDTH OF A 600 MM CHANNEL WITH 3.5 MG ML^{-1} CBS-LC CLPS OF AVERAGE DIAMETER 220 NM IN SUNFLOWER OIL DISPERSION FLOWING AT 50 ML MIN^{-1}, AT 2000 FPS. LINE PROFILES TAKEN FROM A CROSS-CORRELATION PLOT MEAN AVERAGE OF 400 FRAMES. 157

FIGURE 69: GHOST PARTICLE VELOCIMETRY IMAGE OF A WATER DROPLET IN A SUNFLOWER OIL CONTINUOUS PHASE, FORMED AT A FLOW RATE OF 42 ML MIN^{-1} (SUNFLOWER OIL), AND 8 ML MIN^{-1} (WATER). BOTH FLUIDS HAVE CLPS FORMED FROM CBS-LC EXTRACT AT 3.5 MG ML^{-1}. THE FLOW FIELD HAS A LINEAR TRANSFORMATION APPLIED OF V = $^{-}$5.5 PX/FRAME TO EACH VECTOR TO EXTRICATE THE FINE MOVEMENT FROM THE OVERALL MOVEMENT OF THE FRAME. IMAGE (RIGHT) SHOWS THE RECIRCULATION PATTERN FROM DROPLET FORMATION. 159

FIGURE 70: LATERAL COMPONENT OF RECIRCULATION CAUSED BY THE FORMATION OF A DROPLET IN A MICROCHANNEL, TAKEN FROM A LINE PROFILE (RIGHT, DASHED). 160

FIGURE 71: A BAR CHART DEMONSTRATING THE FORMATION TIME OF A DROPLET OF WATER IN OIL UNDER CONDITIONS OF 8 ML MIN^{-1} FLOW RATE OF WATER, AND 42 ML MIN^{-1} FLOW RATE OF SUNFLOWER OIL. WHERE CLPS ARE DISPERSED, THEY ARE DONE SO AT A CONCENTRATION OF 3.5 MG ML^{-1}. ERROR BARS REPRESENT ± 2 STANDARD DEVIATIONS FROM THE MEAN. 164

FIGURE 72: 9:1 WATER IN OIL EMULSIONS FORMED USING WATER AND ISOPROPYL MYRISTATE FORMED BY PROCESSING WITH A HIGH SHEAR MIXER AT 9,000 RPM FOR 2 MINUTES 171

FIGURE 73: LINEAR REGRESSION ANALYSIS OF THE SIZE-WEIGHTED INTENSITIES OF PARTICLE DISPERSIONS FORMED IN TWO CJM DEVICES PLOTTED AS AN X,Y SCATTER. TRENDLINE INDICATES THE LINEAR CORRELATION BETWEEN THE TWO DEVICES (Y = 1.10X), R^2 0.99. 188

FIGURE 74: LINEAR REGRESSION ANALYSIS OF THE SIZE-WEIGHTED INTENSITIES OF PARTICLE DISPERSIONS FORMED IN A CJM DEVICE FROM TWO SEPARATE MATERIAL EXTRACTIONS, PLOTTED

AS AN X,Y SCATTER. TRENDLINE INDICATES THE LINEAR CORRELATION BETWEEN THE TWO DEVICES (Y = 1.10X), R^2 0.98. 189
FIGURE 75: LINEAR REGRESSION ANALYSIS OF THE SIZE-WEIGHTED INTENSITIES OF PARTICLE DISPERSIONS FORMED IN A CJM DEVICE FROM A MATERIAL EXTRACTION CONTAINING LIPID FRACTION (X) AGAINST A HEXANE WASHED LIPID REMOVED VERSION (Y), PLOTTED AS AN X,Y SCATTER. TRENDLINE INDICATES NO LINEAR CORRELATION BETWEEN THE TWO DEVICES (Y = 1.07X), R^2 0.70.....190
FIGURE 76: LINEAR REGRESSION ANALYSIS OF THE SIZE-WEIGHTED INTENSITIES OF PARTICLE DISPERSIONS FORMED IN A CJM FROM TWO BATCHES OF LIPID-REMOVED LIGNIN-RICH COCOA BEAN EXTRACT. TRENDLINE INDICATES THE LINEAR CORRELATION BETWEEN THE TWO DEVICES (Y = 0.94 X). 191

List of Tables

TABLE 1: COMMON SOURCES OF LIGNOCELLULOSIC MATERIALS AND THEIR LIGNIN CONTENT AS REPORTED IN LITERATURE. 4

TABLE 2: REPRESENTATIVE EXAMPLE OF THE COMPOSITION OF COCOA SHELL. REPORTED WT% VALUES NORMALISED TO 100 % TO ALLOW COMPARISON. 5

TABLE 3: INFRARED ABSORPTION WAVELENGTHS ASSOCIATED WITH THE PRESENCE OF LIGNIN AND ASSOCIATED CO-EXTRACTIVES, WITH ASSIGNMENTS TO ASSOCIATED FUNCTIONAL GROUPS AND MOLECULAR VIBRATION (AR – AROMATIC, BR – BROAD PEAK). 8

TABLE 4: FRAGMENT IONS FORMED IN MASS SPECTROMETRY ASSOCIATED WITH THE PRESENCE OF FUNCTIONAL GROUPS IN A MOLECULE (HAYNES 2011). 11

TABLE 5: EXAMPLES OF MICROFLUIDIC MICROREACTOR DEVICES USED FOR ANTISOLVENT PRECIPITATION FOR PARTICLE FORMATION. MANY EXAMPLES OF SOLVENT-ANTISOLVENT PRECIPITATION ARE IN DRUG MANUFACTURE. A SERIES OF GEOMETRIES HAVE DEMONSTRATED DROPLET/PARTICLE FORMATION. 16

TABLE 6: SIEVE CLASS FRACTIONS OF CBS REPORTED AS A WEIGHT PERCENTAGE. 34

TABLE 7: RECOVERY OF LIGNIN FROM A COCOA BEAN SHELL FEEDSTOCK AS DETERMINED BY THE ACETYLBROMIDE ASSAY, WHERE CONCENTRATIONS WERE CALCULATED USING A MOLAR ABSORPTIVITY CONSTANT OF 2.36 L CM^{-1} G^{-1}. 62

TABLE 8: COMPOUNDS IDENTIFIED BY MASS SPECTROMETRY SPECTRA AS PRESENT IN THE LIPID FRACTION OF THE BIORESIDUE OF CBS. 67

TABLE 9: VISCOSITY OF SOLUTIONS OF LIGNIN DISSOLVED IN ETHANOL AND PRECIPITATED IN WATER AT A SERIES OF VOLUMETRIC CONCENTRATIONS AT 20 °C. 75

TABLE 10: DENSITY OF SOLUTIONS OF LIGNIN DISSOLVED IN ETHANOL AND PRECIPITATED IN WATER AT A SERIES OF VOLUMETRIC CONCENTRATIONS AT 20 °C. 75

TABLE 11: COEFFICIENTS OF THE SURFACE PLOT MODEL CALCULATED FROM EXPERIMENTAL DATA. THE VALUES OF EACH COEFFICIENT DETAILED IN EQUATION 3.1 ARE SHOWN BELOW. 105

TABLE 12: STATISTICAL FIT ASSESSMENT OF THE MODEL TRAINED EARLIER IN THE SECTION, INCLUDING THE SUM OF SQUARES DUE TO ERROR (SSE), AND ROOT MEAN SQUARED ERROR (RMSE). 106

TABLE 13: CONTACT ANGLE OF DROPLETS AGAINST A CBS-EXTRACTED LIGNIN SUBSTRATE DEPOSITED ONTO A BOROSILICATE GLASS SLIDE. 127

TABLE 14: AVERAGE VELOCITY OF VECTORS (PX/FRAME) ACROSS A MEAN CROSS-CORRELATION PLOT (400 FRAMES) OF AN AQUEOUS DISPERSION OF CBS-LC PARTICLES WITH A FLOW RATE OF 50 ML MIN^{-1} AND FRAME RATE OF 2000 FPS. 142

TABLE 15: AVERAGE VELOCITY VALUES OF LIGNIN COLLOIDAL PARTICLES DISPERSED IN A SERIES OF PHASES, COMPARED TO THEORETICAL VALUES. 145

TABLE 16: THE EFFECT OF MOLECULAR SURFACTANT PRESENTS IN BOTH LIGNIN BIORESIDUE AND SUNFLOWER OIL ON THE ABILITY TO TRANSFER CLPS INTO A SUNFLOWER OIL-BASED PHASE. ... 162

TABLE 17: EMULSION CONTENTS FOR FIGURE BELOW ALL EMULSIONS ARE 1:9 IPM:WATER, WITH 0.5 WT% STABILISER 170

List of abbreviations and symbols

Abbreviations

Ar – Aromatic (C_6H_6-) substituent

Br – Broad (refers to FTIR peak)

CAM – Contact angle measurement

CBS – Cocoa bean shell

CBS – LC – Lipid containing cocoa bean shell extract

CBS – LR – Lipid removed cocoa bean shell extract

CLP – Colloidal lignin-rich particles

CJM – Coaxial jet mixer

DLS – Dynamic Light Scattering

FFA – Free fatty acids

FTIR – Fourier transform infrared spectroscopy

GC-MS – Gas chromatography coupled mass spectrometry

GPV – Ghost Particle Velocimetry

HFF – Hydrodynamic flow-focusing device

PIV – Particle image velocimetry

s.d – Standard Deviation from the mean

TSO – Treated sunflower oil

Symbols (units)

d – Diameter (m)

E – Applied field (V m^{-1})

I.D. – Internal diameter

L – Length (m)

M – Concentration (mol dm^{-3})

m – Molecular mass (g mol^{-1})

O.D. – Outer diameter

px – Pixels (-)

Q – Flow rate (m^3 s^{-1})

R – Flow velocity ratio

Re – Reynolds number

St – Stokes drag force (N)

Stk – Stokes number (-)

T – Temperature (°C)

u – Transverse velocity (m s^{-1})

v – Velocity (m s^{-1})

V_t – Sedimentation velocity (m s^{-1})

x – Distance (m)

z – Charge on an ion (F)

ε_m – Absorptivity (L cm^{-1} g^{-1})

ε_r - Dielectric constant (F m^{-1})

γ – Surface tension (mN m^{-1})

ζ - Zeta potential (V)

η – Viscosity (Pa s)

θ – Angle (°)

λ – Wavelength (m)

υ – Velocity (m s^{-1})

ρ – Density (kg m^{-3})

A - Cross-sectional area (m^2)

Constants

g – Acceleration due to gravity (9.81 m s^{-1})

1. Introduction

The overall aim of the research presented in this thesis was to develop a continuous process for functional colloid production from a lignin-rich biowaste. Using a naturally derived co-product from a food-grade process offered a great opportunity for valorisation of waste within the framework of circular economy. Colloidal particles with tuneable wetting properties are in high demand in several fields, including for emulsion research, and those using flow fields for diagnostic measurements. The focus of this research was to generate a single crude extract, from which different functional particles could be prepared by altering the precipitation conditions, and removal of basic componentry. Following mild solvent extraction, the crude lignin-rich bioresidue was characterised and precipitated into microparticles. The microparticles were characterised by light scattering and microscopy under storage to observe aggregation before applications in emulsions as Pickering stabilisers and as particles for tracing fluid flows were explored.

The remainder of this chapter addresses the research fundamentals and reviews the relevant literature for this PhD.

1.1. Lignin

1.1.1. Introduction

Lignin, as a co-product from industrial processes, is anticipated to be generated as a component in biomass on a scale of 225 million tons per annum by 2030 (Bajwa *et al.* 2019). Whilst 50 - 70 million tonnes per annum is derived from paper pulping (Luo and Abu-Omar 2017), there are several other large sources such as from brewer's spent grain, with 39 million tonnes produced per year (Lynch *et al.* 2016), and from chocolate

production, which produces 6 million tonnes of cocoa bean shell (CBS) per year (Tayyib 2022). Lignin is a key component of the secondary cell wall of vascular plants, comprising 15 - 40% dry weight (Mahmood *et al.* 2016). Presently, 98 % is incinerated for energy recovery (Kai *et al.* 2016). The naturally complex structure of the biopolymer lignin, comprised principally of aromatically linked monomers (Lievonen *et al.* 2016), has both hydrophobic and hydrophilic characteristics. It is formed principally of three aromatic phenylpropanoid polymer derivatives: p-coumaryl, coniferyl, and sinapyl alcohol. These are often referred to in literature by their monomeric form of p-hydroxyphenyl (H), guaiacyl (G), and syringyl (S) respectively (Vanholme *et al.* 2008), shown in Figure 1.

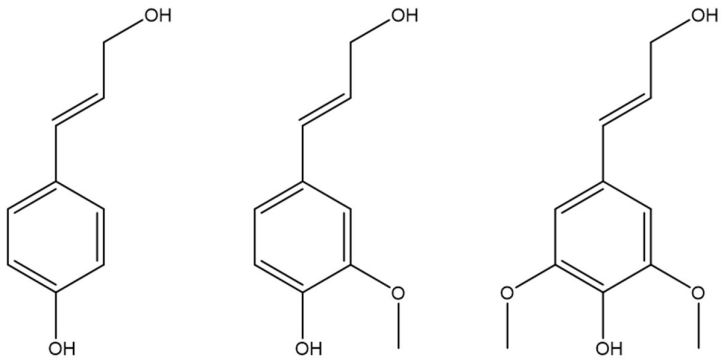


Figure 1: Skeletal formula of key monomeric components of the biomolecule lignin. Shown are p-coumaryl (H, left), guaiacyl (G, centre), and sinapyl (S, right) alcohols.

The monolignols are arranged in an irregular pattern to form the biomolecule lignin, in a structure of the form shown in Figure 2. The monolignols are highlighted within the structure.

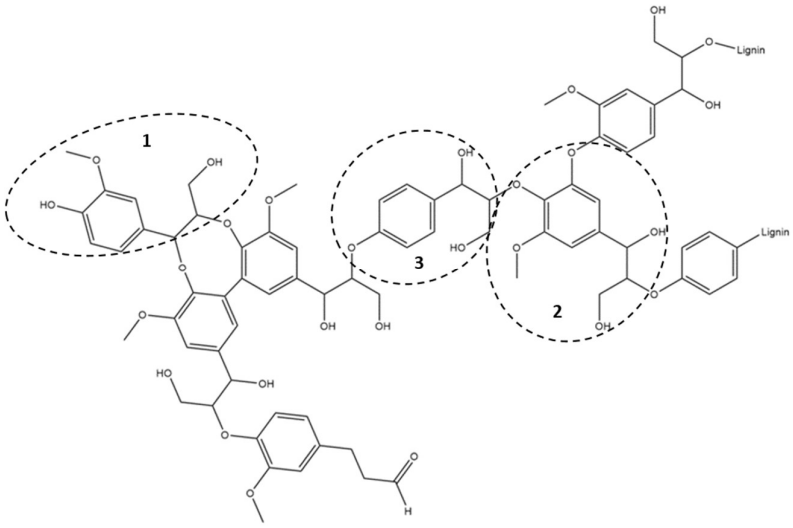


Figure 2: Partial idealised structure of lignin, showing the common sub-units; guaiacyl (1), syringyl (2) and coumaryl (3) alcohols. Redrawn and adapted from (Holladay et al. 2007).

Owing to this abundance, an increasing amount of research focuses on developing materials for consumer goods using feedstocks containing lignin, such as colloidal particles for use as a non-toxic material on the micro- and nanoscale. This demonstrates the great potential of this feedstock, particularly as a potential value-added material valorised from waste (Schneider *et al.* 2021).

1.1.2. Sources of lignin

The largest source of lignin is the paper industry, where the lignocellulosic co-product Kraft lignin is traditionally combusted to provide heat, for the main objective of pulp production for paper (Suhas *et al.* 2007). Lignin is scarcely utilised in consumer goods at present, despite factors which make it suitable for valorisation, such as antioxidancy (Pan *et al.* 2006), and zero calorific content (Holloway *et al.* 1978). By utilising lignin as a commercially viable product, other waste-generating supply chains can be disrupted,

resulting in lower net energy consumption. Whilst lignin is commercially available as a refined alkali powder as a co-product of the Kraft process, there are other forms which represent more suitable feedstocks for consumer goods applications. Kraft lignin is highly water-soluble (Beisl *et al.* 2017), which makes it unsuitable for use as a fat mimetic in consumer goods. This is owing to the production, which generates low molecular weight (M_W) biopolymer, and highly alkali-treated lignin (Suhas *et al.* 2007), (Derkacheva and Sukhov 2008). The negative aspects of using lignin derived from the Kraft process is that the digestion process changes the functionality of lignin. Whilst lignin derived from the Kraft process is water soluble, lignin from other extraction methods are insoluble in water. Examples of feedstocks from a range of sources are detailed in Table 1.

Table 1: Common sources of lignocellulosic materials and their lignin content as reported in literature.

Source	Description	Lignin content (wt %)	Reference
Cocoa pod (husks)	By-product of manufacturing	14-28	(Daud *et al.* 2013), (Lu *et al.* 2017)
Hardwood	Wood derived lignocellulosic material	15-40	(Calvo-Flores and Dobado 2010)
Broad-leaf plants	Non wood derived lignocellulosic material	18-25	(Cao *et al.* 2018)
Wheat straw	Co-product of wheat harvesting	11-26	(Zhang *et al.* 2022)
Coffee waste	By-product of household use	20-27	(Gould *et al.* 2016)
Black liquor	Industrial co-product	27-33	(Zhu and Theliander 2015)
Needle-leaf plants	Non wood derived lignocellulosic material	27-33	(Cao *et al.* 2018)

Softwoods	Wood derived lignocellulosic material	30	(Calvo-Flores and Dobado 2010)
Corn Stover	Residue from the production of grain	34	(Mensah *et al.* 2021)

Cocoa production is an established food process in which CBS is a co-product. CBS represents a useful feedstock owing to its status as a waste product, as well as its hydrophobic componentry. This allows for applications such as Pickering particles, which will be discussed later in this literature review. There is great research interest in the application of CBS and related derivatives (Balentic *et al.* 2018).

A common method of utilising lignin is as a colloidal particle derived from lignin-rich extract. These extracts are shown to have great versatility, such as UV-blocking ability (Qian *et al.* 2015), heavy metal absorption (Zhang *et al.* 2019), and antimicrobial properties (Greco *et al.* 2019). Given that lignin is presently part of the food system, and lignin is reported to have a low cytotoxicity (Siddiqui *et al.* 2020), valorisation of CBS to generate lignin-rich extracts for particle production represents a logical step.

1.1.3. Lignin-rich bioresidues and their extraction

Alongside lignin, other components of the feedstock such as lipids and cellulose are often extracted as co-products. Table 2 shows a representative range of the composition of CBS(Chung *et al.* 2003; Daud *et al.* 2013).

Table 2: Representative example of the composition of cocoa shell. Reported wt% values normalised to 100 % to allow comparison.

Component	Composition of CBS (wt%)
Hemicellulose	30-37
Cellulose	36
Klason Lignin	15-29
Amino Acid	8.6
Lipid	8.9
Ash	8.5-12
Glucose	16

Chung *et al.* (2003) reported that, despite the high amount of lignin recovery quoted in the Klason lignin test, it is strongly possible that sugars and other tannin-like structures underwent condensation as a by-product of the test reagent. Whilst this fits the definition of Klason lignin, the structure is vastly different from the intended definition of lignin, comprised principally of monolignols, as described by Calvo-Flores and Dobado (2010). Klason lignin refers to the residue formed when conducting the Klason lignin quantification test. This contains not only the digested monolignols, but additionally any sugars which can polymerise under the conditions and reagents of the test, notably in the presence of concentrated sulfuric acid. This additionally explains that often reported yields exceed 100 % (Chung *et al.* 2003; Huijgen *et al.* 2012), as sugars such as hydroxymethylfurfural (HMF) can convert into hexoses, causing identification as both Klason lignin and glucose.

Extraction methods, such as those of Stewart *et al.* (2016), produce water-insoluble lignin, with potential applications as fat mimetics, and other food filler particles. Additional benefits such as their zero calorific content add to the desirability of valorisation of this waste stream. However, one drawback is the lack of commercial availability of water-insoluble lignins.

The method selected for this research is organosolv extraction. As discussed in Merklein *et al.* (2016), organosolv requires pre-treatment with acid to depolymerise lignin. One advantage of organosolv, in comparison to some other methods such as the Kraft process, is that it does not necessitate the use of reagents or conditions which have potential to functionalise the extract. However, yield is not often high, unless long extraction times of at least 24 hours are employed. There are several examples of extraction using an ethanol/water mixture with an acid catalyst (Zhao et al. 2009), (Tian et al. 2017), where, to avoid excessive digestion of the polymer, dilute concentrations of mineral acid in the order of 1 - 3 M are used. This is in accordance with the work of Sun *et al.* (2005), who argue that greater concentrations of acid or base have potential to digest cellulose preferentially over lignin. Excessive degradation of lignin biopolymer has the potential to functionalise the polymer as part of the extraction fundamentally changing the chemical properties, and thus removing its status as a naturally derived product.

1.1.4. Quantifying physical-chemical characteristics of lignin extracts

1.1.4.1. Infrared spectroscopy

A common chemical fingerprinting technique used to identify the presence of a compound is Fourier-transform infrared absorption spectroscopy (FTIR). This technique bombards a sample with infrared radiation and measures the response from the sample. Chemical bonds within the sample interact with discrete wavelengths of light to undergo three principal actions; stretching, vibration, and rotation (Burrows *et al.* 2013b), and thus these wavelengths are not transmitted. An analysis of the transmittance spectra can offer an indication of the functional groups, and thus to build a description of the molecule

present. Absorption wavenumbers from the literature used to identify lignin and other common co-extractives are listed in Table 3.

Table 3: Infrared absorption wavelengths associated with the presence of lignin and associated co-extractives, with assignments to associated functional groups and molecular vibration (Ar – Aromatic, Br – Broad peak).

Wavenumber (cm^{-1})	**Bond**	**Type**	**Source**	**Assignment**	**Reference**
3300-2550 (br)	O-H	Stretch	Water	Carboxylic acid, free OH from water	(Smith 2011)
2920	C-H	Vibration	Seeds	Lipids >C10	(Barsberg *et al.* 2018; Sathawong *et al.* 2018; Mao *et al.* 2023)
2850	C-H	Vibration	Roasted Coffee, seeds	Lipids >C10	(Wang and Lim 2012; Barsberg *et al.* 2018)
1725- 1735	C=O	Stretch	Softwood, Hardwood	Unconjugated	(Sharma *et al.* 2000; Kubo and Kadla 2005; Mao *et al.* 2023)
1610-1690	C-C (Ar)	Vibration	Lignin	Aromatic skeletal vibration	(Nada *et al.* 1998)
1658-1660	C=O, C=C	Stretch	Softwood, Hardwood	Conjugated systems C=O stretch, C=C stretching from Fatty acids	(Sharma *et al.* 2000; Wang and Lim 2012)
1603-1605	C-C (Ar), C=O	Vibration, stretch	Hardwood	Aromatic skeletal vibration, with C=O stretching, Lignin	(Kubo and Kadla 2005; Chen *et al.* 2016)
1590				C=C aromatic skeletal vibration	(Shen *et al.* 2008)
1546		Bending	Wood	N-H, Amide bending	(Gupta *et al.* 2015)
1510-1512	C-C (Ar)	Vibration	Softwood	Aromatic skeletal, Lignin	(Martinez *et al.* 1999; Chen *et al.* 2016)
1458	C-H	Deformation	Wheat straw	Alkyl chain	(Chen *et al.* 2016)
1427	C-C (Ar)	Vibration	Softwood, Hardwood	Lignin	(Chen *et al.* 2016)
1390	COO-	Vibration	Wood	Carboxylate	(Peltre *et al.* 2017)
1375	C-H, O-H	Stretch	Softwood, Hardwood	Aliphatic hydrocarbon, phenolic O-H	(Boeriu *et al.* 2004)
1320-1340	C-O	Stretch	Wheat straw	Syringyl C-O stretch from ring breathing	(Chen *et al.* 2016; Lu *et al.* 2017)
1270-1275	C-O	Ring breathing	Softwood, Hardwood	Guaiacyl unit ring breathing	(Lourençon *et al.* 2015)

1265-9	C-C	Ring breathing	Softwood, Hardwood	Guaiacyl ring breathing	(Boeriu *et al.* 2004; Kubo and Kadla 2005; Chen *et al.* 2016; You and Xu 2016)
1230-1235	C-O	Vibration	Wood	Guaiacyl unit	(Lu *et al.* 2017)
1155	C-O	Stretch	Wheat straw	Asymmetric stretch of ester	(Chen *et al.* 2016)
1140	C-H, C=O	Stretch	Softwood, Hardwood	In-plane deformation of Guaiacyl ring, unconjugated C=O stretch	(Martinez *et al.* 1999; Boeriu *et al.* 2004)
1126	C-O	Stretch	Softwood	Ether C-O-C link stretch	(Nada *et al.* 1998)
1116-9	C-H (Ar)	Deformation	Hardwood, Wheat straw	Aromatic C-H deformation in syringyl ring	(Kubo and Kadla 2005; Chen *et al.* 2016)
1025 -1035	C-O, C-H (Ar)	Vibration	Lignin	Aromatic ring and primary alcohol	(You and Xu 2016; Lu *et al.* 2017)
817	C-H (Ar)	Vibration	Softwood	C-H out of plane 2, 5, 6	(Boeriu *et al.* 2004)

1.1.4.2. Gas chromatography and mass spectrometry

A common complimentary method used to identify unknown components in mixtures is the coupled techniques of gas chromatography and mass spectrometry (GC-MS). Gas chromatography in its reverse phase consists of a long column through which an analyte is passed. The tubing is coated internally with a non-polar molecule (stationary phase) and with a polar carrier gas (Roessner *et al.* 2011). When a mixture is heated and inserted into the column, each component has a level of interaction with both the polar carrier phase and the non-polar stationary phase. The relative amount of interaction for each substance is determined by the molecule itself; for example, a pure hydrocarbon (C_nH_{2n+2}) will interact with the stationary phase with greater severity than a more polar molecule, due to van der Waals forces. The process of association and dissociation from both the polar and stationary phases will separate the components in the mixture as they travel down the column, separating compounds with a unique retention time in the column.

Following separation, mass spectrometry is utilised to identify the separated components via fragmentation. Owing to inductive (electron density distribution through sigma bonds based on electronegativity) and mesomeric (pi electron delocalisation creating an uneven distribution of electrons through resonance), effects, the intermolecular forces of a molecule are not equal. As a result, the fission of a molecule is not a random process. Mass spectrometry utilises this feature by bombarding molecules with an electronic pulse, causing fragmentation of a molecule. The fragmented ions are then accelerated along a curved path using a magnetic field, which separates the fragment ions based on their mass (m) to charge (z) ratio (Burrows *et al.* 2013a). This ratio and the relative intensities of the m/z values are unique to a single molecule, which can then be used to assign the identity of the initial molecule. Key fragment ions used for the identification of functional groups are listed in Table 4.

Table 4: Fragment ions formed in mass spectrometry associated with the presence of functional groups in a molecule (Haynes 2011).

m/z	Fragment
14	$[CH_2]^{+\cdot}$
15	$[CH_3]^{+\cdot}$
29	$[CH_3CH_2]^{+\cdot}$
43	$[CH_3CH_2CH_2]^{+\cdot}$
73	$[C_3H_5O_2]^{+\cdot}$, $[Si(CH_3)_3]^{+\cdot}$

In addition to the identification of key fragment ions, the molecular weight can be determined as the molecular ion, M+·. This is often the largest m/z value, although the presence of heteroatoms with significant isotope abundances can lead to the formation of M+1 and higher value species, (Burrows *et al.* 2013a). After establishing the molecular ion, further assignment involves assessing the intensity of fragmentation peaks such as m/z = 15 ($-CH_3$) from the molecular ion. This indicates the presence of such a group at the end of a molecule. Through the correlation of the molecular ion with crucial fragmentation peaks, complete identification of a molecule is achievable, encompassing highly informative features like E/Z isomerisation of unsaturated bonds. When combining the separation ability of gas chromatography and the identification of mass spectrometry, this technique offers the capacity to identify the presence of low molecular weight co-extractives in the bioresidue extracted from CBS.

1.2. Microparticle production

1.2.1. Antisolvent precipitation

This section details the literature relevant to generating microparticles, including their methods and applications. One suggested method of valorisation of CBS is in the form of colloidal lignin particles (CLPs), which have been reported in the literature suggesting applicability ranging from protective coatings (Farooq *et al.* 2020) to emulsion stabilisation (Cuthill *et al.* 2021). Current methods of generating CLPs are generally discontinuous batch processes. Examples of this are present in literature, such as ground coffee waste derived lignin (Gould *et al.* 2016), and Kraft lignin (Lievonen *et al.* 2016). Particles, characterised by size, morphology, and electrophoretic potential, were reported to be roughly 500 nm in diameter, and spherical, with stability against aggregation in the pH range of 3 - 7. There are some examples of using natural feedstocks for particle production via antisolvent precipitation, with Jiang *et al.* (2021) using pressures of 1 MPa and H_2O/THF to prepare lignin particles from corncob, birch wood and pine wood.

For scalable production and implementation into consumer products however, continuous production of colloidal particles represents a crucial step, as it would allow for refinement and standardisation of factors such as size, stability, and componentry. Reported techniques include spray drying by Ago *et al.* (2016) and aerosol processes such as that of Bangalore Ashok *et al.* (2020). The latter production method uses an aerosol process to dry particles from an initial batch-made precursor slurry. An initial dissolved solution is formed by dissolution of Kraft ('lignoboost') lignin in an ethanol/Tetrahydrofuran solution before beaker precipitation in excess water.

Lignin has also been demonstrated to have wetting properties which are dependant on the production method. Farooq *et al.* (2020) report that solvent choice can affect the wetting

properties of lignin. Particles precipitated against THF and acetone have indicated that contact angle can be modified, reporting angles of 21.5 ° and 32.9 ° respectively. This suggests that there is additional functionality present with precipitation conditions. Consequently, using a liquid-liquid system develops the potential for further modification of colloidal particles using antisolvent precipitation. Another benefit of using a liquid-liquid mixing system is the ability to vary the conditions within the system with greater control. The use of a micromixer allows for additional specificity, as indicated by Lintinen *et al.* (2018). Although many examples of particle precipitation have been demonstrated on the batch scale, it has been noted that the conditions for local supersaturation of solvent associated with nucleation dominated particle growth are technically difficult to achieve (Saad and Prud'homme 2016).

Lu *et al.* (2021) prepared colloidal particles from corn stover using THF as an extraction solvent, producing particles on the 250 - 1000 nm scale using dialysis. Particles were generated with no modification, and the process was tuneable by modification of the dialysis tubing. This offers greater tuneability of dispersion size than previously described batch processes.

Once formed through methods such as antisolvent precipitations, microparticles in dispersion are stabilised by the presence of charges in aqueous systems, and the charges in water align to surround a particle to form an electrostatic layer, see Figure 3. Where these are densely packed, this causes layers of charges alternating positive and negative, and the point at which associated charges are present is called the diffuse layer.

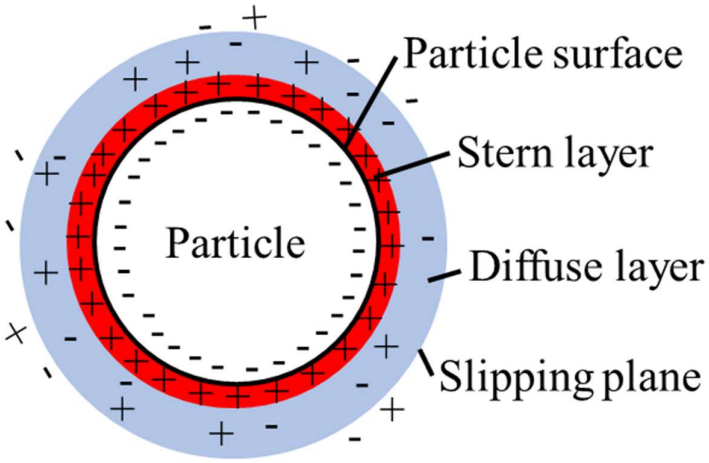


Figure 3: Representation of the arrangement of charges around a particle in an aqueous system. The charges in water rearrange to reduce electrostatic repulsion.

1.2.2. Hydrodynamic flow-focusing devices

Microfluidics offers a highly monodisperse approach to droplet formation on the microlitre scale, and represents a novel route to particle formation through manipulation of multi-phase systems (Whitesides 2006). There are several examples of applications of this type of system, where a particle is precipitated from solution through addition of a solute immiscible phase, miscible with the solvent system, see Table 5.

The use of small flow-focusing devices and the benefit of small sample volumes on the ability to ensure thorough mixing on a nanosecond timescale was discussed by Knight *et al.* (1998). An example of a flow-focusing device forming droplets is shown in Figure 4. A hydrodynamic flow focusing (HFF) device was used in this thesis for droplet formation from a dispersed phase in which lignin is soluble and the continuous phase in which lignin is insoluble.

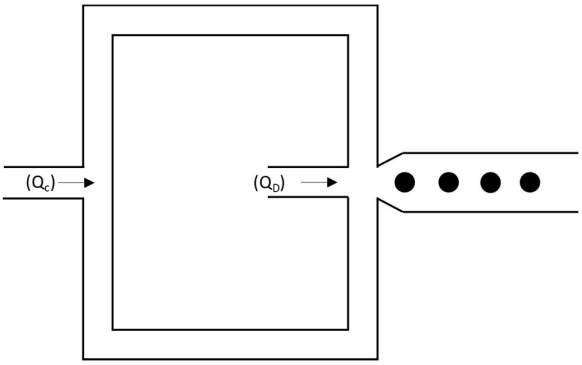


Figure 4: Schematic of a hydrodynamic flow-focusing (HFF) device. Continuous phase Qc forms a channel to envelop the dispersed phase Q_D from either side.

Using a HFF device represents a development on both of the systems employed by Stewart *et al.* (2014) and Ju *et al.* (2019). The development of the former work comes with the design of continuous process allowing for size control of particles in formation, whilst a more complex bioresidue builds on the T-Junction work of Ju et al where the antisolvent precipitation of colloidal particles from a lignin bioresidue was reported, but the presence of additional surfactant aided the droplet formation mechanisms.

As reported by Anna and Mayer (2006), there are four distinct methods of droplet breakup in a flow-focusing device: geometry controlled (squeezing); thread formation (threading); dripping, and jetting. For generation of monodisperse droplets capable of undergoing simple liquid antisolvent precipitation, dripping represents the most suitable model for droplet formation and is shear dominated in terms of droplet breakup (Collins *et al.* 2015). This is predominantly because of high monodispersity, and the ability to generate at a high frequency.

The use of simple solvent-antisolvent systems for microparticle production has found application in pure systems across a range of solutes and device geometries, see Table 5. In each system, droplets of solvent in antisolvent are initially formed, which then undergo

antisolvent precipitation. This technique offers extremely high monodispersity (Cramer *et al.* 2004), as the particle size is determined by the droplet formation before anti-solvent precipitation.

Table 5: Examples of microfluidic microreactor devices used for antisolvent precipitation for particle formation. Many examples of solvent-antisolvent precipitation are in drug manufacture. A series of geometries have demonstrated droplet/particle formation.

Device	Channel	Particle	Solvent	Antisolvent	Reference
PDMS	Flow-focusing	PLGA-PEG	Acetonitrile	Water	(Karnik *et al.* 2008)
PDMS	Flow-focusing	Mesoporous silica	Ethanol:$HCl_{(aq)}$	Hexadecane	(Lee *et al.* 2008a; Lee *et al.* 2008b)
PMMA	Y-junction	Hydrocortisone	Ethanol	Water	(Ali *et al.* 2009)
Stainless Steel	Y-junction	Cefuroxime axetil	Acetone	Isopropyl ether	(Wang *et al.* 2010)
Stainless Steel	T-Junction	Cefuroxime axetil	Acetone	Isopropyl ether	(Zhang *et al.* 2011)
PDMS	Flow-focusing	Glycine	Water	Isopropyl alcohol	(Bhamidi *et al.* 2015)
Borosilicate Glass	Flow-focusing	Hydrocortisone	Ethanol: water	Water	(Odetade and Vladisavljevic 2016)
Glass	Flow-focusing	Fenofibrate	Ethyl acetate	Water	(Lorenz *et al.* 2018)

Given there are several examples of ethanol and water systems, and lignin is demonstrated as ethanol-soluble (Stewart *et al.* 2014), it is expected that an ethanol dispersed phase and a water continuous phase will act appropriately as an antisolvent, forming lignin particles in a water suspension.

1.2.3. Coaxial Jet Mixing

One suggested application for lignin is as a colloidal sized particle. Recent studies have suggested that the impact of using lignin in this way is two-fold; that it can act as a value-

added co-product from an existing industrial side chain (Aro and Fatehi 2017), and that there is potential to displace current colloidal particles with poorer environmental credentials.

Examples of this include as an additive to sunscreens, as discussed by Ju *et al.* (2019) and Tran *et al.* (2021). This would represent a significant improvement in the sustainability of sunscreens, typically utilising metal particles such as zinc or tin oxide, which has been described as having a deleterious effect on coral reefs. Another application is as a dopant in hydrophobic coatings, where Henn *et al.* (2021) report water contact angles of 120 ° alongside increased solvent tolerance with CLP addition.

An application which is tentatively suggested, although yet to be fully developed, is as a Pickering particle to be used in foods and other consumer products for emulsion stabilisation (Sekeri *et al.* 2020; Yaqoob *et al.* 2021). Lignin-rich bioresidues would make an ideal candidate in such formulations, owing to their indigestibility (Holloway *et al.* 1978) and zero calorific value. This would make them a useful filler particle.

One way of fully utilising the versatility of lignin as a resource would be to enable liquid-liquid mixing for multiple antisolvents. The use of antisolvent precipitation for colloidal particle formation has found wide application in inorganic systems, with several studies reporting control on morphology and size, among other characteristics. Coaxial jet mixing (CJM) devices have been indicated as a preferred micromixer for formation of microparticles through antisolvent precipitation. Another method of using solvent-antisolvent precipitation to form colloidal particles is through coaxial jet mixing (CJM). An early example of microparticles formed using a CJM is silver (Baber *et al.* 2015), generating particles with a size range of 2 – 20 nm. This uses a displacement reaction

between silver nitrate and sodium borohydride, where the silver is reduced to form nanoparticles.

More recent literature has utilised CJM devices for flash nanoprecipitation of organic particles (Bovone *et al.* 2019). This represents a step from inorganic to organic systems, as polymeric systems indicate greater versatility, advancing towards more amorphous systems. Recent studies have investigated applying these techniques to single component drug systems for nanoparticle precipitation.

CJM devices are notably more suitable for high flow rates, allowing comparatively greater flow rate velocities and Reynolds number compared to PDMS based microfluidic devices (Kim *et al.* 2012; Lim *et al.* 2014), although still on the microfluidic scale of less than 1 mL min^{-1}. They are also far more resistant to fouling (Bovone *et al.* 2019) than HFF and other small microfluidic devices and their equivalents. The schematic in Figure 5 demonstrates precipitation in a CJM. A dispersed phase containing a lignin solute is passed through an internal capillary, and an external continuous phase in which the solvent is miscible, but the lignin solute is insoluble, is introduced. The collapsing of the jet causes mixing of the phases, causing the solute to be expelled from the solution to form particles.

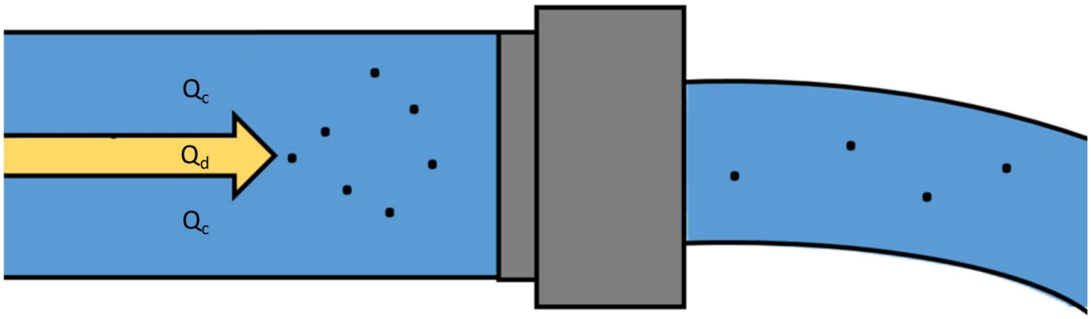


Figure 5: Schematic diagram of antisolvent precipitation. Solute containing phase Q_d jet is fed into a continuous phase Q_c, in which the solvent is miscible, but the solute is insoluble. This results in precipitation.

A large body of literature indicates the importance of characterising the device used for particle production, and the effect of three major factors are stressed, namely Reynolds number, flow velocity ratio, and concentration of solute. Abdelkarim *et al.* (2021), amongst others indicate that particle size and morphology are highly dependent on these factors.

Reynolds number calculation

The Reynolds number (*Re*) is termed as the ratio of inertial forces to viscous forces. This has previously been used in the context of antisolvent precipitation for particle production (Lim *et al.* 2014). The calculation of *Re* is given in the general form of Equation 1.1:

$$Re = \frac{\rho u L}{\eta} \tag{1.1}$$

Where ρ is the density (kg m^{-3}), u is the characteristic velocity (m s^{-1}), L is the characteristic length scale, chosen as the diameter of tubing (m), and η is viscosity (Pa s).

The characteristic velocity is defined as the quotient of flow rate of the combined streams (Q; $m^3\ s^{-1}$) and the cross-sectional area of tubing at the point of the solvent and antisolvent mixing (A; m^2). Substituting this into equation 1.1 allows *Re* to be calculated by 1.2:

$$Re = \frac{\rho_c Q L}{\eta_c A} \tag{1.2}$$

Lim *et al.* (2014) additionally discuss the effect of turbulent/laminar transition at low flow rate velocity ratios; the flow rate ratio, *R*, defines the velocity of the dispersed phase to the continuous phase and is given by Equation 1.3:

$$R = \frac{u_d}{u_c} \tag{1.3}$$

1.3. Emulsions

The size ranges of CLPs are often on the micro-scale of 1 - 10 μm. One common application of these particles is as emulsifier, where they can produce Pickering stability (Aveyard *et al.* 2003).

1.3.1. Emulsion stabilisation

The classical method for stabilisation of two immiscible phases as an emulsion is to use a surfactant. Surfactants are single molecules consisting of a polar head group and a non-polar tail group, which are covalently bonded (Knill and Kennedy 1999). The presence of a surfactant molecule at an interface allows for the polar head group to reach into the opposite phase and stabilise the aqueous phase, and the non-polar tail group to stabilise the non-polar phase. This reduces the interfacial tension, which is turn decreases the force

acting to separate the phases. Destribats *et al.* (2014) demonstrate that by changing the contact angle of Pickering particles around 90 °, the phase of emulsion can be altered, i.e., the formation of a water-in-oil (w/o) emulsion or an oil-in-water (o/w) can be directed.

It is widely accepted that Pickering stabilisation, achieved through stabilising an emulsion by adsorption of particles to an interface, requires particles which have a contact angle of around 90 °, to allow partial wetting of both the hydrophilic and hydrophobic phases (Binks and Lumsdon 2000). As a result of the size of particles being much greater than that of a surfactant, the energy required to remove an absorbed particle from a surface is much greater than that of a surfactant molecule. This can be referred to as a kinetically stabilised emulsion (Fotis Spyropoulos *et al.* 2019). For a spherical particle, the amount of energy holding it at an oil/water interface depends on the contact angle and is at a maximum when the contact angle between the particle and the phases is 90 °. Previous studies have demonstrated a static contact angle of 76 ° of CBS with water, illustrating appropriate wetting properties for stabilising oil in water (o/w) emulsions.

For this, particles used are typically one order of magnitude smaller than the emulsion droplet size desired (F. Spyropoulos *et al.* 2019).

One drawback of using a surfactant molecule to stabilise an interface is that surfactants are in an equilibrium between adsorption and desorption. Whilst the surfactant is not at the interface, coalescence can begin. One mechanism of the breaking down of emulsions is ‘Ostwald ripening’, in which a mass transfer of the dispersed phase occurs due to Laplace pressure from smaller to larger droplets (F. Spyropoulos *et al.* 2019).

1.3.2. Pickering stabilisation

As a dispersion of two immiscible fluids; a non-aqueous phase in an aqueous phase, oil in water (o/w) or vice-versa water in oil (w/o), emulsions are thermodynamically unstable, and phase separation is thermodynamically preferred. This is due to the intermolecular forces such as hydrogen bonding being able to occur in water, however is not possible in non-aqueous phases. By moving from a system where non-aqueous phases and aqueous phases are separated, the system is overall at a lower energy. To prevent phase separation, the energy difference resulting from aqueous and non-aqueous phases mixed must be reduced. This can be achieved using surfactants or by using Pickering particles. Surfactants are molecules which consist of both a polar and non-polar region covalently bonded in the same molecule. These inhibit phase separation by simultaneously interacting with the aqueous and non-aqueous phases. This reduces the interfacial tension between the aqueous and non-aqueous phases and reducing the forces driving phase separation. Using surfactants has some noted drawbacks, with one of them being that the surfactants, particularly ones with a low molecular weight, are prone to dissociation from the interface between the polar and non-polar phases due to thermal energy present in the system. This is described by the Boltzmann distribution, and necessarily means that there is a fraction of molecules which have an energy greater than the energy given by remaining at the interface, allowing dissociation. At this point, the surfactant is unable to reduce the interfacial tension, and the factors driving phase separation begin to dominate. An alternative method for stabilising emulsions with a much greater stability is by using a small particle with a wetting characteristic which is neither hydrophobic nor hydrophilic. These particles can sit at an oil-water interface and are kinetically stabilised, known as Pickering stabilisation. Due to their significantly larger molecular weight than molecular surfactant, Pickeirng emulsions are significantly

more stable, as the energy required to dissociate them from an interface is significantly larger. There are several natural examples of particles being used for Pickering stabilisation, such as phytosterol used by Lan *et al.* (2020). In this setup, a physical barrier exists between the two phases, leading to a kinetically stabilised system. These systems have wide application in emulsion stabilisation, such as in foods. Figure 6 shows an idealised version of a Pickering stabilised oil in water emulsion.

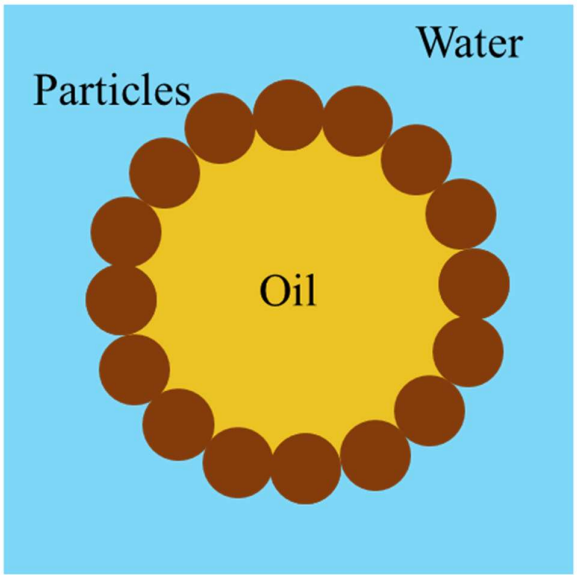


Figure 6: Idealised view of a Pickering stabilised emulsion. An oil phase (yellow) is emulsified in an aqueous continuous phase (blue) using particles which are kinetically stuck at an interface (brown).

Emulsions formed in this way have been shown to have much greater stability than their surfactant stabilised counterparts. Application as a Pickering stabiliser is one example of valorisation of lignin, with several reported examples such as Sipponen *et al.* (2017), and Sekeri *et al.* (2020). Factors such as food grade adjacent status make this a particularly interesting application of lignin. Initial research in using lignin as a Pickering stabiliser used highly processed lignins, with examples such as Yuliestyan *et al.* (2022) and Tian *et al.* (2023) using Kraft lignin. Other research has demonstrated the use of less highly refined lignins for use as a Pickering particle, with examples such as Czaikoski *et al.*

(2020). have developed this further, demonstrating the screening of colloidal particles for use as a Pickering stabiliser. There are many examples of Pickering emulsions used in commercial consumer goods, with an emerging example being hand cream (Peito *et al.* 2022). Pickering emulsions have shown promise, due to their increased stability against coalescence compared to surfactants, and potential to replace synthetic surface-active molecules with more biologically friendly alternatives (Rayner *et al.* 2014).

In addition to stabilising as a Pickering particle, Tortora *et al.* (2014) have suggested that lignin is active under sonochemistry conditions. This offers the potential that lignin could be used to stabilise emulsions by creating a shell which covers droplets, rather than simply kinetically stabilising them.

1.4. Wetting properties of colloidal particles

In addition to the size of particles, wetting properties are a crucial determining factor in using particles to stabilise emulsions.

1.4.1. Contact angle

The work of Lievonen *et al.* (2016) details the formation of colloidal particles, and builds upon this by altering the wetting properties. Bangalore Ashok *et al.* (2020) demonstrate the formation of colloidal particles using an aerosol process, which is shown to produce hydrophobic particles. This is built upon by Gerbin *et al.* (2021), where the surface properties of lignin-rich films are varied. The application is as a coating, however, a way to build on this would be to create liquid-liquid mixing, i.e. form particles in aqueous dispersion by desorption of a solute from a liquid where the solute is soluble to a mixture

where it is insoluble, causing particles to be precipitated. To do this, it would be necessary to create a layer of lignin upon which contact angle can be measured where it is possible to mimic the conditions of antisolvent precipitation, as this would create a similar interface.

One problem of studying nanoscale particles is that direct observation of their behaviour is complex. An example of indirect measurement would be to trap colloids in a gel, and to determine their position at an interface using scanning electron microscopy. This allows for particles on the sub-micron scale to have their wetting properties accurately quantified (Cayre and Paunov 2004). An alternative method for analysis of contact angle is by emulsion stability, where the result of application drives the ability to determine particle functionality. In this, the wetting properties are inferred by application. This could be built upon in two principal ways. One would be an emulsion assay, whereby emulsions comparative to literature are created, and their stability over time is used to infer the properties of particles. A second method is by creating a 50/50 (wt%) o/w system, adding CLPs and forming an emulsion. Using this method, it would be possible to determine the wetting properties by observing the resultant system. An o/w emulsion would indicate that the particles are hydrophilic, whereas a w/o emulsion would indicate the converse, however the presence of any surfactant could affect the ability to use the latter method.

Measurement of contact angle

The ability to form emulsions using Pickering particles has been demonstrated to depend on the three-phase contact angle. The type of emulsion formed in the three-phase contact angle of an oil-particle-water interface governs the ability to form o/w and w/o interfaces (Binks et al. 2013). A general representation of the measurement of contact angle is

depicted in Figure 7. For this analysis, the contact angle was used to infer the polarity of the surface by Young's equation (McClements 2005), with the polarity of the droplet subsequently altered to infer wetting properties.

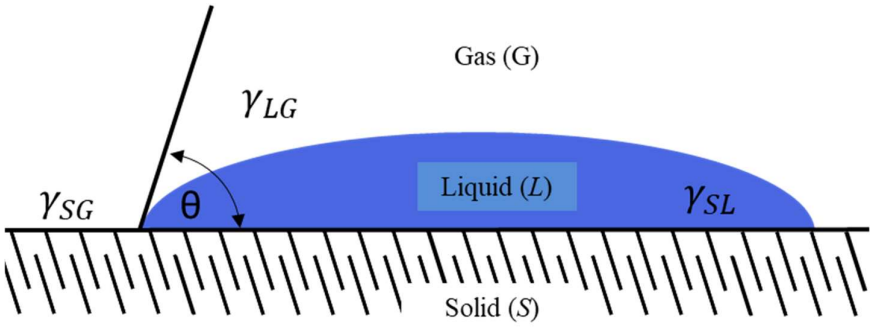


Figure 7: Boundaries between materials for a droplet of liquid on a surface, with interfaces between the solid, liquid, and gas demarked.

To assess the contact angle of a system resembling Figure 7, Young's equation (1.4) is applied in the following manner where γ denotes interfacial tension and θ denotes a contact angle:

$$\gamma_{SG} = \gamma_{SL} + \gamma_{LG}\cos(\theta) \tag{1.4}$$

By evaluating the contact angle, it is possible to quantify differences in surface energy resulting from alternate precipitation conditions. From this, factors such as hydrophobicity or hydrophilicity can be inferred, allowing conclusions about the surface arrangement of the lignin macromolecule to be drawn.

1.5. Flow field analysis in confined flow systems

Experimental visualisation of flows has been sought by tracking the movement of dispersed particles within a flow system. In this way, visualisation of flow fields is a

crucial technique for the understanding of microfluidic processes, as the mixing processes within a system determine performance metrics such as completion time and yield.

Ghost Particle Velocimetry (GPV), discussed in 1.5.2 has been demonstrated as a reliable tool for real-time generation of flow field patterns in continuous flows (Riccomi *et al.* 2018). However, in segmented flow or drop microfluidics, quantifying flow presents challenges due to the lack of a dispersible non-aqueous tracer particle.

One way to generate particles which are capable of being dispersed in non-aqueous phases is the addition of an amphiphile or molecular surfactant, however, the presence of this will alter the interfacial tension, which can further impact the droplet formation time and characteristics.

1.5.1. Flow in confined channels

When considering the laminar flow of a fluid though a channel, there are a series of factors which can affect the profile of flow, shear, viscosity, and density. For a two-dimensional fluid travelling with a constant input velocity flow, Q, the profile should follow a parabolic flow profile condition, Figure 8.

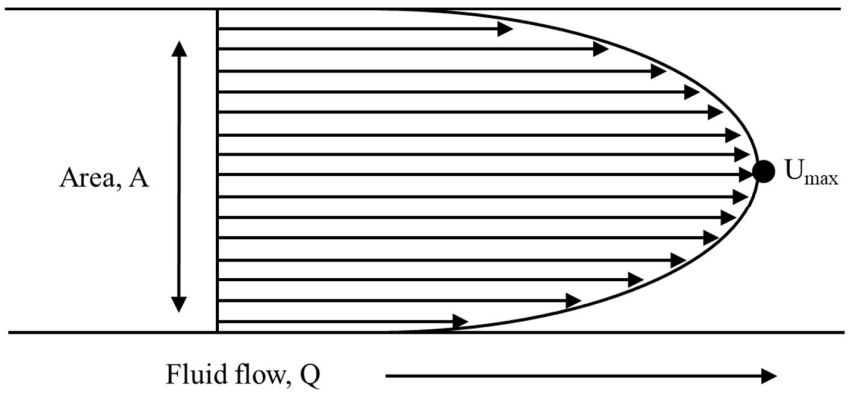


Figure 8: A parabolic flow profile demonstrating the two-dimensional velocity profile of a fluid between two surfaces in a straight channel.

In a flow, the superficial velocity in a channel is given by

$$\bar{v} = \frac{Q}{A} \tag{1.6}$$

Where the superficial velocity in a channel is given by $\bar{v}$ (m s^{-1}), the fluid flow rate is Q (m^3 s^{-1}), and A is the cross section of the channel (m^2).

In a fluid flow, the maximum flow in a channel is given by

$$v_{\max} = \frac{2Q}{A} \tag{1.7}$$

Assuming parabolic flow.

1.5.2. Quantifying flow in micromixers

Microscale particle image velocimetry (μ-PIV) represents the most utilised technique for quantification of flows within a micromixer. PIV typically utilises a microscope setup involving a laser which illuminates fluorescent particles at a given time-step, and images

are captured using a camera. The triggered pulses allow for quantification of the movement of the fluorescent particles on a given time-step.

The drawback of this technique, however, is the requirement for a laser to excite the fluorescent particles, limiting the ability to conduct the analysis continuously and at a range of time-steps.

Another technique to image flow fields is Ghost Particle Velocimetry (GPV). This technique operates by dispersing particles with a diameter smaller than the diffraction limit of white light in the 300 nm range, meaning that they are not directly resolvable by the microscope (Riccomi *et al.* 2018). Illuminating a sample containing these particles with white light from a standard bright-field microscope will generate a 'speckle' pattern, which is well ordered and can be detected using a camera as fluctuation in grey level value. By recording a large number of frames and subtracting the median image from each, it is possible to reveal the position of the 'speckle' pattern in each image. Through timing the capture of images, it is therefore possible to track the movement of particles frame-to-frame, in a similar manner to other velocimetry techniques. The recorded videos are pre-processed with ImageJ (Schneider *et al.* 2012), to reduce noise, and then analysed with PIVlab for Matlab (Thielicke and Stamhuis 2014). Examples of GPV have been demonstrated for continuous flows (Riccomi *et al.* 2018), yet its application to segmented flows or drop microfluidics has been largely limited to aqueous dispersions, owing to the lack of particles in the required size range which are both stable and dispersible in non-aqueous media.

1.5.3. Flow field evaluation in segmented flows

For systems such as micro reactors, there is a need for simultaneous visualisation of two phases. To generate hydrophobic tracer particles, there are noted issues with production of colloidal particles. Bonham *et al.* (2014) identifies multiple methods for particle production, surfactants and charges on initiators, and polymerisation with low polymer content monomers. Research on oil dispersible colloidal particles generally focuses on lubricants, and specifically the dispersal of metal particles in non-aqueous phases to avoid fouling of industrial machinery (Chen *et al.* 2019). In applying these particles to GPV, the system requires limited or no surfactant, and as such research in this area has been restricted. Given that literature has demonstrated the ability of lignin-rich particles to modify their wetting properties, there is potential for using these particles in GPV. This would not only address a gap in the literature but would offer a further novel valorisation route for lignin as a bioresidue.

1.6. Summary of the literature review

This literature review explores the current state of available literature in the utilisation of bioresidues for colloidal particle production and application. Extraction of lignin as a bio-residue predominantly explores use from paper industry co-products, which undergo bleaching as part of the extraction, and possess dissimilar properties to native lignin. The limitations of such studies hinder a comprehensive understanding of naturally occurring co-products and using them in direct application. Other limitations of the work such as those by Cuthill et al include the absence of full characterisation profiles of lignin-rich extracts. It is hypothesised that by including a comprehensive characterisation of the chemical properties of any extracts, that the resulting features used for formulation such as contact angle can be related to specific chemical functional groups.

The literature has demonstrated many examples of precipitating colloidal particles, however there is a noted absence of continuous processes for liquid-liquid precipitation as the literature focuses on batch precipitation methods. There is therefore a gap in the literature for generating particles continuously. In achieving this, it may be possible to generate particles with a specifiable particle diameter. In using CBS, a lignin-rich extract as a co-product of an established industrial process, the resulting research is anticipated to retain scalability, and offer facile integration to an existing commercial process should the opportunity arise. In using an ethanolic extraction process, the degradation and functionalisation identified in Kraft lignin is anticipated to be avoided.

Research on batch processes has demonstrated examples of using extraction and solvent choices to modify the wetting characteristics of colloidal particles. There is as yet no direct evidence of the impact of precipitation conditions on the surface properties of formed colloidal particles.

There are many examples of applications of colloidal lignin-rich particles, with examples such as Pickering stabiliser demonstrated in a wide range of literature sources. There is however limited understanding of the impact of using an inhomogeneous extract as a Pickering stabiliser. In addition, the sub-micron size of the particles described in literature offer an opportunity to apply them in systems where colloidal particle dispersions are required, such as tracer particles for microfluidic flow systems.

1.7. Research objectives

This literature review has highlighted that whilst colloidal particles have been produced from lignin-rich feedstocks and precipitated by antisolvent precipitation in batch processes, there is no example of a continuous process for liquid-liquid precipitation in literature at present. Additionally, most literature focuses on the production of colloidal lignin particles from co-products of the paper industry, which has dissimilar properties to native lignin owing to bleaching, and additionally limits investigation of naturally occurring co-products. Several examples of lignin-rich dispersion used for Pickering stabilisation of emulsions are evidenced in literature, however the application is defined by the properties of the extract, rather than influencing the functionality of any lignin-rich bioresidue for a designed application.

The following research objectives were identified from published literature and investigated in this PhD thesis:

O1: To characterise the componentry of a lignin-rich mild organosolv bioresidue of cocoa bean shell biomass as a precursor for particle production, using spectroscopic and spectrometric techniques;

O2: To establish a process for continuous production of colloidal particles using antisolvent precipitation and assess the use of processing conditions to influence the size and stability properties of particle dispersions;

O3: To assess the impact of co-extractives of a lignin-rich bioresidue on the surface properties of resulting extracts such as contact angle and solubility, and assess the ability to manipulate the bioresidue by variation of precipitation conditions;

O4: To assess the stabilisation of emulsions using lignin colloidal particle dispersions; and investigate the impact of co-extractives on the efficacy of stabilisation of oil in water (o/w) and water in oil (w/o) emulsions such as those in consumer goods; and

O5: To validate the use of colloidal particle dispersions formed from cocoa bean shell extracted lignin for application as a tracer field for imaging of flow fields in confined micro channels.

1.8. Thesis structure

This thesis is structured as follows: In Chapter 2, the materials and analytical methods used throughout the research are outlined. In Chapter 3, the extraction and characterisation of lignin-rich bioresidue of two types of cocoa bean shell are discussed, in line with the O1. Specific attention was paid to the chemical composition of the extract for later insight into the role of componentry. In Chapter 4, a negative result aimed at continuous production of colloidal particles by desorption is presented, towards research objectives O2 and O3. A hydrodynamic flow-focusing device was chosen to form macro-scale droplets of solubilised lignin-rich bioresidue in an antisolvent continuous phase to observe precipitation by desorption in real time. In Chapter 5, the results of continuous colloidal particle production in coaxial jet mixing device are reported. In Chapter 6, the ability to induce a variation in wetting properties is presented, in the context of contact angle measurement, and emulsion stability. This is based on research objectives O3 and O4. In Chapter 7, the ability to use the formed colloidal particles to visualise flow fields in static and dynamic flow systems in both aqueous and non-aqueous phases are demonstrated, fulfilling research objective O5. In Chapter 8, the conclusions of this research are presented and future work to develop the findings of this research are presented.

2. Materials and Methods

This chapter details the materials and methods used in this thesis. It is divided into separate methods sections for those used in bioresidue analysis, microparticle production via both microfluidics and coaxial jet mixing (CJM), and finally emulsified particle methods.

2.1. Materials

2.1.1. Cocoa bean shell

Cocoa bean shell (CBS) as feedstock for bioresidue preparation was kindly donated by Mondelēz (Mondelēz International, Birmingham, UK) and milled to a fine powder using a hammer mill (24 series Circ-u-flow hammer mill, Schutte, Buffalo, USA). Size class fractions of milled CBS were determined where a diameter *d* indicated the percentage of CBS between the mesh sized of sieves, by using 1 kg of CBS, see Table 6. The weighted mean diameter was 473 μm.

Table 6: Sieve class fractions of CBS reported as a weight percentage.

Size range	≥ 710 μm	710 > d ≥ 250 μm	250 > d ≥ 90 μm	< 90 μm
Wt%	0.19	58.27	26.89	14.65

2.1.2. Reagents and solvents

Ethanol (> 98% reagent grade, Fisher Scientific, Loughborough, UK) was used as the principal solvent for the extraction of a lignin-rich fraction from CBS. To aid extraction by digestion of the plant cell wall, HCl (37% w/w concentrate in water) was purchased

from Fisher Scientific (UK) and diluted to a concentration of 2 mol dm^{-3} (2 M) using deionised water (Elix® Essential 5, Merck, Darmstadt, Germany). Hexane (fraction from petroleum, reagent grade, from Fisher Scientific, UK) was used to remove co-extracted molecular surfactants, amphiphiles, and free fatty acids, henceforth referred to collectively as 'lipid' when generating a lipid-removed bioresidue (CBS-LR) was desired. Antisolvents used for the precipitation of particles were deionised water, n-dodecane (99% anhydrous, Fisher Scientific, UK), and isopropyl myristate (< 98%, Fisher Scientific, UK). Emulsions were prepared with sunflower oil purchased from a local supermarket.

As reagents for assays, hydroxylamine hydrochloride was used as a dilute in distilled water and was purchased as a solid from Sigma (Sigma Aldrich, Gillingham, UK) alongside glacial acetic acid, acetyl bromide and alkali lignin, which was used as a calibration standard. For adjustment of pH, deionised water was used to prepare solutions of acid (HCl) and base (NaOH) at a concentration of 0.1 M from 37% HCl and NaOH pellets (Fisher Scientific), respectively. For contact angle measurements, isopropyl myristate (IPM) and dichloromethane (DCM) was purchased from Fisher Scientific (UK). For GPV studies, medium chain triglyceride (MCT) oil (Ketosource, London, UK) was purchased, alongside silicone oil (40 cST), mineral oil, and magnesium silicate to treat sunflower oil (all Sigma). 220 nm polystyrene particles (dispersion of 10% solid, Sigma Aldrich, diluted 1:50 (v/v)) were used for GPV in the aqueous phase at concentrations of 0.01 – 0.5% (v/v). For washing microfluidic devices, Isopropyl alcohol and-dodecane were purchased from Sigma. Sunflower oil was purchased from a local supermarket.

2.1.3. Materials for hydrodynamic flow-focusing device fabrication

For the manufacture of a hydrodynamic flow-focusing device, poly(dimethylsiloxane) (PDMS) was used. The polymer was cured from a two-part elastomer kit (Sylgard 184, Dow Corning, Midland, USA). For device surface treatment, poly(vinyl alcohol) (PVA, 87-89% Hydrolysed, Alfa Aesar, Heysham, UK) was used. For alternative device surface treatments, sodium hydroxide, poly(allylamine hydrochloride) (PAH), and poly(sodium 4-styrene sulfonate) (PSS) were purchased as reagent-grade chemicals (> 98%) from Fisher Scientific (UK) and diluted to solutions of 0.1% (w/w) using deionised water.

2.2. Lignin-rich cocoa bean shell extract: Preparation, characterisation, and manipulation methods

2.2.1. Organosolv extraction of a lignin-rich bioresidue from cocoa bean shell

Lignin was extracted from the milled cocoa shell using an acidified organosolv reflux to obtain a crude lignin-rich bioresidue (Cuthill *et al.* 2021). Extraction was conducted using a quick-fit Soxhlet extraction apparatus fitted with a reflux condenser, Figure 9. The milled CBS was dehydrated at 130 °C in a dry heat oven (Carbolite Eurotherm 91e, Carbolite Furnaces, Sheffield, UK), and 30.0 g was added to a cellulose thimble (Whatman, UK) within the Soxhlet reflux condenser Figure 9.To make the extraction medium, the 250 mL round bottom flask of the set-up was charged with a stirrer bar, deionised water (10 mL), 2 M HCl (20 mL), and ethanol (150 mL). The system was stirred and brought to reflux for 4 h.

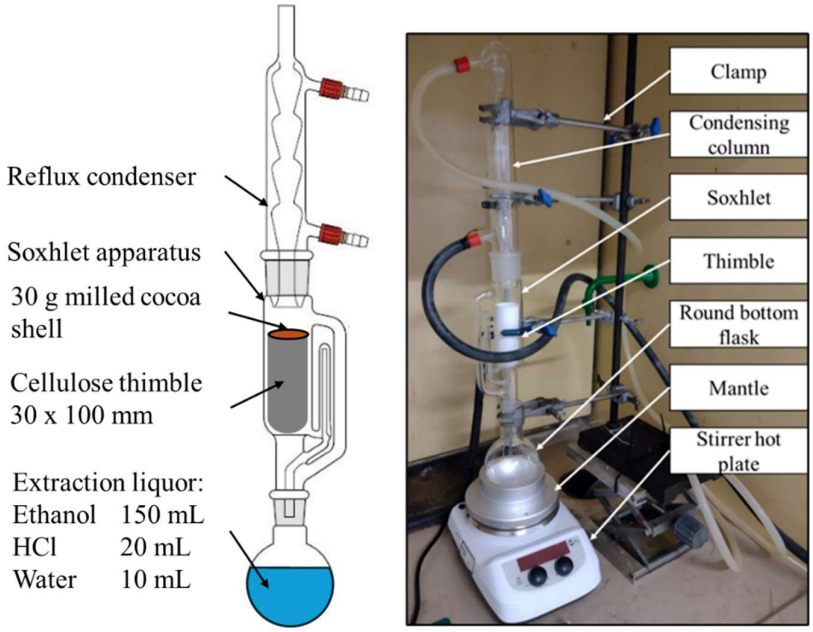


Figure 9: Setup of the Soxhlet extraction of lignin from cocoa shell, schematic (left) and actual setup (right). A 250 mL round-bottom flask was fitted with a Soxhlet containing a CBS filled thimble, and a condensing column.

The resultant bioresidue was labelled as CBS-LC, with "LC" for "lipid-containing", and concentrated by rotary evaporation (Büchi R215, Germany), followed by subsequent drying at 130 °C to constant mass. The paste-like residue was sealed in a watchglass using parafilm, covered in tin foil and stored at 20 °C until use.

2.2.2. Lipid extraction

Preparation of *lipid-removed* cocoa bean shell extract, labelled CBS-LR, involved extraction per 2.2.1 with an additional processing step. Dried CBS-LC bioresidue was transferred into a flask containing n-hexane, agitated for 8 h to solubilise the lipid, and left to stand for 72 h. The resultant supernatant containing the dissolved lipid was

removed by filtration. The sedimented CBS-LR phase was concentrated *in vacuo* and dried in an oven at 130 °C (Carbolite Furnaces) to obtain a dry paste, which was subsequently sealed in a watchglass using parafilm covered in tin foil and stored at 20 °C.

2.2.3. Quantification of extraction yield

The yield of the bioresidue obtained from the CBS was calculated per Equation 2.1. The mass of recovered bioresidue was taken as the mass of the residue obtained by evaporating the extraction liquor following the reflux described in 2.2.1 to a constant mass at 130 °C.

$$yield\ (\%) = \frac{mass\ of\ recovered\ extract\ (g)}{mass\ of\ feedstock\ (g)} \text{ x } 100\% \qquad (2.1)$$

2.2.4. Quantification of lignin in extract

The acetyl bromide assay was used to quantify the amount of lignin in the extracts prepared (Fukushima and Kerley 2011; Moreira-Vilar *et al.* 2014; Fukushima *et al.* 2015; Mao *et al.* 2023). 100 mg of bioresidue was placed into a screw-cap centrifuge tube containing 4 mL of acetyl bromide (25% v/v in glacial acetic acid) and incubated at 50 °C for 2 h. Afterwards, the sample was cooled in an ice bath and further diluted in glacial acetic acid to a final volume of 15 mL. The solution was allowed to settle for 30 minutes and centrifuged at 3,900 × g for 20 min (Sigma 2-6 centrifuge, Sigma Zentrifugen, Osterode am Harz, Germany). An aliquot (0.5 mL) of this solution was mixed with 2.5 mL of glacial acetic acid, 1.5 mL of 0.3 M NaOH, 0.5 mL of 0.5 M hydroxylamine

hydrochloride solution, and further diluted with 5.0 mL of glacial acetic acid to a final volume of 10.0 mL. The absorbance was measured at 280 nm on a UV-Visible spectrophotometer (Jenway Genova series, Stone, UK) against a blank; a sample treated as above in the absence of dissolved lignin. A standard curve was generated using aqueous solutions of alkali lignin of concentrations ranging from 80 to 400 mg L^{-1}. To determine the lignin content of a sample, the Beer-Lambert Law, a relationship between absorbance and concentration was used, Equation 2.2:

$$A = \varepsilon_m C l \tag{2.2}$$

Where A is absorbance (no units), ε_m is the absorptivity of a substance (units here L cm^{-1} g^{-1}), C is concentration (g L^{-1}), and l is path length of sample (cm).

Calibration curve

Figure 10 shows the calibration curve generated using a series of standard solutions produced using commercially available Kraft lignin up to 400 mg L^{-1} in concentration including the baseline value at 0 mg Kraft lignin subjected to the acetyl bromide assay. The absorptivity per litre of sample was determined by the gradient of the line in Figure 10, offering a value of 0.00236 L mg^{-1}, or 2.36 L cm^{-1} g^{-1} (SI units). The concentration of unknown lignin samples was determined from the absorbance values.

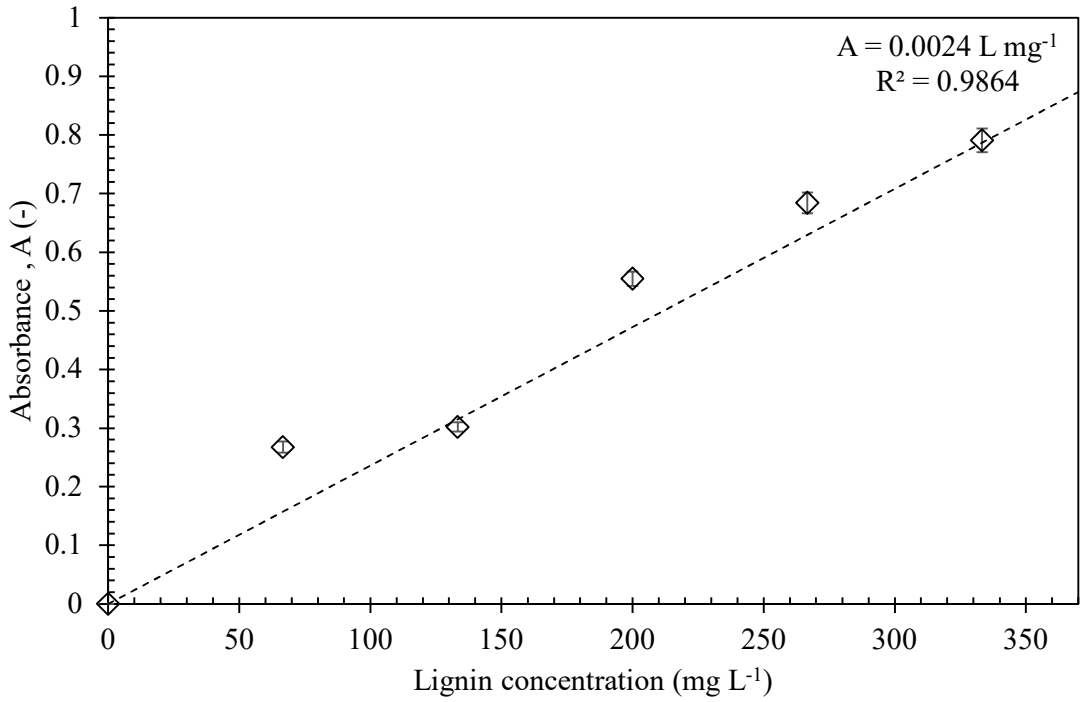


Figure 10: Calibration curve of samples to determine the absorptivity constant of lignin using a commercially available Kraft lignin at 280 nm, and concentrations between 0 (represented by a solvent blank) and 400 mg L^{-1}. Markers show the mean values, and error bars represent ± 1 s.d. The gradient of the resulting linear trendline of 0.0024 L mg^{-1}. (R^2 value of 0.9864) was used in the Beer-Lambert law to determine the absorptivity constant for lignin.

2.2.5. Solvent solubility of lignin-rich bioresidue

The solubility of the lignin bioresidue in a selected solvent was determined at room temperature (20 °C) as the residual solids content after solubilisation. To 10 mL of solvent, excess amount of dried lignin bioresidue was added followed by agitation on a whirlmixer (Camlab MX-S, Over, UK) for 30 minutes to allow for dissolution. The resultant mixture was centrifuged at 2,400 x g for 30 minutes (Sigma 2-6 centrifuge, Sigma Zentrifugen, Osterode am Harz, Germany) leaving a sediment and a supernatant

phase. The latter was poured off, and the sediment dried at 130 °C in an oven (Carbolite Furnaces). The solubility (wt%) was calculated using Equation 2.3.

$$solubility\ (wt\%) = \frac{mass\ of\ extract\ added\ (g) - mass\ of\ dried\ residue\ (g)}{mass\ of\ solvent\ added\ (g)} \text{ x } 100\ \%\ (2.3)$$

2.2.6. Identification of bioresidue lipid fraction

The lipids present in the lignin-rich bioresidue were obtained as a separate fraction per the method outlined in 2.2.2 and further separated and analysed by gas chromatography-mass spectrometry (GC-MS). For molecular surfactant determination, a column (Rxi-5sil, Restek, USA) was held at 120 °C for 2 minutes and heated at 10 °C min^{-1} to 300 °C. For mass spectrometry, electron ionisation (EI) was used at 70 mV.

To assess triglyceride content, the sample underwent base hydrolysis (2 M NaOH, 24 h). To silylise the resultant glycerides, N, O-Bis(trimethylsilyl)trifluoroacetamide (BSTFA) was used as a donor of trimethylsiloxane (TMS) and reacted with the base hydrolysed sample for 60 minutes at 60 °C. The presence of a triglyceride was identified by species appearing in the column following the hydrolysis step, which were not present in the initial pre-hydrolysis column run. Sample was provided to the University of Bedfordshire where the GC-MS was conducted, and the data were returned in raw format for processing.

2.2.7. Fourier-transformed infrared spectroscopy for lignin component identification

The absorbance values associated with chemical bonds present in the structure of lignin were characterised by Fourier-transformed infrared spectroscopy (FTIR) (Chakar and Ragauskas 2004; Derkacheva and Sukhov 2008). For analysis, 200 mg of sample was placed on a diamond crystal and a spectrum was obtained using attenuated total resonance (ATR)-FTIR (Nicolet 380, ThermoFisher, Waltham, USA), baselined against air with a sampling frequency of 256 samples per measurement at a resolution of 1 cm^{-1}. The presence of lignin was typified by the presence of a series of general aromatic absorbances, which are not present in other bioresidues such as cellulose, and finer structural detail such as guaiacyl, sinapyl, and coumaryl moieties. These absorbances and their literature basis has been extensively documented in the literature review, section 1.2.4.1.

2.2.8. Ancillary bioresidue analysis methods

This section details methods which were applied to obtain data necessary for surface tension measurement (see section 2.5.3), light scattering experiments (see section 2.6.1), and dimensionless number calculations (see section 1.7).

2.2.8.1. Viscosity

To calculate the Reynolds number (*Re*), viscosity data are required. For three volumetric ratios of water to ethanol (*R* values) of 1, 0.5, and 0.1. Ethanol and water mixtures were prepared at volumetric ratio of ethanol to water of 1, 0.5, and 0.1, and their viscosity was

measured on a shear rheometer (Kinexus, Malvern Instruments, Malvern, UK) using an 8 cm cone geometry (cone angle = 2°) and a stainless-steel plate, at shear rates from 0.01 – 1,000 s^{-1} and 5 data points per decade were collected at 20 °C. The samples were Newtonian and results are reported as viscosity data averaged across the shear rate range tested. Results are reported in section 3.3.2.

2.2.8.2. Density

The density of the solutions assessed for viscosity was also required for *Re* number calculation. Density was measured using a force tensiometer fitted with a Wilhelmi plate in density measurement mode at 21°C (K100, Kruss, Hamburg, Germany). Results are reported in section 3.3.3.

2.2.8.3. Refractive index

The refractive index of CBS-LC was measured at 20 °C using a refractometer (J35, Rudolph Analytical, USA). The Refractive index was generated by extrapolation of a series of dilute solutions, and the results reported, in Figure 11 were extrapolated to give a refractive index value for 100% the standard deviation was determined from linear regression analysis of the points. The resulting value was 1.57 ± 0.02.

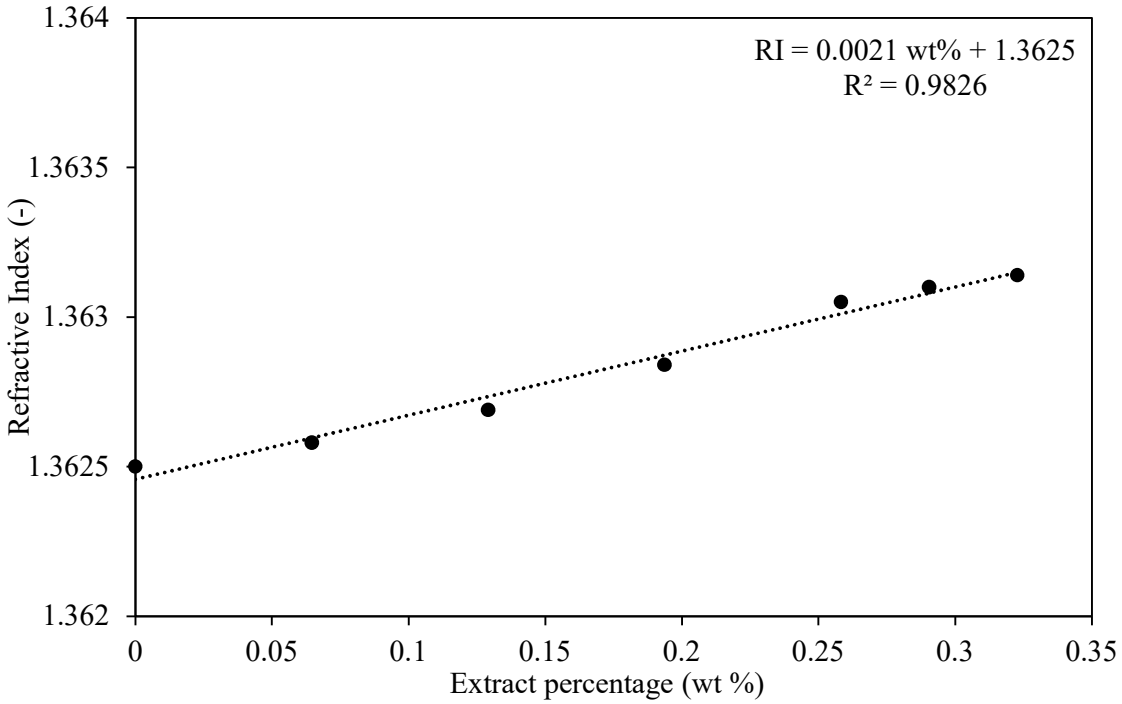


Figure 11:Refractive index of a series of concentrations of CBS-LC lignin, in ethanol, yielding an approximation of the refractive index at 100 wt%.

2.2.9. Lignin bioresidue solution preparation

A solution was prepared containing lignin-rich bioresidue at 5 mg mL^{-1} by taking the solids bioresidue as prepared in section 2.2.1, and dissolving in ethanol by stirring at rom temperature for 24 h. The solution was sterilised using a 0.2 μm syringe filter (Millipore, Burlington, USA), per (Leskinen *et al.* 2017). The final concentration was determined by evaporation of solvent from a 2 mL aliquot and determining the mass of the remaining residue. Based on the result, ethanol was added to achieve the required concentration. The prepared solutions were filtered and the supernatant used in later sections as the dispersed solvent phase for particle production by antisolvent precipitation.

2.3. Flow-focusing method for precipitation of lignin-rich microparticles

For initial particle production, a PDMS based hydrodynamic flow-focusing (HFF) device was made from a negative using soft lithography following published method (Anna and Mayer 2006; Whitesides 2006). The construction of the device using PDMS was chosen due to noted reproducibility and simplicity of geometry modification compared to other construction materials. As detailed in Chapter 4, fouling was identified as a persistent issue inhibiting microparticle production by antisolvent precipitation in the devices as constructed. Surface modification methods explored to suppress fouling were applied and these are also detailed.

2.3.1. Flow-focusing device manufacture

Hydrodynamic flow-focusing (HFF) devices of the geometry depicted in Figure 12 were constructed from a negative imprinted onto a silicon wafer (device top) using standard soft-lithography techniques on a maskless aligner (μMLA, Heidelberg Instruments, Heidelberg, Germany). The device was constructed using PDMS prepared in a 10:1 (w/w) mixture (polymer to curing agent) cured in an oven (Carbolite Furnaces) at 70 °C for 90 minutes. To generate the device top, the PDMS was poured into the negative mould and cut out once the polymer had cured. To generate the device bottom, 0.5 g of PDMS was placed on a borosilicate glass slide and coated at 1200 rpm for 1 minute in a spin coater (150i, POLOS, Putten, The Netherlands) and cured as described above. The coated slide (device bottom) was bonded to the device top using a 12 W plasma laser (Sisomm, Hasselt, Belgium). Each side was exposed to the laser for 30 seconds before being

compressed together manually and placed on a hot plate at 90 °C for 1 hour, and storage at 20 °C for 36 h to allow curing to complete before use.

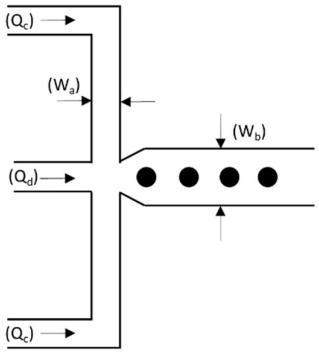


Figure 12: Setup of flow-focusing microfluidic device. Q_c denotes inlets for the continuous phase, and Q_d denotes the inlet for the dispersed phase. The channel was rectangular with the following dimensions; W_a was 200 μm, W_b was 600 μm, and channel height was 150 μm.

2.3.2. Device surface treatments

Surface treatments reported in literature were applied to alter the surface wetting properties of the flow-focusing device. Poly(vinyl alcohol) (PVA) (Trantidou *et al.* 2017) and poly(electrolyte) treatments (Bauer *et al.* 2010) were applied to both the top and bottom to generate a device with hydrophilic wetting properties, rather than the initial hydrophobic state of PDMS devices.

2.3.2.1. PVA treatment

The following method was adapted from Trantidou *et al.* (2017). PVA was dissolved in deionised water (1 wt%) and stirred at 20 °C for 40 min, on a magnetic stirrer. The temperature was increased gradually (5 °C min^{-1}) until the boiling point was reached, followed by stirring for another 40 min. Afterwards, the temperature was gradually

lowered (5 °C min^{-1}) to 65 °C and the mixture stirred for a further 8 hours. Evaporated water was replenished regularly to maintain a consistent volume, retaining sample concentration of 1 wt% at 20 °C.

The PDMS device top and bottom prepared as described in section 2.3.1 were thoroughly degreased in isopropyl alcohol followed by dehydration in an oven at 110 °C for 40 min. The degreased PDMS top and bottom were then surface treated by corona discharge at 12 W (Sisomm) for 30 seconds and submerged in the prepared PVA solution for 10 minutes before being sealed and stored as described in 2.3.1.

2.3.2.2. Polyelectrolyte treatment

The following method by Bauer *et al.* (2010) was applied as an alternative method to generate a device with hydrophilic surface characteristics. Solutions of poly(allylamine hydrochloride) (PAH) and poly(sodium 4-styrene sulfonate) (PSS) were prepared as 0.1% (w/v) in 0.5 M aqueous sodium hydroxide, alongside a solution of 0.1 M NaCl. A PDMS device prepared as outlined in 2.3.1 was hydrophilized by passing PAH, NaCl, and PSS sequentially through 10 times at 50 μL h^{-1}, to generate a hydrophilic coating. The device was subsequently washed with 0.1 M NaCl solution and dried using compressed air, before the device was sealed and stored at 20 °C until use.

2.3.3. Colloidal particle production set-up

For the antisolvent precipitation research using microfluidics in chapter 4, the flow-focusing devices were connected to two syringe pumps (World Precision Instruments, Hitchin, UK). One pump fed both inlets for the antisolvent phase and the other fed the

solvent phase, both operated at flow rates between 1 and 50 μL min^{-1} As described in Section 2.3.1.

2.4. Coaxial jet mixing method for precipitation of lignin-rich microparticles

To form colloidal particles using antisolvent precipitation, coaxial jet mixing (CJM) was used as an alternative production method, negating observed fouling. Particle production by CJM uses a central tube as the carrier for the continuous phase (solvent), and an external tube to carry the dispersed phase (antisolvent).

2.4.1. Coaxial jet mixing device manufacture

The CJM device shown in Figure 13 was constructed following a published method with minor modifications (Bovone *et al.* 2019).

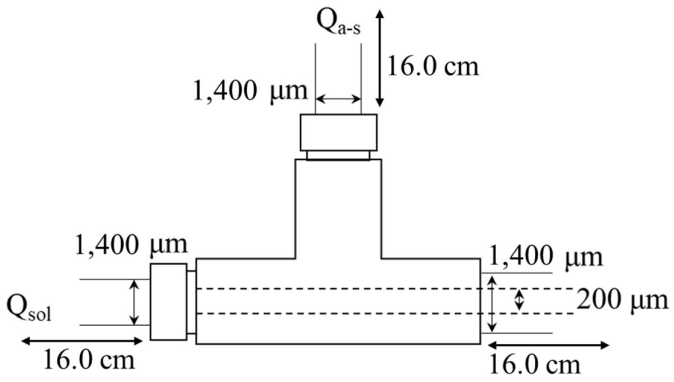


Figure 13: Schematic of the CJM device, consisting of a concentric internal glass tube with an outer flow phase. The solvent stream (Q_{sol}) was passed through a coaxial channel of inner diameter 200 μm and mixed with the antisolvent stream passing through the channel of inner diameter 1,4000 μm at a given flow rate

($Q_{a\text{-}s}$). Inlet tube and outlet outer tube lengths are 16.0 cm, and the internal glass capillary has a length of 4.6 cm.

A glass capillary (200 µm I.D., Cole Parmer, Illinois, USA) was inserted into plastic tubing (I.D. 510 µm, Saint Gobain, Charny, France) followed by sealing at 70 °C for 1 h with PDMS (Dow Corning), Figure 14 Left part A, magnified right. The glass outlet of the internal capillary was threaded through a T-junction (1 mm I.D.) (Figure 14 left part B) and secured with a ferrule and PEEK nut (both O.D. 1.59 mm) to complete the feed for the dispersed phase, Figure 14 left part C.

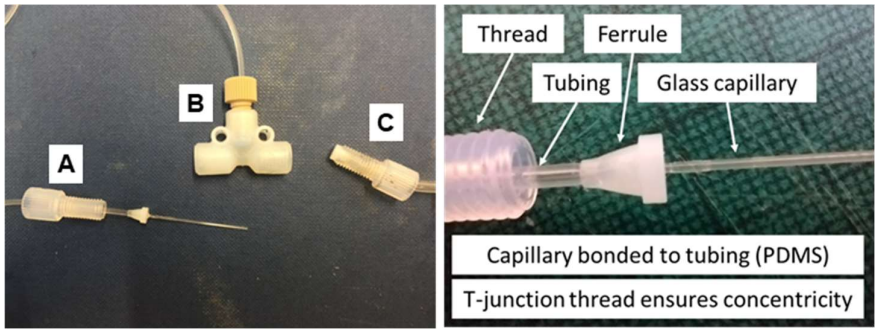


Figure 14: (Left): CJM device for antisolvent precipitation is shown in three parts; A) the solvated lignin was injected through a capillary, B) the antisolvent was injected around the capillary, C) the precipitated CLP was collected. (right) a close view off (left) part a, showing the glass capillary inserted into the ferrule to generate a water-tight concentric capillary for CJM.

2.4.2. Colloidal particle production conditions

10 mL syringes (Beckton Dickson, Franklin Lakes, USA) containing solubilised lignin bioresidue and the antisolvent phase fluid respectively were placed into syringe pumps (World Precision Instruments). The syringe pumps were connected to the CJM device using 1.4 mm tubing (Saint Gobain, France). The solvent phase flow rates were varied

between 50 and 1,500 μL min^{-1}, and the antisolvent phase flow rates between 50 and 1,500 μL min^{-1}. The process was run at 20 °C, the exit stream collected, and the processing solvent removed by evaporation before storage of the particle dispersion at 20 °C in a sealed glass vial until further use.

2.5. Methods for assessing surface characteristics of lignin-rich extracts

The wetting properties of prepared colloidal lignin-rich particle (CLP) dispersions were tested for Pickering functionality by preparing emulsions and observing their stability and by assessing their wetting properties. Methods for preparation of emulsions are detailed, followed by methods for characterisation of particle properties.

2.5.1. Treated sunflower oil preparation method

To allow for assessment of the ability for CLPs to act at Pickering particles in the absence of lipid fraction, surface active molecules indigenously present in native sunflower oil were removed as follows. 4 wt% magnesium silicate (Sigma, UK) was added to sunflower oil, and stirred at 20 °C for 30 minutes at 600 rpm. The magnesium silicate was then removed via centrifugation at 8,500 x g (J2-21 floor model centrifuge, Beckman, Indianapolis, USA) to obtain so-called treated sunflower oil (TSO).

2.5.2. Preparation of emulsions

Both water-in-oil (w/o) and oil-in-water (o/w) emulsions (10 g) were prepared by adding a colloidal particle dispersion to the continuous phase of emulsions (treated sunflower oil or distilled water), and the emulsions 1:9 (w/w), were processed using a high-shear overhead mixer (Ultraturrax T25 mixer, IKA, Oxford, UK) at 9,000 rpm for 120 seconds. Alternatively, emulsions were processed using a sonication probe (Sonics VibraCell CX 750, Sonics Inc., Newtown, USA) on a 30-second cycle with 5 seconds on and 5 seconds off (3 x 5 s pulses).

2.5.3. Surface tension of particle suspensions

The surface tension of the particle suspensions was assessed at 20 °C with a profile analysis tensiometer (PAT - 1M, Sinterface, Berlin, Germany) in pendant drop mode. A drop with cross-sectional area of 27 mm^2 was suspended from a stainless-steel capillary of external diameter 3 mm, and data recorded at a sampling frequency of 1 s^{-1}. Phase densities required to analyse the data were determined at 20 °C using the method outlined in section 2.2.8.2: Distilled water (0.997 g cm^{-3}), air (0.0012 g cm^{-3}), n-dodecane (0.750 g cm^{-3}), sunflower oil (0.918 g cm^{-3}).

2.5.4. Contact angle measurement method

As direct determination of the wetting properties of individual CLPs was not possible due to the small particle size, bulk analysis was carried out instead. It is anticipated that by assessing the contact angle of bulk precipitated lignin extract, the surface properties of resulting particles can be inferred. An interface was prepared whereby the characteristics

of the colloidal particle could be inferred, by mimicking the precipitation steps performed in the CJM. Contact angle was measured to mimic the surface of the CLPs.

Sample preparation

For observation of the wetting properties of the lignin-rich extract, surfaces of lignin were prepared by depositing ethanol solubilised CBS-LC and CBS-LR dropwise on a borosilicate glass coverslip (22 x 22 mmm, SLS Laboratory supplies, Dublin, Ireland). For each sample, 0.5 g of CBS-LC and CBS-LR were added, and the ethanol was removed in an oven at 130 °C, generating a layer on which contact angle could be measured, Figure 15. The approach was validated by taking a borosilicate glass slide, and measuring the contact angle, Figure 15.

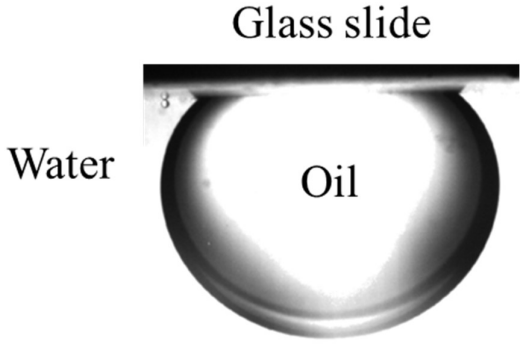


Figure 15: Image of an interface between an oil droplet (20 µL) and a borosilicate glass slide (22 x 22 mm).

The dynamic contact angle of each sample was measured by depositing a 20 µL droplet of water or oil onto a stage on a PAT - 1M tensiometer (Sinterface Technologies) in sessile drop mode at 20 °C.

Contact measurement was achieved by placing a droplet of water onto a dried surface of CBS-LC submerged in sunflower oil, however for reversed phases, the coverslip was placed onto a stand, shown in Figure 16a to allow a rising oil droplet to be introduced for contact angle measurement. Figure 16a shows the construction of the stand, and Figure 16b shows an oil droplet introduced to a glass coverslip.

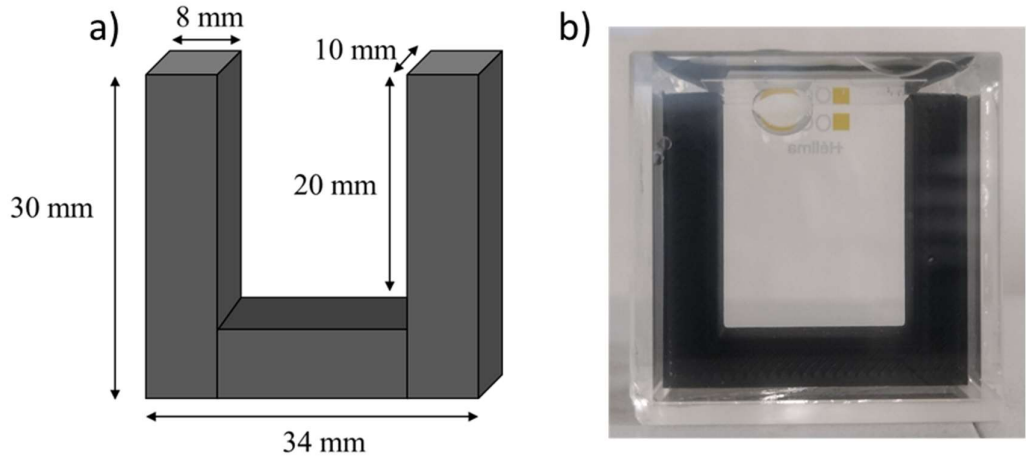


Figure 16: a) Schematic diagram of a 3-D printed stand to allow coverslips to be balanced for contact angle measurement, constructed from poly (lactic acid). b) A droplet of sunflower oil introduced to a glass coverslip supported by the 3-D printed stand in a distilled water.

2.6. Characterisation methods applied to precipitated lignin-rich particles

2.6.1. Dynamic light scattering

The size distributions of precipitated colloidal particle aqueous dispersions were measured by dynamic light scattering (DLS) using a Zetasizer Nano (Malvern Instruments). Emulsions were measured using a Mastersizer (Malvern Instruments) and solutions were dispersed using Hydro SM small volume wet dispersion unit (Malvern

Instruments, Malvern, UK). The samples were dispersed in water, and refractive index of lignin was described in 2.2.8.3, and was in agreement with the refractive index for lignin of 1.55 in literature (Fink 1992). An absorption index of 0.01 was used. Mean size and z average values are reported as the mean of triplicates, and distributions of particle size and volume fraction were used for analysis.

Span

The parameter known as span was used to quantify the width of the particle size distributions. It is defined in Equation 2.4, where dw_{10}, dw_{50}, and dw_{90} refer to the size of particles (nm) at the 10^{th}, 50^{th} and 90^{th} percentiles respectively. Analysis was conducted on triplicates of collected samples.

$$Span = \frac{dw_{90} - dw_{10}}{dw_{50}} \quad (2.4)$$

2.6.2. Electrophoretic mobility

The ζ–potential of the colloidal particle dispersions was determined by electrophoretic mobility using a Zetasizer (Zetasizer Nano, Malvern Instruments, Malvern, UK) with a folded capillary cell (DTS1070, Malvern Instruments, Malvern, UK) at 25 °C. Samples were diluted by a factor of 300 in distilled water to prevent multiple scattering. The pH was adjusted to the range of 2.5 – 9.5 by use of 0.1 M stock solutions of NaOH and HCl as required. Samples were reported as the mean average of three replicates.

2.6.3. Optical microscopy

Optical microscopy was used as a method to visualise the microstructure of particle dispersions as well as emulsions prepared from the particles dispersions, see 2.4.2. 20 µL

of sample was pipetted using a mechanical pipette onto a borosilicate glass slide, covered with a coverslip, and imaged on a microscope (Leica DM 2500, Leica, St Gallen, Switzerland) fitted with 10, 20, 40, and 100x objectives (Nikon, Tokyo, Japan).

2.7. Methods for flow field analysis using CLPs for Ghost Particle Velocimetry

Based on observations made in Chapters 6 and 7 that the particles could be dispersed in oil, particles were used as tracers in ghost particle velocimetry (GPV). Particles of diameter below 300 nm under bright-field (white) light do not diffract and are therefore not directly resolvable (Riccomi *et al.* 2018). However, they do scatter light, causing a 'speckle' pattern to appear. This pattern can be compared across a pair of images with a known time step (cross-correlation) referred to as a frame, and by the differences in location of disturbances, the movement of the fluid can be plotted following subtraction of the background static contribution.

2.7.1. Channel construction for flow field visualisation

To visualise flows, channels were constructed from PDMS using standard soft lithography techniques described in Section 2.3.1. Devices with a rectangular cross-section measuring 600 μm x 150 μm were used. For droplet visualisation, a flow-focusing device as depicted in Figure 17 was similarly constructed from PDMS with the same dimensions.

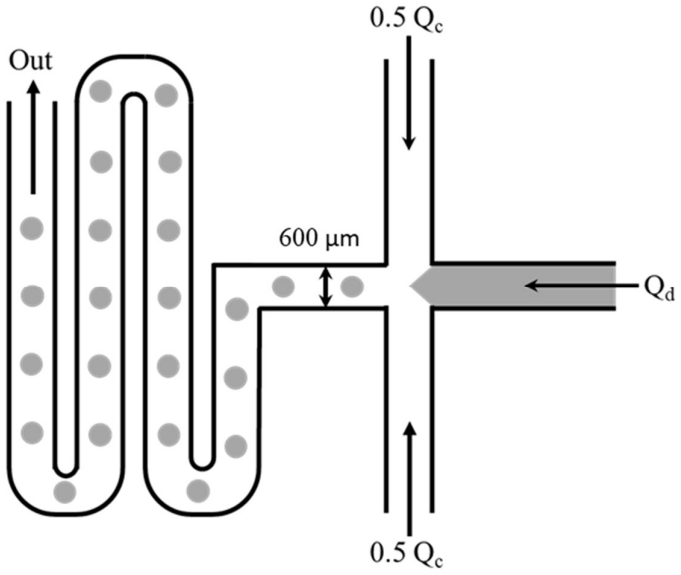


Figure 17: PDMS cast hydrodynamic flow-focusing device with a channel width of 600 µm, showing droplet formation. Droplets are formed of a dispersed phase (Q_d) in a continuous phase (Q_c) applied using syringes. Channel height was 150 µm.

2.7.2. Preparation of particle dispersions for flow field visualisation

To validate the flow field data obtained by CLPs, results were compared to poly(styrene) particles used for GPV, which are frequently used for GPV analysis. Poly(styrene) particles (of average diameter 220 nm were used for GPV in the aqueous phase at concentrations of 0.01 – 0.5% by dilution from a stock solution and agitation in a Whirlmixer (Camlab MX-5, UK). The lignin nanoparticles were used as prepared in 2.4.2 for flow visualisation in both aqueous and oil phases at 0.01 – 0.5% (w/w). Fluid velocities ranged from 5 – 100 µL min^{-1}. To generate particles in an oil phase, aqueous dispersions were pipetted and stirred into an oil phase using a magnetic stirrer, and the water was removed through evaporation by heating.

2.7.3. Quantification of flow fields by cross-correlation

Flow fields were visualised using cross-correlation of successive frames recorded with a high-speed camera (Photron SA-5, Photron, High Wycombe, UK) connected to an inverted microscope (Nikon Eclipse Ti2-U) at 2,000 - 10,000 fps. For analysis, microfluidic devices prepared per Section 2.3.1 were observed under a 20x objective. Spatial resolution was in the range of 0.5 – 2 μm/pixel. To determine a flow field, the movement of a fluid containing dispersed particles through a channel was recorded as a series of successive frames. Figure 18a shows the particle-laden fluid flow through a straight channel section. For cross-correlation, all static features in the image sequence were removed, leaving the speckle pattern caused by particles in motion scattering, Figure 18b. The remaining speckles caused by light diffraction of the particles in dispersion was plotted between pairs of frames, Figure 18c, using PIVLab for MatLab software (Thielicke and Stamhuis 2014). Following vector formation, vectors caused by erroneous cross-correlation are excluded (orange), leaving vectors which correspond to the movement of the fluid in the channel (green). Finally, averaging a series of cross-correlations generates the flow field image, see Figure 18d. Where the movement of the fluid through the channel was at a consistent velocity, averaged flow fields represent the motion of the system through the channel.

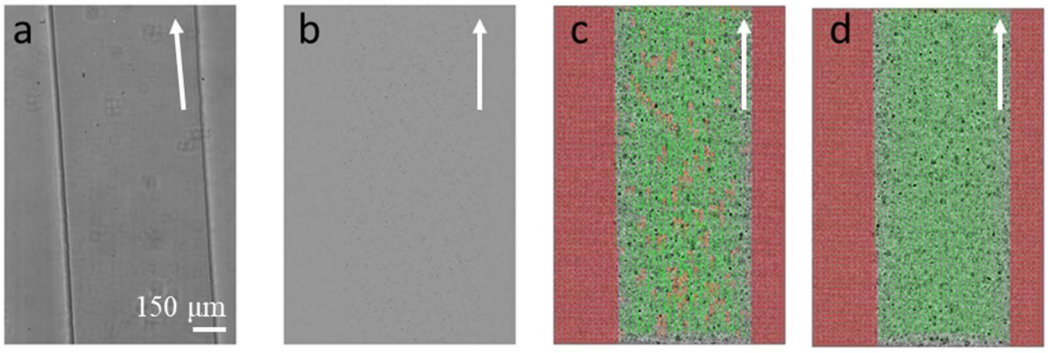


Figure 18: Steps for flow field visualisation using cross-correlation imaging of fluids containing dispersed colloids. a) fluid with dispersed poly(styrene) particles passing through a microfluidic channel. b) the channel rotated to vertical and the mean intensity of each pixels across the image corresponding to any static features was subtracted leaving a speckle pattern caused by particle light scattering. c) cross-correlation plot showing vectors due to motion of speckle pattern (green) and removed vectors due to Brownian motion (orange). d) a flow field made of an average of 400 cross-correlation images. White arrows indicate direction of flow, and scale bar is accurate for all images in the figure.

2.8. Statistical analysis

For datasets based on two sample sets, such as those for validation of the CJM device construction an unpaired two tailed t-test was performed. Additionally, correlation plots were used to demonstrate the nature of the similarity of the datasets. For calibration curves, linear regression analysis was conducted using the Microsoft Excel analysis tool pack, with confidence intervals of 95%. For datasets based on three or more repeat measurements such as average particle diameter of particles in dispersion, zeta potential, contact angle, surface tension, and flow field analyses. Analysis of variance (ANOVA) and a paired t-test was used to examine the significance of the batch-to-batch variation, and construction of the device for the CJM process, with a significance level set at $P = 0.05$.

3. Characteristics and extraction efficiency of a lignin - rich bioresidue of cocoa bean shell

In this chapter, the results of characterisation of an organosolv bioresidue of CBS are reported. The chapter is split into two sections. Firstly, yield and properties of the extract, such as refractive index, and lignin content are reported. Secondly, the chemical features of the bioresidue characterised by Fourier-transform infrared spectroscopy (FTIR), and gas chromatography coupled with mass spectrometry (GC-MS) to generate a fingerprint of the organosolv extract are introduced.

The presence of lignin was identified using absorption wavelengths from literature, and via comparison to Kraft lignin. The identities of co-extractives were quantified using GC-MS analysis.

3.1. Physical extract properties

This section details the physical properties of the lignin-rich extract. This encompasses appearance, yield of crude extract, and density.

Figure 19 shows a digital photo image of the pasteous lignin-rich bioresidue prepared as described in Section 2.2.1 Following removal of the lipid by hexane wash, the originally shiny bioresidue appears much duller but it remained paste-like.



Figure 19: Lignin-rich organosolv bioresidue prepared from CBS before (left) and after (right) removal of the lipid fraction.

3.1.1. Extraction yield

The extraction yield (see Equation 2.1; averaged over 9 extractions) was 10 ± 1% for the original bioresidue (CBS-LC) and 7 ± 0.5% after lipid removal (CBS-LR). Literature values on lignin content in cocoa bean shell suggest that a yield of up to 32% could have been expected (Chung *et al.* 2003). Optimisation of yield was not the focus of the present research and the extraction process selected here was chemically less aggressive than alternative methods such as sulfite pulping, as described in Section 1.1.3. The milder

extraction method was chosen to preserve the native polymeric structure of lignin and functionality, offering opportunity for easier integration to food systems.

3.1.2. Refractive index

The refractive index of the lignin-rich bioresidue was measured as 1.58 ± 0.02 which was in good agreement with the literature value of 1.61 (Fink 1992).

3.1.3. Density

The density of the lignin-rich bioresidue was determined as 1.50 ± 0.05 g cm^{-3}, which is at the higher end but within the range of 1.35-1.5 g cm^{-3} quoted in literature (Wypych 2018).

3.2. Chemical profile

This section pertains to the components of the lignin-rich extract, reporting recovery of lignin (yield), and composition.

3.2.1. Lignin content

The lignin recovery from the CBS feedstock is reported l in Table 7, both as a percentage of the available lignin from the feedstock, and purity of the bioresidue. The overall recovery of lignin from the feedstock is detailed, by considering the results of the bioresidue yield by solids content, along with the lignin content of the extracts once recovered.

Table 7: Recovery of lignin from a cocoa bean shell feedstock as determined by the acetylbromide assay, where concentrations were calculated using a molar absorptivity constant of 2.36 L cm^{-1} g^{-1}.

Sample	Absorbance (-)	Mass extracted from CBS (%)	Lignin content (%)	Lignin recovery (%)
CBS	0.262 ± 0.0139	-	33.55 ± 1.50	-
CBS-LC	0.410 ± 0.00330	7 ± 0.5	52.52 ± 0.46	10.85
CBS-LR	0.481 ± 0.0135	7 ± 0.5	61.67 ± 1.72	12.87

The lignin content found for CBS was in agreement with the value of 32.4% reported in literature (Soares and Oliveira 2022).

The data reported in Table 7 reveal that the lignin content of the bioresidue was considerably lower than literature values. For example, utilising sulfite pulping a lignin content of 62% (Deshpande *et al.* 2022) (as indicated by 17 of the available 27% available) (Areej *et al.* 2023) or deep-eutectic solvent extraction yields of > 85% (Meindl *et al.* 2022) were previously reported. This difference was no doubt due to the mild extraction, as outlined in 1.2.3.

3.2.2. Chemical composition analysis of CBS bioresidue using FTIR spectroscopy

The presence of lignin and other co-extractives were qualitatively identified using FTIR absorbance spectra, from Table 3 in 1.2.4.1. As the energy required to induce a stretch, vibration, or rotation of a bond is specific to the environment in which the molecule exists,

a series of specific absorbance values allows for identification of the presence of a molecule in solution (Burrows *et al.* 2013b). Figure 20 shows the spectra acquired for CBS-LC, and Kraft lignin as a reference.

Assignments at 825 cm^{-1} and 1025 cm^{-1} show the presence of an aromatic system, evidencing the presence of lignin in the sample. In addition, absorbances at 1342 cm^{-1} and 1116 cm^{-1} show assignments attributed to the syringyl sub-unit idented in the literature review 1.2.4.1, a characteristic moiety of the lignin biomolecule.

Furthermore, the CBS-LC spectra demonstrate absorbances at values associated with cellulosic, hemicellulosic, and lipid classes of biomolecules, and absorbances at 1145 cm^{-1} and 1130 cm^{-1} which are associated with the guaiacyl and syringyl monomer units respectively.

In addition to the presence of lignin, several assignments suggest the presence of lipids as co-extractives. The two peaks at 2920 cm^{-1} and 2850 cm^{-1} are characteristic of free fatty acids, as they indicate a conjugated C-H vibration of an aliphatic system with chain length greater than 10 carbon atoms (C10), which are not found within the aromatic lignin macromolecular structure. Lignin is a biomolecule containing an aromatic ring substituted with branching hydrocarbon substituents, as identified in the literature review 1.2.1, however the C10 length of the chain is further evidence that the absorbance at this wavelength is the result of a co-extractive of lignin.

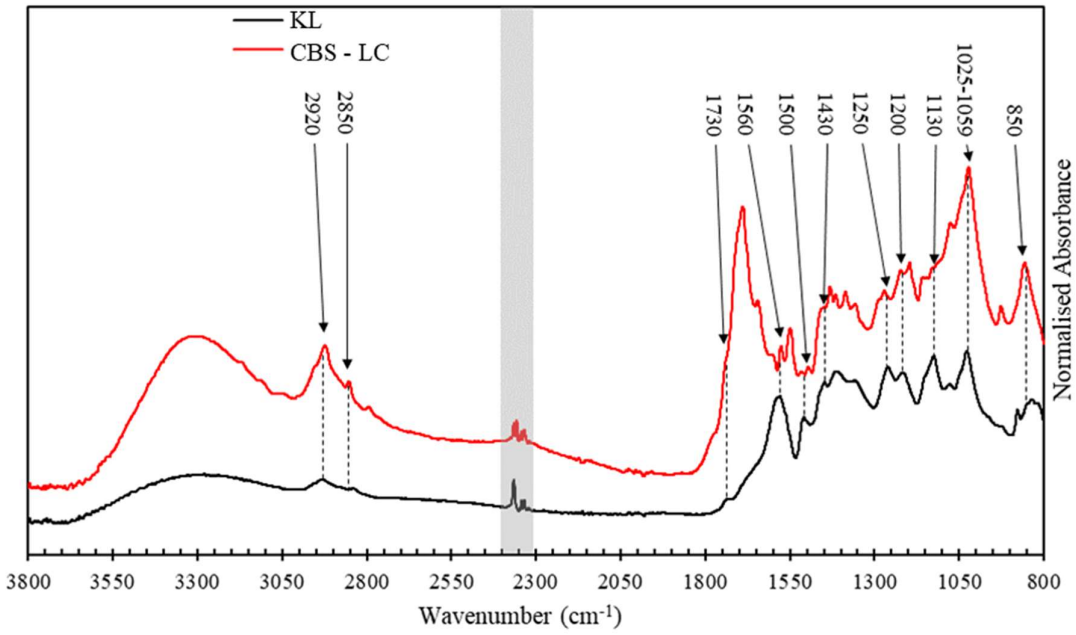


Figure 20: FTIR absorbance spectra (4,000 – 800 cm^{-1}) of CBS-LC(red/top data trace) and commercially available Kraft lignin (black/bottom data trace) as reference. The data traces were shifted vertically to facilitate comparison.

As highlighted in the literature review, the presence of molecular surfactant and amphiphiles in the system can impact both the formation of CLPs and their subsequent wetting properties. The removal of these molecular surfactants and amphiphiles was assessed by FTIR, with a hexane extracted version henceforth referred to as 'lipid removed, LR' compared for the removal of associated peaks, Figure 21.

The absence of the lipid fraction was demonstrated by key absorptions associated with free fatty acids (FFA), at 2920 cm^{-1}, and 2850 cm^{-1}. In addition, the lipid fraction itself was analysed by FTIR to offer an indication of the functionalities of lipids present in the extract. Absorbances at 1658-1660 cm^{-1} indicated double bond carbon, carbon conjugation, and therefore at least some degree of unsaturation of the FFA.

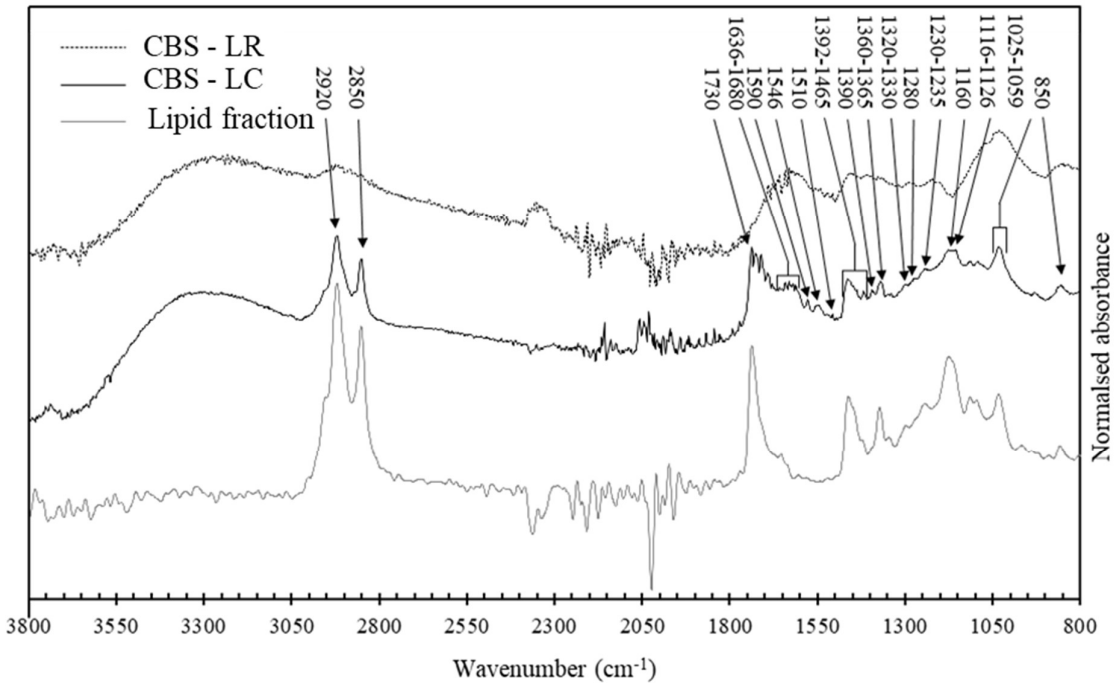


Figure 21: FTIR absorbance spectrum of an organosolv extracted residue of CBS. CBS-LC (black, central) spectra are compared to the spectra of a hexane wash. Indicated are the soluble (grey, solid) and insoluble (black, top) fractions of a hexane wash.

3.2.3. Quantification of the lipid fraction of CBS using GC-MS spectrometry

The profile of the lipid fraction identified by FTIR in 3.2.2 was characterised by GC-MS. Five major components were identified, Table 8. The m/z fragments used to assign a structure to each spectrum are indicated on each molecule. Figures 23-27 show GC-MS spectra with inset molecules and fragments used for identification. Spectra were compared to the American National Institute of Standards (NIST) database.

These were characterised by an initial peak at m/z = 15 (CH_3), however, low m/z value fragments are commonly difficult to discern due to species with multiple charges (z = 2).

Peaks at 29 (CH_3-CH_2) and 43 (CH_3-CH_2-CH_2) are far more reliable and confirm the presence of an alkyl chain. The response column offers quantification of the presence of each lipid fraction in the system, indicating the relative amounts of substance of each lipid. The molecules in Table 8 are referred to as surfactants for the remainder of this research, owing to their polarity caused by the presence of an ester link. This contains two oxygen heteroatoms, which can undergo hydrogen bonding and therefore induce greater polarity than the pure hydrocarbon end of the molecule. As a result, the action of the 'lipid' fraction is analogous to the action of weak surfactants, hence their description as surfactants throughout this research.

Table 8: Compounds identified by mass spectrometry spectra as present in the lipid fraction of the bioresidue of CBS.

Component	**Response (%)**	**Molecular ion (g mol^{-1})**	**Density (g cm^{-3})**	**Boiling point (°C)**	**Spectrum**
Isopropyl Myristate	44.4	271	0.850	167	Figure 23
Octadecanoic acid ethyl ester	28.0	312	0.941	361	Figure 24
Trimyristin*	15.9	300	0.885	311	Figure 25
Ethyl hexadecanoate	9.81	284	0.864	192 - 193	Figure 26
Ethyl Oleate	1.89	310	0.870	216 - 218	Figure 27

**Trimyristin was identified as a triglyceride by hydrolysis to tetradecenoic acid silylisation, thus identification peaks refer to the silyl ester of the hydrolysed ester.*

Isopropyl Myristate

Isopropyl myristate (IPM) could be identified in Figure 23 due to multiple key ion peaks and intensities. The peak at 271 showed the molecular ion. The large intensity of the peak at 43 was due to chains at both ends of the molecule having the C_3H_7 fragment, plus the 2° nature of the β-carbon being able to stabilise charge. Isopropyl myristate has previously been identified as a component within CBS (Chung *et al.* 2003).

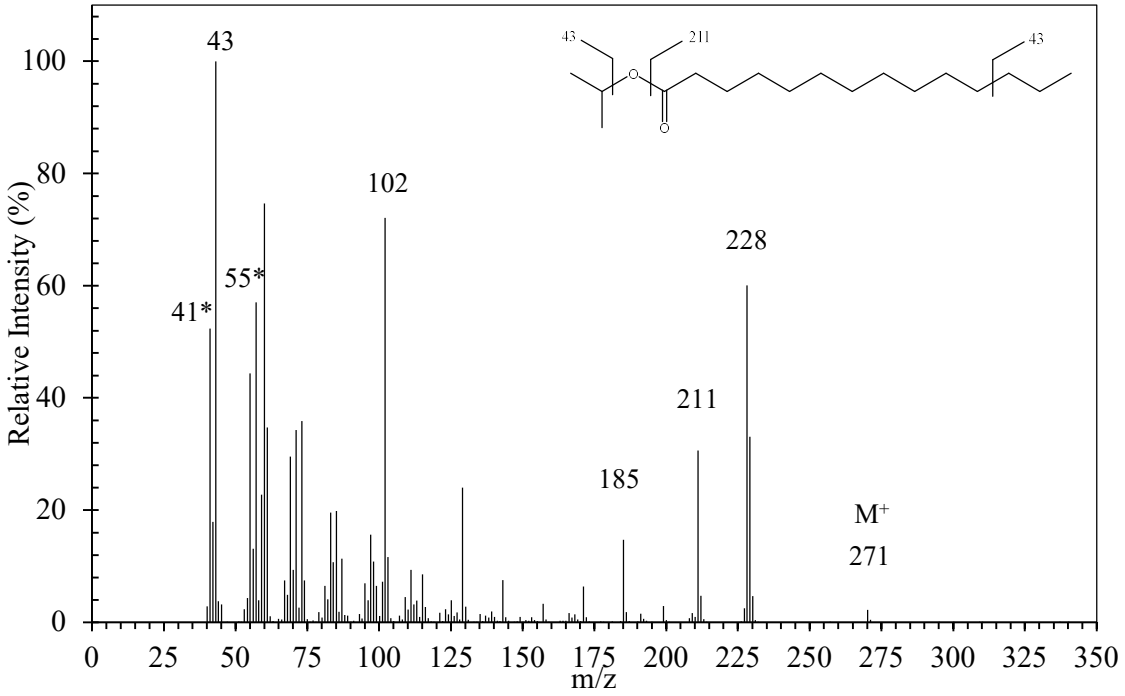


Figure 23: Mass spectrum of Isopropyl myristate on a normal phase mass spectrum. Lipid was separated from a crude bioresidue of cocoa shell on a Rxi sil-MS column in gradient mode between 120 and 300 °C at a ramp of 10 °C per minute. The mass spectrum was obtained by electrospray ionisation at 70 mV, with an interface temperature of 250 °C. Key fragment assignment of the molecule (top right). Peaks with an asterisk (*) denote rearrangements of fragments. Spectrum was compared to the NIST database to aid identification.

Octadecanoic acid

The presence of an ethyl ester of octadecanoic acid was shown by the spectrum depicted in Figure 24. Key fragments at 43 m/z units demonstrated the presence of an alkyl chain, and the ester group was identified by the peak at 73 m/z units. The molecular ion identifies the mass of the molecule as 312 m/z units, allowing for identification of the length of the alkyl chain as c17.

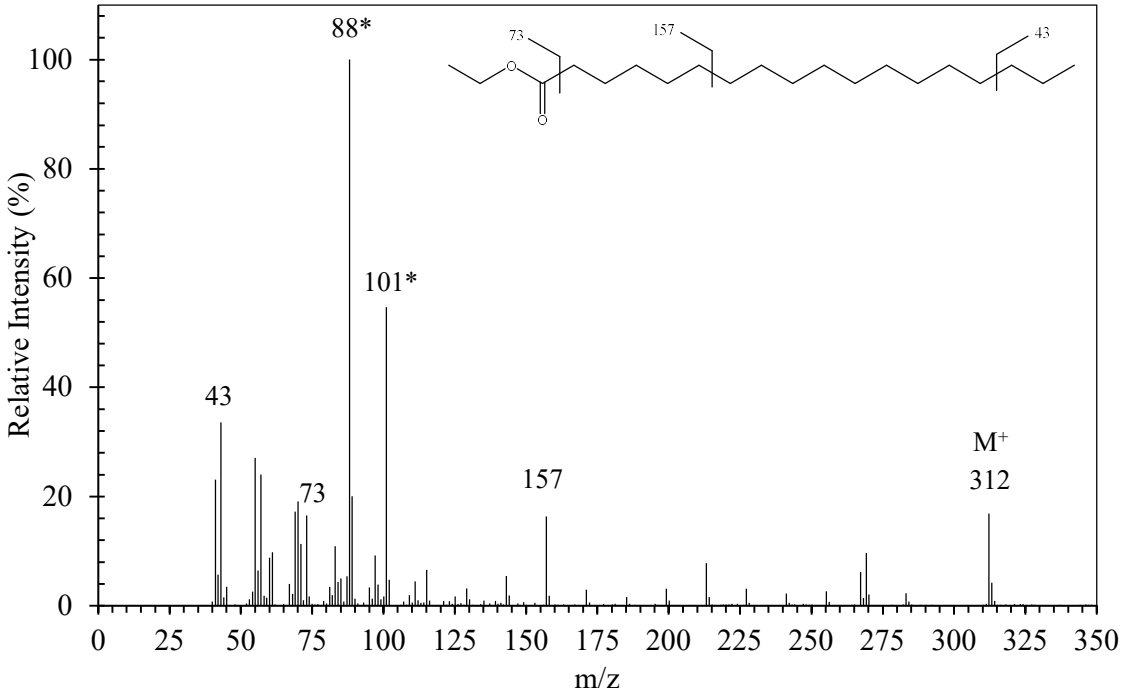


Figure 24: Mass spectrum of octadecenoic acid ethyl ester on a normal phase mass spectrum. Lipid was separated from a crude bioresidue of cocoa shell on a Rxi sil-MS column in gradient mode between 120 and 300 °C at a ramp of 10 °C per minute. The mass spectrum was obtained by electrospray ionisation at 70 mV, with an interface temperature of 250 °C. Key fragment assignment of the molecule (top right). Peaks with an asterisk (*) denote rearrangements of fragments. Spectrum was compared to the NIST database to aid identification.

Trimyristin

The componentry of triglycerides can be distinguished from FFA by conducting a selective base hydrolysis. The presence of the silyl ester of tetradecenoic acid indicated by comparison to NIST database that the triglyceride version was present in the initial sample, before hydrolysis. Trimyristin has the name formula 2,3-di(tetradecanoyloxy)propyl tetradecanoate (IUPAC), referred to commonly as trimyristin. The silyl ester has been identified by fragmentation mass-spectrometry,

Figure 25. As trimyristin was the only silyl ester identified in the GC-MS analysis, it can be concluded that this was the only triglyceride present in significant enough quantity as a co-extractive of lignin in this organosolv extraction to be detected.

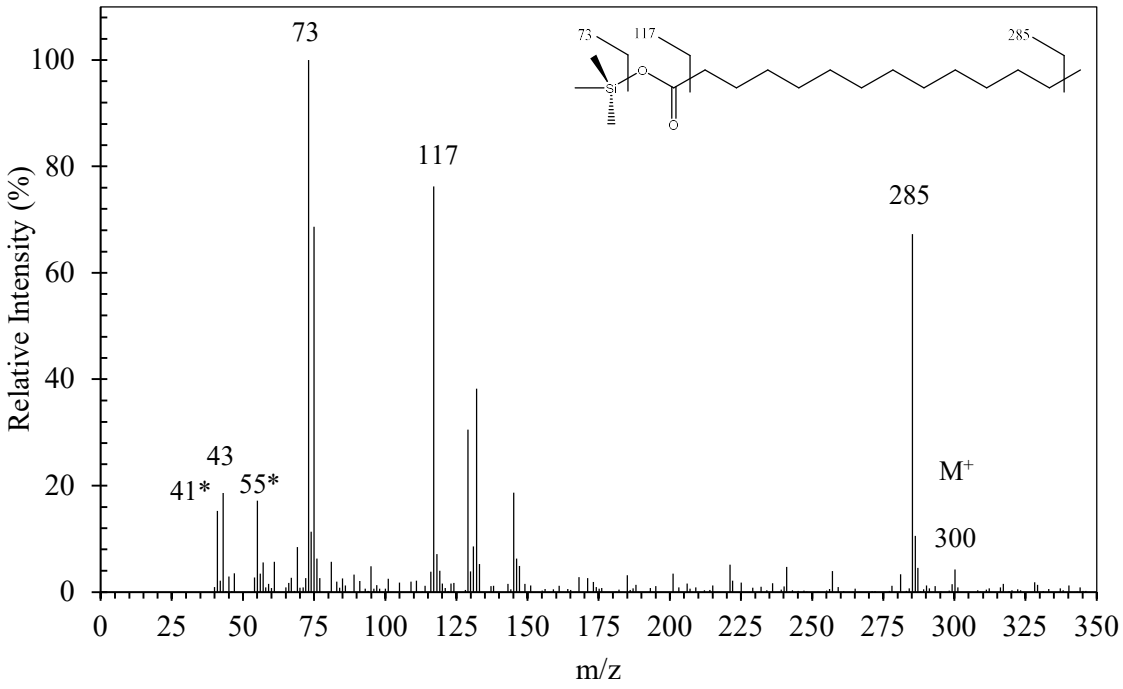


Figure 25: Mass spectrum of tetradecenoic acid trimethylsilyl ester on a normal phase mass spectrum. Lipid was separated from a crude bioresidue of cocoa shell, hydrolysed, and reacted with a donor of trimethylsilane for 60 minutes at 60 °C, before separation on a Rxi sil-MS column in gradient mode between 120 and 300 °C at a ramp of 10 °C per minute. The mass spectrum was obtained by electrospray ionisation at 70 mV, with an interface temperature of 250 °C. Key fragment assignment of the molecule (top right). Peaks with an asterisk (*) denote rearrangements of fragments. Spectrum was compared to the NIST database to aid identification.

Ethyl hexadecanoate

The presence of ethyl hexadecanoate was identified by the GC-MS spectrum, Figure 26. The key peak at 73 m/z units identifies the presence of an ethyl ester, and the peak at 42 m/z units identifies the alkyl chain.

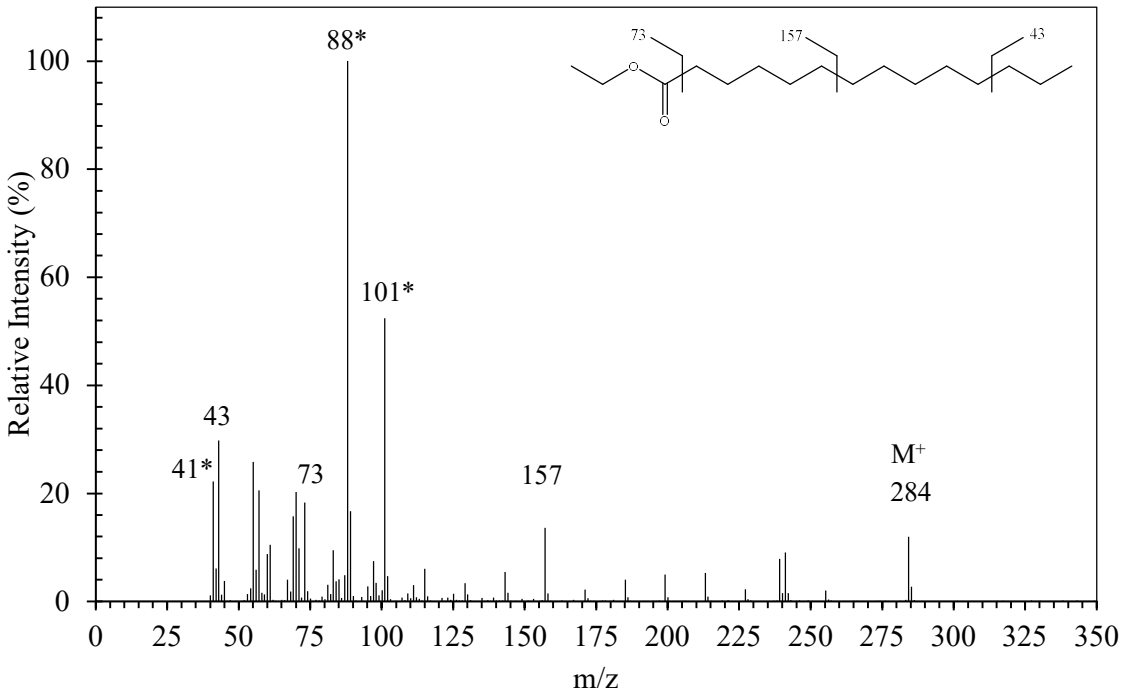


Figure 26: Mass spectrum of ethyl hexadecanoate on a normal phase mass spectrum. Lipid was separated from a crude bioresidue of cocoa shell on a Rxi sil-MS column in gradient mode between 120 and 300 °C at a ramp of 10 °C per minute. The mass spectrum was obtained by electrospray ionisation at 70 mV, with an interface temperature of 250 °C. Key fragment assignment of the molecule (top right). Peaks with an asterisk (*) denote rearrangements of fragments. Spectrum was compared to the NIST database to aid identification.

Ethyl oleate

Ethyl oleate was identified by GC-MS spectrum, Figure 27. The ethyl oleate molecule was particularly fragmented compared to other FFAs identified in this system. This was likely due to the presence of the unsaturated double bond in the system. Upon fragmentation of the double bond, the radical is likely to undergo secondary fragmentation to stabilise the charge, which can lead to further molecular fragmentation Burrows *et al.* (2013b). The E- isomerisation around the double bond was indicated by the relative magnitude of the peaks for fragments on either side.

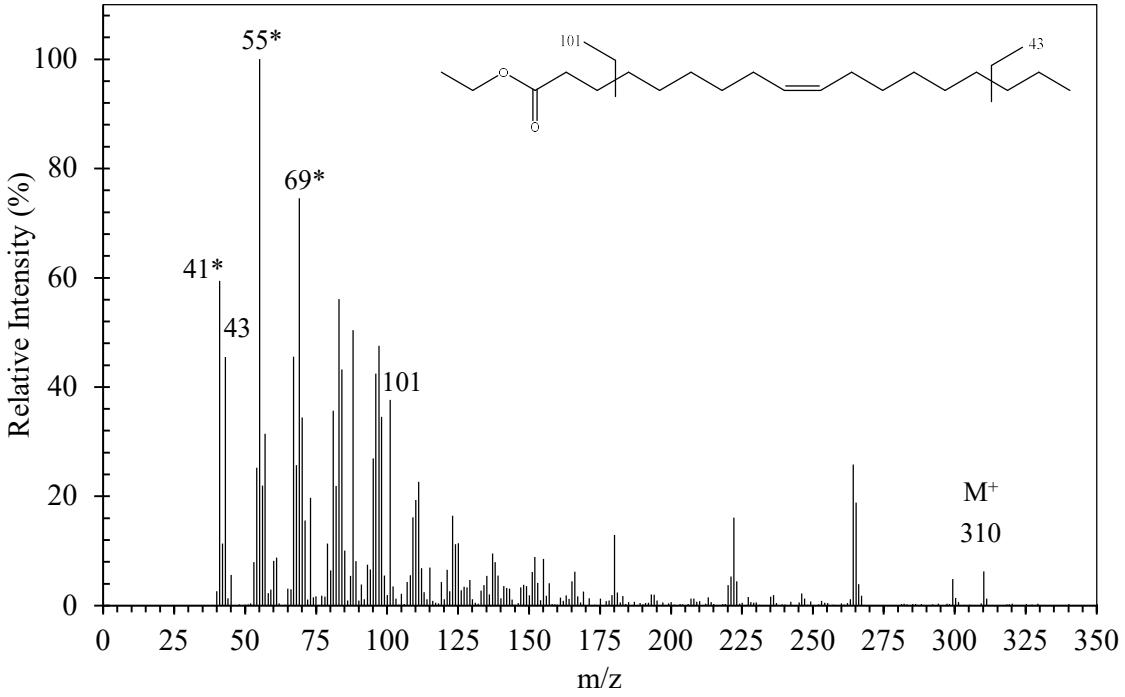


Figure 27: Mass spectrum of ethyl oleate on a normal phase mass spectrum. Lipid was separated from a crude bioresidue of cocoa shell on a Rxi sil-MS column in gradient mode between 120 and 300 °C at a ramp of 10 °C per minute. The mass spectrum was obtained by electrospray ionisation at 70 mV, with an interface temperature of 250 ℃. Key fragment assignment of the molecule (top right). Peaks with an asterisk (*) denote rearrangements of fragments. Spectrum was compared to the NIST database to aid identification.

The properties of each lipid are presented in Table 8 The boiling points of the lipids are greater than the boiling point of both solvents used later processing: ethanol (78.4 °C), and water (100 °C). As a result, the lipids cannot be removed from the system by distillation. To reduce the amount of processing required, and to retain the 'crude' nature of the extract, the lipids were retained in the system for further research unless specifically noted.

3.3. Selected physical properties of bioresidue solutions

In this section, the solubility, viscosity, and density data for both extracts (CBS-LC and CBS-LR) are reported.

3.3.1. Solubility

As detailed in section 2.2.5, the solubility of CBS-LC and CBS-LR was determined by solids content, Figure 28. Although the principal solvent, ethanol, solubilises lignin at a maximum of 8 wt%, the relative insolubility in water (< 2 wt%) means that it was still a suitable system for antisolvent precipitation.

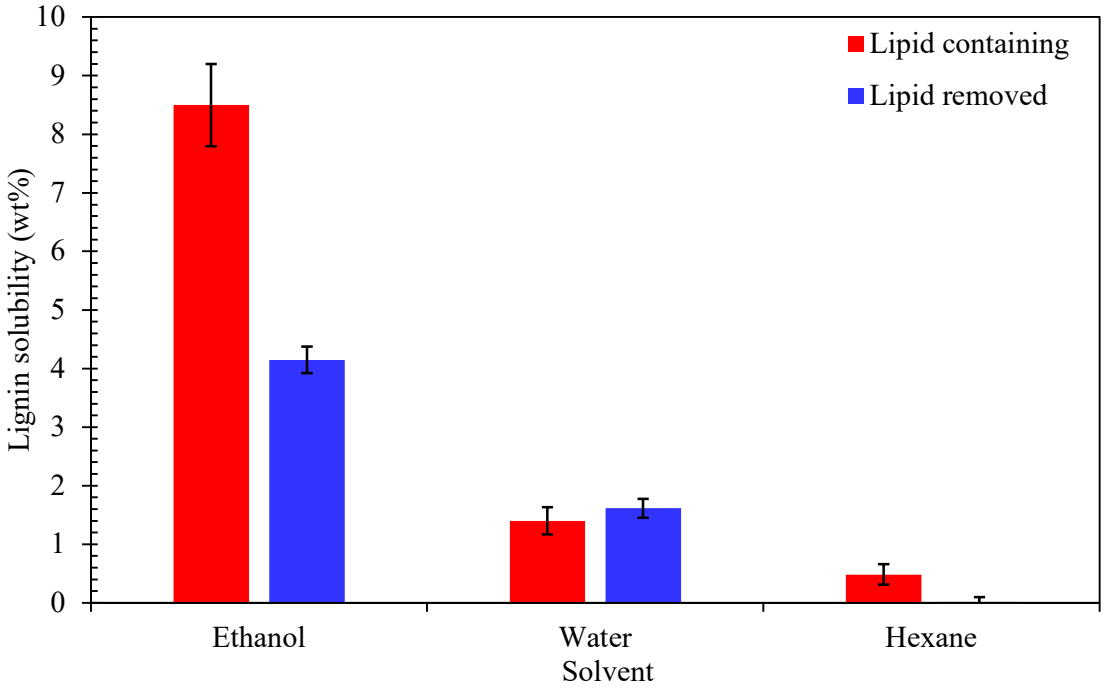


Figure 28: Solubility by solids content of lignin-rich CBS bioresidue in a selected range of common solvents. Error bars indicate ± 1 standard deviation.

For full precipitation, miscibility between solvent and antisolvent must be retained. Therefore, this limits the choice of solvent/antisolvent pairings for particle production. As previous literature (Lievonen *et al.* 2016; Cuthill *et al.* 2021) primarily utilise water and ethanol as their system, this method was also adopted here. Two extracts were studied; lipid containing, and lipid removed. Retaining the lipids facilitated investigation of the properties of the bioresidue close to its native form.

3.3.2. Viscosity

For calculation of the Reynolds number (*Re*), the viscosity of lignin in solution was measured at a series of concentrations, Table 9.

Table 9: Viscosity of solutions of lignin dissolved in ethanol and precipitated in water at a series of volumetric concentrations at 20 °C.

Ethanol:water ratio (v/v)	Viscosity (mPa s)
1:1	3.2 ± 0.4
0.5:1	3.0 ± 0.5
0.1:1	2.6 ± 0.2

3.3.3. Density

To calculate the *Re* of the solutions and provide values for parameters used in Dynamic Light Scattering (DLS), the viscosity of lignin in solution was measured at a series of concentrations were measured, Table 10.

Table 10: Density of solutions of lignin dissolved in ethanol and precipitated in water at a series of volumetric concentrations at 20 °C.

Ethanol:water ratio (v/v)	Density of solution (g cm^3)
1:1	0.914
0.5:1	0.977
0.1:1	0.986

3.4. Conclusions

This chapter meets Objective 1 of this thesis, by evaluating the componentry of a crude lignin bioresidue, and conducting analysis to identify componentry both qualitatively and quantitatively.

By washing CBS-LC hexane, it was possible to extract a series of co-products alongside lignin, which have previously been referred to as ‘lipids’. The use of separation and analysis techniques to identify isopropyl myristate, ethyl oleate, octadecanoic acid ethyl ester, and hexadecenoic acid ethyl esters was demonstrated.

As corroborated by literature, a significant component of the bioresidue was lignin. One notable difference from similar literature was the composition of the lipid fraction, which contains a greater fraction of low weight molecular surfactant.

Additionally, it has been possible to identify a triglyceride, tetradecenoic acid, by identification of its trimethylsilate ester. In identifying these lipids as co-extractives, there is now a greater understanding of the types of lipid present in extracts of CBS. This will inform further investigation into the wetting properties of the bioresidue and derived colloidal particles, for applications such as emulsion stabilisation or tracer particles.

4. Hydrodynamic flow-focusing for microfluidic droplet formation

This chapter introduces the setup of a hydrodynamic (HFF) device for formation of droplets of lignin-solubilised ethanol in water, which would then desolve to form large particles. It was hypothesised that the presence of lignin would allow for formation of an interface between the ethanol and water, alowing for formation of a droplet of ethanol and lignin. The ethanol would then desorb from the droplet, allowing precipitation of a lignin partichle on which further analysis could be conducted. HFF devices are known for their ability to control droplet volumes with a high degree of monodispersity. By varying droplet volume, it was hoped that the corresponding particle diameters could be controlled. Both lignin-rich cocoa bean shell bioresidues, with and without the associated lipid (CBS-LC, and CBS-LR respectively) were applied.

This chapter consists of three main sections; the first is establishing appropriate conditions for dropelt formaiton such that the solubilised system can be used for particle production. The second shows the interfactions between the device and the solubilised lignin, inhibiting the droplet formation step and therefore desorption. The final section of this chapter demonstrates attempts to modify the wetting properties of the device to mitigate the interactions between lignin and the device.

4.1. Optimisation of conditions for droplet formation in a hydrodynamic flow- focusing device

As described in the literature review section 1.4.1, hydrodynamic flow-focusing (HFF) for particle production is widely documented in the medical field, with a focus on precipitating particles of single solute systems. This section attempts to build on this to precipitate particles of CBS-LC after initial validation of the experimental conditions required.

4.1.1. Droplet formation for antisolvent precipitation

To determine appropriate conditions for droplet formation, solutions for the dispersed phase of equal density to ethanol-solubilised lignin were produced, and a range of droplets were surveyed to identify a region suitable for droplet formation. Figure 29 shows the droplet formation of a series of ethanol and water mixtures in an oil phase, indicating the impact of varying the concentration on droplet formation.

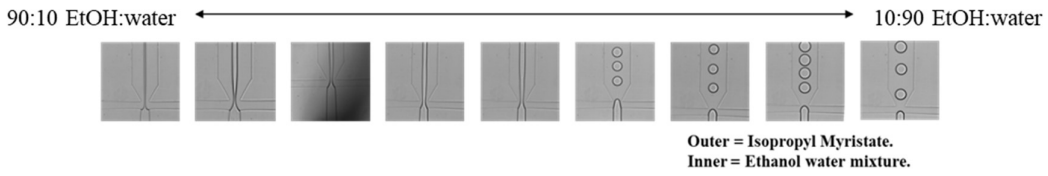


Figure 29: Droplet formation conditions and impact of an ethanol:water mixture dispersed in an oil phase with flow conditions of 10 μL min^{-1} (internal) and 40 μL min^{-1} (external).

4.2. Fouling behaviour caused by interactions between polydimethylsiloxane polymer and lignin

Using the conditions from 4.1.1 and solubilised lignin (3.5 mg mL^{-1}), attempts to make large droplets of lignin and desolve them into particles were made. Upon introduction of the solvent phase and the antisolvent, there was immediate precipitation of lignin, leading to fouling of the device, and loss of a controllable interface, Figure 30. Whilst there is an interface, precipitation occurs before the droplet formation phase.

When attempting droplet formation for particle production by antisolvent precipitation from ethanol dissolved CBS-LC in the prepared flow-focusing device, the antisolvent precipitation step occurred more quickly than droplet formation. As a result, it was hypothesised that owing to the precipitation into the water, a hydrophobic substrate would inhibit precipitation on the device. Figure 30 shows the early stages of precipitation upon introduction of the dispersed phase to the continuous phase. In Figure 30, the flow rates of 5 and 15 μL min^{-1} for the dispersed and continuous phases respectively indicating droplet formation will occur in the dripping regime. However, the flow regime shown most closely resembles threading (Cubaud and Mason 2008). Precipitation is shown to begin within 0.05 seconds, with complete infiltration of water into the ethanol achieved by 20 seconds; however, precipitation occurs faster than both droplet formation and dispersed phase egress. Precipitation occurs far faster than dispersed phase egress, allowing precipitation to occur within the channel. Figure 30 shows that droplet breakup is not occurring, an apparent 'threading' regime (Cubaud and Mason 2008), however reduction of the dispersed phase flow rate does not result in droplet formation by dripping, therefore the flow dynamics are not responsible for the observation. This is likely due to

precipitation occurring immediately on contact between the two solutions, solidifying the interface by precipitation of lignin.

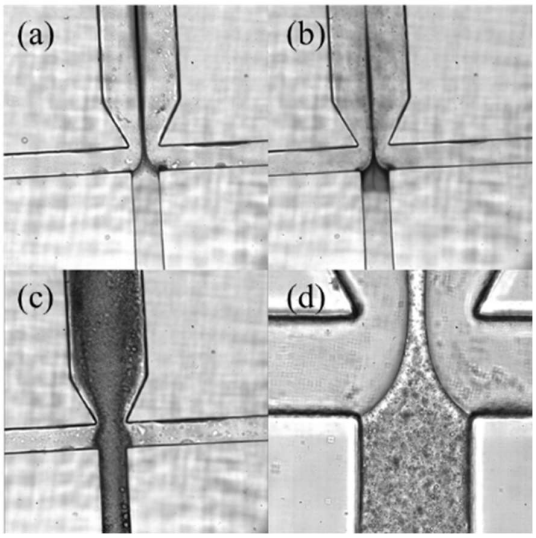


Figure 30: CBS antisolvent precipitation in a water continuous phase (d = 5 μL min-1, c = 15 μL min^{-1}, demonstrating precipitation of particles from dispersion. Time as follows at 10 x magnification: (a), t = 0.00 s, (b), t = 0.05 s.

As precipitation is occurring on a faster time scale then droplet formation, it is not possible to form the larger particles through solvent desorption as initially hypothesised. One possible explanation for this is an interaction between the CBS-LC extract and the polydimethylsiloxane (PDMS) device itself. In forming large particles of lignin through solvent desorption, it had been hoped that a direct measure of the surface properties of particles could be achieved. As modifying the bioresidue to accommodate precipitation would be counterproductive to the aims of studying lignin in its close to native form, device modification for precipitation was sought.

4.3. Surface treatment of a PDMS microchannel to mitigate fouling in the microchannel

This section describes the surface treatments applied to the PDMS HFF channel to generate a more hydrophilic layer to remove the fouling observed in section 4.2.

4.3.1. PDMS surface treatment methods

To alter the wetting properties of the device, and avoid the fouling observed earlier, a series of surface treatments were applied to the device. The resulting contact angles were measured per Section 2.5.4 immediately after application, and 24 h after application when left in air are shown in Figure 31. In selecting the treatment for testing in the microchannel, it was decided that 24 h of stability represented a sensible criterion. The consideration for this is that, per objective 2 of this thesis, a continuous method for the production of colloidal particles is sought. Were a treatment to enable particle production, only for the system to degrade over a short time, the system would cease to be continuous.

As a result of this criterion, plasma treatment, and HCL submersion were immediately disregarded as suitable treatments. A likely reason for the recovery of the hydrophobic nature of the device is that the PDMS in the device exists as a structure with an uncured polymer capable of leaching through the device, even after prolonged curing times (Lee *et al.* 2003). As a result of this, following treatment, the polymer can migrate to the surface of the device, increasing hydrophobicity and thereby negating the effects of plasma and HCl treatments.

Conversely, polyelectrolyte and PVA treatment cover the surface of the device, forming a physical layer of coating between the PDMS and the fluid moving within. This allows the treated surface coating to be retained.

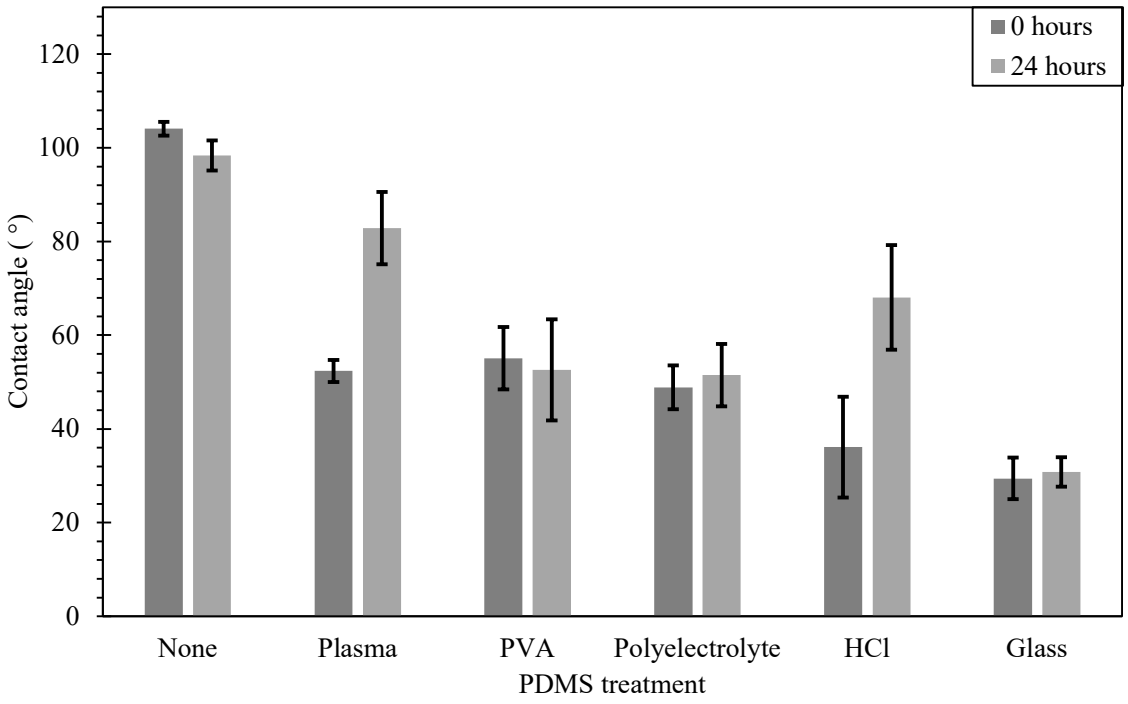


Figure 31: Contact angle of PDMS containing several treatment methods immediately after treatment, and 24 h after treatment. Samples are the results of 10 repeats, and error bars are ± 2 standard deviations.

Trantidou *et al.* (2017) reported PVA contact angles below 40 °, lower than the average of 55.1° reported here over the same timeframe. The likely reason for this is the lower energy corona discharge used in this study of 12 W, lower than the 50 and 100 W used.

4.3.2. Interactions between lignin and device

Figure 32 shows the result of passing ethanol-solubilised lignin through a polyelectrolyte-treated HFF device under the conditions determined earlier of 5 μL min^{-1} for the dispersed and 30 μL min^{-1} for the continuous flow rate. It can be observed that the previously

determined flow conditions for droplet formation are not replicating formation, and thus droplet production and desorption are not established in the device, likely owing to interactions between the device and the solubilised lignin.

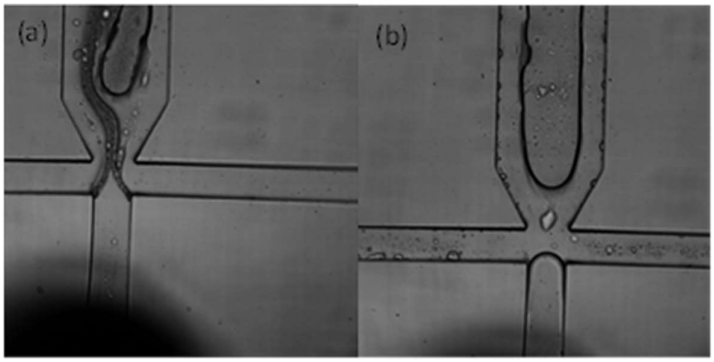


Figure 32: Example of a polyelectrolyte-treated HFF device at 10 x magnification. In (a) CBS (5 mg mL^{-1}) in ethanol dispersed phase (5 µL min^{-1}) is passed through the device in a water continuous phase (30 µL min^{-1}), In (b), a hydrophobic domain inhibiting droplet formation within the device.

Here, a secondary problem was encountered, in that the surface treatment was removed from the device, causing fouling to occur in the device. As the only potential source of the damage is the extract, it is almost certain that the presence of amphiphilic extractives has allowed for interaction between the surface coating and a CBS extractive. With the observed interactions between the hydrophilic coating and the extract, whereby a component such as palmitic acids are theorised to adsorb to the surface, this represents a barrier to droplet formation. Adsorption of these amphiphiles to a hydrophilic coating would explain the hydrophobic domain observed. When taken with the objective of not modifying the crude extract, the issue of droplet formation in an HFF appears to be structural and therefore particle formation in a HFF is not possible under the constraints. It was anticipated that in using this device, antisolvent precipitation would occur on a timescale slower than droplet formation, allowing for large droplet formation before the antisolvent condensed the droplet into a particle.

Following the persistent fouling demonstrated, a change in process was required to satisfy the objective of particle formation. The use of coaxial jet mixing (CJM) provides a physical barrier between phases before antisolvent precipitation. Given the objective of forming a robust method for particle formation, CJM represents a method where particle generation is possible. For pure systems not involving precipitation from inhomogeneous extracts, the device can be optimised such that there are no interactions between a solute and the device such as those identified in the literature review Section 1.3.1; however, when dealing with a complex system with undefined and variable surface-active composition, there are not presently any suitable coating methods. CJM dispenses with the droplet formation stage, reducing the monodispersity of the formation process to facilitate particle formation.

One alternative way to mitigate the fouling identified in this chapter whilst retaining a flow-focusing device process is by increasing channel height sufficiently, such that device height is significantly greater than channel width. This would minimise the likelihood of interactions between the dispersed phase and the wall. For droplet formation, the dispersed phase should never interact with the wall, suggesting long-range interactions are present.

One consequence of using PDMS-based devices is that the device itself is hydrophobic. Subsequent modification to generate a hydrophilic surface was unable to form droplets due to interaction between the bioresidue and the coating. A stable, hydrophilic device, for example constructed of glass, would hypothetically be able to form particles.

4.4. Conclusions

This chapter demonstrates the development of a hydrodynamic device for the controlled formation of lignin-solubilized ethanol droplets. The initial hypothesis, of creating an interface between CBS-LC solubilised ethanol and water through lignin presence faced obstacles in the form of fouling interactions between the PDMS and lignin. Attempts to induce large droplets for subsequent particle production were hindered by uncontrolled precipitation and subsequent loss of a controllable interface, despite initial validation. Surface treatments, aimed at mitigating fouling were unsuccessful, with interactions persisting between the PDMS device and solubilized lignin, likely due to the amphiphilic nature of the lignin and its co-extractives. Ultimately, the envisioned particle formation in a hydrodynamic focusing device was unattainable. To this end, a micromixer which eliminates this was sought for subsequent research.

5. Coaxial jet mixing for colloidal particle formation from crude extracts of cocoa bean shell

In this chapter, the application of a continuous coaxial jet mixing (CJM) process for the formation of colloidal lignin-rich particles (CLPs) is reported. Particles were formed through antisolvent precipitation, with lignin-rich extracts of cocoa bean shell (CBS) solubilised in ethanol precipitated in distilled water.

The chapter is organised into three sections followed by conclusions. The first section concerns the establishment and validation of the CJM introduced in Chapter 2 as a continuous process to produce CLPs in aqueous phase dispersion via antisolvent precipitation. The CLPs were produced from CBS-LC as characterised in Chapter 3 dissolved in ethanol.

Utilising CBS-LC and CBS-LR as characterised in Chapter 3, the second section discusses the effect of the Reynolds number (*Re*), and the volumetric solvent to antisolvent flow rate ratio (*R*) on the average particle diameter. These variables are examined by Cumulants analysis and span, a quantification of size distribution width defined later in the section of the particle dispersions and interpreted in the context of nucleation- and growth-dominated formation.

Finally, the third section presents evidence of dispersion stability and discusses the effects of dilution on suspended particle properties and dispersion stability, including data for CBS-LC and CBS-LR, Chapter 3.

5.1. Application of a coaxial jet mixer for antisolvent particle precipitation

This section concerns the establishment and validation of the CJM process for colloidal particle production. The processing parameters governing colloidal particle production are defined, followed by experimental data offering evidence of validation of the production process for the lipid-containing CBS extract.

5.1.1. Definition of processing parameters

A CJM assembled per section 2.5.2 was used to generate colloidal particle distributions through the precipitation of solubilised lignin-rich CBS in an antisolvent. Figure 33, reproduced from an earlier section, shows a schematic of the CJM device.

Device setup

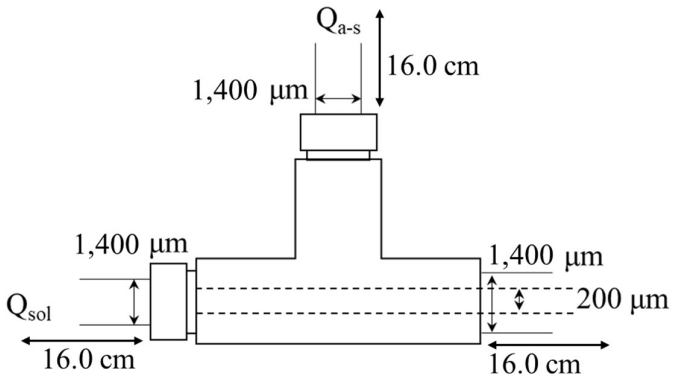


Figure 33: Schematic of a T-junction derived CJM device, consisting of a concentric internal glass tube with an outer flow phase. A phase containing the solvent stream (Q_{sol}) is passed through a coaxial channel with an internal diameter of 200 µm and external diameter of 1,400 µm.

For the production of CLPs using a CJM device, the following processing variables have been previously considered in literature (Villermaux and Rehab 2000); *Re*, *R*, concentration, and mixing time.

In this research, the focus has been on assessing the impact of *R* and *Re*.. CLPs are formed by solvent and antisolvent from filtered stock solutions, altering the concentration of lignin would require the batch concentration to change, thus making the process discontinuous. Conversely, processing variables such as *R* and *Re* allow for induced variation in a continuous process. For the following, a single concentration of solubilised lignin in ethanol solvent was examined, 5 mg mL^{-1}. This concentration was chosen to maintain comparability with similar batch-produced CLPs from literature, such as those in (Cuthill *et al.* 2021) who used 5 mg mL^{-1} solutions.

Span

The Span of a particle size distribution is given by Equation 5.1. This offers a quantitative description of how broad the distribution of particles are in a dispersion, allowing for the polydispersity of a particle size distribution to be compared.

$$Span = \frac{Diameter_{90th} - Diameter_{10th}}{Diameter_{50th}} \tag{5.1}$$

Where the diameter is given at the 10^{th}, 50^{th}, and 90^{th} percentile respectively.

Reynolds number definition

The definition of the *Re* is given in Equation 5.2:

$$Re = \frac{\rho u L}{\eta} \tag{5.2}$$

where ρ is the density (kg m^{-3}), u is the characteristic velocity (m s^{-1}), L is the characteristic length (m), and η is viscosity (Pa s). *Re* is the ratio of inertial forces to viscous forces which has previously been used in the context of flow processes for antisolvent precipitation for particle production (Lim *et al.* 2014; Bovone *et al.* 2019). In these studies, the parameters *v*, was substituted for the cross-section of the channel and flow rate, Equation 5.3.

$$u = \frac{Q_{total}}{A} \tag{5.3}$$

Where *v* is the velocity of fluid flowing through a channel, Q_{total} is the combined volumetric flow rate of both the inner and outer phases, and A is the channel cross section at the point where the solvent and antisolvent meet (m^2).

Flow velocity ratio definition

The second variable chosen to manipulate antisolvent precipitation is the flow velocity ratio, R, as defined in Equation 2.1 (Lim *et al.* 2014). In this case, ethanol solubilised lignin was the solvent and distilled water, the antisolvent, Equation 5.4.

$$Flow\ velocity\ ratio\ (R) = \frac{Q_{solvent}}{Q_{antisolvent}} \tag{5.4}$$

Where Q denotes the flow rate of solvent or antisolvent (per subscript) in μL min^{-1}.

5.1.2. **Validation of coaxial jet mixer setup**

Two CJM devices were independently assembled, and the particle size distribution of processed colloidal particle dispersions was measured by dynamic light scattering (DLS).

This meant that the device was the only variable, and thus, the variation in particle dispersion size distribution data offered evidence of the inherent variability caused by the device construction. For the use of a similar device for particle creation (Bovone *et al.* 2019), it was previously reported that the least reproducible step is the threading of the capillary, and therefore each device was disassembled and reassembled between individual repeats.

The material used to create particles under the same conditions to assess for reproducibility was CBS-LC (5 mg mL^{-1} in ethanol, filtered with 200 nm filter) which was precipitated in water in two separately assembled jet mixer devices labelled Rig 1 and Rig 2. Flow conditions were as follows; $Q_{CBS\text{-}LC:ethanol}$ = 50 µL min^{-1}, Q_{water} = 300 µL min^{-1}, corresponding to Re = 100, R = 0.17.

The data reported in Figure 34 show that the two particle size distributions overlap, with sizes ranging from 80 to 1000 nm and a peak in the region of 200 nm. It can be concluded following an independent samples t-test that the assembly and reassembly of the devices had no impact on the particle size data, as the P value 0.73 returned is 0.73, which is significantly greater than the P=0.05 required to reject the null that the samples are equal. Further statistical comparison by linear regression of the two datasets was conducted, and a resulting gradient of 1.10, R^2 of 0.99 was found, see Appendix A, Figure 73.

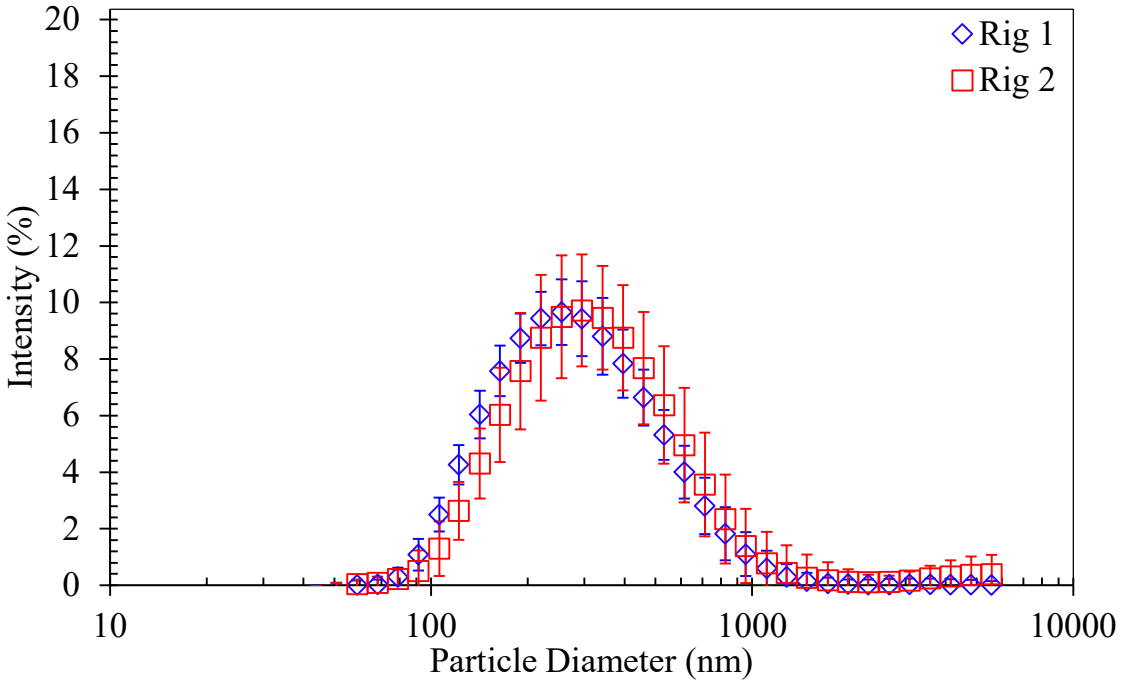


Figure 34: Particle diameter intensity distributions of particle dispersions formed in two independently assembled CJM devices, Rig 1 (blue) and Rig 2 (red). Dispersed lignin in ethanol (5 mg mL^{-1}) was fixed at a volumetric flow rate of 50 µL min^{-1}, with a continuous phase of water fixed at 300 µL min^{-1}, resulting in a *Re* value of 100. Recorded as triplicated repeats of each system using two separately prepared CJM devices. Error bars denote ± 1 standard deviation.

Following validation of the CJM setup, next considered was the impact of batch-to-batch variability of the material system on the diameter of CLPs formed from extracted CBS-LC. The componentry of the system was reported in 3.2. Two separate material extractions were used to generate CBS-LC (5 mg mL^{-1} in ethanol, sterilised with a 200 nm filter) which was precipitated against water using CJM, with three replicates per CBS-LC solution, 6 replicates total at $Q_{CBS\text{-}LC:\ ethanol}$ = 50 µL min^{-1}, Q_{water} = 1,100 µL min^{-1}, corresponding to a *Re* value of 329.

To assess the reproducibility of the extraction, the particle size distribution of two separate extracts are shown in Figure 35. The peak particle size of the 2 dispersions is 220 ± 10 nm, and the span is 0.94 ± 0.09.

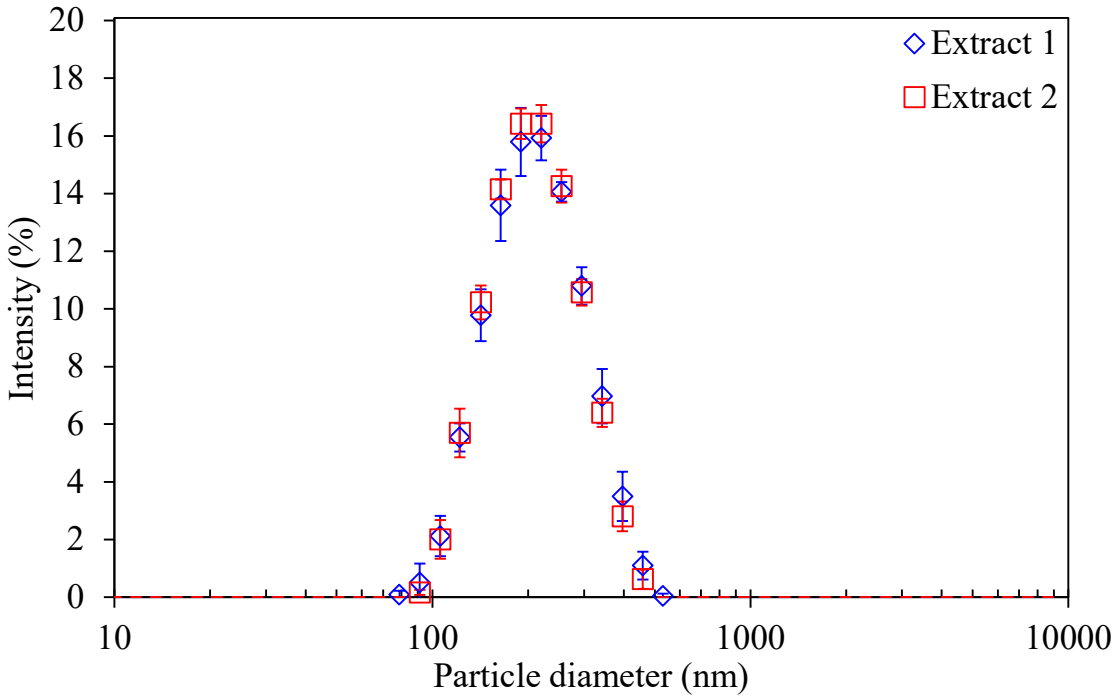


Figure 35: Particle diameter intensity distributions of particle dispersions formed in CJM Rig 1 & 2. Dispersed lignin in ethanol (5 mg mL^{-1}) was fixed at 50 µL min^{-1}, with a continuous phase of water fixed at 1,100 µL min^{-1}, corresponding to a *Re* value of 329. Distributions were collected as triplicated repeats of two separate samples. Error bars denote ± 1 standard deviation.

As with the reproducibility of the device, the material system was analysed by linear regression, see Appendix A, Figure 73 and Figure 74. In both instances the gradient was 1.10. In the instance of the CJM, the R^2 was 0.99 and for material system, R^2 was 0.98, indicating a high degree of correlation. A Paired t-test reported a value of P=0.97,

suggesting that the two datasets shown are not statistically different, and therefore the extraction does not affect the particle sizes.

To conclude, variation in particle diameter distributions arising from the variation of the identified processing parameters is the result of such parameters, and not simply variation inherent in the CJM or material system.

5.1.2.1. Effect of dilution of colloidal particle dispersions on particle diameter of dispersions

One factor which may affect the particle diameter is dilution. DLS works closer to theoretical infinite dilution. The impact of dilutions on particle diameter was assessed. The system was diluted in both water and ethanol, Figure 36. As demonstrated by the overlap of the error bars, the distributions are indistinguishable.

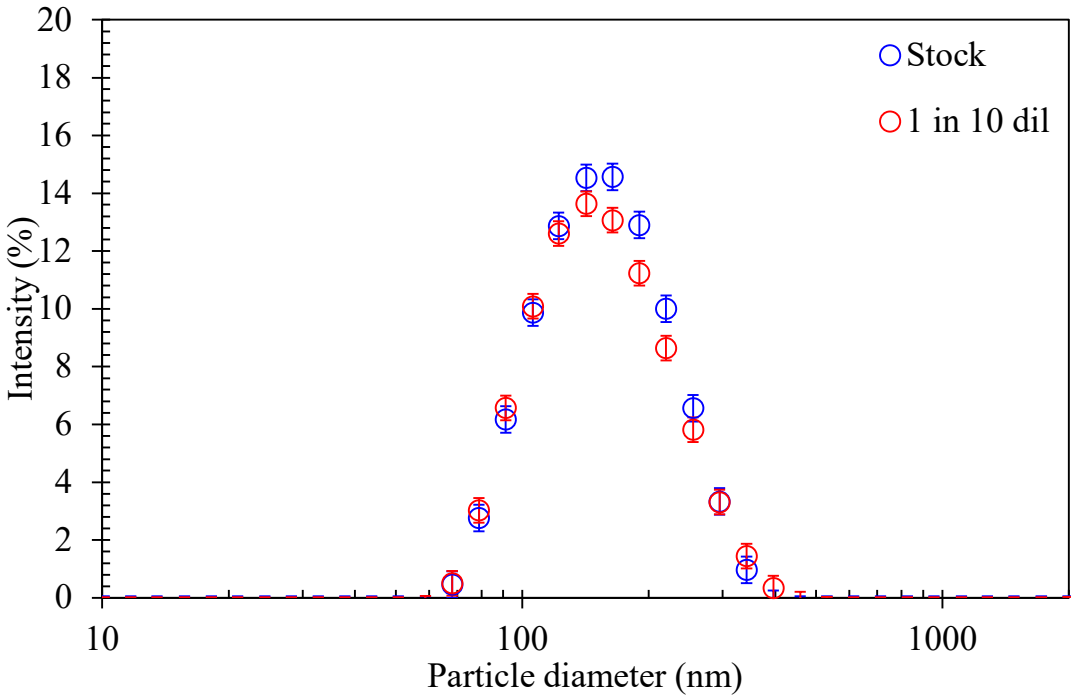


Figure 36: Influence of dilution on colloidal particle dispersions. A stock solution (5 mg mL^{-1}) of aqueous CLPs formed via antisolvent precipitation (R = 0.5, Re = 573) (blue) were diluted 1 in 10 in distilled water (red). Error bars denote ± 2 standard deviations

As demonstrated, the particles retained their distribution profile according to DLS. This offers evidence of the ability for the formed particle distributions to be diluted and concentrated between the concentration of 5 mg/mL and 0.05 mg/mL per the ranges tested.

5.2. Impact of Re and flow ratio (R) on diameter of lignin-rich particle dispersions

5.2.1. Profile of particle diameter distributions

The effects of the two processing variables *Re* and *R* on the diameter of particles in a colloidal dispersion formed at Re between 129 and 358 were investigated. To change

these variables, the volumetric flow rate of both the solubilised CBS-LC and water was varied between 50 and 1,500 μL min^{-1}. *R* was varied between 0.1 and 1.

Figure 37 shows the particle diameter distributions of three colloidal particle suspensions precipitated from a 5 mg mL^{-1} solution at increased *Re*. At the lowest *Re* value considered (129), the average diameter was 260 ± 40 nm, and the span was 1.02 ± 0.11. With an increase in *Re* to 358, the average diameter decreased to 207 ± 10 nm, and the span to 0.64 ± 0.12.

At *Re* =129, there is a shoulder at the lower end of the particle diameter distribution, between 40 and 100 nm. This is consistent among many low (Re <100) dispersions but does not appear in dispersions formed at greater Re, as shown in Figure 37. One possible explanation for this is the generation of an area of inhomogeneous mixing within the device due to the flow rates below 200 μL min^{-1}, resulting in multimodal populations. One possible way this could be confirmed by the use of a pH such as phenolphthalein placed into the central channel with a base such as NaOH, and acid used in the external channel. This would allow for direct imaging of the path of the dispersed phase, which would confirm of disprove the presence of inhomogeneous mixing.

The particle size distribution of has an additional large size population with peak at 6000 nm, separated from the main population with maximum size of 40-100 nm. As this was reproducibly observed, as demonstrated by the error bars, it warrants further examination. One possible explanation for the peak was due to aggregation of the CLPs. This was assessed by microscopy, the results of which are presented later in this chapter.

There is a trend across the three distributions that an increased *Re* value contributes to a smaller average particle diameter. This is consistent with reported literature on systems

used for antisolvent precipitation, such as (Odetade and Vladisavljevic 2016) for non-lignin systems, which report particle diameter of 210-280 nm.

In the context of DLS represented as an intensity distribution, it is anticipated that any particles or aggregates such as those shown at 6,000 nm are larger than the principal population of particles in dispersion. This is because measuring scattering intensity favours larger particle diameters, as their relatively larger particle diameter contributes more greatly to scattering. The low intensity relative to the much larger 200 nm primary peak indicates that where any larger particle is present, it is an extremely low relative concentration. As a result, it is unlikely they are present in the system, however, this will be corroborated using optical microscopy in a later section.

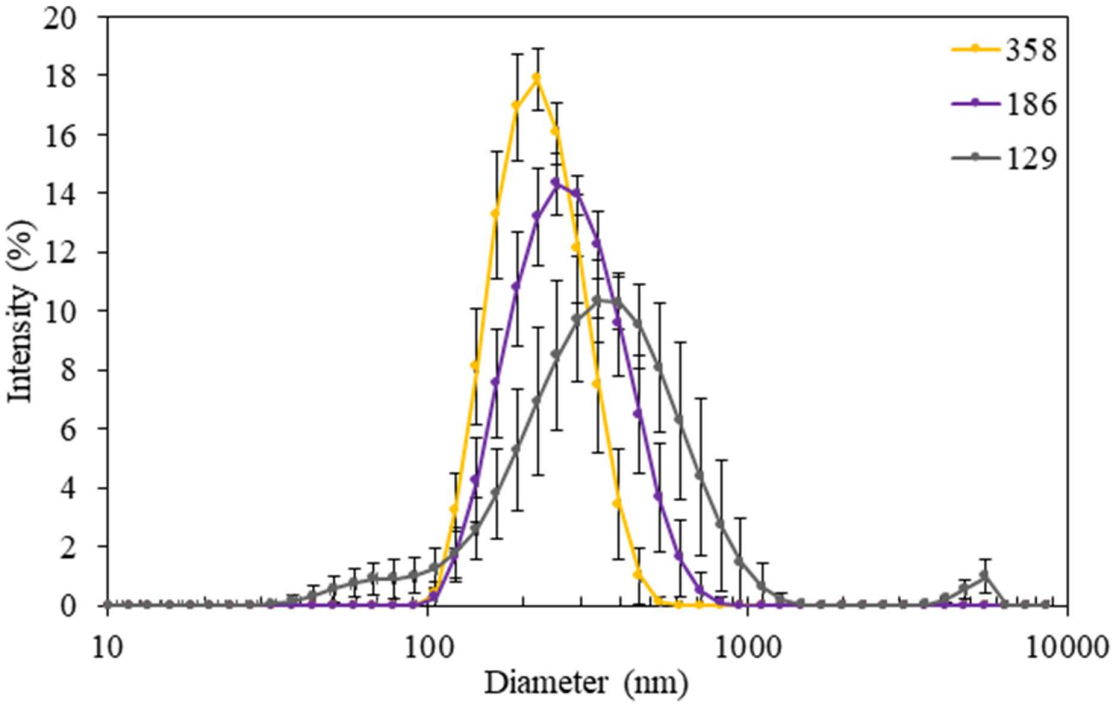


Figure 37: Particle diameter intensity distributions of particle dispersions formed in the CJM device. Dispersed lignin in ethanol (5 mg mL^{-1}) was fixed at 50 µL min^{-1}, with a continuous phase of water varied,

generating Reynolds values of 129, 186, and 358. Distributions were collected as triplicated repeats of two separate samples. Error bars denote ± 1 standard deviation.

At *Re* of 186 and above, the dispersions observed in Figure 37 were no longer present. As a result, the dispersions can conclusively be described as monomodal. Figure 38 represents the above data using particle diameter and span. This demonstrates that with increasing Re, a decrease in average particle diameter is observed, alongside a decrease in span.

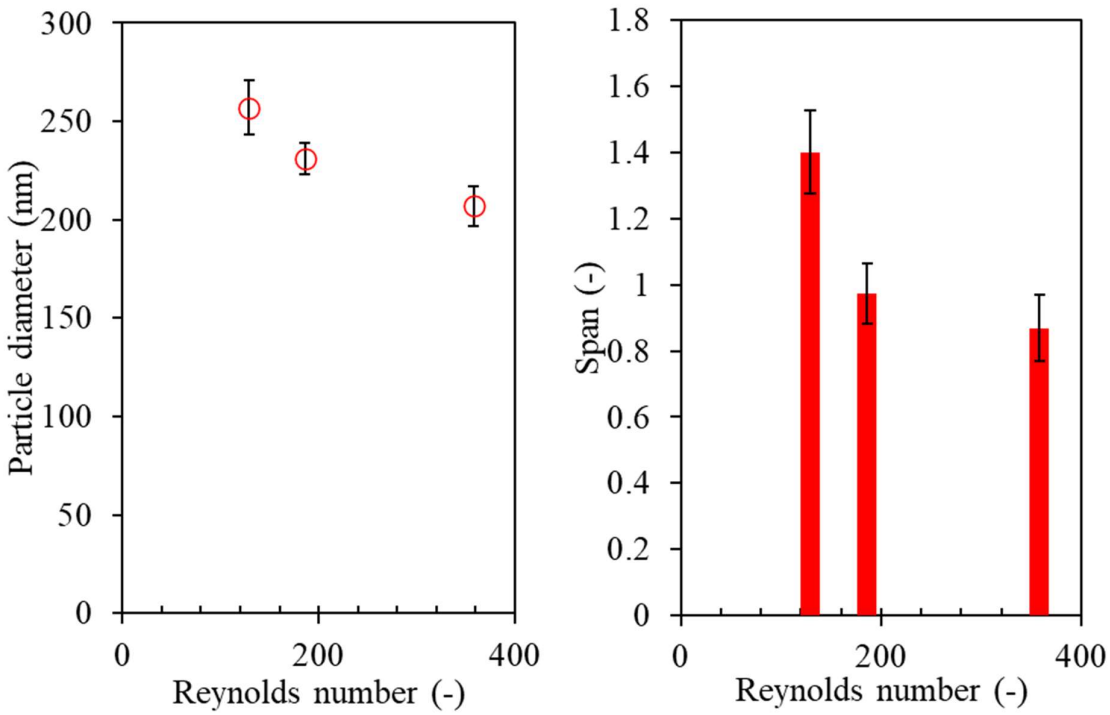


Figure 38: Representation of the effect of *Re* on the features of a particle diameter distribution measured by DLS using two features of the distribution; average particle diameter (left), and particle distribution span (right). Error bars denote ± 1 standard deviation.

5.2.2. **Influence of R and Re on average size and span of colloidal particle distributions**

In this section, the range of particle diameters produced are interpreted as a function of the *R* and *Re*. The CBS-LC was used as a standard, before the influence of lipids was examined later in this thesis.

Figure 39 shows a data set where both *R* and *Re* were systematically varied, to maximise the separation of the two variables. In Figure 39 (A), the influence of *Re* on the diameter of the particles in suspension is demonstrated, at *R* values of 1, 0.5, and 0.1, for a *Re* range of 50-500.

In the instance of $R = 1$, there is a marked decrease in particle diameter with increasing Re. This is also observed at $R = 0.5$, although less pronounced. In both instances, there was an observed plateau, at which point the particle diameter did not appear to further decrease. This was not the case for the same *Re* conditions at $R = 0.1$, the range of particle diameters were far less *Re* dependant than at higher *R* values.

One model which describes the results of flow conditions on particle diameter is the relative dominance of nucleation of particles against the particle growth following precipitation. Antisolvent precipitation occurs when a particle is nucleated upon expulsion from solution, followed by a growth phase whereby solvated material is deposited onto the surface of the nucleated particle, leading to diffusion-limited stepwise growth (Saad and Prud'homme 2016).

A nucleation-dominated system has a small amount of time between a nucleation event occurring, and the solubilised lignin being precipitated. As a result, the growth phase, at which point the solubilised lignin is deposited onto the surface of the seed particle is small. This inhibits particle growth, and as such particles have a reduced diameter.

Another factor which leads to this conclusion is the magnitude of the standard deviation, which is far smaller at *Re* values < 100, which is ± 5 nm at $R = 1$, $Re = 500$, compared to ± 63 nm at $R = 1$, $Re = 50$. In addition to the observed reduction in particle diameter, there was a reduction in the magnitude of the standard deviation, from ± 62 nm, corresponding to 10.7% of the average diameter, at $Re = 50$ ($R = 1$) to ± 5 nm, corresponding to 1.5% of the average diameter, at $Re = 500$ ($R = 1$). This observed decrease in variance offers further evidence of the nucleation and growth-based description of the formation of CLPs through antisolvent precipitation.

Variation in particle diameter is a feature of a growth-based deposition mechanism, this again provides evidence that initial growth-based particle precipitation was replaced by a nucleation-based precipitation mechanism at higher *Re* values.

Another feature of Figure 39 (A) is that the particle diameters plateau at 200 nm. The size is similar to that reported by (Li *et al.* 2021), in which a plateau was observed in diameter in a process where stirrer speed in a braker for a batch process was used as a variable, rather than using a CJM. It is understood that the flow within a CJM is similar to that of turbulent flow, owing to vortices within the device, with examples such as Lim et al. (2014) demonstrating turbulent flow characteristics at *Re* values of 200 among others reporting similar within a CJM device.

To interrogate these data further, the impact of *R* was examined. For the same material system, at the same *Re* value, *R* was reduced from 1 to 0.1. The impact of this is the reduction of solvent and solute in favour of more antisolvent. As a result, it was expected that nucleation-dominated precipitation would be observed at a lower value of *Re*. Figure 39 (B) provides evidence of this, by showing smaller particle diameters at lower values of *R* for all tested values of Re. Moreover, the effect is so pronounced that at $R = 0.1$, the

system becomes far less dependent on Re, with all particle dispersions having diameters of 150-170 nm.

This is again anticipated to be the effect of moving from a growth-based particle precipitation model at high R, low Re, to a nucleation-dominated model at low R, low Re.

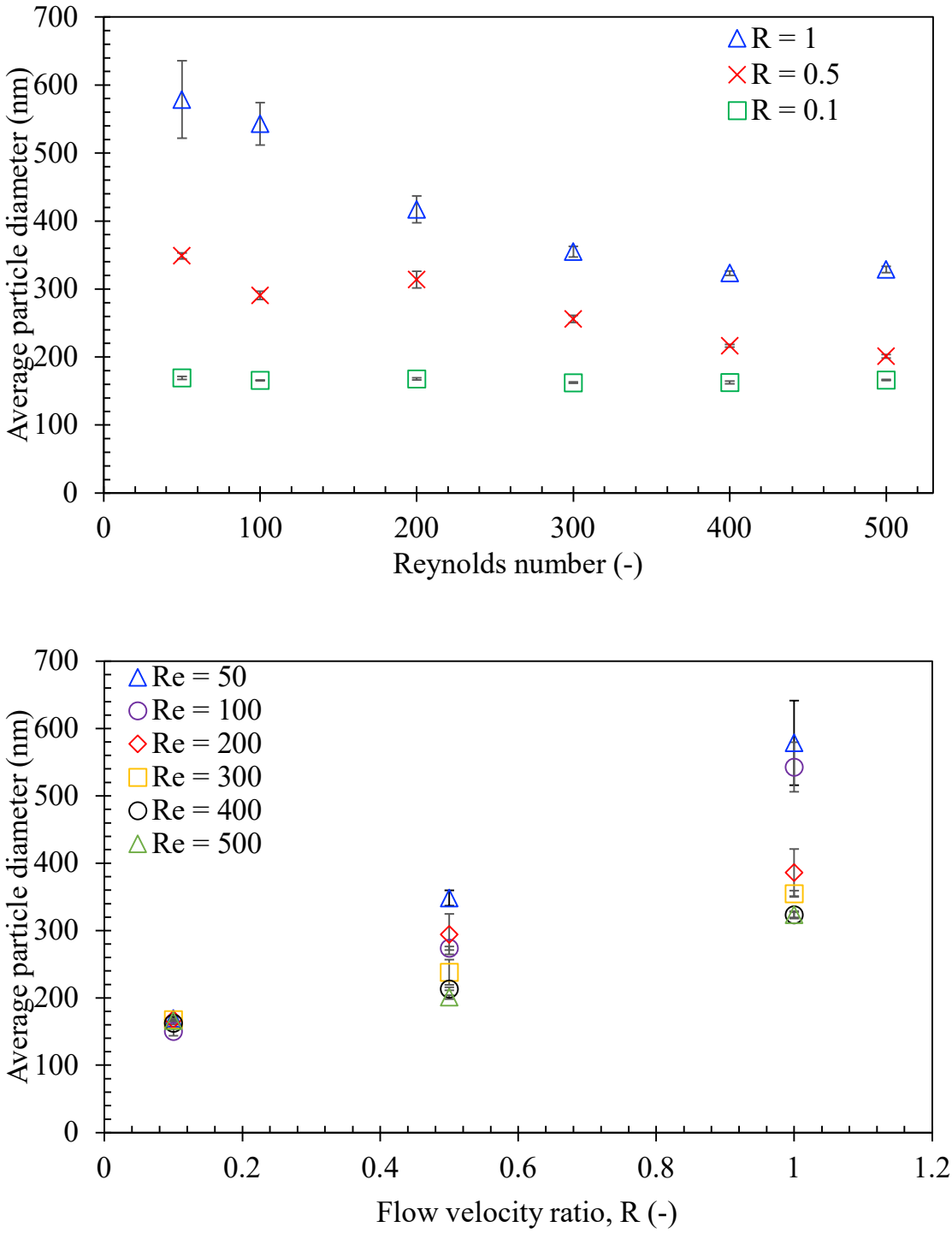


Figure 39: A) Impact of *Re* value on (Cumulants) average particle diameter of CLPs measured by DLS. Particles were formed by the CJM at a series of *R* values. Error bars denote ± 1 standard deviation. B) Impact of *R* (0.1, 0.5, 1) on (Cumulants) average particle diameter of colloidal particle dispersions as determined by DLS for an Re range between 50 and 500. Error bars indicate ± 1 standard deviation.

This suggests that within the tested range of *Re* 30 - 500, *R* = 0.1 – 1, an increasing *R* correlated with a reduction in the variation of particle diameters, as measured by the ability to produce a range of colloidal particle diameters.

Within the context of processing crude extracts, this offers an advantage, as CLPs are thus expected to be produced irrespective of minor compositional changes, which naturally would affect the viscosity or density of the solution.

Conversely, at a higher value of *R*, the *Re* has a much greater impact of colloidal particle diameter, varying from 200-600 nm. At this value of *R*, a variation of viscosity and density is likely to influence particle diameter.

5.2.3. **Span of colloidal particle distributions**

In addition to particle diameter, using the span value of a particle distribution allows for the impact of flow conditions on formed particles to be quoted by a single value. Figure 40 shows the span of a series of colloidal particle distributions formed at an increasing *Re* values.

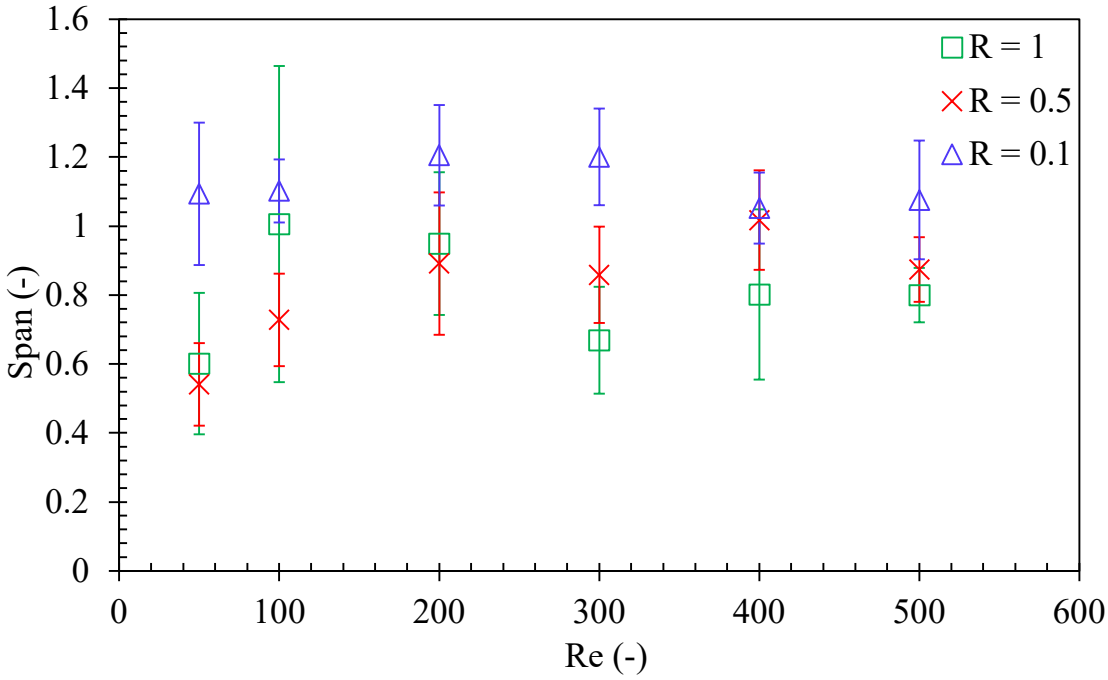
In Figure 40 (A), the data are displayed as a function of Re, with the *R* value datasets separated. A lower value of *R* appears to correspond to a greater value of span. A larger value of span would correspond to a wider distribution of particle sizes within a peak. This would corroborate the findings of the previous section, where the discussion of the nucleation and growth-dominated system was established.

In Figure 40 (B), the data are displayed as a function of *R*, with each *Re* shown as a class. It can be concluded that the range of span values at an *R* of 0.1 (0.9 -1.3) is far smaller than the equivalent at an *R* value of 1.

The span trends are consistent with the particle size trend identified with DLS, where a low value of *R* corresponded to a small variation in particle diameter. Conversely, at an *R* value of 1, the distribution of span is far greater, ranging from 0.4 - 1.6. This adds to the interpretation of the results in the context of a nucleation and growth-based model of particle precipitation.

At a high *R* value, there are two factors which would increase the broadness of a peak, and therefore span. The first is that there is proportionally greater solvent to antisolvent, which will act to delay the nucleation process, as supersaturation will take longer to achieve.

The second factor is that there is a greater amount of lignin present in the system relative to the amount of antisolvent present, thus allowing for a longer growth phase during particle precipitation.



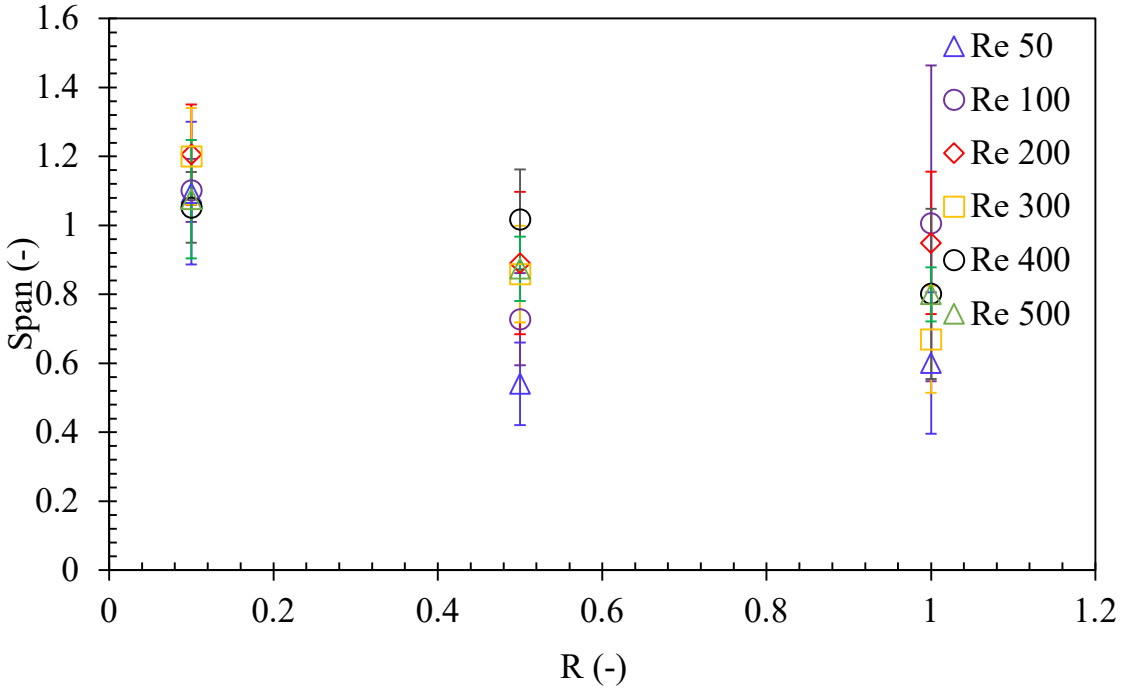


Figure 40: (A) Impact of *Re* on span average particle diameter of CLPs measured by DLS. Particles were formed by a CJM at a series of *R* values. Error bars denote ± 1 s.d. (B) Impact of *R* (0.1, 0.5, 1) on (span of particle dispersions as determined by DLS at a series of *Re* values between 50 and 500. Error bars indicate ± 1 standard deviation.

One pitfall of using DLS as a technique for analysis of particle distributions is the concern that at too high a concentration, the shoulders of a particle distribution are broadened, as multiple scattering effects are present. From the above section, it is possible to conclude that *R* has a greater effect on the value of span than Re.

5.2.4. **Multivariable analysis of particle dispersions**

Building on both the validation of the device, and the impact of *R* and *R*e independently as processing variables, the next section addresses the impact of multiple processing conditions on the diameter and span of CLP dispersions. Previous data demonstrated the influence of *Re* and *R* on particle diameter in isolation, and this section develops such findings by adjusting multiple variables. To assess the ability of the system to produce such a result, a model will be built using curve fitting from the primary dataset presented earlier, and assessed against new data collected across a range of *R* and *Re*.

A curve fitting model of a quadratic form was used, Equation 3.1, where A-F are constants, x is the Reynolds number, and y is the mean particle diameter.

$$f(x,y) = A + Bx + Cy + Dxy + Ex^2 + Fy^2 \quad (3.1)$$

The model itself will offer an interpretation based upon statistical analysis alone, rather than a constant related to the model of antisolvent precipitation, or nucleation and growth dominated particle production.

From the earlier section, a value of $R = 1$ was shown to generate the largest diameter particles, and $R = 0.1$ is the smallest. It is therefore anticipated that a high *R* and low *Re*

correspond to large particles, and a low *R* combined with a high *Re* will generate small particles. To assess this, the two factors were varied simultaneously, with a fixed volumetric flow rate of CLPs of 50 μL min^{-1}. The experimental values for simultaneously varied *R* and *Re* are compared against the findings earlier in the chapter, Figure 41.

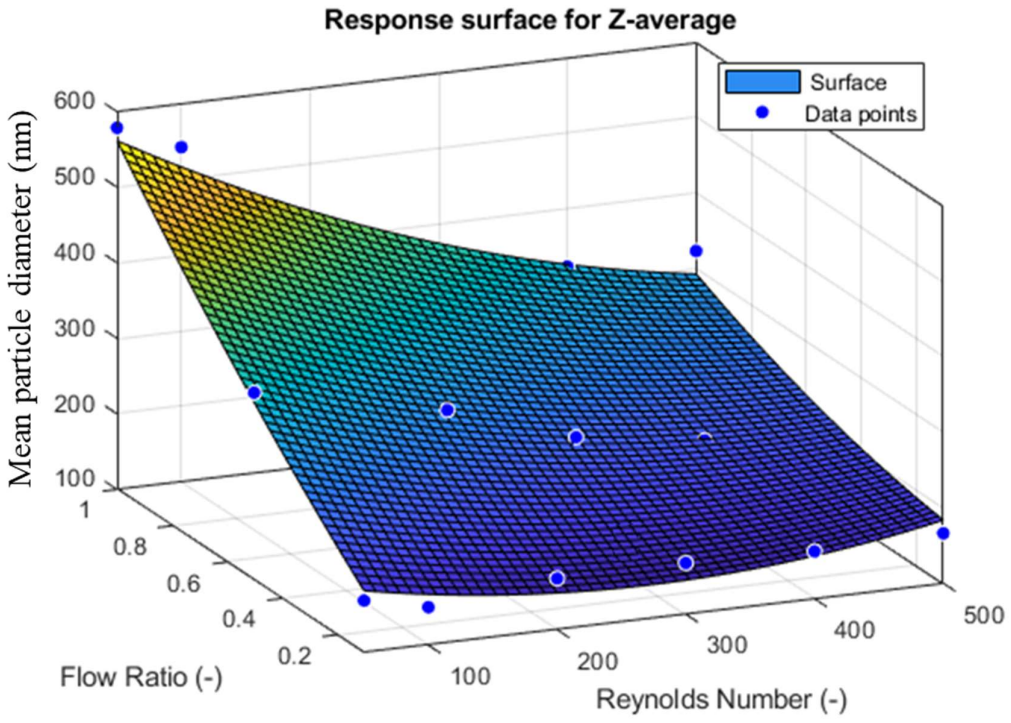


Figure 41: A surface plot showing the influence of two processing parameters *Re* and *R,* on average particle diameter in nm. The particle dispersion is formed in a CJM device via antisolvent precipitation of an extract of CBS in water.

Table 11: Coefficients of the surface plot model calculated from experimental data. The values of each coefficient detailed in Equation 3.1 are shown below.

Coefficient	Value (3 s.f.)	95 % confidence interval
A	163	(98.7, 228.2)
B	-0.347	(-0.765, 0.07192)
C	369.8	(184.6, 554.9)
D	-0.666	(-0.91,-0.42)
E	0.0007577	(4.5E-5,0.0014)
F	77.08	(-74.93,229.1)

Table 12: Statistical fit assessment of the model trained earlier in the section, including the Sum of Squares due to error (SSE), and Root Mean Squared Error (RMSE).

Metric	Value (3 s.f.)
SSE	9307
R-square	0.9664
Adjusted R-square	0.9524
RMSE	27.85

The choice of statistical model does not correlate with the kinetics of the CLP formation. The model does however have application as a predictive model, as data collected subsequently do lie within range of the surface plot. The Re based decay in average particle diameter is likely logarithmic, owing to the earlier analysis. The *R* ratio decay appears to be more linear, and therefore the model was decided as appropriate.

The particle diameters demonstrated are similarly in the colloidal range demonstrated by batch precipitation methods, with values ranging from 100-500 nm typical (Sipponen *et al.* 2017; Lintinen *et al.* 2018), however, the tunability offered by a continuous process is advantageous. The only other continuous process present in the literature is an aerosol process, with an average particle diameter of 500 nm (Bangalore Ashok *et al.* 2020).

Batch tunability has been demonstrated using dialysis, with diameter ranges of 250-950 nm, and tunability to 100 nm resolution (Lu *et al.* 2021). This method used tetrahydrofuran as the solvent, and water as the antisolvent. There are other examples of smaller particles in literature, with (Zou *et al.* 2021) and (Yaqoob *et al.* 2021) reporting colloidal particles with an average diameter below 100 nm. Whilst the jet mixer sub-100 nm diameter particles could not be produced, the range of nearly one order of magnitude with no batch-to-batch variation offers great promise for application.

One critique of this process over an aerosol process is that there is a large mass of solvent for recovery, and relatively large energy is required for processing such a large volume of solvent. When considering the environmental impacts of this, one method of reducing this issue would be to increase the volatility of the antisolvent. From this section, evidence has been presented that an increase in *Re* correlated to a smaller average particle diameter of CLPs. Above a *Re* value of 200, there appears to be a plateau, whereby the impact of an increase in *Re* is diminished. The reduction in particle diameter is marked, with the highest *Re* value producing particles with a diameter of only 46% of those produced at the lowest value of Re. One can examine that there is a multivariable result which is evidenced by the surface, suggesting that a further kinetic study would further increase the specificity of particles diameters above the ± 50 nm we can from this work.

5.3. Characterisation of particle dispersions

This final section of this chapter focuses on characterising the particle dispersions. Initially, lipid co-extractives of the system are assessed by way of colloidal dispersions formed from a lipid removed precursor. Secondly, the dispersions are assessed by stability testing and zeta potential are presented. Finally, the dispersions are assessed under phase change, including concentration and dilution, and transfer into non-aqueous phases.

5.3.1. Effect of lipids on particles

In section 3.2.3, a series of molecular surfactants (lipids) were identified as co-extractives from CBS alongside lignin. Previous studies have identified that the surfactants themselves are part of the stabilisation of the CLP system, by either decoration of solid structures (Xiao *et al.* 2018), or by their presence in solution. This section aims to identify the influence of lipids.

The lipid removal from the CBS system was conducted in hexane as per 2.2.2. As per section 5.1.2, the batch-to-batch variability of the system was assessed, Figure 42.

Despite the greater amount of processing required, the error bars of the two extracts are overlapping suggesting that they are indistinguishable. Additionally, the similarity was demonstrated by linear regression, see Appendix A, Figure 76 by an R^2 value of 0.94 and a gradient of 0.94. Whilst this is not as high as the lipid-containing samples, it is worth noting that there is an additional extraction step in hexane. As a result, any effect of the lipid on particle diameter during the formation step would likely contribute. Notwithstanding the lower correlation coefficient than the lipid-containing equivalent,

the value is still high enough to indicate a reasonable degree of reproducibility between the samples.

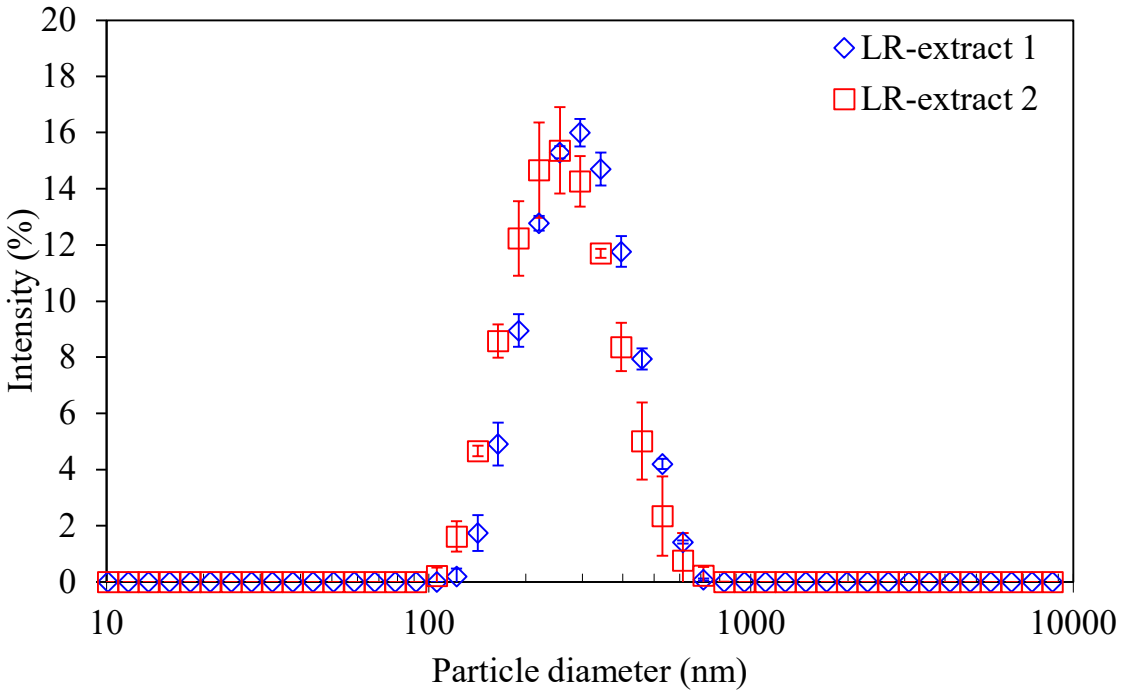


Figure 42: Particle diameter intensity distributions of particle dispersions formed in a CJM device. Dispersed lipid-removed lignin in ethanol (5 mg mL^{-1}) was fixed at 50 µL min^{-1}, with a continuous phase of water fixed at 1,100 µL min^{-1}, corresponding to a *Re* value of 329. Distributions were collected as triplicated repeats of two separate samples. Error bars denote ± 1 standard deviation.

To assess whether the removal of the lipid affected particle diameter, the mean particle diameter of the two batches of lipid-containing and lipid-removed lignin bioresidue was correlated, see Appendix A Figure 75. With a low R^2 value of 0.67 compared to the validation of each sample, one can assess the system as being different upon the removal of lipids. Despite the gradient of 1.07 offering evidence of similarity between the datasets, the R^2 value of 0.67 demonstrates a significantly worse correlation than comparisons between repeats of the same material, with the similarity of particles formed by extracts from CBS-LC and CBS-LR values of 0.99 and 0.94 respectively. In addition, a paired t-

test returned a value of 0.018. Given this value is less than 0.05, the hypothesis that they are the same is rejected, therefore suggesting the two systems are independent. The large magnitude of difference between the correlation of the two systems suggests that there is a significant difference between the two systems. This further suggests that the presence of the lipid is an important factor in determining the particle diameter distribution during antisolvent precipitation. In the absence of lipids, the presence of increased aggregation is indicative of lipids likely serving as a factor inhibiting aggregation. If there are changes in particle diameter, it suggests that surfactants may decorate the particles. On the other hand, if the diameter remains unchanged, it is likely that the particles are present in solution. Additionally, due to their larger size, particles without lipids experience a longer growth phase during antisolvent precipitation.

As with the lipid-containing equivalent, particles were produced at a *Re* range of 30-360, and the particle diameter distributions were measured by DLS, Figure 43. The key difference between the two material systems is that in the absence of the lipid, the average particle diameter is lower.

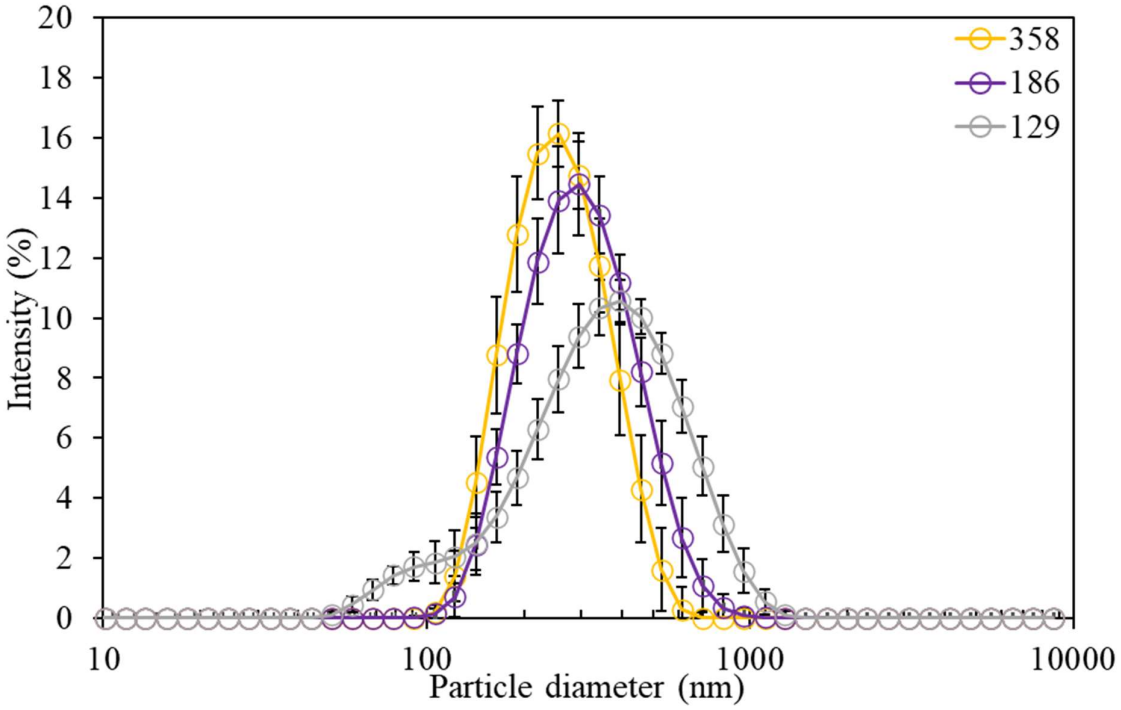


Figure 43: Particle diameter intensity distributions of particle dispersions formed in a CJM device. Dispersed lipid-removed lignin bioresidue in ethanol (5 mg mL^{-1}) was fixed at 50 µL min^{-1}, with a continuous phase of water varied, generating Reynolds values of 129, 186, and 358. Distributions were collected as triplicated repeats of two separate samples. Error bars denote ± 1 standard deviation.

Displaying the two together, it can be observed that an absence of lipid causes greater particle diameter and span, Figure 44.

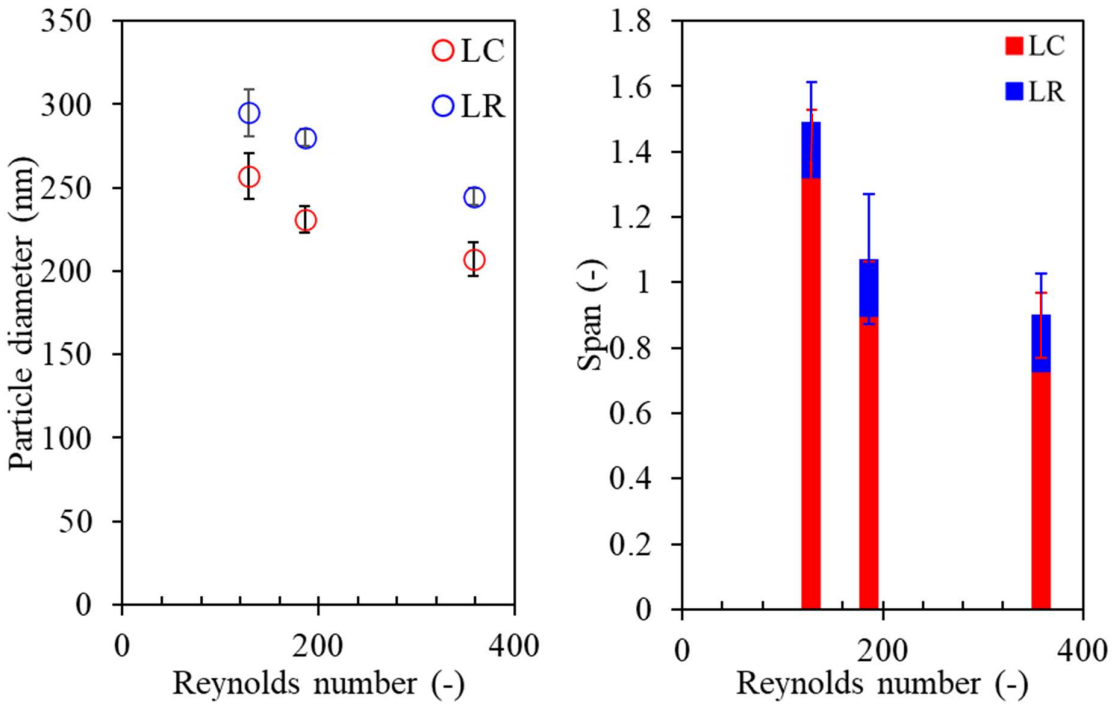


Figure 44: Representation of the effect of *Re* on the features of a particle diameter distribution measured by DLS using two features of the distribution; average particle diameter (left), and particle distribution span (right). The data demonstrate the difference between lipid-containing (red) and lipid removed (blue) lignin solutions. Error bars denote ± 1 standard deviation.

5.3.2. **Stability of particle dispersions**

To assess the stability of the precipitated particles in dispersion, the electrophoretic potential was measured across the pH range of 2-10, Figure 43. The lipid was hypothesised to affect the stability of the system by acting as a surfactant to stabilise the system. In this regard, good stability is defined as an absolute value of zeta potential greater than or equal to forty ($-40 \geq x \leq 40$) (Kumar and Dixit 2017; Stanisz *et al.* 2021) was found to exist at the extremes of the tested range; below pH = 2.5, and above pH = 6.3. The lipid was found to not cause the anticipated effect on particle stability, with stability ranges being consistent for both datasets.

The values in Figure 45 agree with those reported previously, notably those of (Cuthill *et al.* 2021), who reported values of -45 mV, and those of (Lievonen *et al.* 2016) and (Bangalore Ashok *et al.* 2020), who reported values of – 40 mV, which is achieved here in both systems at pH >6. In addition, (Sipponen *et al.* 2017) reported a similar trend of positive zeta potential tending to low zeta potential across the pH range tested. Their work saw a difference in values, whereby the reported stable pH range was 2-6, instead of below 2.5 and above 6.3. One potential explanation for this is the choice of feedstock for the CLPs. Sipponen *et al.* (2017) used Kraft lignin, which is also often referred to as alkali lignin, due to the functionalisation associated with the bleaching during the Kraft process. Equally, for other Kraft lignin-based systems differing pH dependence for similarly sized CLP systems was reported, with (Stanisz *et al.* 2021) reporting an isoelectric point of 2.0, hypothesised to be related to the precipitation conditions. Overall, this offers evidence that processing may have a greater impact on the stability of the CLP system. This is further corroboration that a continuous process, which allows for consistent and reproducible CLP dispersions is advantageous over batch equivalents.

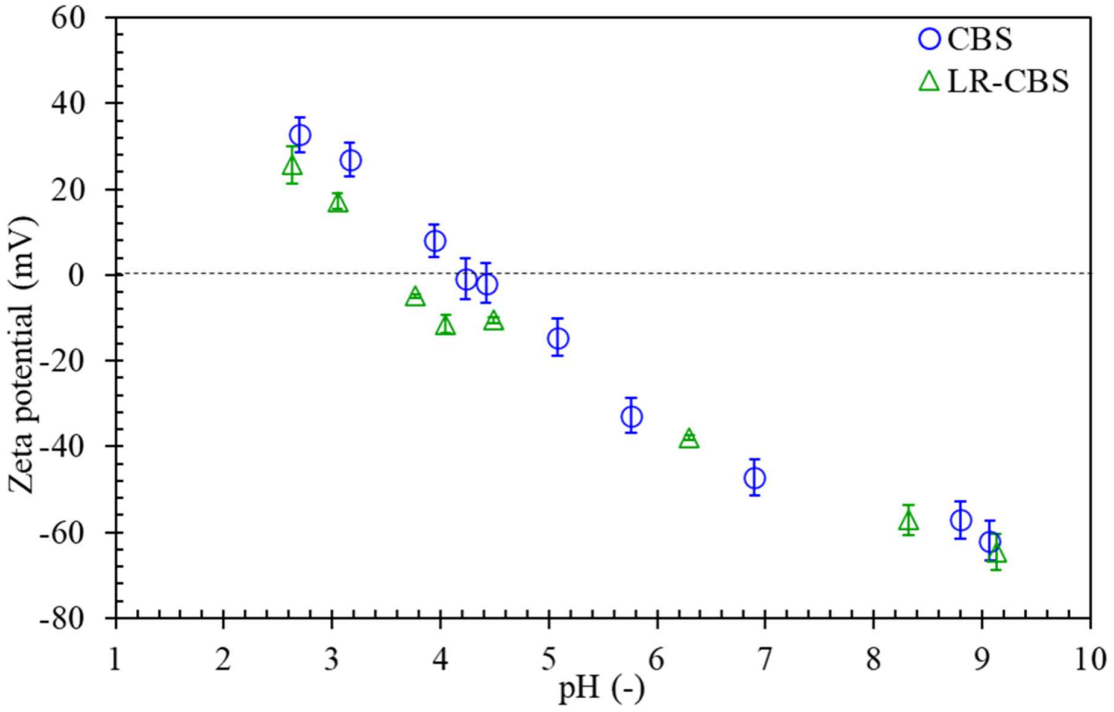


Figure 45: Zeta potential of CLPs in a suspension formed at a *Re* value of 100 in a CJM with a hydrodynamic radius of 235 nm. The pH range was adjusted using sodium hydroxide and hydrochloric acid. Error bars denote ± 1 standard deviation.

In addition to electrostatic stability, storage tests were conducted to assess the aggregation of the particles in the system, Figure 46. This was assessed at the precipitation pH of 4.3, which is in a position of low zeta potential, and therefore low expected stability against aggregation. For the first 7 days, the particles appeared to be stable to aggregation irrespective of the presence of lipids. After 14 days, there is a marked difference in stability, with lipid-containing particles appearing to have greater stability, defined as not having visible aggregation. After 30 days, both systems appear to aggregate, with large structures appearing.

A secondary hypothesis as to the stability of the particles was that charge was present on the hydroxyl groups of the lignin, providing partial solubility in water, and thus inhibiting aggregation.

The steric stability indicated by the microscopy adds further weight to the nucleation-dominated hypothesis for particle precipitation using CJM at *Re* values above 100. If particles, once formed are stable in the antisolvent solution, aggregation is unlikely to occur. This then will prohibit an aggregation step required for particle diameter to increase. If both aggregation and growth mechanisms are prohibited, then once precipitated, particle diameter is liable to be fixed.

This was chosen as a suitable technique despite the 1 μm sizing being near the resolution limit, as 6 μm particles would be facile to visualise.

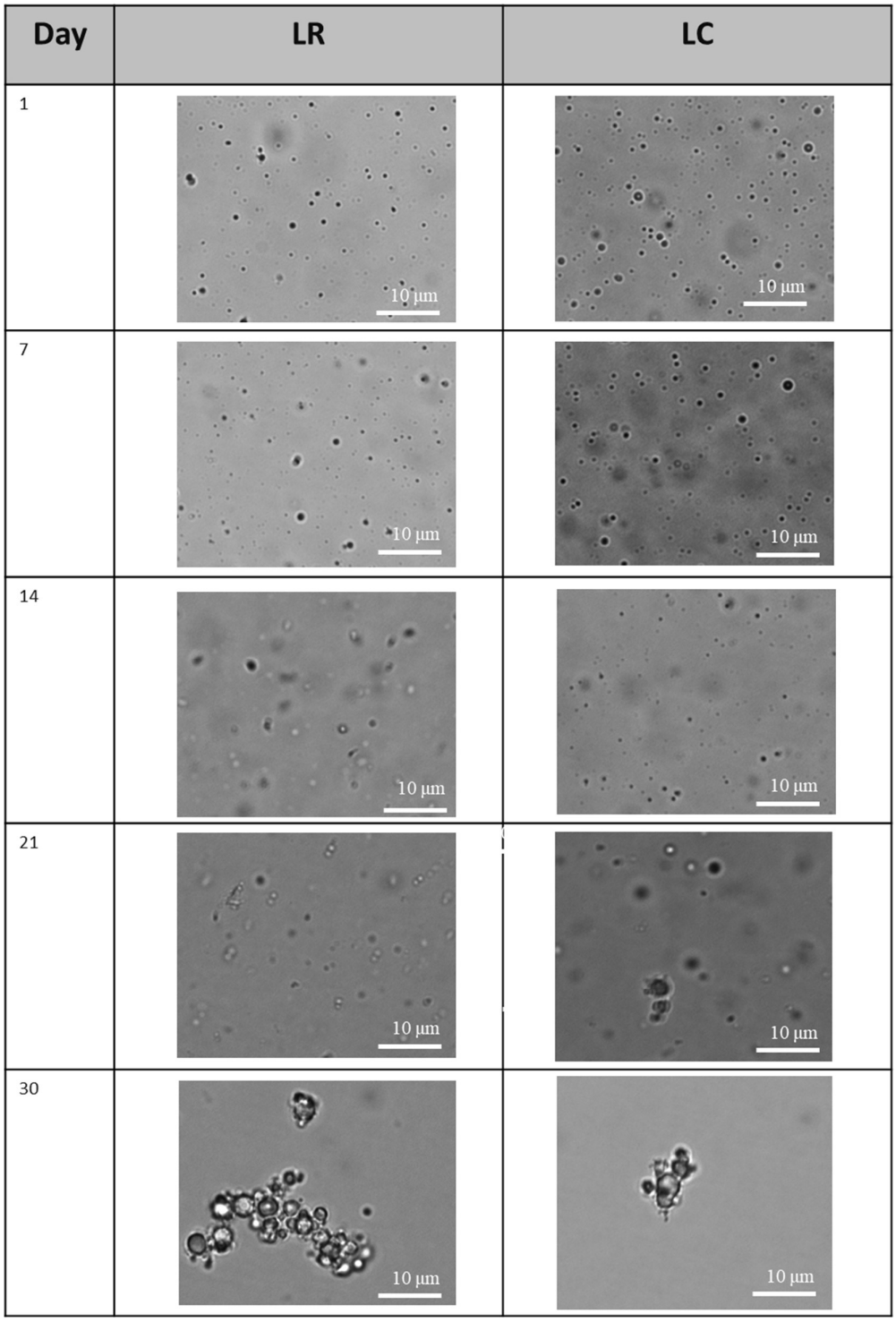


Figure 46: Microscopy images of colloidal particle suspensions (initial average diameter of 600 nm) precipitated from ethanol-dissolved cocoa bean shell extract (5 mg mL^{-1}) in distilled water at *Re* of 29, *R* = 0.5) and stored at 20 °C for 30 days with periodic microscopy of 10 µL aliquots at pH 4.3.

5.4. Conclusions

This research chapter offers the first evidence for the continuous production of CLPs using liquid-liquid mixing and antisolvent precipitation. The establishment of a continuous process is advantageous over existing batch processes for a myriad of reasons, including throughput, tuneability, and reproducibility of colloidal particle production. The key factor affecting tuneability is the interplay between nucleation and growth-dominated precipitation, which was systematically varied using *R* and Re.

As discussed in the initial experimental setup, the concentration of the solute system could be varied, and the effects could be studied. One potential benefit of this would be to extend the range of colloidal particle diameters available in the system.

At slow mixing associated with a low *Re* value, data suggested that there were particles of both small (40 nm) and large (6,000 nm) diameters. The small diameter particles were not found to exist at greater *Re* values. To achieve direct visualisation, one could use scanning electron microscopy.

The larger diameter particles were hypothesised to be aggregates however a lack of corroboration with microscopy alongside considerations of the instrument suggests that they are either not present, or present in immeasurably small concentrations. The particles were however assessed to be prone to aggregation if left in suspension for 30 days, however, altering the pH to one with a greater electrophoretic potential will counteract this by electrostatic repulsion.

The impacts of concentration and mixing time scale were not investigated in this research chapter, instead focusing on the impacts of Re and R. An increased concentration may have led to larger amount of particles, owing to the greater amount of solute present undergoing precipitation at the same time scale. An alternative outcome may be that the

particles become smaller, which would be the case as the concentration of solute reaches the solubility limit of lignin, upon mixing with an antisolvent, the particles would 'crash' out, resulting in smaller size.

One drawback of the current process is that lignin extraction is presently batch processed on the gram scale, however, new extraction recovery techniques are being established, such as deep eutectic solvent extraction, which has the potential for large yields.

One potential application of particles may be a suitable tracer for oil-based systems, should their dispersibility in oil be demonstrated. This would be unique, as oil-dispersible tracer particles have not been demonstrated to date. Another conclusion which may be drawn from the oil dispersibility of the CLPs is that the system is likely to undergo surface rearrangement depending on the solvent present. This opens the possibility of tuning the surface by choice of antisolvent, and therefore generating a formulation space of CLPs with a tuneable wettability. Antisolvent precipitation offers a powerful technique for achieving this, as the variation of solvents is facile, providing the solubility conditions are appropriate for lignin, and miscibility between solvent and antisolvent.

Another conclusion from this chapter is that the presence of lipids as a co-extractive of the system affect the particle size, however, do not appear to greatly affect stability. Further investigation on the effects of the lipid on the system could yield information on the compatibility with other systems than ethanol and water, and thus broaden the formulation space for lignin-based CLPs.

The expectation before this research was that the lipid fraction would have an impact on the characteristics of the particles, particularly stability. This was corroborated by the difference in particle diameter between the lipid-containing and lipid-removed systems.

6. Assessing the wetting properties of CBS lignin extracted, and the influence of the lipid fraction on their ability to stabilise emulsions

It is understood from Chapter 3 that the CBS-LC extract is a multi-component system, consisting of lignin and a series of co-extractives referred to as 'lipids'. To characterise the effects of these lipids on the surface properties of the particles, two approaches were pursued in this chapter. Firstly, is to observe the ability of CBS-LC particles to work as Pickering stabilisers. Observations in Chapter 5 were that the particles were stable against aggregation in solution, suggesting that there may be a stabilisation occurring. Measurement of contact angle was performed on layers of lignin-rich extract precipitated in solvent conditions analogous to those of the particles formed in Chapter 5. Contact angle measurement allowed for quantification of the influence of the lipid fraction identified in Chapter 3 on the surface properties of lignin, offering an indirect assessment of the local environment surrounding dispersed CLPs. This could be due to the lipid fraction coating the surface of the CLPs, and thus it is hypothesised that when in dispersion, lipid is acting in solution to stabilise the CLPs.

6.1. Application of CLPs as a Pickering particle for emulsion stabilisation

6.1.1. Validation of emulsion stabilising performance of CLPs

Given that the formed CLPs formed using the CJM mixer have demonstrated stability in both aqueous and non-aqueous dispersion using analysis of size, zeta potential for the aqueous dispersion and microscopy in Chapter 5, one application which they may be suited to is as Pickering stabilisers, of which there are numerous examples in literature as identified in 1.5.2. For initial comparison of the action of CLPs as a Pickering stabiliser, their ability to stabilise a 9:1 w/o emulsion at 0.5 wt% was assessed (section 2.5.2), in line with a literature example, Figure 47. Upon formation, an emulsion was formed, with a peak droplet population of 7.5 μm, in keeping with the expected results from the literature. There were two other populations however, a shoulder at 0.8 μm, which is anticipated to be the result of the CLPs free in solution, and another peak at 70 μm. This peak appears to demonstrate the presence of larger emulsion droplets, which differs from literature. After 24 h, large droplets of peak diameter 800 μm had formed and the population at 10 μm had significantly reduced, suggesting that Ostwald ripening, a process where larger particles grow at the expense of smaller ones in a solution, due to differences in solubility and chemical potential, leading to a more stable, lower energy state over time (Taylor 1998) was occurring in the emulsion, with the emulsion collapsing completely after 5 days. It was found that the emulsifying ability of the CBS-LC particles was poor, compared to other similar examples such as those detailed by (Czaikoski *et al.* 2020), who prepared emulsions which were stable for at least 28 days.

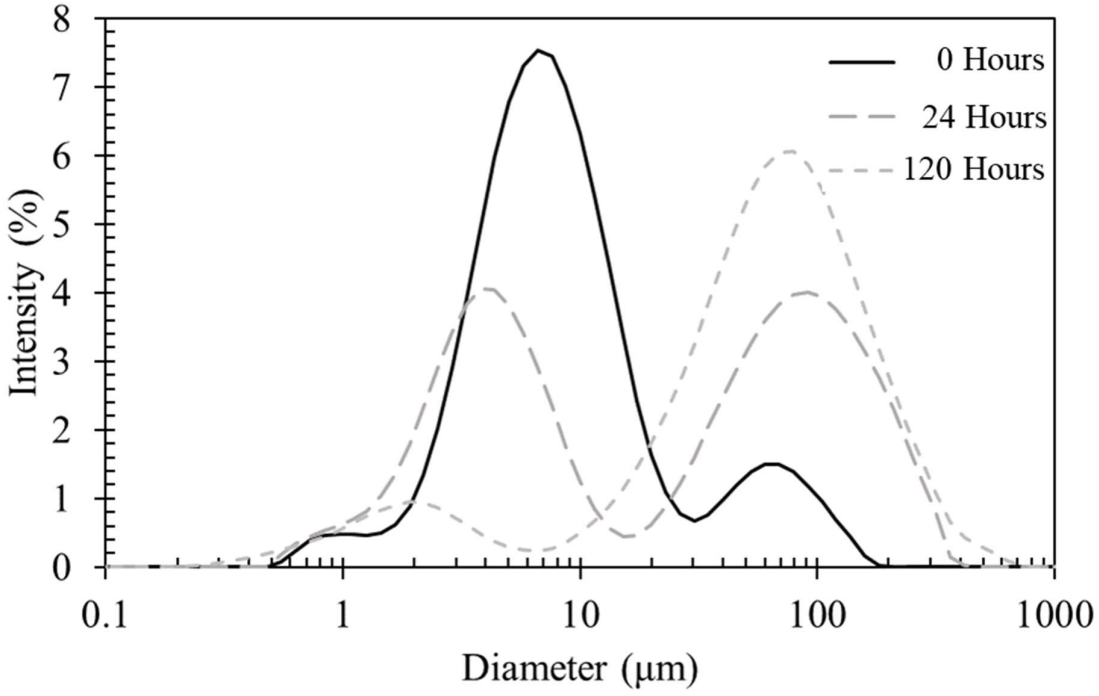


Figure 47: Droplet diameter of oil in water emulsion (1:9 w/w) with CBS-LC CLPs (220 nm, 0.5 wt%) formed via high shear mixing at 9,000 rpm for 2 minutes. Oil phase is sunflower oil, and aqueous phase is distilled water. Samples were stored at 4 °C, and diameter of droplets were measured at 0 h (black) ,24 h (grey, long dash) and 5 days (grey, short dash).

Following comparisons between the emulsions, it was concluded that the colloidal particles prepared from the CBS extract in this project did not work effectively as an emulsifier under the same conditions as those identified in by Cuthill *et al.* (2021). One possible explanation is the presence of co-extracted lipids, or the lack of an additional surfactant used in the extraction process, dimethyl sulfoxide (DMSO).

Another potential reason is that the surfactants identified in 3.2.3, particularly those with longer hydrocarbon tails such as isopropyl myristate may be competing with the CLPs for position at the oil/water interface. In this case, the emulsion would not be fully Pickering stabilised despite the concentration of particles (0.5 wt%) at 220 nm being sufficient to cover each emulsion particle fully considering an emulsion diameter of 10

μm. To address this, the influence of doubling the particle concentration to 1wt% under otherwise unchanged processing conditions in a 1:9 o/w emulsion was assessed, Figure 48. Upon immediate testing, the shoulder associated with the larger droplets at 70 μm observed at 0.5 wt% was not observed in the 1wt% system, suggesting that the oil may have been encapsulated more efficiently than at the lower concentration. However, after 24 h, the same loss of encapsulation is observed, indicating that the concentration of the CLPs is not the factor inhibiting Pickering stabilisation.

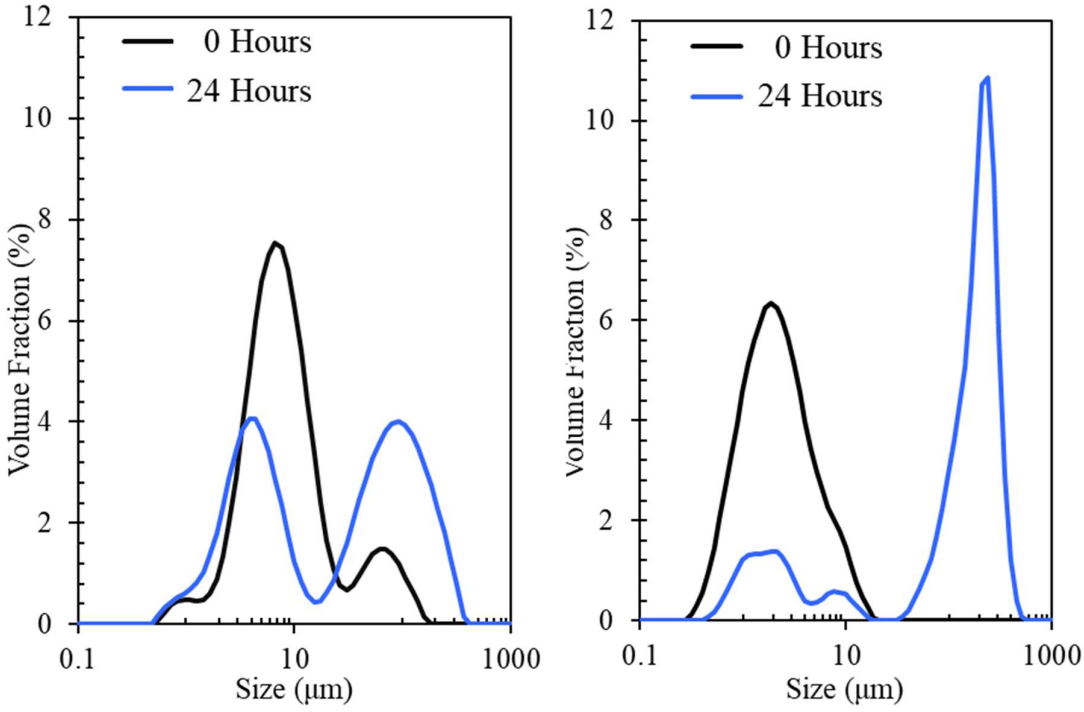


Figure 48: Droplet diameter distribution of dispersions of an oil in water emulsion (1:9 w/w) with CBS-LC CLPs (220 nm) dispersed at 0.5 wt% (left) and 1 wt% (right).Emulsions were formed via high shear mixing at 14,000 rpm for 5 minutes. Oil phase is sunflower oil, and aqueous phase is distilled water. Samples were stored at 4 °C, and diameter was measured at 0 h (black) and 24 h (blue).

Given that it was not possible to replicate the encapsulation observed previously, it can be concluded that CBS-LC CLPs are not migrating to the interface in the same way as similar CLPs. The likely explanation is the interaction between the CLPs and the lipid.

6.1.2. Impact of emulsion processing conditions on emulsion stability

Initially, the establishment of emulsions using high-shear mixing was sought, per previous research on similar lignin bioresidues (Czaikoski *et al*. 2020; Cuthill *et al.* 2021). In this chapter so far, the data have suggested that there is an interaction between the lipid and the CLPs which inhibit the migration of the CLPs to the oil water interface of an emulsion, where literature reviewed in section 1.5.2 has suggested they are capable of acting as a Pickering stabiliser.

As molecular surfactant is more liable to dominate the surface tension effects than a particle Pichot *et al.* (2012), one hypothesis resulting from the data in the previous section 6.1.1 is that the lipid fraction is reaching the interface before the CLPs, inhibiting the Pickering stability to be established. This would not be solved by increasing the concentration, as the migration timescale would remain slower than the surfactant timescale. One way to assess whether this may be the case is to disrupt the migration of the lipids to the interface, which can be achieved by increasing the energy supplied to the system. The suggestion in this instance is that the increased turbulence caused by processing an emulsion at a higher energy allows a greater chance that the particle can reach an interface, and therefore stabilise it. Two methods of emulsification with energy supplied to the system were selected, alongside the control conditions of 9,000 rpm and 2 minutes processing time; 14,000 rpm for 5 minutes, and sonication, at a power of 750

W for 3 x 5 s bursts. Figure 49 shows the same 1-in-10 o/w emulsion formed using three methods of shear selected from literature where Kraft lignin was used to form emulsions.

One initial observation from this system is that the emulsions formed are all the same diameter, in the region of 10 μm. Given that the droplets are dispersed using methods which impart vastly different amount of energy on the sample, this suggests that the diameter formed of the emulsion is characteristic of the presence of the particles. This suggests that initial stabilisation of the emulsion by Pickering functionality is occurring.

Within 24 h, the emulsion formed at the lowest energy has started to separate, and the emulsion droplets are tending towards a larger value, however the two higher energy formation conditions retain their average droplet size, indicating that the emulsions are intact. Over longer-term storage however, the only emulsion that can retain the droplet diameter is the sonicated emulsion, which despite a shoulder at 10 days, has retained 10 μm as the principal droplet diameter.

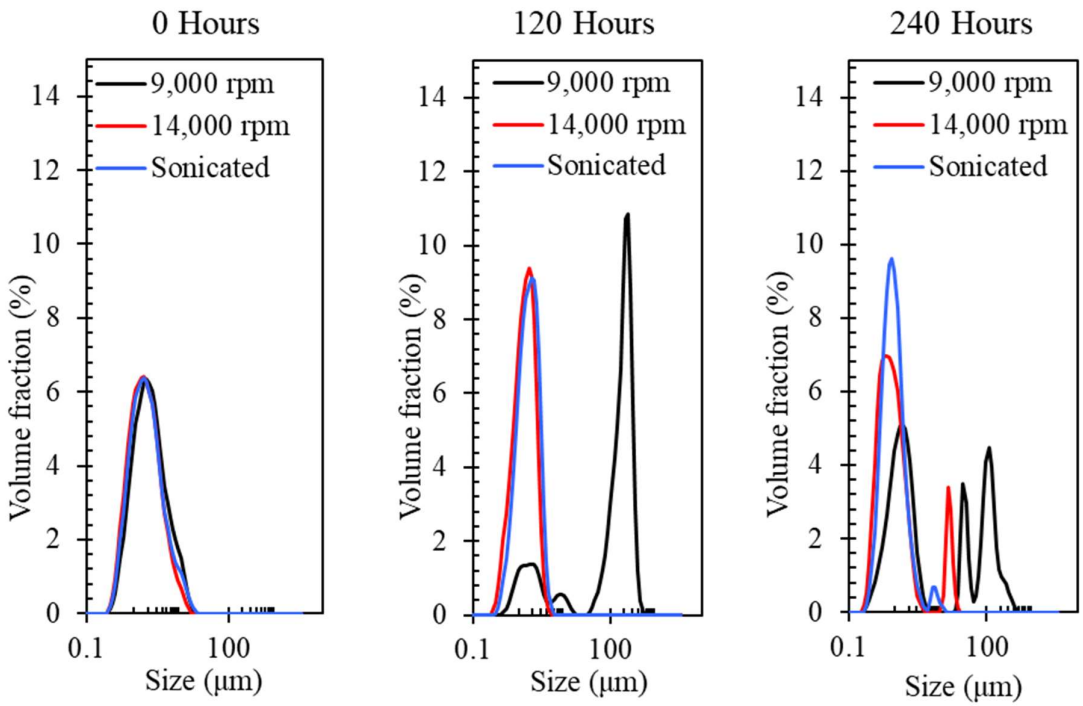


Figure 49: Droplet diameter distribution of dispersions of an oil in water emulsion (1:9 w/w) with CBS-LC CLPs (220 nm) dispersed at 0.5 wt%. Emulsions were formed via high shear mixing at 9,000 rpm for two minutes (black), 14,000 rpm for 5 minutes (red), and via sonication at 750 W for 25 seconds, consisting of 5 x 5 s pulses, with a 5 second rest period. Oil phase is sunflower oil, and aqueous phase is distilled water. Samples were stored at 4 °C, and diameter was measured at 0 h (left), 5 days (centre), and 10 days (right).

One possible additional explanation for the marked stability of emulsion diameter at 10 µm in the sonicated sample is the formation of lignin cages activated by sonochemistry of the aromatic ring (Tortora *et al.* 2014). Rather than the stabilisation by the presence of particles at an interface indicated by the literature review, a cage of covalently linked lignin biopolymer would be formed from activated aromatic rings forming a shell around the droplet. This could be investigated and confirmed using direct imaging analysis techniques such as scanning electron microscopy.

This section offers evidence that the ability to form emulsions using CLPs may be dependent on the presence of the lipid co-extractives. In addition, there is evidence that the presence of the CLPs drives the formation of emulsions at 10 μm. As emulsion formation did not yield a conclusive result of Pickering stabilisation, and increasing in energy may be causing stabilisation by a secondary effect in sonochemistry, alternative methods were pursued throughout this chapter to directly resolve the impact of the lipids and CLPs independently.

6.2. Interfacial properties of lignin-containing system

To assess whether the lipid fraction is interacting with the particle phase or the interface, tensiometry is reported in this section. It is anticipated that particles in an aqueous CLP dispersion will migrate to an interface with oil or air, owing to their chemistry indicating amphiphilicity, reducing the surface tension. Figure 50 shows that there is a marked difference in the surface tension of a 1:1 (v/v) aqueous mixture of ethanol against air in the presence of CLPs (green), compared to without (red) reducing the surface tension by 3 mN m^{-1}. The constant surface tension value suggests that the surfactant or particles in the system either reaches the interface on a timescale too small to register with this method, or it does not go to the interface. If micelles were present in the system, resulting from them not being present at the surface of the particles or interface, then there would be an observable drop in interfacial tension. The literature value for this ethanol:water mixture is 28.51 mN m^{-1} (Vázquez *et al.* 1995). This suggests that the lipids offer small reduction of interfacial tension to 26.25 mN m^{-1} for the system, and the CLPs offer a further reduction to 25.5 mN m^{-1}.

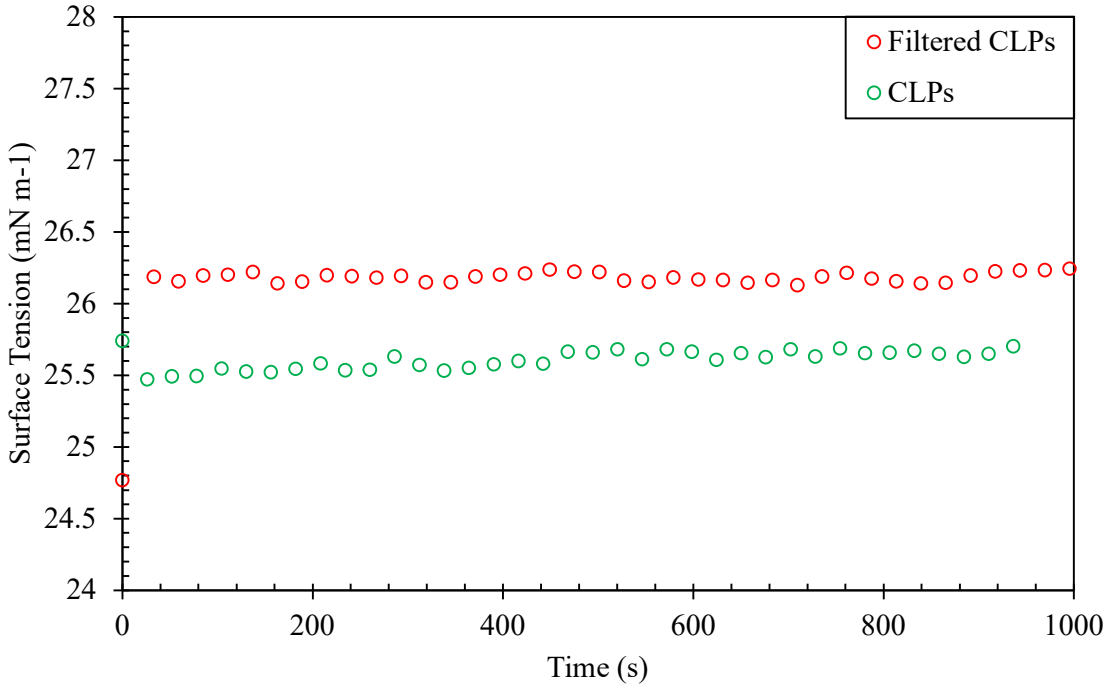


Figure 50: Surface tension of an aqueous ethanol and water (50:50 v/v) droplet containing a 3.5 mg mL^{-1} CBS-LC CLP dispersion in the presence of CLPs (green) and with them removed by filtration (red).

Potentially these particles are naturally hydrophilic, which would explain their ability to remain dispersed in an aqueous phase despite no lipid fraction to aid this. But the presence of the lipids means that they can be amphiphilic. But this doesn't mean they can stabilise an interface, as it is the surfactant only that is offering the amphiphilicity.

6.3. Influence of lipids on the wetting properties of precipitated lignin

Given the long-chained nature of the hydrocarbons such as the C-17 chain identified in 3.2.3, it is likely that any lipids coating the surface of the particles would be hydrophobic.

The findings of the wetting research are then used to inform suitable conditions and precipitation conditions for colloidal particles suitable for emulsions stabilisation by use of Pickering functionality.

As a first comparison between the ability of lipid containing and lipid removed particles to stabilise emulsions was conducted. Particles were precipitated using the CJM at an Re of 350 and R of 0.1 (lipid containing) and 355 and R of 0.1 (lipid removed), producing particle dispersions with a mean diameter of 220 ± 26 nm (lipid containing), and 255 ± 21 (lipid removed) respectively. Figure 50 shows the droplet size of emulsions immediately after emulsions formation (black) and after 5 days of storage at 4 °C (blue). Immediately after formation, it can be observed that in addition to the principal population size of the emulsion of 10 μm, there is a population of o/w emulsions which has a peak at 69 μm for the emulsions formed using lipid removed particles (triangles). This is likely due to some coalescence occurring on a short timescale, and is consistent with the peaks observed after 5 days when the emulsions had began to visibly break down. The data suggests that the emulsion breakdown was occurring immediately in the case of the LR emulsion, but not in the LC emulsions, which does not have an associated peak in the same size range. After 5 days, the LC and LR emulsions both show a significant drop in the population of droplets with a diameter of 10 μm, and growth of the population at 70 μm. This suggests that in both the LC and LR cases, the emulsions have began to coalesce. In the LR version, the peak at 70 μm has a broader tail, suggesting that there is a greater

fraction of droplets with a larger average diameter than the LC population. This suggests that the LR particles are less able to stabilise an o/w emulsion than LC particles, however in both cases, this increase in population size occurs on a significantly shorter time scale than would be expected had the Pickering stabilisation mechanism been successful.

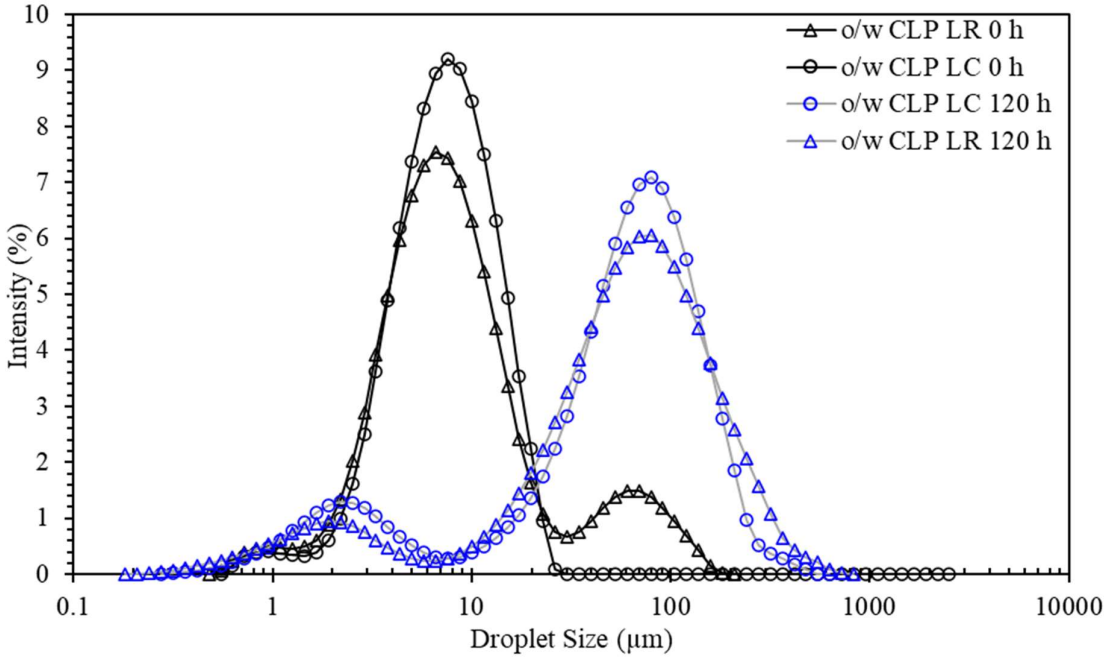


Figure 50: Static light scattering plots of two o/w emulsions formed using high shear processing conditions as outlined in section 2.5.2 with a mixing speed of 14,000 rpm, and processing time of 5 minutes. Particles of 230 nm in diameter prepared from CBS extracted lignin both lipid containing (LC, circles) and lipid removed (LR, triangles) using a CJM device were used to aid stability of the emulsions. Average diameter of emulsion droplets was measured at time of formation (black) and after 120 h (blue).

To confirm the model for position of lipids in the system, a secondary method for measurement of the wetting properties was pursued. If, as hypothesised, the lipid fraction coats the surface of dispersed CLPs, then this would also occur on a flat layer of CBS-LC, providing that a layer of water (the antisolvent in Chapter 5) facilitates arrangement of the lipids. This would not be possible in their absence with the CBS-LR system. Performing this on a layer of lignin allows for direct measurement of contact angle, and observation of the difference between the two phases. To validate this system, the contact

angle in sunflower oil was measured and compared to literature values for such systems, Table 13. The contact angle is measured through contact angle between the droplet and the substrate.

Table 13: Contact angle of droplets against a CBS-extracted lignin substrate deposited onto a borosilicate glass slide.

Substrate	External phase	Droplet	Contact angle (°)
CBS-LC	Sunflower oil	Water	113 ± 4
	Water	Sunflower Oil	57 ± 2

These values are indicative of a significantly more hydrophobic surface than the angles of 33 ° reported by Colucci *et al.* (2023) for Kraft lignin. Modification of Kraft lignin has been shown to increase contact angle, with acylation reporting a value of 77.2 ° Gordobil *et al.* (2015). The mild extraction conditions are likely to have further increased hydrophobicity compared to the highly functionalised lignin, by retaining the biopolymer structure rather than functionalising with hydrophilic character such as hydroxyl groups. Other lignin extractions report large water contact angles, with Cuthill *et al.* (2021) and reporting angles of 98 ± 5 °. This offers strong evidence that the particles are hydrophobic, as precipitation in water per Chapter 5 represents the most likely method to produce hydrophilic particles. As sunflower oil (0.93 g cm^{-3}) is less dense than water (0.997 g cm^{-3}), measuring the three-phase contact angle with sunflower oil in an aqueous system requires an emerging bubble system.

Figure 51 shows the contact angle of a droplet of sunflower oil in contact with a layer of lignin in a water continuous phase, precipitated in two constating conditions, air and water. The hypothesis that lipids in the system undergo rearrangement to stabilise an interface is examined. It was found that the contact angle was indeed modified by the

contrasting conditions. Air provides a hydrophobic surface and as such a more hydrophobic contact angle is anticipated compared to water precipitation. This is observed in Figure 51, with the oil droplet wetting the surface to an angle of 57 ± 2°. Conversely, the lignin layer precipitated against water, which was hypothesised to encourage lipid rearrangement to expose the polar head group had a much greater contact angle of 120 ± 1°, corresponding to the hydrophobic oil droplet not wetting the surface. Given that it is possible to modify the contact angle using the precipitation conditions, it can be concluded that there must be some rearrangement occurring at the surface of lignin to facilitate the contact angle change. These data suggests that the particles are initially in their most hydrophobic state, however, are able to rearrange at the surface to present hydrophobic structures. But when presented with the option of having non-polar 'tails' in

water or on surface of lignin, they may align such that these non-polar components are aligned with the particle surface, leaving the more polar groups on the surface.

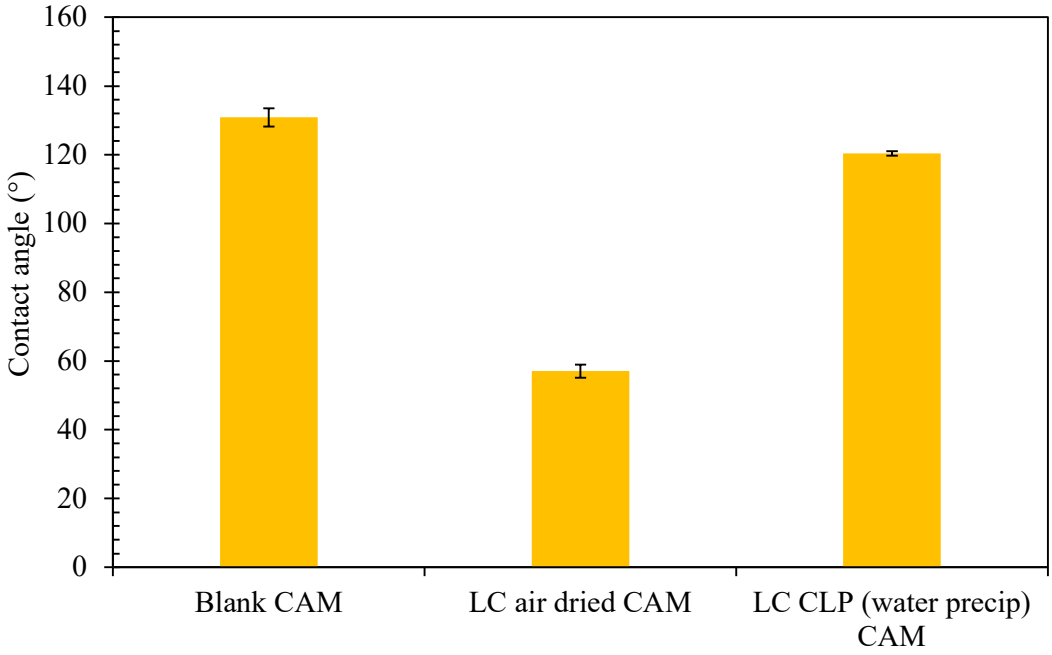


Figure 51: Contact angle measurements of a droplet of sunflower oil on a series CBS-LC extract surfaces, with precipitation conditions altered to replicate precipitation of lignin using antisolvent precipitation.

6.4. Role of the lipid in stabilising CLPs

Figure 52 represents a proposed setup of a CLP dispersed in an aqueous phase and stabilised by the presence of a lipid co-extractive. As evidenced by the interfacial data, there appears to be a limited amount of free surfactant in the solution. This would suggest that there is a coating of lipids on the particles.

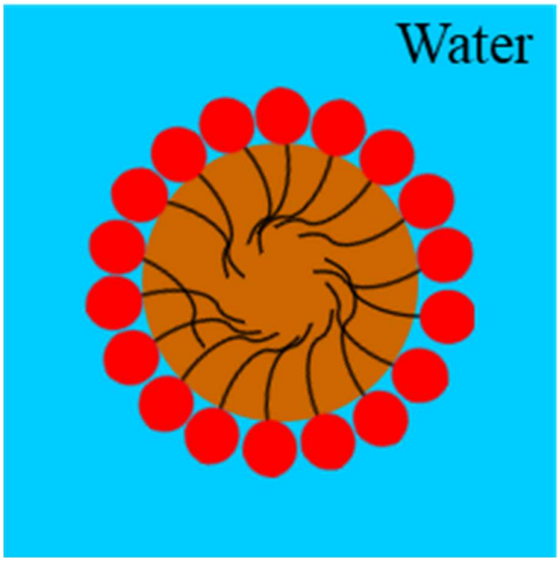


Figure 52: A pictorial representation of the hypothesised position of lipids, represented by a polar head group (red) and a hydrophilic tail group (black) relative to a precipitated colloidal linin-rich particle (brown) in aqueous dispersion.

For the CBS-LR setup, the lipids are no longer present in solution, however stability is still observed as demonstrated by the microscopy in Chapter 5.

Given the presence of surfactants, it was hypothesised that the system could be transferred from an aqueous suspension to an oil-based one. Figure 53 shows the particle diameter distribution of a colloidal suspension inside a sunflower oil dispersion. The diameter of the particles at a similar diameter of 220 nm to that of the aqueous system (190 nm) under similar conditions. This represents a significant result; in that it demonstrates the amphiphilicity of the colloidal particles in the system. The diameter of particles in the distribution has overlapping error bars, showing that the datasets are indistinguishable.

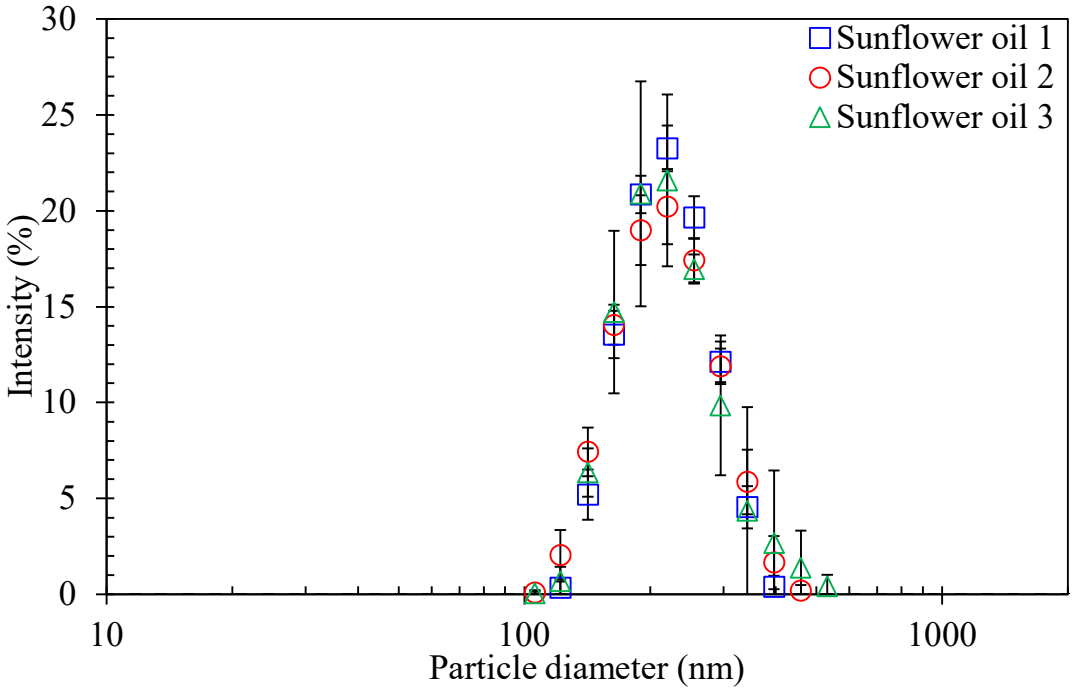


Figure 53: Particle intensity distributions of colloidal particle dispersions formed in a coaxial jet mixer. The dispersed phase containing 5 mg mL^{-1} lipid-removed lignin in ethanol was fixed at 50 µL min^{-1}, and water varied corresponding to a Reynolds number range of 500. Following the evaporation of the solvent, 5 mL of aqueous dispersion was added to 5 mL of sunflower oil, and the water was removed by heating. The solution was filtered with a 1 µm syringe filter. The error bars denote ± 1 standard deviation.

From these data, it is concluded that, in addition to the earlier identified stability of CBS-LC CLPs in aqueous dispersion, they are stable in a non-aqueous sunflower oil phase. One potential explanation for the ability of the same CLPs to be stable as dispersions in both aqueous and non-aqueous phases is the presence of the lipid at the surface of the CLPs. In this instance, the polar head group which was hypothesised to be responsible for the stabilisation in aqueous dispersion would undergo rearrangement to place the long hydrophobic tail groups into the sunflower oil phase, Figure 54. If the lipids are indeed at the surface, then the position of the lipids may be reflected per the figure.

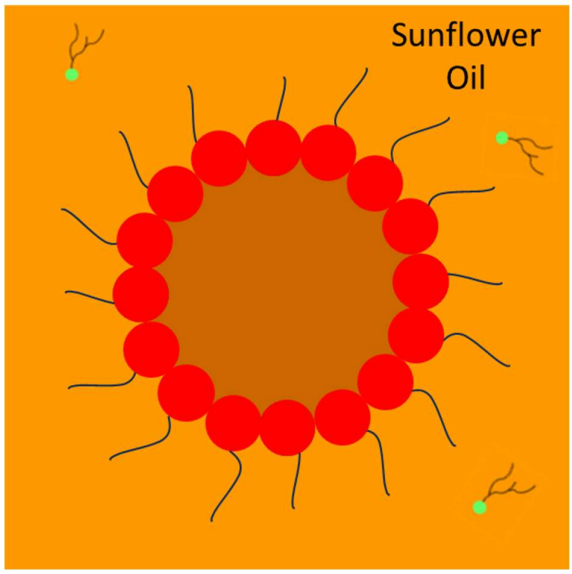


Figure 54: A pictorial representation of the hypothesised position of lipids, represented by a polar head group (red) and a hydrophilic tail group (black) relative to a precipitated colloidal linin-rich particle (brown) in a sunflower oil dispersion.

Despite the success of this in sunflower oil, attempts to establish a similar result in mineral and silicone oil were unsuccessful. One potential reason for this is the presence of molecular surfactants in the sunflower oil, as well as the CBS-LC material system. There are noted challenges in generating oil-dispersible particles present in literature (Bonham *et al.* 2014), and even more interesting is the ability to disperse in both oil and water phases. Further work is suggested to understand the role of the molecular surfactants within the system, to allow for a more general approach to phase transfer.

One can hypothesise that the lipids are decorating the interface offering some stability to the particles. This would explain the stability observed in Chapter 5, and the inability to reach an interface observed in Chapter 6. To corroborate this, it is demonstrated that the lipids present would be able to facilitate dispersion in a non-aqueous phase, as they would have potential to undergo rearrangement at the surface.

6.5. Conclusions

This chapter increases knowledge of the wetting parameters of colloidal particles formed from an extract of CBS. It was hypothesised at the outset of this chapter that the presence of lipids would allow the dispersions to remain stable against aggregation in solution in aqueous phase. By measuring contact angle of the system in the presence and absence of lipids, it was possible to determine the hydrophobic nature of the lipid fraction on the surfaces. Contact angle measurements on a lignin layer validate the model for lipid positioning. Varying precipitation conditions is likely to impact contact angles, supporting the hypothesis that lipids stabilise particle interfaces and are capable of rearrangement to stabilise CLPs in non-aqueous phases.

7. Water and oil dispersible colloidal particles for Ghost Particle Velocimetry imaging

This chapter concerns the use of colloidal lignin particles (CLPs) formed in earlier chapters for the application of imaging flow fields in both oil and aqueous phases. In Chapter 5, the ability to influence the particle diameter of continuously produced colloidal particle dispersions by varying the Reynolds number and flow ratio was demonstrated. GPV requires particles of average diameter < 300 nm, which was demonstrably achieved by a coaxial jet mixing process. This chapter presents an example of an application of CLP dispersions, which are manufactured using the conditions described earlier in this research thesis. The application of ghost particle velocimetry (GPV) requires particles of a sub 300 nm diameter, which remain dispersed in flow to allow quantification.

Chapter 6 explored the wetting properties of the co-extractives of lignin in the CBS–LC and CBS–LR extracts. By manipulating the componentry, the contact angle was found to be variable, indicating potential ability to specify this when formulating colloidal particles. GPV is a technique which has several noted examples of particles suitable for aqueous flow field visualisation, however, there are presently no oil dispersible tracer particles to expand the application of GPV from aqueous to non-aqueous systems. The result from the emulsion studies in Chapter 6 indicated that CLPs were stable in an oil phase, which offered evidence that they may be suitable for such a GPV application.

In the first section of this research, initial validation for stationary flow fields against polystyrene-based beads (henceforth referred to simply as polystyrene) for aqueous flow field analysis is followed by similar work for non-aqueous phases. The second part of this chapter identifies the effect of molecular surfactant, present in both the sunflower oil non-

aqueous phase and the colloidal particle suspensions. This infers the ability to expand the dispersibility from a model system in oil to a more general form.

Thirdly, the quantification of a flow field in a segmented flow is reported in the form of droplets in a restricted-flow channel. To do this, hydrodynamic flow-focusing (HFF) devices will be used to form droplets. Whilst Chapter 4 demonstrated that these devices are unsuitable for the antisolvent precipitation step of CBS-LC CLPs, once the particles are in dispersion, the monodispersity afforded in droplet formation using this type of device offers a significant advantage in generating the reproducible conditions required to analyse the flow fields. This aids understanding of the vortices present in droplet microreactors of this kind, which allows for optimisation of analogous droplet microreactors.

Whilst it is understood that one strength of GPV is the ability to visualise a flow field in multiple planes, allowing the ability to build 3D flow fields (Buzzaccaro S *et al.* 2013), this chapter will limit all experimental data collection to the central plane of the microfluidic channel unless otherwise stated, as this thesis is principally focused on demonstrating the applicability of lignin-rich colloids for the application of GPV in pursuit of thesis objective 5.

7.1. Formation of colloidal particle dispersions of suitable diameter for GPV

In Figure 55, the particle diameter distribution of colloidal particles used for GPV are reported. Polystyrene particles (black) had an average diameter of 220 nm, which

represents a benchmark for GPV testing, owing to their wide scale usage as discussed in the review of the literature, 1.7.

Using conditions of *R* of 1, and *Re* of 450 as defined in Chapter 5, CLPs on the same scale as polystyrene, dispersible in both aqueous and non-aqueous (sunflower oil) phases were prepared using a CBS-LC extract, Figure 55. The sunflower oil dispersed particles had an almost identical diameter distribution to that of the polystyrene particles, with peak z-average diameter being 220 nm in both instances, and a span value of 0.93 (polystyrene) and 1.10 (sunflower oil). In aqueous dispersion, the CLPs had a smaller average peak average diameter (190 nm), and a larger span (1.49). These data suggest the average diameter of particles in dispersion was comparable to commercially available polystyrene particles, which have extensive use in GPV (Kovalchuk *et al.* 2018; Kiratzis *et al.* 2022). From this preliminary data it is hypothesised that CBS-LC CLPs have a suitable application in GPV on a diameter and particle distribution basis.

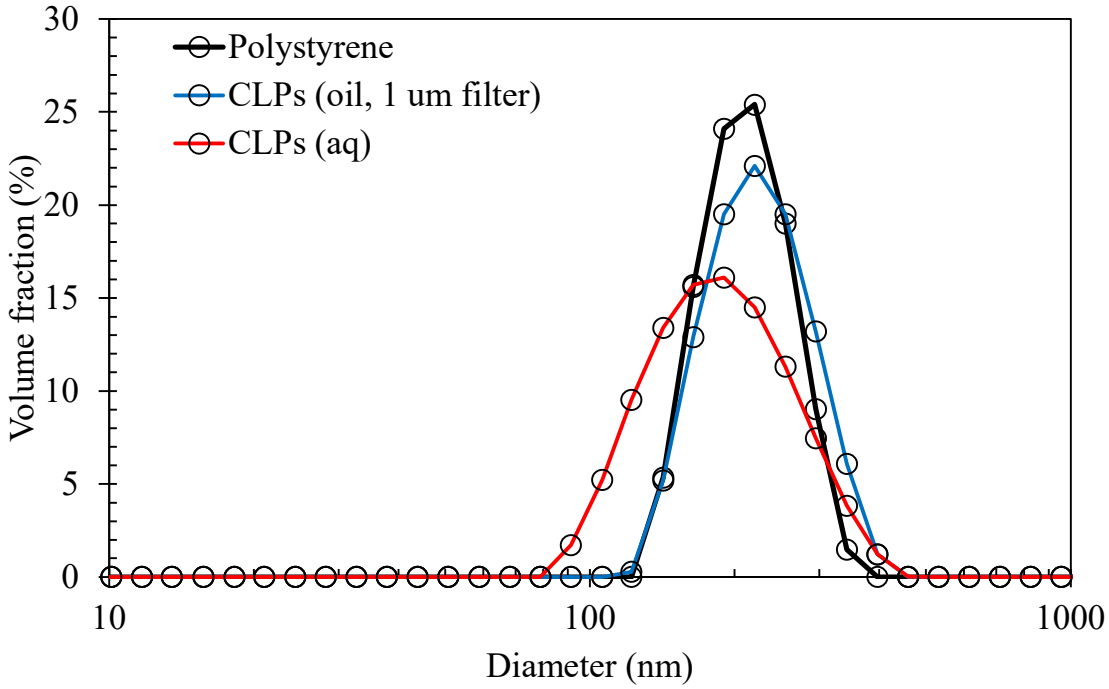


Figure 55: Dynamic light scattering diameter intensity distributions of dispersions of polystyrene nanoparticles; a standard tracer particle for GPV showing a diameter of 220 nm (black). For comparison, CLPs formed using antisolvent precipitation and dispersed in aqueous (red), and non-aqueous (sunflower oil, blue) phases are shown.

Another factor which makes the CLPs suitable for GPV is the large difference in refractive index between the particles (1.58) polystyrene (1.59), water (1.33) and sunflower oil (1.46).

7.2. Quantifying flow fields in GPV

In this section, the baseline for using colloidal-sized particles for the observation of flow fields in aqueous systems was established. Appropriate conditions for flow field visualisation using CLPs were identified, and the optimised conditions were compared to the current literature standard of polystyrene. This was further developed to examine non-

stationary flow fields formed in droplets. Additionally, the capture settings of frame rate, concentration, and volumetric flow rate were varied, to assess the most effective conditions for flow field visualisation.

7.2.1. Determination of flow rates and camera speed suitable for GPV

To utilise the CLP dispersions for GPV, appropriate conditions were established to visualise flow fields using the technique. The factors affecting this were frame rate, fluid velocity and camera speed. Preliminary signal testing was conducted at a CLP concentration range of 0.01 – 0.5 wt%, and signal was observable at concentrations of 0.3 wt% and greater. Initial validation of the setup was sought by examining the velocity magnitude profiles obtained through cross-correlation across the width of the channel, averaged across 400 images, generating 200 frames. As the cross-correlation was merely a statistical analysis of the movement between frames, replication of a parabolic flow velocity magnitude profile as discussed in 1.7.1 represented a validation, in that the particles could visualise the flow field.

Figure 56 demonstrates a distribution plot of the velocity vectors produced by cross-correlation across the width (x) of the channel, at 2000 and 10,000 fps, and 50 and 100 μL min^{-1} using CBS-LC particles of a diameter 200 nm. Given the dimensions of the channel of 600 x 150 μm, the velocity was expected to be highest in the centre of the device, and slowest at the edges. At 2000 fps and 50 μL min^{-1}, the profile follows the expected distribution, with an average movement inferred from the speckle pattern of 6.2 px/frame. At 10,000 fps and 50 μL min^{-1}, the profile was closer to the expected velocity magnitude profile, however at a velocity of 1.25 px/frame it still appeared to have an error

contribution from the slow movement of particles. At lower flow rates, the profile was disrupted, which was likely a consequence of the low movement of particles on the recorded images between frames; 1.67 px/frame at 2000 fps and 0.24 px/frame at 10,000 fps leading to poorly resolved feature of the flow profile. It was also possible that at low flow rates contributions from thermal movement processes such as Brownian motion caused deviation from the induced flow profile. From this, it can be concluded that conditions of 50 µL min^{-1} is the minimum to produce acceptable flow profiles in the flow channel with dimensions of 600 x 150 µm, and an interrogation area of 32 px.

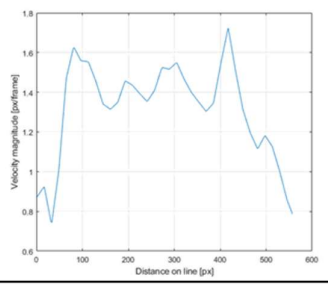
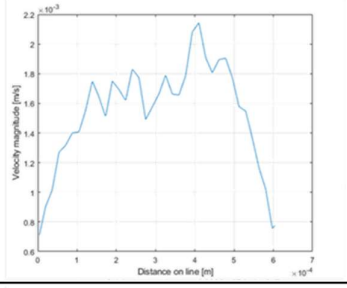
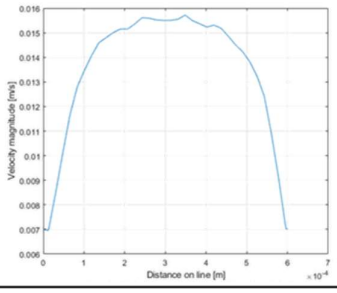
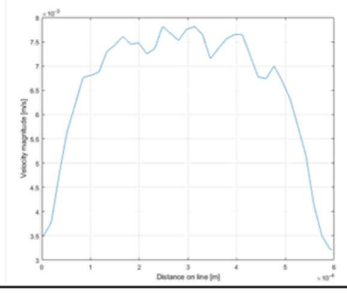
		2,000 fps	10,000 fps
Flow rate	10 µl min^{-1}		
	50 µl min^{-1}		

Figure 56: Line profile matrix showing the distribution of magnitude of velocity vectors across the width of a 600 µm channel with 3.5 mg mL^{-1} CBS-LC CLPs of average diameter 220 nm in aqueous dispersion flowing at 10 and 50 µL min^{-1}, with frame rates of 2000 and 10,000 fps. Line profiles taken from a cross-correlation plot mean average of 400 frames.

7.2.2. Precision of vectors in GPV conducted using CLPs

In addition to assessing the ability of CLPs to accurately determine the flow field pattern within a channel, the resolving quality of particles was determined. For PIV of a Poiseuille flow field, the displacement of a particle between t and t+1 time step is anticipated to be linear and related to the distance from the wall of the channel. Per Figure 57, the displacement between the two time-steps can be imaged using a high-speed camera, and represented using a vector showing displacement in u and v. GPV uses dispersed particles which scatter light and generate a speckle pattern which can be resolved by scientific cameras, and by accurately determining the time step, can generate vectors relating to the movement of the fluid. By plotting the vectors across a series of successive frames and applying statistical analysis to remove outliers, a profile of the movement of fluid in a channel can be determined. Figure 57 shows two instances of displacement of a particle in a flow and the resulting position of a vector on a vector plot. In the instance where a particle has moved in accordance with a laminar flow, there will be little or no horizonal movement. In the instance where there is lateral movement, such as in the blue vector, then the resulting vector will be recorded as such.

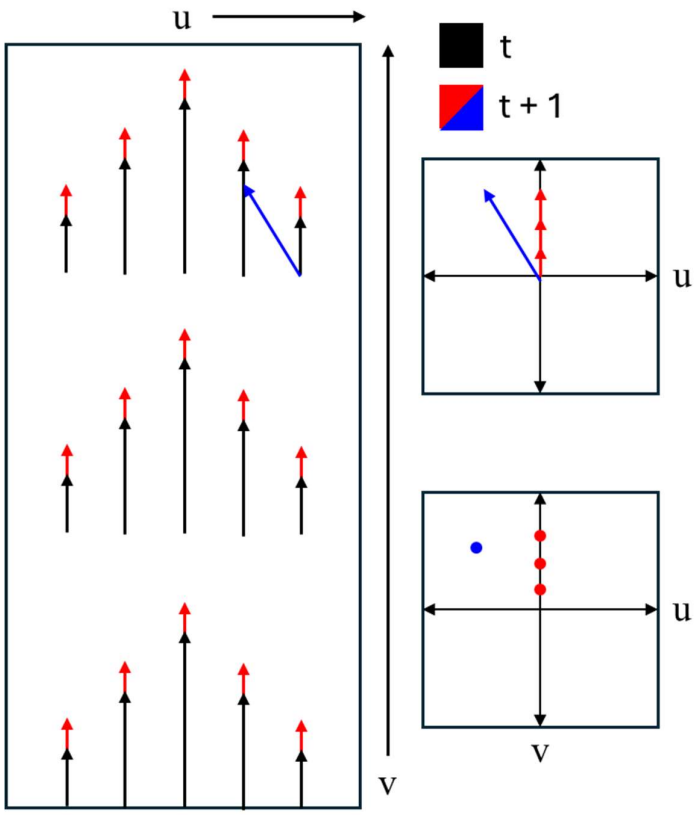


Figure 57: A schematic interpretation of the method of formation of vectors in a Poiseuille flow for a static flow field in a microfluidic channel. The vectors in a channel (left) represent the movement of a fluid at a given point in space between time t (black) and time t+1 timestep (red, blue). The movement of the particle during this time frame can be used to plot a vector representing its movement (right, top), from which the movement in both u and v (right, bottom can be determined.

Figure 57 demonstrates the scatter of vectors determined by cross-correlation in the mean images formed from 100 and 400 frames, for each of CBS-LC CLPs at 3.5 mg mL^{-1} in aqueous dispersion and sunflower oil dispersion and is compared to aqueous polystyrene particles. It is anticipated that the low flow rate of 50 µL min^{-1}, corresponding to a maximum velocity of around 20 mm/s, and an Re of 40 is sufficiently low to use as

conditions to generate laminar flow, and therefore test the ability of dispersed particles to determine the flow profile. One way of representing this is by plotting the scatter of vectors, and quoting the magnitude of difference between their u and v values. Given the conditions in the flow, it is anticipated that there should be a greater magnitude of v than of u.

An immediate conclusion from the data is that flow fields derived from CLP dispersions are far less precise than their polystyrene equivalents. Using an average from 100 frames (comparison between 50 pairs), there was a large degree of scatter of vectors across the co-ordinate space, indicating that despite taking an average, there was still poor precision.

One explanation for this is that the distribution of particle sizes present in solution is greater in the aqueous system than in the other two systems, see Figure 55. This monodispersity, whilst still generating particles below the diffraction limit, could cause the 'speckle' pattern created to have minor differences between particles, offering a wider distribution of values collected. This explains why the sunflower oil dispersed particles, whilst still having significant variance in vectors, are noticeably more precise in u at 100 frames than the aqueous dispersion.

Considering the systems as an average of 400 frames (200 pairs), all three systems converge much more precisely. The range of scatter in horizontal (u) of the polystyrene at 100 frames is 4.77×10^{-3} m s^{-1} and 1.2×10^{-2} m s^{-1} in vertical (v), a much smaller fraction of the available co-ordinate space (7%), indicating increased precision. This is comparable to the values of 400 frame averages using CLPs, which are 4×10^{-3} m s^{-1} horizontal, 6.4×10^{-3} vertical for aqueous and $x10^{-3}$ m s^{-1} horizontal and 1.85×10^{-2} m s^{-1} for oil respectively. From this, it can be concluded that polystyrene offers much greater resolving precision than CLP equivalents for the same number of frames. The range of

vectors in u is marginally narrower at 400 frames for CLPs than 100 frames of polystyrene, and in v it is greater, although it remains on the same order of magnitude.

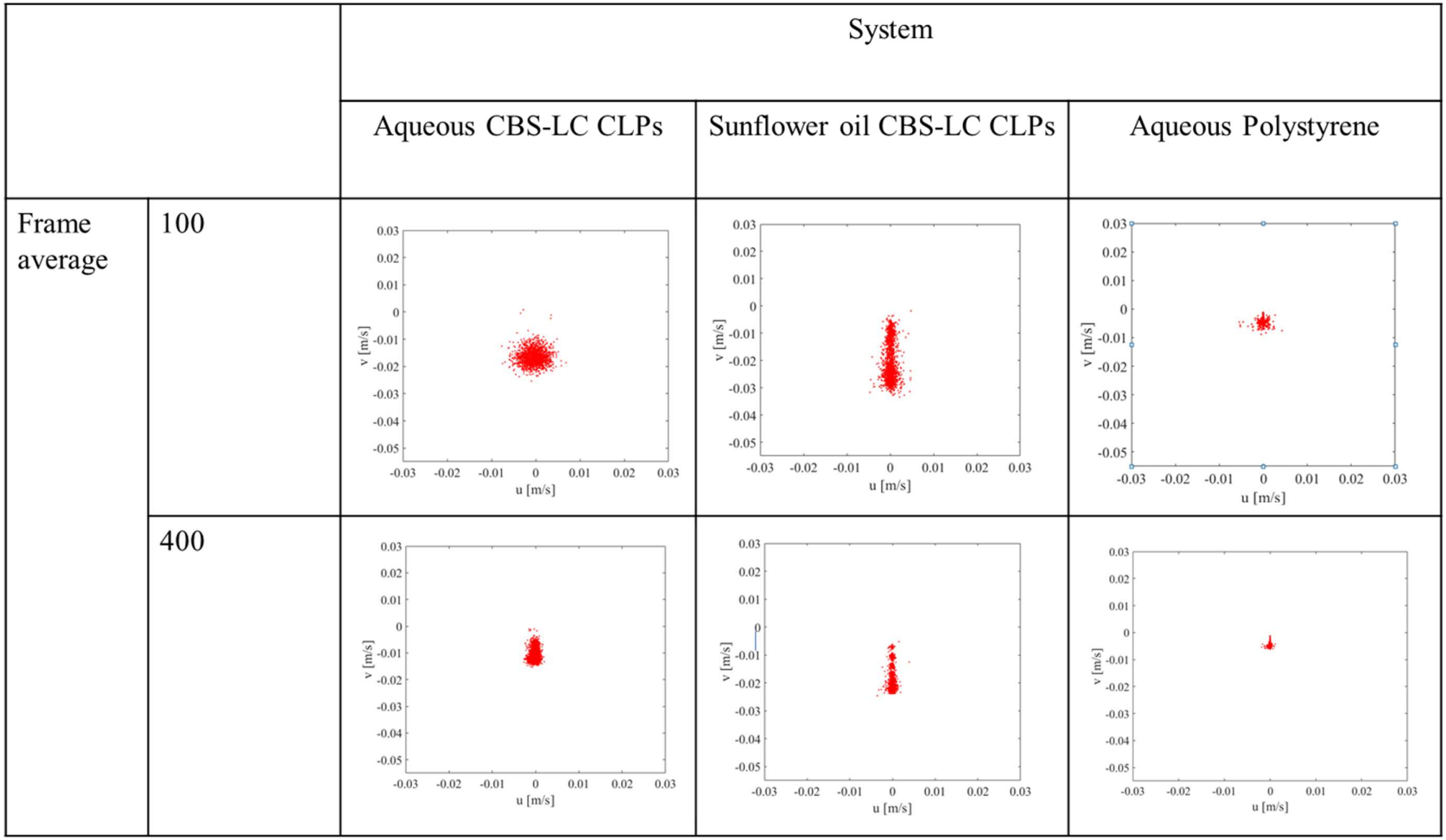


Figure 57: A series of scatter plots, showing velocity magnitudes of vectors in a mean cross-correlation plot at 50 and 400 frames, created by GPV. Three systems; aqueous dispersed CBS-LC derived CLPs, sunflower oil dispersed CBS-LC derived CLPs, and polystyrene derived particles are shown.

From the above, it is possible to conclude that the resolving quality of aqueous dispersed polystyrene particles is far greater than that of any CLPs at the same number of frames, irrespective of phase. The aqueous dispersion has the second-best resolving quality and offer greater precision of vectors than sunflower oil dispersed CLPs aqueous dispersion. By using 400 frames, the resolving quality of the CLPs is similar to that of 100 frames (50 pairs) of polystyrene, considering the same value in u, and whilst the resolving quality was poorer in v, it is the same order of magnitude. There are several examples in literature where 100 frames is regarded as sufficient for GPV analysis (Kovalchuk *et al.* 2018; Kovalchuk and Simmons 2021), offering strong evidence that the precision of data collected from 400 frames using CLPs is sufficiently precise for flow field measurement, however this precision can be improved further by increasing the number of frames averaged even further.

7.2.3. Reproducibility and accuracy of flow fields determined by CLPs

Using the conditions from 7.2.1 of 50 μL min^{-1} and frame rate of 2000 fps, the reproducibility of velocity capture using CBS-LC particles for GPV is reported, Table 14, giving a mean velocity of 6.2 ± 1.6% (0.1 px $frame^{-1}$).

Table 14: Average velocity of vectors (px/frame) across a mean cross-correlation plot (400 frames) of an aqueous dispersion of CBS-LC particles with a flow rate of 50 μL min^{-1} and frame rate of 2000 fps.

Repeat	Velocity (px/frame)
1	6.06
2	6.18
3	6.26

Figure 58 shows the full vector profile for a fluid moving through a straight channel at 50 µL min^{-1}, as an average of 400 frames. Despite the large number of frames, there are still some erroneous vectors, shown in orange, which have been replaced by the mean value of the rest of the row. Despite this, the values collected of 0.0155 m s^{-1} (max) and 0.0136 m s^{-1} (mean), are similar to that which would be expected from theory for the flow in this channel at 50 µL min^{-1} of 0.0185 m s^{-1} (max) and 0.0112 m s^{-1} (mean).

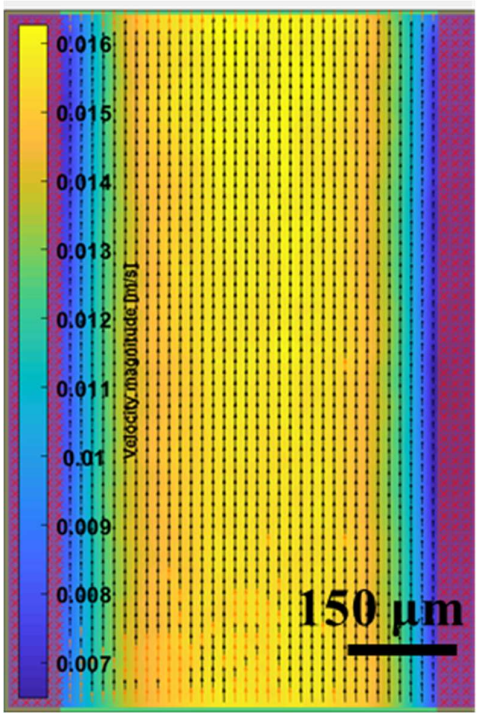


Figure 58: A flow field formed by dispersing CLPs at 3.5 wt% in distilled water and passing the fluid through a PDMS channel with a width of 600 µm and a height of 150 µm, and a flow rate of 50 µL min^{-1}. Image an average profile of 200 frames.

CLPs were also tested in non-aqueous dispersion of sunflower oil, Figure 59, which shows a flow field profile of a straight channel at 2000 fps and 50 µL min^{-1}. The values found agree with those for both the aqueous system and theory giving values of 0.0132 m s^{-1} (max) and 0.0105 m s^{-1} (mean), demonstrating the aptitude of CLPs for visualisation of flow fields in both aqueous and non-aqueous phases. Compared to the aqueous

dispersion, there are no erroneous vectors, indicating that the cross-correlation was more easily able to detect the 'speckle' pattern from sunflower oil dispersed particles.

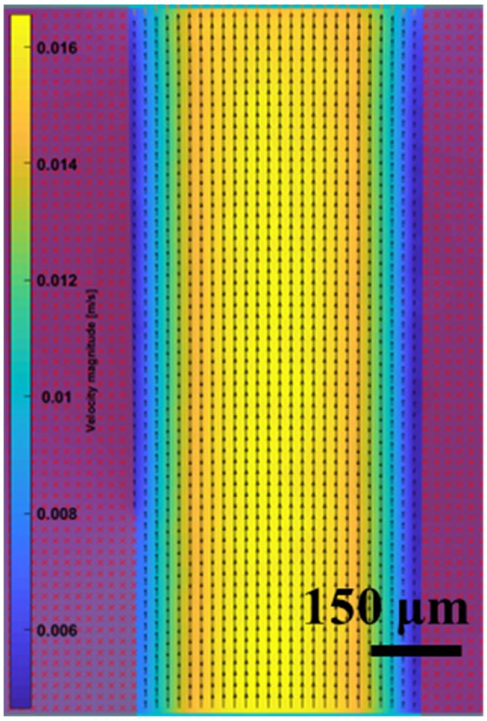


Figure 59: A flow field formed by dispersing CLPs at 3.5 wt% in sunflower oil and passing the fluid through a PDMS channel with a width of 600 µm and a height of 150 µm and a flow rate of 50 µL min^{-1}. Image an average profile of 200 frames.

Given the difference in particle span identified earlier in the chapter, one conclusion which may be drawn is that span is a significant metric for GPV, and the larger the span of the particle dispersion, the greater the variation in vector values determined by cross-correlation in the resulting GPV flow field. Another discrepancy between the values measured and calculated can be from the effects of the RI, which can distort the experimentally determined values.

This section offers evidence for the capability of lignin-rich colloidal particles for accurately determining the movement of a flow in a channel. Using 400 frame averages

of flow in a channel, it was possible to experimentally determine the maximum velocity of the fluid as 0.0132 m s^{-1}.

The accuracy of the system was determined experimentally by comparison to polystyrene-based particles and the theoretical calculation, where the width of the channel, 600 μm, was considered, Table 15.

Table 15: Average velocity values of lignin colloidal particles dispersed in a series of phases, compared to theoretical values.

Dispersant	**Phase**	**Maximum velocity (m s^{-1})**	**Mean velocity (m s^{-1})**
Theoretical		0.0185	0.0112
Polystyrene	Water	0.0120	0.0096
Lignin	Water	0.0155	0.0136
	Oil	0.0132	0.0105

The likely reason behind the erroneous values at both high and low frame rates is that the difference between frames in cross-correlation may be a deviation from the central focal plane, which would cause a reduction of velocity value measured compared to the theoretical maximum. At the extremes of the ranges testing, the movement of the particles between two frames, the movement of a 'speckle' in pixels relative to the interrogation area of 32 pixels is a likely source of error. From the data in Figure 56, visualisation is optimised for this channel at frame rates of 2000 frames per second, volumetric flow rates of 50 μL min^{-1} For a more general result, the displacement of 6 pixels compared to an interrogation area of 32 pixels can be considered, with a result of 10-20% of the interrogation area representing the best result. In addition to commercially available polystyrene, flow fields were visualised using lignin-rich CLPs. This research

demonstrates the potential for another valorisation route of CBS. It is also notable that the particles appear to be dispersible in sunflower oil, representing the first example of stable dispersible particles in a non-aqueous phase for flow field imaging.

7.2.4. GPV using CLPs to visualise complex single-phase flows

As described in 1.7.2, one advantage of using GPV is the ability to more accurately measure non-linear pathways, as the comparatively smaller particles, which are on the hundreds of nanometre scale, can more closely follow flow profiles than comparatively larger (μm-scale) PIV tracer particles. Figure 60 shows a channel with a cross-section geometry, with sunflower oil as the fluid, and CBS-LC CLPs as the dispersed particles. Using these particles, the movement of fluid out of the central channel, and the corresponding reduction of velocity associated with leaving the central channel is demonstrated.

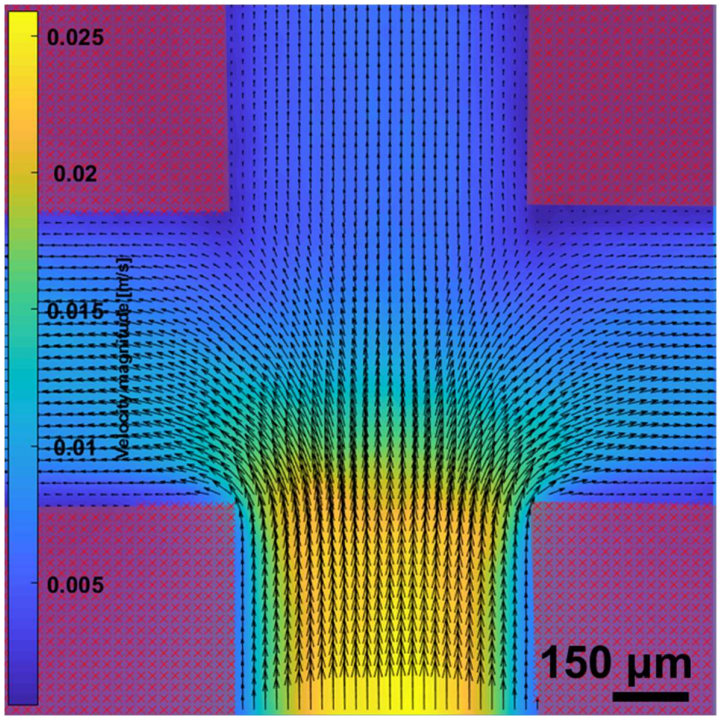


Figure 60: A flow field formed by dispersing CLPs at 3.5 wt% in sunflower oil and passing the fluid through a PDMS channel with a diameter of 600 µm and a height of 150 µm and a flow rate of 50 µL min^{-1}. Image an average profile of 200 frames.

Through the results of this section, the system has been validated to demonstrate that CLPs can be used to determine flow velocity profiles accurately and precisely for a flow rate of 50 µL min^{-1}, using a frame rate of 2k fps, and averaging a minimum of 400 pictures (200 frames). The 200 images required to accurately resolve a flow field is greater than the 100 required for polystyrene in aqueous dispersion, however there is a significant application advantage in the ability to disperse lignin CLPs in sunflower oil, a non-aqueous phase. The next section will use the optimised parameters from the first section of this chapter to image a dynamic system in multiphase (oil in water) flows.

7.3. Imaging segmented flow fields in GPV

In this section, the earlier results of this chapter demonstrating visualisation of flow fields using CBS-derived CLPs in aqueous and non-aqueous phases are combined. An application of flow field imaging is the design of microreactors; reactions can be performed in an oil phase as well as an aqueous phase. There can be also reactions without coalescence, where reactants are brought together from several streams during the drop formation as referred to in the literature review. In all cases mixing inside the reactor is important and it depends on the flow fields. This section presents visualisation of aqueous droplets in non-aqueous phases.

7.3.1. Vector validation in segmented flows

When considering movement of droplets in a channel, where one phase has tracer particles, the moving object is often moved backwards, to align with the initial image point. This is sufficient for generating a flow profile in instances where there is only one medium with dispersed tracer particles. Figure 61 shows a schematic of this approach, whereby two successive frames are pulled back (n+2 & n+3) through post-processing to align the position n & n+1 an original position in pairs for the same droplet, allowing for the movement between frames to build be used for cross-correlation as the initial pairs would be.

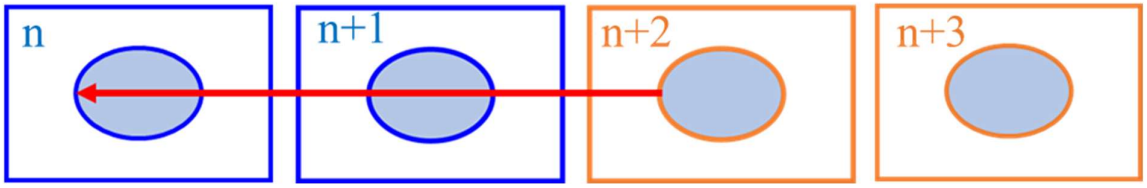


Figure 61: Schematic diagram showing the image analysis method by cross-correlation for mapping the flow field of a droplet moving in a channel, by moving later frames of the same droplet to a consistent part of the field of view.

This approach is not possible in instances where the flow field for both the continuous phase and a droplet phase is being characterised, as moving to a set point in one phase may distort the field in the other phase artificially. An alternative method for generating an average of a flow field is to use cross-correlation on a series of droplets as they pass a predetermined point in space, represented by n & n+1, and a different drop t & t+1, Figure 62. In this way, the movement of the droplet and internal recirculation are resolvable, allowing for cross-correlation by GPV.

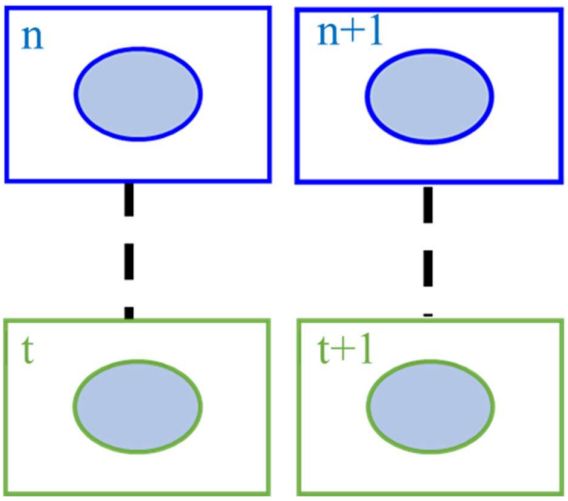


Figure 62: Schematic diagram showing the image analysis method by cross-correlation for mapping the flow field of a droplet moving in a channel by averaging successive droplets passing the same area in space.

The success of using CBS-LC for cross-correlation can be determined by examining the vector validation. As cross-correlation builds a pattern of movement between pairs of frames, the number of pairs of frames in succession will affect how accurate the image is.

As a baseline, Figure 63 shows a vector distribution for a cross-correlation performed on a system where only one image per droplet is taken. The distribution pattern of vectors is random, as there are no pairs of images to allow tracking of the 'speckle' pattern created by the dispersed particles. As a result, the vectors returned are distributed across indicated the maximum reaches of the co-ordinate space, where most of movement is expected to be along the channel. This should result in large u velocities and low v velocities. The result of uniform distribution around 0 suggests that this is not an accurate flow profile.

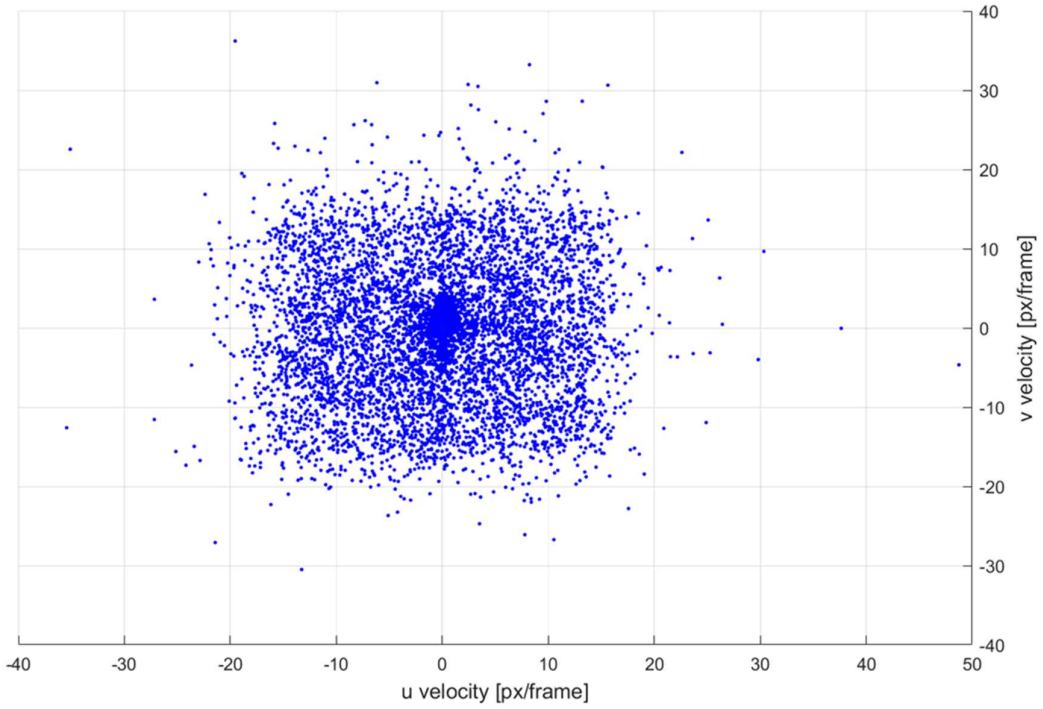


Figure 63: Distribution plot of the vector magnitude and direction generated by cross-correlation of a scattering pattern indirectly caused by a colloidal particle dispersion. The particles are simultaneously

dispersed in a droplet and a continuous phase in a microchannel. For each droplet, one image is taken as it reaches a set point in a field of view.

Figure 64 displays the first instance where the technique can accurately determine movement between images. Here, two images are taken per droplet, allowing for the movement of the speckle pattern to be plotted. Despite this, there is a significant amount of error in both u and v regarding vector position.

One possible explanation for this is that whilst there are pairs of frames whist show the movement of the fluid, there is error arising from the repositioning of the next droplet. Were the first method discussed for cross-correlation pursued, this error would be endemic to the technique, as by moving the droplet back, the minor variations between placement of the droplet would be picked up by the cross-correlation.

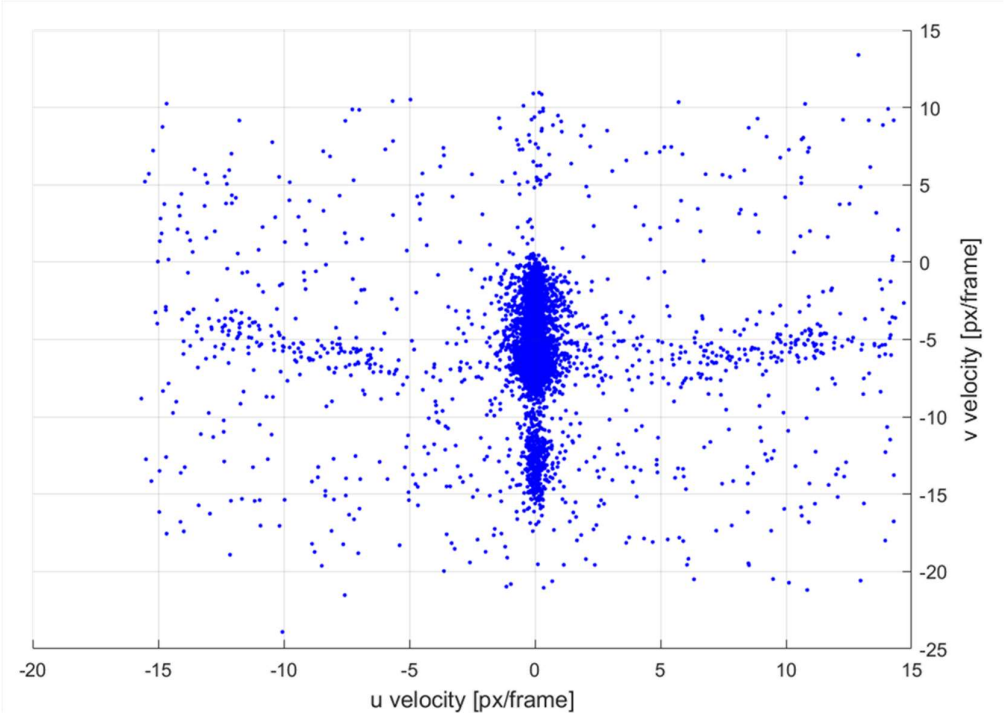


Figure 64: Distribution plot of the vector magnitude and direction generated by cross-correlation of a scattering pattern indirectly caused by a colloidal particle dispersion. The particles are simultaneously

dispersed in a droplet and a continuous phase in a microchannel. For each droplet, two successive images are taken as it reaches a set point in a field of view.

Addressing the wide distribution of vectors under the conditions shown, four images (two frames) per droplet were taken, Figure 65. Here, there is a dramatic difference in the placement of vectors, with almost no displacement in *u*. By including four frames from each droplet, the precision is greatly increased, as there is a greater number of vectors which can be accurately mapped, as when new droplets are fixed to the same distribution, the position of the 'speckles' caused by the particles is random in space, and therefore the correlation is not as strong.

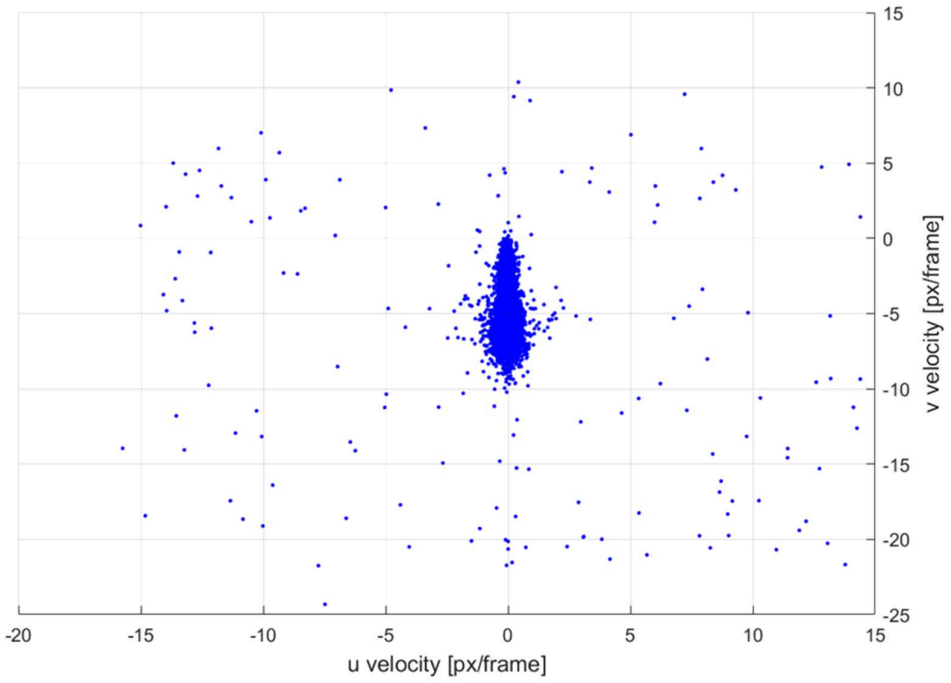


Figure 65: Distribution plot of the vector magnitude and direction generated by cross-correlation of a scattering pattern indirectly caused by a colloidal particle dispersion. The dispersion is simultaneously dispersed in a droplet and a continuous phase in a microchannel. For each droplet, four successive images are taken as it reaches a set point in a field of view.

Whilst there are still some vectors which do not conform to the flow pattern, this is likely due to an error in cross-correlation, or possibly from experimental factors such as Brownian motion, although this is more likely to occur at lower flow rates owing to the relative movement of particles. Providing these are an insignificant fraction of the dataset arising from including these errors, they can be removed to retain a significant dataset. From the above data, it can be determined that using an average of four frames per droplet allows for resolution of the vectors. To generate a flow field, the average of 100 such droplets was used.

One drawback of using a larger number of consecutive images is that, whilst this improves vector quality, it leads to a significant blur at interfaces. Figure 66 shows an image of a droplet taken using the conditions optimised earlier in this chapter. As the number of images per droplet is increased, there is a clear increase in blur at the interface of the water droplet and the continuous phase.

Another valid criticism is the large refractive index shadow formed by the difference between the values of water (1.33) and sunflower oil (1.46). This makes visualisation of movement at the boundary between the droplet and the continuous phase impossible. Given that this system contains molecular surfactant however, there is likely to be some non-standard behaviour at the boundary, such as a mobile interface Kovalchuk and Simmons (2023).

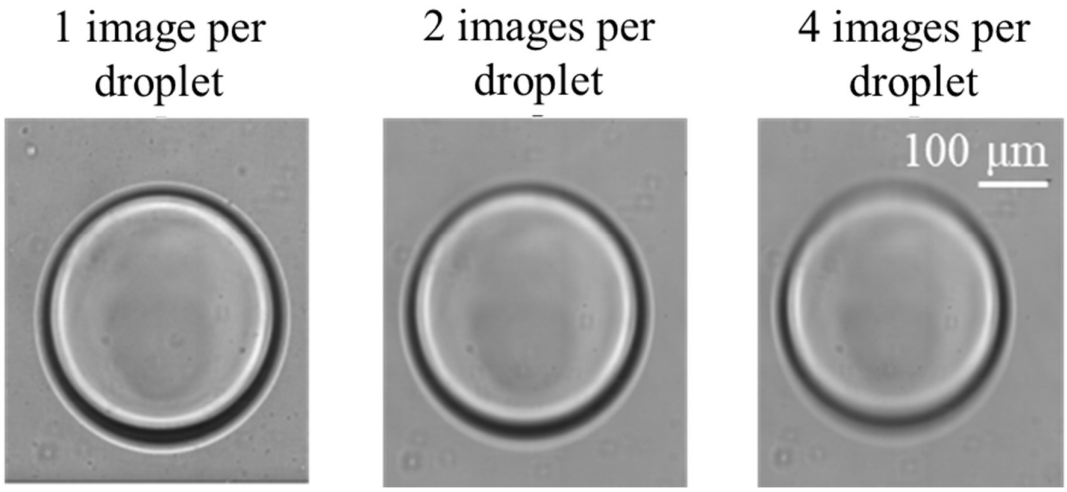


Figure 66: A series of images showing a droplet of water dispersed in oil captured as 1 frame (left), and the mean of two frames (centre) and four frames (right).

One criticism of GPV, alongside other techniques which use cross-correlation, is that at a boundary, there is potential for error, due to the nature of integration. The cross-correlation technique may either pick up movement across the interface, generating a vector which travels across the interface, or generate a vector which is far smaller than the real value, as the number of particles generating signal is significantly lower compared to the free-flowing bulk of the system.

For observing flow pertaining to the entire droplet, such as recirculation, and other fluid flow concerning the geometry, the inability to measure meaningfully the flow near the interface of the droplet is a significant limitation. This can be rectified by matching the RI of both the phases. This could be achieved by the addition of glycerol to the aqueous phase; however, this is outside of the scope of this research at present. There is however a great deal of information which can be gained from this setup, particularly in intricate geometries, where theoretical prediction may prove difficult.

Therefore, to produce the most optimal image, it was chosen to have the greatest number of frames per drop to resolve the vectors fully. However, by going beyond four frames the blur would make the fine structure of the image impossible to resolve. One way to address this would be to increase the frame rate, however given the optimisation conditions set out earlier in the chapter, this was chosen as the best balance of conditions to pursue.

7.3.2. Flow fields in a segmented flow

Figure 67 shows a vector profile formed of the average of 100 droplets, each showing the movement of particles across 2 successive frames per Figure 66 (centre). As earlier, the summed flow rate through the channel was 50 μL min^{-1} and the flow range had a maximum velocity of 0.016 m s^{-1}, and mean value of 0.0106 m s^{-1}. Considering that the channel had a compressed aspect ratio, with a 150 μm height and 600 μm width, it is possible that recirculation was caused by shear interaction between the channel top and bottom of the device and the droplet. The formed droplet is compressed in the vertical plane, and has a volume of 6 nL.

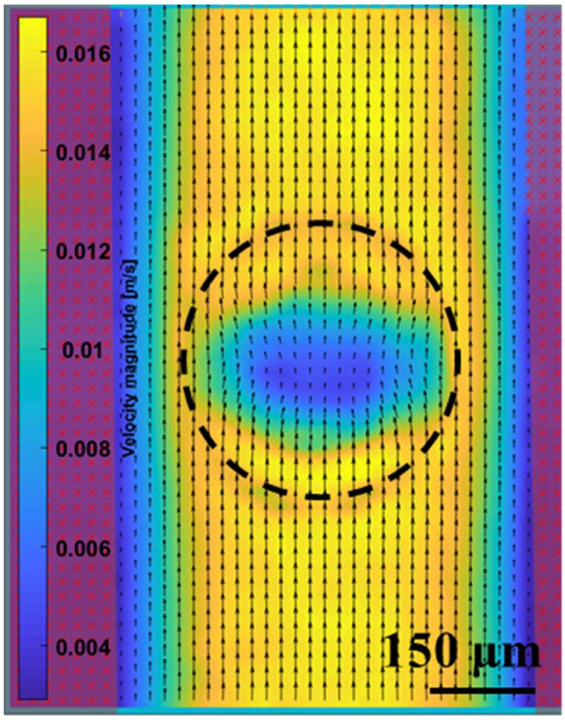


Figure 67: An average flow field profile of 100 droplets of water in a sunflower oil continuous phase in a microchannel. Each vector is generated from two pairs of two successive (four in total) images by cross-correlation per droplet. The flow rate of the dispersed phase is 8 µL min^{-1}, and the continuous phase is 42 µL min^{-1}. The aqueous contains 3.5 wt%. Lipid containing (LC) colloidal lignin particles of average diameter 220 nm. The external phase of sunflower oil contains the same tracer particles at a concentration of 3.5 wt%.

The flow profile of the continuous phase, Figure 68, demonstrates a vector in the continuous phase of the system 200 µm ahead of the droplet. The flow profile retains the parabolic profile identified as consistent with a channel of this design, suggesting that the system can retain the flow conditions suitable for quantification as identified. There is a noticeable reduction in the velocity profile observed in Figure 68 at distances across the channel (in u) of both 200 and 400 µm. One possible explanation for this, given that variation in the material system has been excluded using validation in 7.2.1 is the influence of vortices introduced by the presence of the droplet in the microchannel.

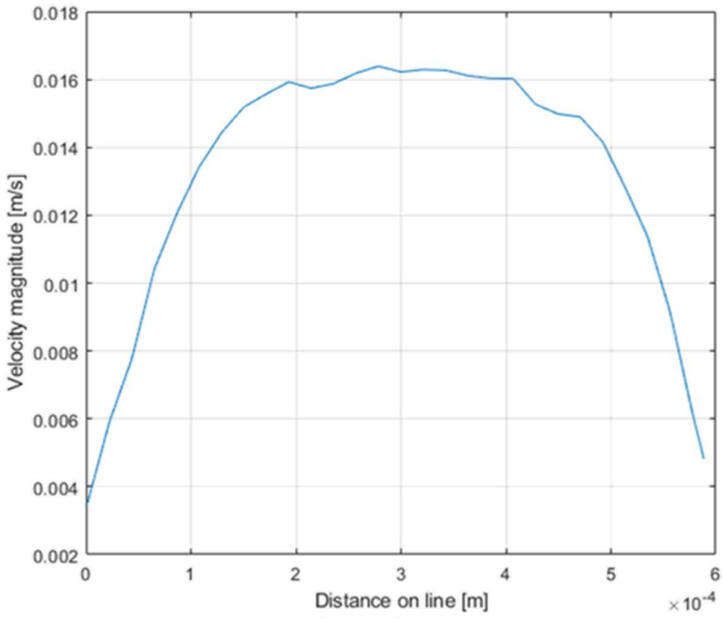


Figure 68: Line profile matrix showing the distribution of magnitude of velocity vectors across the width of a 600 μm channel with 3.5 mg mL^{-1} CBS-LC CLPs of average diameter 220 nm in sunflower oil dispersion flowing at 50 μL min^{-1}, at 2000 fps. Line profiles taken from a cross-correlation plot mean average of 400 frames.

To interrogate the low value of velocity (v) inside the droplet, and the recirculation in the continuous phase, the velocity of the droplet, 5.5 pixels per frame, was subtracted from the entire co-ordinate space. This was kept in px $frame^{-1}$ as this represents quantitative analysis of the presence of recirculation, rather than flow field quantification.

In Figure 69, two clear patterns which are characteristic for this system can be observed. The first is the flow field inside the droplet, which is now in the opposite direction to the travel of the droplet through the channel at a value of 4 px/frame. From this, one can infer that during the travel through the channel, there is an effect on the droplet causing circulation vortices within the droplet counter to the direction of the flow are visible against the continuous phase velocity.

This is a sensible and significant finding considering the channel aspect ratio, which is 4:1 width to height (600 μm x 150 μm), meaning that the droplets are not spherical. The droplet seems to have adapted to the shape of the channel in the plane of the 150 μm dimension, which is likely to cause recirculation. Were this to be a channel with dimensions much greater than that of the droplet, or an aspect ratio closer to 1:1, these recirculation vortices would be likely to change.

The second feature which can be resolved following the removal of the direction of flow of droplet is the recirculation in the sunflower oil phase. In Figure 69 (right), one can see that the formation of the droplet using the HFF device has caused recirculation to occur in the fluid. There are similar recirculation patterns visible above the droplet in the field of view, but these are almost certainly the result of similar recirculation generated from previous droplets in this continuous process.

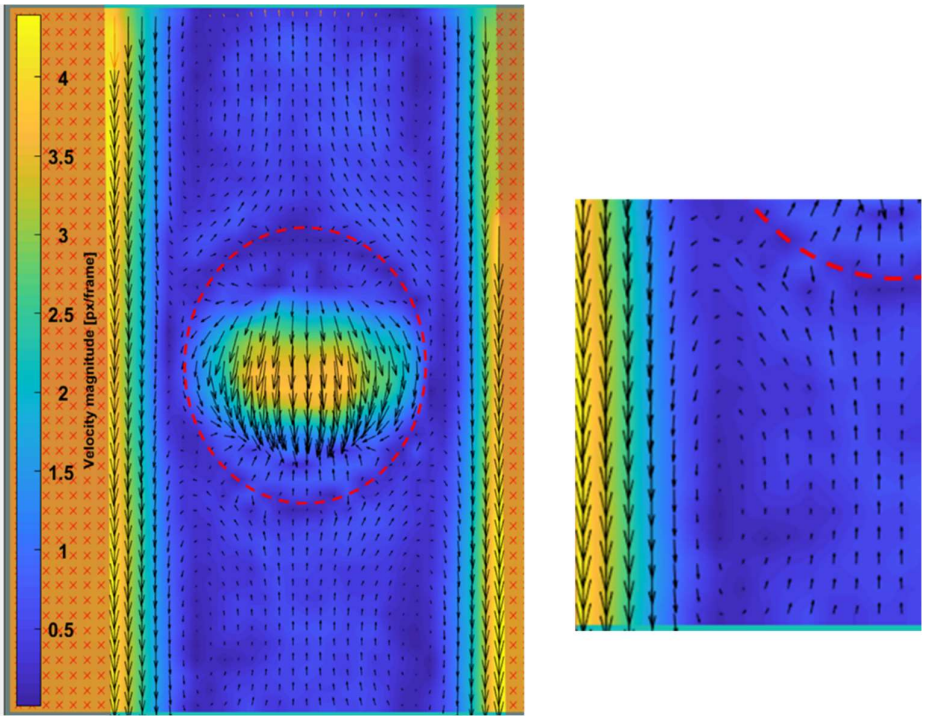


Figure 69: Ghost particle velocimetry image of a water droplet in a sunflower oil continuous phase, formed at a flow rate of 42 µL min^{-1} (sunflower oil), and 8 µL min^{-1} (water). Both fluids have CLPs formed from CBS-LC extract at 3.5 mg mL^{-1}. The flow field has a linear transformation applied of v = -5.5 px/frame to each vector to extricate the fine movement from the overall movement of the frame. Image (right) shows the recirculation pattern from droplet formation.

In removing the contribution to the velocity of the droplet of 5.5 px per frame to elucidate the recirculation, the magnitude of the values becomes self-consistent, but no longer quantitative, and therefore analysis is conducted in the units of px $frame^{-1}$. Nonetheless, the lateral component of the flow is observable in Figure 70 (left). From the construction of the microfluidic device, it is expected that the droplet would be in the central position of the channel. As validated, the CLPs present can generate a 'speckle' pattern, allowing for the flow field to be visualised. What can be seen is the recirculation in the device in a sunflower oil phase resulting from the presence of a droplet in the channel. From this, the

vortices caused by the presence of the droplet can be qualitatively observed, simultaneously with the recirculation inside the droplet as discussed.

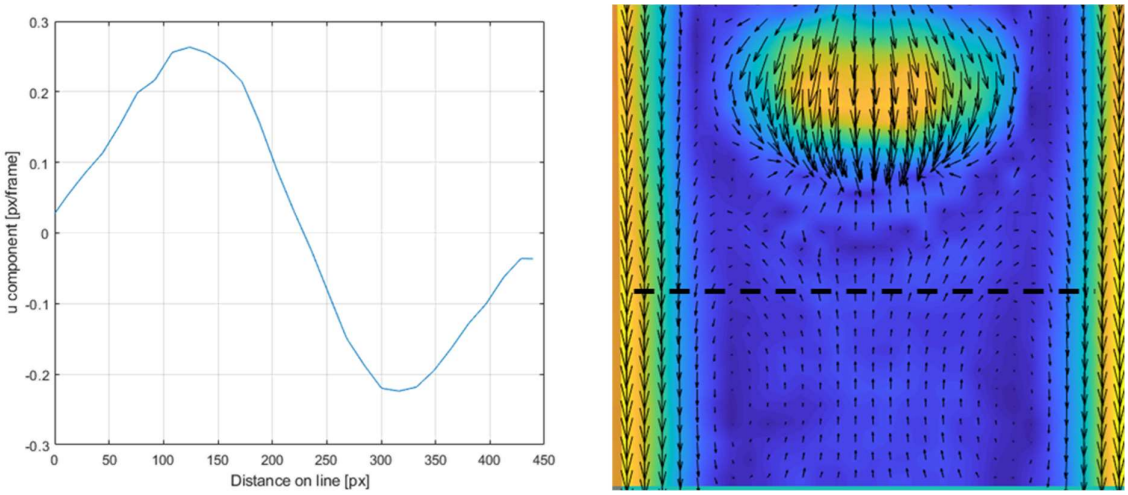


Figure 70: Lateral component of recirculation caused by the formation of a droplet in a microchannel, taken from a line profile (right, dashed).

Whilst this system remains a model example of the ability to quantify these fields, this is not a trivial result, as by using such particles in both phases, and used to inform the design of devices which can be used to aid the design of micro-reactors such as those described at the outset of the chapter.

This chapter demonstrates the ability of CLPs to visualise multiphase flows. Whilst the result is significant, representing an example of simultaneous flow field visualisation in both aqueous and non-aqueous phases, its usability in the current form is limited, as both the CLPs and the sunflower oil non-aqueous phase contains molecular surfactant (lipid), which will directly affect the droplet formation phase. For use as a model system for micro-reactor modelling, a consistent surface tension is required. Whilst the use of a bio-residual extract from a waste product for quantification of flow fields represents an interesting result, offering a circular economy novelty over polystyrene, the presence of

co-extractives, particularly lipids are a significant disadvantage in attempts to use these particles directly.

7.4. Effect of surfactant on GPV

To rationalise the role of the lipid within the system described throughout this chapter, the final section concerns the effect of manipulating the molecular surfactants inherent to the system, in the context of dispersibility of particles, and influence on droplet formation in a selected range of oils, and for a range of particle systems.

7.4.1. Effect of surfactant on the dispersibility of CBS-LC CLPs for GPV analysis

The learning of Chapter 7 offers insight into the conditions within a specific channel for a model system, and as such one can learn about the impacts of geometry modification on the flow inside a device. One limitation of the research, however, was the retention of the lipid fraction within the system resulting from co-extractives as defined in Chapter 3, and in the sunflower oil phase.

Table 16 shows the dispersibility of CLPs formed from CBS both with and without the presence of lipid co-extractives in a series of synthetic and natural oils. For the case of CBS-LC CLPs, where there are lipids associated with the particles, dispersal is possible in both natural oils (sunflower and vegetable), and in treated sunflower oil (TSO) where the lipid fraction was removed. In CBS-LR CLPs, where the associated lipid fraction was removed before dispersal, it was again possible to disperse the CLPs in the natural oils, although it was not possible to disperse them in the TSO. From this, it was concluded that

the particles were only dispersible in the presence of a lipid, although this can be from either the particle system or the oil systems. In both LC and LR cases, it was not possible to disperse the particles in a synthetic (mineral or silicone) oil.

Table 16: The effect of molecular surfactant presents in both lignin bioresidue and sunflower oil on the ability to transfer CLPs into a sunflower oil-based phase.

	CBS-LC CLPs	**CBS-LR CLPs**
Vegetable Oil	Dispersible	Dispersible
Sunflower oil	Dispersible	Dispersible
Treated sunflower oil	Dispersible	X
Mineral oil	X	X
Silicone oil	X	X

As a result of these data, it was concluded that molecular surfactant is critical for dispersibility of CLPs. This is in line with the conclusions of Chapter 6, where the role of the lipid in the dispersal of CLPs was posited.

7.4.2. Effect of surfactant inherent in the CBS-LC CLP system on droplets for segmented GPV analysis

In the final section of this chapter, the impact of surfactant on the segmented flow system is quantified. It has been established that molecular surfactant is required for dispersal of CLPs in a non-aqueous phase. In quantifying the impact of surfactants, both present in the natural oils and the CBS-LC extract itself, the impact of the surfactant can be quantified. Droplets of water in oil were formed using a HFF device, and the time between droplets was assessed relative to a blank system in the absence of dispersed CLPs, Figure 71.

From this data, three conclusions may be drawn. The first conclusion may be drawn by comparison between the normal sunflower and that with molecular surfactants removed (TSO). Between these two systems, given the overlapping error bars, it is suggested that there is a conclusive difference in formation time related to the removal of amphiphiles from the CBS bioresidue, and molecular surfactant from the non-aqueous phase. The second conclusion from this is that in the absence of lipids in either the water or oil phase, the formation time of droplets is increased. This would suggest that given a constant flow rate, the droplets formed are larger. As this is the case in both systems independently of the lipid, this suggests that the CLPs are interacting with the oil and water interface. Previous work in Chapter 6 indicated that the particles do not remain kinetically stabilised at the interface, without a large amount of energy supplied to the system.

In nearly every example, the LR system had the quickest formation time, suggesting that in this instance, the interaction between the CLPs and the interface is greatest. This would offer an indirect corroboration that the lipids co-extracted from CBS are decorating the CLPs, as this would inhibit the migration to the interface of the CBS-LC CLPs, explaining the droplet formation time being closer to that of distilled water.

The third observation is that filtering the system with a 1 μm filter does not affect the droplet formation time. This removes the possibility that larger aggregates are responsible for the surfactancy effect during droplet formation, rather than action from molecular surfactant or CLPs.

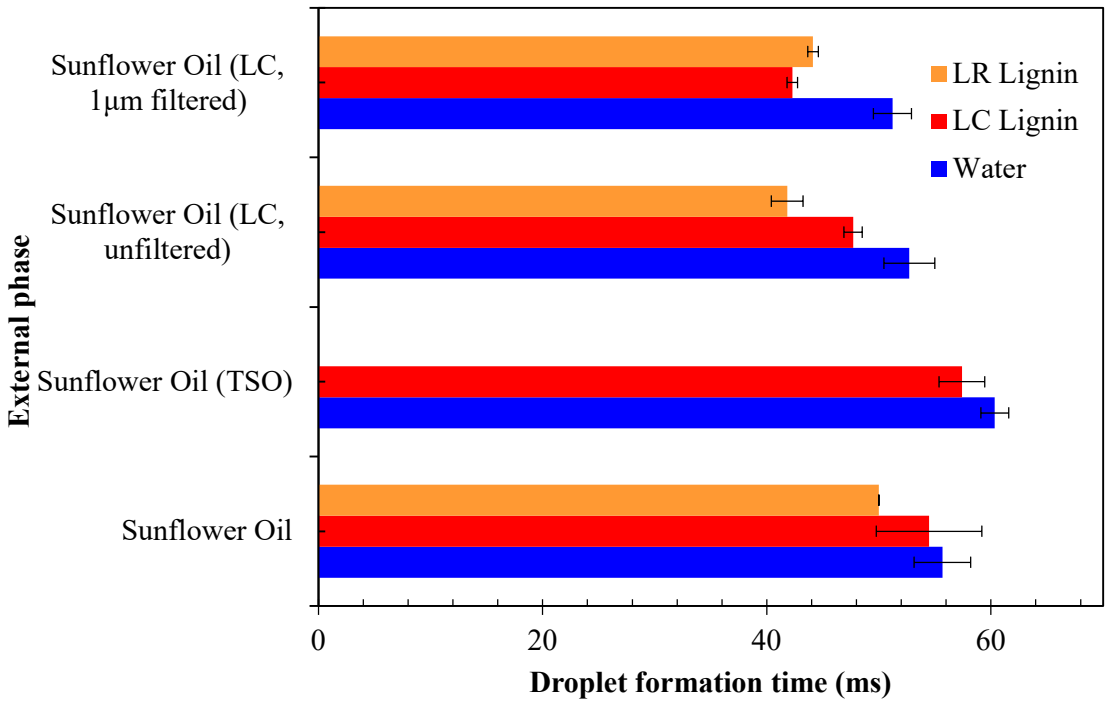


Figure 71: A bar chart demonstrating the formation time of a droplet of water in oil under conditions of 8 µL min^{-1} flow rate of water, and 42 µL min^{-1} flow rate of sunflower oil. Where CLPs are dispersed, they are done so at a concentration of 3.5 mg mL^{-1}. Error bars represent ± 2 standard deviations from the mean.

The implications of having a system containing amphiphiles or surfactant is that the interface could be mobile dependant on the concentration, owing to the presence of surfactant coating it. In addition to the refractive index mismatch described earlier, this is a significant limitation in using this setup to observe phenomena at or near the interface.

The results of this section do however demonstrate suitability for measuring the movement of fluid within a dynamic system. This is significant, particularly for confined flow geometries, which may have unusual circulation patterns. To expand the use of lignin CLPs to other systems, it is necessary to increase the inertness of the system compared to a channel is much greater than the droplet dimensions such as plug flow. For this, an oil with a constant surface tension and CBS-LR CLPs is required.

7.5. Conclusions

In this chapter, an application of lignin-rich colloidal particles as a dispersible particle for imaging fluid flows by GPV was demonstrated. The initial findings of this chapter were that the lignin-rich particles formed in earlier chapters of this research thesis were capable of imaging flow fields both precisely and accurately in a similar fashion to a commercially available equivalent. In addition, it was discovered that the same particles are dispersible in non-aqueous media, with sunflower oil demonstrated as an example. The precision of flow fields generated using CLPs as the dispersed particle are lower than polystyrene, however this was overcome by averaging a greater number of frames to achieve an accurate determination of the flow in a straight channel.

The finding of Chapter 6 that the lignin-rich particles were dispersible in sunflower oil represents a significant result, as scarce examples of non-aqueous dispersible particles exist. This is exploited here to present an application of such dispersed particles in GPV. Typical micro-reactors use a non-aqueous medium to transport aqueous reactants as droplets. The ability to disperse lignin-rich particles as demonstrated in this research chapter offers the potential for further characterisation of the kinetics of such coalescence in real time, and on the system in question. This research offers a significant contribution in both the applicability of lignin-rich particles for tracing applications and represents the first example of lignin valorisation for this application.

The ability to disperse particles in both phases and simultaneously quantify the flow field suggested some novel functionality, to include qualitatively assessing the behaviour of a droplet in its recirculation pattern, and the impact it had on the continuous phase, simultaneously. This is of particular interest in the field of microfluidics, where the recent influx of applications has given rise to microchannels of vastly different geometries.

Examples of another application of this would be heat exchangers, where regime of heat transfer could be evaluated using dispersed colloidal particles. Of particular interest is the ability to utilise the study of dynamic systems using tracer particles in multiphase flows. The application of this is for modelling restricted flow channels for micro-reactors.

The principal drawback of this work at present is that it has not been able to demonstrate either dispersion of particles of quantification of flow fields in the absence of a surfactant. Should this be addressed in future research, it would be possible to quantify flow fields related to many microfluidic processes including drop formation, mixing in the moving drop, coalescence of droplets, and potentially even the kinetics of a coalescence driven reaction inside a micro-reactor.

Further theoretical assessment could be conducted, considering factors such as the shear impacts at the wall, and the 3D profile of the confined channel could be examined by altering the focal plane, however this was assessed to be beyond the scope of this research chapter, which is focused on achieving objective 5 of this thesis. This has been achieved, not only by validation of the system, but by simultaneous imaging of a droplet and continuous phase, and resolution of recirculation within a droplet.

8. Overall conclusions and future work

This research thesis demonstrates the extraction and application of a lignin-rich extract from cocoa bean shell in the form of colloidal particles.

Chapter 3 focused on the characterisation of a crude organosolv extract of cocoa bean shell and introduced new research by the identification and relative quantification of co-extracted molecular amphiphiles and identification of a triglyceride present in the extract. The recovered bioresidue had a significant lignin component (>50%) and was used as a crude extract. The characterisation of this extract fulfilled the first research objective set out in the introduction, of extracting and characterising an extract of cocoa bean shell.

Should future work be undertaken to further characterise the extract, two main routes are proposed. The first route would be to use multiple ionisation mass spectrometry to identify the molecular weight of the extracted lignin. As the molecular weight is too large for normal mass spectrometry, multiple ionisation techniques such as matrix assisted laser desorption and ionisation would allow for characterisation of the molecular weight up to 10,000 Da. In understanding this information, one would be able to more precisely correlate extraction conditions and molecular weight to the observed wetting properties. Conducting this on multiple sources of lignin would further expand the relevance of this research and offer other potential valorisation avenues for co-products of industry, such as wheat straw and others identified in the literature review.

A second extension of the work of Chapter 3 would be to use more advanced spectroscopy to resolve the position of lignin in space more accurately, such as Raman spectroscopy. In identifying the spatial arrangement of the functional groups in these structures, it may be possible to direct functionalisation reactions using basic chemical synthesis methods

and specify the desired functional groups present on the outer shell of the particle. Another avenue which could be taken would be to alter the extraction method. Using an ethanol extraction process has limitations in that co-extractives from the process are soluble in ethanol. This will influence the character of the lignin and resulting particles. Future work on alternative extraction methods would address the limitation in this research, as by extraction methods which can produce co-extractives other than ethanol soluble could offer potential for resulting lignin rich particles to have alternative surface properties. This could offer a route to the specification of the wetting properties of particles as desired. This would allow for another factor to be controlled in generating particles, and the effects of functionalisation would be observable in the form of emulsion stability, in the same way work in Chapter 6 identified wetting properties of the CBS-LC extract.

Chapter 4 focused on the use of hydrodynamic flow-focusing (HFF) devices for continuous preparation of droplets of a lignin-rich extract solubilised in ethanol, for subsequent precipitation against water to generate lignin-rich particles, in pursuit of research objectives 2 and 3. HFF was chosen due to the ability to control the size of droplets formed, thus allowing for generation of particles large enough for direct contact angle measurement. Ultimately, the use of these devices in such a way proved unsuccessful, due to fouling caused by interactions between the PDMS-based device and the componentry of the extract. As modifying the componentry of the extract would be contrary to the motivation of using an inhomogeneous extract for particle production, device modification methods were sought, and modification of the contact angle demonstrated. Nonetheless, fouling was persistent, thus necessitating an alternative method for particle production.

Should further research be undertaken to develop this method, the principal suggestion is that further modification of the HFF device be pursued further, to mitigate the interaction between the dispersed lignin phase and the PDMS. This could be achieved in two ways; by significantly increasing the channel height of the device to form a plug flow, or by altering the construction material. A plug flow would likely remove the interaction between the device and the device edges identified in Chapter 4, owing to the increased distance between a formed droplet and the boundaries.

Chapter 5 evidenced the ability to use flow conditions in a coaxial jet mixing device to aid precipitation of CLPs in a controllable manner from a crude CBS extract offering fulfilment of research objectives 2 and 3.. In this research chapter, the wetting characteristics of the system was investigated, offering evidence that the wetting characteristics can be controlled and influenced by the precipitation process.

By varying volumetric flow conditions of the ethanol solubilised lignin rich extract and water as antisolvent such that the Reynolds number ranged from 30 – 500, it was found that particle dispersions with the average particle diameter between 150 – 600 nm could be produced. In aqueous dispersion, these particles were found to be stable against aggregation for 14 days, irrespective of the presence of the lipid fraction in the extract. This offers a new method for continuous production of colloidal lignin-rich particles from a crude extract of CBS and provides an example of the ability to produce colloidal particle dispersions with specifiable average diameter. Another factor which was demonstrated to affect the particle diameter was the volumetric flow ratio of solvent to antisolvent, termed R. By increasing the R value, the average particle diameter of resulting dispersions generated was increased.

Were further research into this system to be pursued, there are two principal avenues which could extend this research. The first would be to develop another solvent antisolvent pairing for particle production and compare features such as the solvent parameters to the resulting size and stability of resulting particle dispersions. Should another pairing be developed, it would be possible to assess the impact of this on the surface chemistry of the precipitated particles by examining the wetting properties. This research has indicated that the surface properties are dependent on the precipitation conditions, and as such, using an alternative solvent for antisolvent precipitation could develop the research shown in Chapter 5 by altering the surface properties of formed colloidal particles. This approach to designed colloids from a food adjacent resource would offer a large formulation space for using CBS derived lignin as a mimetic for current Picking stabilisers in food systems. This would have significant 'green labelling' potential, where a naturally derived product replaces a less sustainable ingredient.

The second avenue which could be pursued would be to assess the impact of solute concentration on the size of particles produced in dispersion. In this research, a single concentration was pursued, rather than alteration of solute concentration, as the validation of the setup remained the most important goal in pursuit of research objective 2. Adding this as a third variable would likely increase the range of particle diameters achievable and available for formulation.

Chapter 6 focused on expanding the relatability of the lipid fraction identified in chapter 3 to the colloidal particle dispersions formed in chapter 5, to offer fulfilment of research objectives 3 and 4 by assessing the ability to use colloidal lignin rich particles to stabilise emulsions.

Chapter 7 demonstrated an application of the colloidal particle dispersions produced in chapter 5 as a tracer particle, using the wetting parameters identified in Chapter 6. It was found that by specifying a Reynolds number of 500, particles of 150 nm were producible, which was in the same diameter range of colloidal particle dispersions used to generate a diffraction pattern in solution which can be traced by particle imaging techniques to experimentally model flow fields, fulfilling research objective 5 of this thesis. The system was initially validated against the current literature standard in polystyrene particles, and then expanded to include segmented flows, specifically for droplet formation and recirculation in oil and water systems. This is a significant development on current capability of the Ghost Particle Velocimetry technique, which had noted limitations in being able to quantify non-aqueous phases, due to a lack of particles which are dispersible in non-aqueous media. One limitation of the particle system used was the presence of amphiphiles or surfactants being required to maintain dispersibility of the CLPs. As a result, one avenue of research for future work would be to continue the initial work into dispersibility in oils with a constant surface tension, to allow for greater scope of application. One result which shows promise is the use of IPM as a non-aqueous phase. As the CLPs require lipids for transfer from the aqueous to non-aqueous phase, the use of the largest lipid present inherently to the extract of IPM as identified in Chapter 3 offers potential. IPM has a constant surface tension of 24.5 mN m^{-1}. Naturally, there is a limitation in that other molecular surfactants are present in the system which can act at the interface. Attempts to disperse lignin CLPs in synthetic oils such as mineral and silicone oil were proven unsuccessful in Chapter 7.

Another validation of the use of GPV as a technique would be 3D imaging of flow fields, as suggested by literature in 1.7. CLPs derived from CBS-LC and CBS-LR are capable of visualising flow fields in multiphase (oil and water) flows. The work presented in this

thesis focused more strongly on the material properties of the extract, using GPV as an application, and thus all work was conducted in the focal plane of the channel.

Given that there is a large amount of cocoa bean shell present, the feedstock represents a suitable choice for scale up. Industrial scale up oof colloidal particle production can utilise the presence of CBS and as such there are likely to be no issues with scale-up. The major challenges for scale-up would be twofold. One challenge would be the extraction method, which is currently performed at the gram scale. Other methods which are beginning to gain interest such as deep eutectic solvent extraction as identified in the literature review can negate the limitation observed by small-scale extraction identified in this research. The findings such as colloidal particle production and application as ghost particles can be applied to another extraction process, which should allow for scale up to be pursued.

The second scale-up challenge is the precipitation of colloidal particles. Whilst the current process is continuous, which is far easier to increase to scale than a batch process, the process for particle production uses microfluidic processes on the mL per minute scale. One method of scaling the process would be to have many of the microfluidic devices demonstrated in this research thesis in parallel, however this would still be significantly below the kilogram scale.

References

Abdelkarim, M., Abd Ellah, N.H., Elsabahy, M., Abdelgawad, M. and Abouelmagd, S.A. (2021) 'Microchannel geometry vs flow parameters for controlling nanoprecipitation of polymeric nanoparticles', *Colloids and Surfaces A: Physicochemical and Engineering Aspects*, 611, available: http://dx.doi.org/10.1016/j.colsurfa.2020.125774.

Ago, M., Huan, S., Borghei, M., Raula, J., Kauppinen, E.I. and Rojas, O.J. (2016) 'High-Throughput Synthesis of Lignin Particles (approximately 30 nm to approximately 2 mum) via Aerosol Flow Reactor: Size Fractionation and Utilization in Pickering Emulsions', *ACS Appl Mater Interfaces*, 8(35), 23302-10, available: http://dx.doi.org/10.1021/acsami.6b07900.

Ali, H.S., Blagden, N., York, P., Amani, A. and Brook, T. (2009) 'Artificial neural networks modelling the prednisolone nanoprecipitation in microfluidic reactors', *Eur J Pharm Sci*, 37(3-4), 514-22, available: http://dx.doi.org/10.1016/j.ejps.2009.04.007.

Anna, S.L. and Mayer, H.C. (2006) 'Microscale tipstreaming in a microfluidic flow focusing device', *Physics of Fluids*, 18(12), available: http://dx.doi.org/10.1063/1.2397023.

Areej, F., Mohd Ashadie, K., Zakiah, S. and Ainun, Z.M.A. (2023) 'Pulping process for nonwoody plants' in *Pulping and Papermaking of Nonwood Plant Fibers*, 17-32.

Aro, T. and Fatehi, P. (2017) 'Production and Application of Lignosulfonates and Sulfonated Lignin', *ChemSusChem*, 10(9), 1861-1877, available: http://dx.doi.org/10.1002/cssc.201700082.

Aveyard, R., Binks, B.P. and Clint, J.H. (2003) 'Emulsions stabilised solely by colloidal particles', *Advances in Colloid and Interface Science*, 100-102, 503-546, available: http://dx.doi.org/10.1016/s0001-8686(02)00069-6.

Baber, R., Mazzei, L., Thanh, N.T.K. and Gavriilidis, A. (2015) 'Synthesis of silver nanoparticles in a microfluidic coaxial flow reactor', *RSC Advances*, 5(116), 95585-95591, available: http://dx.doi.org/10.1039/c5ra17466j.

Bajwa, D.S., Pourhashem, G., Ullah, A.H. and Bajwa, S.G. (2019) 'A concise review of current lignin production, applications, products and their environmental impact', *Industrial Crops and Products*, 139, available: http://dx.doi.org/10.1016/j.indcrop.2019.111526.

Balentic, J.P., Ackar, D., Jokic, S., Jozinovic, A., Babic, J., Milicevic, B., Subaric, D. and Pavlovic, N. (2018) 'Cocoa Shell: A By-Product with Great Potential for Wide Application', *Molecules*, 23(6), available: http://dx.doi.org/10.3390/molecules23061404.

Bangalore Ashok, R.P., Xiao, Y., Lintinen, K., Oinas, P., Kostiainen, M.A. and Österberg, M. (2020) 'Self-assembly of colloidal lignin particles in a continuous flow tubular reactor', *Colloids and Surfaces A: Physicochemical and Engineering Aspects*, 587, available: http://dx.doi.org/10.1016/j.colsurfa.2019.124228.

Barsberg, S.T., Lee, Y.I. and Rasmussen, H.N. (2018) 'Development of C-lignin with G/S-lignin and lipids in orchid seed coats – an unexpected diversity exposed by ATR-FT-IR spectroscopy', *Seed Science Research*, 28(1), 41-51, available: http://dx.doi.org/10.1017/s0960258517000344.

Bauer, W.A., Fischlechner, M., Abell, C. and Huck, W.T. (2010) 'Hydrophilic PDMS microchannels for high-throughput formation of oil-in-water microdroplets and water-in-oil-in-water double emulsions', *Lab Chip*, 10(14), 1814-9, available: http://dx.doi.org/10.1039/c004046k.

Beisl, S., Miltner, A. and Friedl, A. (2017) 'Lignin from Micro- to Nanosize: Production Methods', *Int J Mol Sci*, 18(6), available: http://dx.doi.org/10.3390/ijms18061244.

Bhamidi, V., Lee, S.H., He, G., Chow, P.S., Tan, R.B.H., Zukoski, C.F. and Kenis, P.J.A. (2015) 'Antisolvent Crystallization and Polymorph Screening of Glycine in Microfluidic Channels Using Hydrodynamic Focusing', *Crystal Growth & Design*, 15(7), 3299-3306, available: http://dx.doi.org/10.1021/acs.cgd.5b00420.

Binks, B.P., Isa, L. and Tyowua, A.T. (2013) 'Direct measurement of contact angles of silica particles in relation to double inversion of pickering emulsions', *Langmuir*, 29(16), 4923-7, available: http://dx.doi.org/10.1021/la4006899.

Binks, B.P. and Lumsdon, S.O. (2000) 'Influence of Particle Wettability on the Type and Stabilityof Surfactant-Free Emulsions', *Langmuir*, 16(23), 8622 - 8631, available: http://dx.doi.org/https://doi.org/10.1021/la000189s.

Boeriu, C.G., Bravo, D., Gosselink, R.J.A. and van Dam, J.E.G. (2004) 'Characterisation of structure-dependent functional properties of lignin with infrared spectroscopy', *Industrial Crops and Products*, 20(2), 205-218, available: http://dx.doi.org/10.1016/j.indcrop.2004.04.022.

Bonham, J.A., Faers, M.A. and van Duijneveldt, J.S. (2014) 'Non-aqueous microgel particles: synthesis, properties and applications', *Soft Matter*, 10(47), 9384-98, available: http://dx.doi.org/10.1039/c4sm01834f.

Bovone, G., Guzzi, E.A. and Tibbitt, M.W. (2019) 'Flow-based reactor design for the continuous production of polymeric nanoparticles', *AIChE Journal*, 65(12), available: http://dx.doi.org/10.1002/aic.16840.

Burrows, A., Holman, J., Parsons, A., Pilling, G. and Price, G. (2013a) *Chemistry³: Introducing inorganic, organic and physical chemistry.*, Oxford University Press.

Burrows, A., Holman, J., Parsons, A., Pilling, G. and Price, G. (2013b) 'Molecular Spectroscopy' in Press, O. U., ed., *Chemistry³*, 2 ed., Oxford: Oxford University Press, 444 - 507.

Buzzaccaro S, Secchi E and R., P. (2013) 'Ghost particle velocimetry: accurate 3D flow visualization using standard lab equipment.', *PHYSICAL REVIEW LETTERS*, 111, available: http://dx.doi.org/10.1103/PhysRevLett.111.048101.

Calvo-Flores, F.G. and Dobado, J.A. (2010) 'Lignin as renewable raw material', *ChemSusChem*, 3(11), 1227-35, available: http://dx.doi.org/10.1002/cssc.201000157.

Cao, L., Yu, I.K.M., Liu, Y., Ruan, X., Tsang, D.C.W., Hunt, A.J., Ok, Y.S., Song, H. and Zhang, S. (2018) 'Lignin valorization for the production of renewable chemicals: State-of-the-art review and future prospects', *Bioresour Technol*, 269, 465-475, available: http://dx.doi.org/10.1016/j.biortech.2018.08.065.

Cayre, O.J. and Paunov, V.N. (2004) 'Contact Angles of Colloid Silica and Gold Particles at Air-Water and Oil-Water Interfaces Determined with the Gel Trapping Technique', *Langmuir*, 20(22), 9594 - 9599, available: http://dx.doi.org/https://doi.org/10.1021/la0489615.

Chakar, F.S. and Ragauskas, A.J. (2004) 'Review of current and future softwood kraft lignin process chemistry', *Industrial Crops and Products*, 20(2), 131-141, available: http://dx.doi.org/10.1016/j.indcrop.2004.04.016.

Chen, X., Li, H., Sun, S., Cao, X. and Sun, R. (2016) 'Effect of hydrothermal pretreatment on the structural changes of alkaline ethanol lignin from wheat straw', *Sci Rep*, 6, 39354, available: http://dx.doi.org/10.1038/srep39354.

Chen, Y., Renner, P. and Liang, H. (2019) 'Dispersion of Nanoparticles in Lubricating Oil: A Critical Review', *Lubricants*, 7(1), available: http://dx.doi.org/10.3390/lubricants7010007.

Chung, B.Y., Iiyama, K. and Han, K.W. (2003) 'Compositional Characterization of Cacao (Theobroma cacao L.) Hull', *Journal of Agricultural Chemistry and Biotechnology*, 46, 12-16.

Collins, D.J., Neild, A., deMello, A., Liu, A.Q. and Ai, Y. (2015) 'The Poisson distribution and beyond: methods for microfluidic droplet production and single cell encapsulation', *Lab Chip*, 15(17), 3439-59, available: http://dx.doi.org/10.1039/c5lc00614g.

Colucci, G., Santamaria-Echart, A., Silva, S.C., Teixeira, L.G., Ribeiro, A., Rodrigues, A.E. and Barreiro, M.F. (2023) 'Development of colloidal lignin particles through particle design strategies and screening of their Pickering stabilizing potential', *Colloids and Surfaces A: Physicochemical and Engineering Aspects*, 666, available: http://dx.doi.org/10.1016/j.colsurfa.2023.131287.

Cramer, C., Fischer, P. and Windhab, E.J. (2004) 'Drop formation in a co-flowing ambient fluid', *Chemical Engineering Science*, 59(15), 3045-3058, available: http://dx.doi.org/10.1016/j.ces.2004.04.006.

Cubaud, T. and Mason, T.G. (2008) 'Capillary threads and viscous droplets in square microchannels', *Physics of Fluids*, 20(5), available: http://dx.doi.org/10.1063/1.2911716.

Cuthill, H., Elleman, C., Curwen, T. and Wolf, B. (2021) 'Colloidal Particles for Pickering Emulsion Stabilization Prepared via Antisolvent Precipitation of Lignin-Rich Cocoa Shell Extract', *Foods*, 10(2), available: http://dx.doi.org/10.3390/foods10020371.

Czaikoski, A., Gomes, A., Kaufmann, K.C., Liszbinski, R.B., de Jesus, M.B. and Cunha, R.L.d. (2020) 'Lignin derivatives stabilizing oil-in-water emulsions: Technological aspects, interfacial rheology and cytotoxicity', *Industrial Crops and Products*, 154, available: http://dx.doi.org/10.1016/j.indcrop.2020.112762.

Daud, Z., Mohd Kassim, A.S., Mohd Aripin, A., Awang, H. and Hatta, M.Z.M. (2013) 'Chemical Composition and Morphological of Cocoa Pod Husks and Cassava Peels for Pulp and Paper Production', *Australian Journal of Basic and Applied Sciences*, 7(9), 406-411.

Derkacheva, O. and Sukhov, D. (2008) 'Investigation of Lignins by FTIR Spectroscopy', *Macromolecular Symposia*, 265(1), 61-68, available: http://dx.doi.org/10.1002/masy.200850507.

Deshpande, R., Sundvall, L., Grundberg, H., Henriksson, G. and Lawoko, M. (2022) 'Structural basis for lignin recalcitrance during sulfite pulping for production of

dissolving pulp from pine heartwood', *Industrial Crops and Products*, 177, available: http://dx.doi.org/10.1016/j.indcrop.2021.114391.

Destribats, M., Gineste, S., Laurichesse, E., Tanner, H., Leal-Calderon, F., Heroguez, V. and Schmitt, V. (2014) 'Pickering emulsions: what are the main parameters determining the emulsion type and interfacial properties?', *Langmuir*, 30(31), 9313-26, available: http://dx.doi.org/10.1021/la501299u.

Farooq, M., Zou, T., Valle-Delgado, J.J., Sipponen, M.H., Morits, M. and Osterberg, M. (2020) 'Well-Defined Lignin Model Films from Colloidal Lignin Particles', *Langmuir*, 36(51), 15592-15602, available: http://dx.doi.org/10.1021/acs.langmuir.0c02970.

Fink, S. (1992) 'Transparent Wood – A New Approach in the Functional Study of Wood Structure', *Holzforschung*, 46(5), 403-408, available: http://dx.doi.org/10.1515/hfsg.1992.46.5.403.

Fukushima, R.S. and Kerley, M.S. (2011) 'Use of lignin extracted from different plant sources as standards in the spectrophotometric acetyl bromide lignin method', *J Agric Food Chem*, 59(8), 3505-9, available: http://dx.doi.org/10.1021/jf104826n.

Fukushima, R.S., Kerley, M.S., Ramos, M.H., Porter, J.H. and Kallenbach, R.L. (2015) 'Comparison of acetyl bromide lignin with acid detergent lignin and Klason lignin and correlation with in vitro forage degradability', *Animal Feed Science and Technology*, 201, 25-37, available: http://dx.doi.org/10.1016/j.anifeedsci.2014.12.007.

Gerbin, E., Riviere, G.N., Foulon, L., Frapart, Y.M., Cottyn, B., Pernes, M., Marcuello, C., Godon, B., Gainvors-Claisse, A., Cronier, D., Majira, A., Osterberg, M., Kurek, B., Baumberger, S. and Aguie-Beghin, V. (2021) 'Tuning the functional properties of lignocellulosic films by controlling the molecular and supramolecular structure of lignin', *Int J Biol Macromol*, 181, 136-149, available: http://dx.doi.org/10.1016/j.ijbiomac.2021.03.081.

Gordobil, O., Delucis, R., Egüés, I. and Labidi, J. (2015) 'Kraft lignin as filler in PLA to improve ductility and thermal properties', *Industrial Crops and Products*, 72, 46-53, available: http://dx.doi.org/10.1016/j.indcrop.2015.01.055.

Gould, J., Garcia-Garcia, G. and Wolf, B. (2016) 'Pickering Particles Prepared from Food Waste', *Materials (Basel)*, 9(9), available: http://dx.doi.org/10.3390/ma9090791.

Greco, L., Ullo, S., Rigano, L., Fontana, M. and Berardesca, E. (2019) 'Evaluation of the Soothing and Protective Properties of a Lignin Hydrolyzate', *Cosmetics*, 6(3), available: http://dx.doi.org/10.3390/cosmetics6030038.

Gupta, B.S., Jelle, B.P. and Gao, T. (2015) 'Application of ATR-FTIR Spectroscopy to Compare the Cell Materials of Wood Decay Fungi with Wood Mould Fungi', *International Journal of Spectroscopy*, 2015, 1-7, available: http://dx.doi.org/10.1155/2015/521938.

Haynes, W.M. (2011) 'Analytical Chemistry' in Lide, D. R., ed., *CRC Handbook of Chemistry and Physics*, 1 ed., Boca Raton: Taylor & Francis Group.

Henn, K.A., Forsman, N., Zou, T. and Österberg, M. (2021) 'Colloidal Lignin Particles and Epoxies for Bio-Based, Durable, and Multiresistant Nanostructured Coatings', *ACS Applied Materials & Interfaces*, 13(29), 34793-34806, available: http://dx.doi.org/10.1021/acsami.1c06087.

Holladay, J.E., Bozell, J.J., White, J.F. and Johnson, D. (2007) *Results of Screening for Potential Candidates from Biorefinery Lignin*, 1, U.S. Department of Energy: Pacific Northwest National Laboratory, University of Tennessee, National Renewable Energy Laboratory.

Holloway, W.D., Tasman-Jones, C. and Lee, S.P. (1978) 'Digestion of certain fractions of dietary fiber in humans', *Am J Clin Nutr*, 31(6), 927-30, available: http://dx.doi.org/10.1093/ajcn/31.6.927.

Huijgen, W.J.J., Smit, A.T., de Wild, P.J. and den Uil, H. (2012) 'Fractionation of wheat straw by prehydrolysis, organosolv delignification and enzymatic hydrolysis for production of sugars and lignin', *Biosource Technology*, (114), 389-398, available: http://dx.doi.org/10.1016/j.biortech.2012.02.143.

Jiang, Z., Ma, Y., Guo, X., Remon, J., Tsang, D.C.W., Hu, C. and Shi, B. (2021) 'Sustainable production of lignin micro-/nano-particles (LMNPs) from biomass: Influence of the type of biomass on their self-assembly capability and physicochemical properties', *J Hazard Mater*, 403, 123701, available: http://dx.doi.org/10.1016/j.jhazmat.2020.123701.

Ju, T., Zhang, Z., Li, Y., Miao, X. and Ji, J. (2019) 'Continuous production of lignin nanoparticles using a microchannel reactor and its application in UV-shielding films', *RSC Advances*, 9(43), 24915-24921, available: http://dx.doi.org/10.1039/c9ra05064g.

Kai, D., Tan, M.J., Chee, P.L., Chua, Y.K., Yap, Y.L. and Loh, X.J. (2016) 'Towards lignin-based functional materials in a sustainable world', *Green Chemistry*, 18(5), 1175-1200, available: http://dx.doi.org/10.1039/c5gc02616d.

Karnik, R., Gu, F., Basto, P., Cannizzaro, C., Dean, L., Kyei-Manu, W., Langer, R. and Farokhzad, O.C. (2008) 'Microfluidic Platform for Controlled Synthesis of Polymeric Nanoparticles', *Nano Letters*, 8, 2906-2912.

Kim, Y., Lee Chung, B., Ma, M., Mulder, W.J., Fayad, Z.A., Farokhzad, O.C. and Langer, R. (2012) 'Mass production and size control of lipid-polymer hybrid nanoparticles through controlled microvortices', *Nano Lett*, 12(7), 3587-91, available: http://dx.doi.org/10.1021/nl301253v.

Kiratzis, I., Kovalchuk, N.M., Simmons, M.J.H. and Vigolo, D. (2022) 'Effect of surfactant addition and viscosity of the continuous phase on flow fields and kinetics of drop formation in a flow-focusing microfluidic device', *Chemical Engineering Science*, 248, available: http://dx.doi.org/10.1016/j.ces.2021.117183.

Knight, J.B., Vishwanath, A., Brody, J.P. and Austin, R.H. (1998) 'Hydrodynamic Focusing on a Silicon Chip: Mixing Nanoliters in Microseconds', *PHYSICAL REVIEW LETTERS*, 80(17), 3863-3866.

Knill, C.J. and Kennedy, J.F. (1999) 'Surfaces, G. Attard & C. Barnes, Oxford Chemistry Primer 59. Oxford University Press, Oxford, 1998, 96 pp., ISBN 0-19-855686-1', *Bioseparation*, 8(6), 340-340, available: http://dx.doi.org/10.1023/A:1008154326666.

Kovalchuk, N.M., Chowdhury, J., Schofield, Z., Vigolo, D. and Simmons, M.J.H. (2018) 'Study of drop coalescence and mixing in microchannel using Ghost Particle Velocimetry', *Chemical Engineering Research and Design*, 132, 881-889, available: http://dx.doi.org/10.1016/j.cherd.2018.01.034.

Kovalchuk, N.M. and Simmons, M.J.H. (2021) 'Effect of Surfactant Dynamics on Flow Patterns Inside Drops Moving in Rectangular Microfluidic Channels', *Colloids and Interfaces*, 5(3), available: http://dx.doi.org/10.3390/colloids5030040.

Kovalchuk, N.M. and Simmons, M.J.H. (2023) 'Review of the role of surfactant dynamics in drop microfluidics', *Adv Colloid Interface Sci*, 312, 102844, available: http://dx.doi.org/10.1016/j.cis.2023.102844.

Kubo, S. and Kadla, J. (2005) 'Hydrogen Bonding in Lignin: A Fourier Transform Infrared Model Compound Study', *Biomacromolecules*, 6, 2815-2821.

Kumar, A. and Dixit, C.K. (2017) 'Methods for characterization of nanoparticles' in *Advances in Nanomedicine for the Delivery of Therapeutic Nucleic Acids*, 43-58.

Lan, M., Song, Y., Ou, S., Zheng, J., Huang, C., Wang, Y., Zhou, H., Hu, W. and Liu, F. (2020) 'Water-in-Oil Pickering Emulsions Stabilized Solely by Water-Dispersible Phytosterol Particles', *Langmuir*, 36(49), 14991-14998, available: http://dx.doi.org/10.1021/acs.langmuir.0c02301.

Lee, I., Yoo, Y., Cheng, Z. and Jeong, H.-K. (2008a) 'Generation of Monodisperse Mesoporous Silica Microspheres with Controllable Size and Surface Morphology in a Microfluidic Device', *Advanced Functional Materials*, 18, 4014-4021, available: http://dx.doi.org/10.1002/adfm.200801093.

Lee, I., Yoo, Y., Cheng, Z. and Jeong, H.-K. (2008b) 'Generation of Monodisperse Mesoporous Silica Microspheres with Controllable Size and Surface Morphology in a Microfluidic Device', *Advanced Functional Materials*, 18(24), 4014-4021, available: http://dx.doi.org/10.1002/adfm.200801093.

Lee, J.N., Park, C. and Whitesides, G.M. (2003) 'Solvent Compatibility of Poly(dimethylsiloxane)-Based Microfluidic Devices', *Analytical Chemistry*, 75(23), 6544 - 6554, available: http://dx.doi.org/10.1021/ac0346712.

Leskinen, T., Witos, J., Valle-Delgado, J.J., Lintinen, K., Kostiainen, M., Wiedmer, S.K., Osterberg, M. and Mattinen, M.L. (2017) 'Adsorption of Proteins on Colloidal Lignin Particles for Advanced Biomaterials', *Biomacromolecules*, 18(9), 2767-2776, available: http://dx.doi.org/10.1021/acs.biomac.7b00676.

Li, S., Zhou, S. and Zhao, G. (2021) 'Tuning the morphology of micro- and nano-spheres from bamboo shoot shell acetosolv lignin', *Industrial Crops and Products*, 171, available: http://dx.doi.org/10.1016/j.indcrop.2021.113860.

Lievonen, M., Valle-Delgado, J.J., Mattinen, M.-L., Hult, E.-L., Lintinen, K., Kostiainen, M.A., Paananen, A., Szilvay, G.R., Setälä, H. and Österberg, M. (2016) 'A simple process for lignin nanoparticle preparation', *Green Chemistry*, 18(5), 1416-1422, available: http://dx.doi.org/10.1039/c5gc01436k.

Lim, J.-M., Swami, A., Gilson, L.M., Chopra, S., Choi, S., Wu, J., Langer, R., Karnik, R. and Farokhzad, O.C. (2014) 'Ultra-High Throughput Synthesis of Nanoparticles with Homogeneous Size Distribution Using a Coaxial Turbulent Jet Mixer', *ACS Nano*, 8(6), 6056-6065, available: http://dx.doi.org/10.1021/nn501371n.

Lintinen, K., Xiao, Y., Bangalore Ashok, R., Leskinen, T., Sakarinen, E., Sipponen, M., Muhammad, F., Oinas, P., Österberg, M. and Kostiainen, M. (2018) 'Closed cycle production of concentrated and dry redispersible colloidal lignin particles with a three solvent polarity exchange method', *Green Chemistry*, 20(4), 843-850, available: http://dx.doi.org/10.1039/c7gc03465b.

Lorenz, T., Bojko, S., Bunjes, H. and Dietzel, A. (2018) 'An inert 3D emulsification device for individual precipitation and concentration of amorphous drug nanoparticles', *Lab Chip*, 18(4), 627-638, available: http://dx.doi.org/10.1039/c7lc01313b.

Lourençon, T.V., Hansel, F.A., da Silva, T.A., Ramos, L.P., de Muniz, G.I.B. and Magalhães, W.L.E. (2015) 'Hardwood and softwood kraft lignins fractionation by simple sequential acid precipitation', *Separation and Purification Technology*, 154, 82-88, available: http://dx.doi.org/10.1016/j.seppur.2015.09.015.

Lu, X., Zhang, Y., Chen, J., Zhang, D., Dong, C., Zhiqiang, P. and Xia, T. (2021) 'Preparation of tailored lignin nanospheres with specific size and tunable structure by self-assembly of lignin from corn straw', *Industrial Crops and Products*, 172, available: http://dx.doi.org/10.1016/j.indcrop.2021.113993.

Lu, Y., Lu, Y.-C., Hu, H.-Q., Xie, F.-J., Wei, X.-Y. and Fan, X. (2017) 'Structural Characterization of Lignin and Its Degradation Products with Spectroscopic Methods', *Journal of Spectroscopy*, 2017, 1-15, available: http://dx.doi.org/10.1155/2017/8951658.

Luo, H. and Abu-Omar, M.M. (2017) 'Chemicals From Lignin' in *Encyclopedia of Sustainable Technologies*, 573-585.

Lynch, K.M., Steffen, E.J. and Arendt, E.K. (2016) 'Brewers' spent grain: a review with an emphasis on food and health', *Journal of the Institute of Brewing*, 122(4), 553-568, available: http://dx.doi.org/10.1002/jib.363.

Mahmood, N., Yuan, Z., Schmidt, J. and Xu, C. (2016) 'Depolymerization of lignins and their applications for the preparation of polyols and rigid polyurethane foams: A review', *Renewable and Sustainable Energy Reviews*, 60, 317-329, available: http://dx.doi.org/10.1016/j.rser.2016.01.037.

Mao, Y., Gerrow, A., Ray, E., Perez, N.D., Edler, K., Wolf, B. and Binner, E. (2023) 'Lignin recovery from cocoa bean shell using microwave-assisted extraction and deep eutectic solvents', *Bioresource Technology*, 372, available: http://dx.doi.org/10.1016/j.biortech.2023.128680.

Martinez, A.T., Almendros, G., Gonzalez-Vila, F.J. and Frund, R. (1999) 'Solid-state spectroscopic analysis of lignins from several Austral hardwoods', *Solid State Nuclear Magnetic Resonance*, 15, 41-48.

McClements, D.J. (2005) 'Interfacial properties and their characterization' in McClements, D. J., ed., *Food Emulsions: Principles, Practices, and Techniques*, 2 ed., Boca Raton: CRC Press, 175-230.

Meindl, A., Petutschnigg, A. and Schnabel, T. (2022) 'Microwave-Assisted Lignin Extraction-Utilizing Deep Eutectic Solvents to Their Full Potential', *Polymers (Basel)*, 14(20), available: http://dx.doi.org/10.3390/polym14204319.

Mensah, M.B., Jumpah, H., Boadi, N.O. and Awudza, J.A.M. (2021) 'Assessment of quantities and composition of corn stover in Ghana and their conversion into bioethanol', *Scientific African*, 12, available: http://dx.doi.org/10.1016/j.sciaf.2021.e00731.

Merklein, K., Fong, S.S. and Deng, Y. (2016) 'Biomass Utilization' in *Biotechnology for Biofuel Production and Optimization*, 291-324.

Moreira-Vilar, F.C., Siqueira-Soares Rde, C., Finger-Teixeira, A., de Oliveira, D.M., Ferro, A.P., da Rocha, G.J., Ferrarese Mde, L., dos Santos, W.D. and Ferrarese-Filho, O. (2014) 'The acetyl bromide method is faster, simpler and presents best recovery of lignin in different herbaceous tissues than Klason and thioglycolic acid methods', *PLoS One*, 9(10), e110000, available: http://dx.doi.org/10.1371/journal.pone.0110000.

Nada, A.-A.M.A., Yousef, M.A., Shaffei, K.A. and Salah, A.M. (1998) 'Infrared spectroscopy of some treated lignins', *Polymer Degradation and Stability*, 62, 157-163.

Odetade, D.F. and Vladisavljevic, G.T. (2016) 'Microfluidic Fabrication of Hydrocortisone Nanocrystals Coated with Polymeric Stabilisers', *Micromachines (Basel)*, 7(12), available: http://dx.doi.org/10.3390/mi7120236.

Pan, X., Gilkes, N., Kadla, J., Pye, K., Saka, S., Gregg, D., Ehara, K., Xie, D., Lam, D. and Saddler, J. (2006) 'Bioconversion of hybrid poplar to ethanol and co-products using an organosolv fractionation process: optimization of process yields', *Biotechnol Bioeng*, 94(5), 851-61, available: http://dx.doi.org/10.1002/bit.20905.

Peito, S., Peixoto, D., Ferreira-Faria, I., Margarida Martins, A., Margarida Ribeiro, H., Veiga, F., Marto, J. and Claudia Paiva-Santos, A. (2022) 'Nano- and microparticle-stabilized Pickering emulsions designed for topical therapeutics and cosmetic applications', *Int J Pharm*, 615, 121455, available: http://dx.doi.org/10.1016/j.ijpharm.2022.121455.

Peltre, C., Gregorich, E.G., Bruun, S., Jensen, L.S. and Magid, J. (2017) 'Repeated application of organic waste affects soil organic matter composition: Evidence from thermal analysis, FTIR-PAS, amino sugars and lignin biomarkers', *Soil Biology and Biochemistry*, 104, 117-127, available: http://dx.doi.org/10.1016/j.soilbio.2016.10.016.

Pichot, R., Spyropoulos, F. and Norton, I.T. (2012) 'Competitive adsorption of surfactants and hydrophilic silica particles at the oil-water interface: interfacial tension and contact angle studies', *J Colloid Interface Sci*, 377(1), 396-405, available: http://dx.doi.org/10.1016/j.jcis.2012.01.065.

Qian, Y., Qiu, X. and Zhu, S. (2015) 'Lignin: a nature-inspired sun blocker for broad-spectrum sunscreens', *Green Chemistry*, 17(1), 320-324, available: http://dx.doi.org/10.1039/c4gc01333f.

Rayner, M., Marku, D., Eriksson, M., Sjöö, M., Dejmek, P. and Wahlgren, M. (2014) 'Biomass-based particles for the formulation of Pickering type emulsions in food and topical applications', *Colloids and Surfaces A: Physicochemical and Engineering Aspects*, 458, 48-62, available: http://dx.doi.org/10.1016/j.colsurfa.2014.03.053.

Riccomi, M., Alberini, F., Brunazzi, E. and Vigolo, D. (2018) 'Ghost Particle Velocimetry as an alternative to μPIV for micro/milli-fluidic devices', *Chemical Engineering Research and Design*, 133, 183-194, available: http://dx.doi.org/10.1016/j.cherd.2018.03.005.

Roessner, U., Nahid, A., Chapman, B., Hunter, A. and Bellgard, M. (2011) '1.33 - Metabolomics – The Combination of Analytical Biochemistry, Biology, and Informatics' in Moo-Young, M., ed., *Comprehensive Biotechnology (Second Edition)*, Burlington: Academic Press, 447-459.

Saad, W.S. and Prud'homme, R.K. (2016) 'Principles of nanoparticle formation by flash nanoprecipitation', *Nano Today*, 11(2), 212-227, available: http://dx.doi.org/10.1016/j.nantod.2016.04.006.

Sathawong, S., Sridach, W. and Techato, K.-a. (2018) 'Lignin: Isolation and preparing the lignin based hydrogel', *Journal of Environmental Chemical Engineering*, 6(5), 5879-5888, available: http://dx.doi.org/10.1016/j.jece.2018.05.008.

Schneider, C.A., Rasband, W.S. and Eliceiri, K.W. (2012) 'NIH Image to ImageJ: 25 years of image analysis', *Nature Methods*, 9(7), 671-675, available: http://dx.doi.org/10.1038/nmeth.2089.

Schneider, W.D.H., Dillon, A.J.P. and Camassola, M. (2021) 'Lignin nanoparticles enter the scene: A promising versatile green tool for multiple applications', *Biotechnol Adv*, 47, 107685, available: http://dx.doi.org/10.1016/j.biotechadv.2020.107685.

Sekeri, S.H., Ibrahim, M.N.M., Umar, K., Yaqoob, A.A., Azmi, M.N., Hussin, M.H., Othman, M.B.H. and Malik, M. (2020) 'Preparation and characterization of nanosized lignin from oil palm (Elaeis guineensis) biomass as a novel emulsifying

agent', *Int J Biol Macromol*, 164, 3114-3124, available: http://dx.doi.org/10.1016/j.ijbiomac.2020.08.181.

Sharma, R.K., Hajaligol, M.R., Martoglio Smith, P.A., Wooten, J.B. and Baliga, V. (2000) 'Characterization of Char from Pyrolysis of Chlorogenic Acid', *Energy & Fuels*, 14, 1083-1093.

Shen, Q., Zhang, T. and Zhu, M.-F. (2008) 'A comparison of the surface properties of lignin and sulfonated lignins by FTIR spectroscopy and wicking technique', *Colloids and Surfaces A: Physicochemical and Engineering Aspects*, 320(1-3), 57-60, available: http://dx.doi.org/10.1016/j.colsurfa.2008.01.012.

Siddiqui, L., Bag, J., Seetha, Mittal, D., Leekha, A., Mishra, H., Mishra, M., Verma, A.K., Mishra, P.K., Ekielski, A., Iqbal, Z. and Talegaonkar, S. (2020) 'Assessing the potential of lignin nanoparticles as drug carrier: Synthesis, cytotoxicity and genotoxicity studies', *Int J Biol Macromol*, 152, 786-802, available: http://dx.doi.org/10.1016/j.ijbiomac.2020.02.311.

Sipponen, M.H., Smyth, M., Leskinen, T., Johansson, L.-S. and Österberg, M. (2017) 'All-lignin approach to prepare cationic colloidal lignin particles: stabilization of durable Pickering emulsions', *Green Chemistry*, 19(24), 5831-5840, available: http://dx.doi.org/10.1039/c7gc02900d.

Smith, B.C. (2011) *Fundamentals of Fourier Transform Infrared Spectroscopy*, 2 ed., Boca Raton: Taylor and Francis Group.

Soares, T.F. and Oliveira, M. (2022) 'Cocoa By-Products: Characterization of Bioactive Compounds and Beneficial Health Effects', *Molecules*, 27(5), available: http://dx.doi.org/10.3390/molecules27051625.

Spyropoulos, F., Duffus, L.J., Smith, P. and Norton, I.T. (2019) 'Impact of Pickering Intervention on the Stability of W1/O/W2 Double Emulsions of Relevance to Foods', *Langmuir*, 35(47), 15137-15150, available: http://dx.doi.org/10.1021/acs.langmuir.9b01995.

Spyropoulos, F., Lazidis, A. and Norton, I. (2019) *Handbook of Food Structure Development*, The Royal Society of Chemistry.

Stanisz, M., Smułek, W., Popielski, K., Klapiszewski, Ł., Kaczorek, E. and Jesionowski, T. (2021) 'Sustainable design of lignin-based spherical particles with the use of green surfactants and its application as sorbents in wastewater treatment', *Chemical Engineering Research and Design*, 172, 34-42, available: http://dx.doi.org/10.1016/j.cherd.2021.05.028.

Stewart, H., Golding, M., Matia-Merino, L., Archer, R. and Davies, C. (2014) 'Manufacture of lignin microparticles by anti-solvent precipitation: Effect of preparation temperature and presence of sodium dodecyl sulfate', *Food Research International*, 66, 93-99, available: http://dx.doi.org/10.1016/j.foodres.2014.08.046.

Stewart, H., Golding, M., Matia-Merino, L., Archer, R. and Davies, C. (2016) 'Surfactant stabilisation of colloidal lignin microparticulates produced through a solvent attrition process', *Colloids and Surfaces A: Physicochemical and Engineering Aspects*, 498, 194-205, available: http://dx.doi.org/10.1016/j.colsurfa.2016.03.001.

Suhas, Carrott, P.J. and Ribeiro Carrott, M.M. (2007) 'Lignin--from natural adsorbent to activated carbon: a review', *Bioresour Technol*, 98(12), 2301-12, available: http://dx.doi.org/10.1016/j.biortech.2006.08.008.

Sun, X.F., Sun, R., Fowler, P. and Baird, M.S. (2005) 'Extraction and Characterization of Original Lignin and Hemicelluloses from Wheat Straw', *Journal of Agricultural Food Chemistry*, (53), 860-870, available: http://dx.doi.org/10.1021/jf040456q.

Taylor, P. (1998) 'Ostwald ripening in emulsions', *Advances in Colloid and Interface Science*, 75, 107-163.

Tayyib, S. (2022) *Crops and livestock products*, Online database from: http://www.fao.org/faostat/en/#data/qc.: United Nations.

Thielicke, W. and Stamhuis, E.J. (2014) 'PIVlab – Towards User-friendly, Affordable and Accurate Digital Particle Image Velocimetry in MATLAB', *Journal of Open Research Software*, 2, available: http://dx.doi.org/10.5334/jors.bl.

Tian, J., Chen, J., Guo, J., Zhu, W., Khan, M.R., Fu, Q., Jin, Y., Xiao, H., Song, J. and Rojas, O.J. (2023) 'Pickering emulsions produced with kraft lignin colloids destabilized by in situ pH shift: Effect of emulsification energy input and stabilization mechanism', *Colloids and Surfaces A: Physicochemical and Engineering Aspects*, 670, available: http://dx.doi.org/10.1016/j.colsurfa.2023.131503.

Tortora, M., Cavalieri, F., Mosesso, P., Ciaffardini, F., Melone, F. and Crestini, C. (2014) 'Ultrasound driven assembly of lignin into microcapsules for storage and delivery of hydrophobic molecules', *Biomacromolecules*, 15(5), 1634-43, available: http://dx.doi.org/10.1021/bm500015j.

Tran, M.H., Phan, D.-P. and Lee, E.Y. (2021) 'Review on lignin modifications toward natural UV protection ingredient for lignin-based sunscreens', *Green Chemistry*, 23(13), 4633-4646, available: http://dx.doi.org/10.1039/d1gc01139a.

Trantidou, T., Elani, Y., Parsons, E. and Ces, O. (2017) 'Hydrophilic surface modification of PDMS for droplet microfluidics using a simple, quick, and robust method via PVA deposition', *Microsyst Nanoeng*, 3, 16091, available: http://dx.doi.org/10.1038/micronano.2016.91.

Vanholme, R., Morreel, K., Ralph, J. and Boerjan, W. (2008) 'Lignin engineering', *Curr Opin Plant Biol*, 11(3), 278-85, available: http://dx.doi.org/10.1016/j.pbi.2008.03.005.

Vázquez, G., Alvarez, E. and Navaza, J.M. (1995) 'Surface Tension of Alcohol + Water from 20 to 50 °C', *Journal of Chemical Engineering Data*, 40, 611-614.

Villermaux, E. and Rehab, H. (2000) 'Mixing in coaxial jets', *Journal of Fluid Mechanics*, 425, 161-185, available: http://dx.doi.org/10.1017/s002211200000210x.

Wang, J.-X., Zhang, Q.-X., Zhou, Y., Shao, L. and Chen, J.-F. (2010) 'Microfluidic synthesis of amorphous cefuroxime axetil nanoparticles with size-dependent and enhanced dissolution rate', *Chemical Engineering Journal*, 162(2), 844-851, available: http://dx.doi.org/10.1016/j.cej.2010.06.022.

Wang, N. and Lim, L.T. (2012) 'Fourier transform infrared and physicochemical analyses of roasted coffee', *J Agric Food Chem*, 60(21), 5446-53, available: http://dx.doi.org/10.1021/jf300348e.

Whitesides, G.M. (2006) 'The origins and the future of microfluidics', *Nature*, 442(7101), 368-73, available: http://dx.doi.org/10.1038/nature05058.

Wypych, A. (2018) *Databook of Adhesion Promoters*, 1 ed., ChemTec Publishing.

Xiao, M., Xu, A., Zhang, T. and Hong, L. (2018) 'Tailoring the Wettability of Colloidal Particles for Pickering Emulsions via Surface Modification and Roughness', *Front Chem*, 6, 225, available: http://dx.doi.org/10.3389/fchem.2018.00225.

Yaqoob, A.A., Sekeri, S.H., Othman, M.B.H., Ibrahim, M.N.M. and Feizi, Z.H. (2021) 'Thermal degradation and kinetics stability studies of oil palm (Elaeis Guineensis) biomass-derived lignin nanoparticle and its application as an emulsifying agent', *Arabian Journal of Chemistry*, 14(6), available: http://dx.doi.org/10.1016/j.arabjc.2021.103182.

You, T. and Xu, F. (2016) 'Applications of Molecular Spectroscopic Methods to the Elucidation of Lignin Structure' in *Applications of Molecular Spectroscopy to Current Research in the Chemical and Biological Sciences*.

Yuliestyan, A., Partal, P., Navarro, F.J., Martin-Sampedro, R., Ibarra, D. and Eugenio, M.E. (2022) 'Emulsion Stabilization by Cationic Lignin Surfactants Derived from Bioethanol Production and Kraft Pulping Processes', *Polymers (Basel)*, 14(14), available: http://dx.doi.org/10.3390/polym14142879.

Zhang, L., Larsson, A., Moldin, A. and Edlund, U. (2022) 'Comparison of lignin distribution, structure, and morphology in wheat straw and wood', *Industrial Crops and Products*, 187, available: http://dx.doi.org/10.1016/j.indcrop.2022.115432.

Zhang, Q.-X., Xu, L.-M., Zhou, Y., Wang, J.-X. and Chen, J.-F. (2011) 'Preparation of Drug Nanoparticles Using a T-Junction Microchannel System', *Industrial & Engineering Chemistry Research*, 50(24), 13805-13812, available: http://dx.doi.org/10.1021/ie201291r.

Zhang, Y., Ni, S., Wang, X., Zhang, W., Lagerquist, L., Qin, M., Willför, S., Xu, C. and Fatehi, P. (2019) 'Ultrafast adsorption of heavy metal ions onto functionalized lignin-based hybrid magnetic nanoparticles', *Chemical Engineering Journal*, 372, 82-91, available: http://dx.doi.org/10.1016/j.cej.2019.04.111.

Zhu, W. and Theliander, H. (2015) 'Precipitation of Lignin from Softwood Black Liquor: An Investigation of the Equilibrium and Molecular Properties of Lignin', *Bio Resources*, 10(1), 1696-1714.

Zou, T., Nonappa, N., Khavani, M., Vuorte, M., Penttila, P., Zitting, A., Valle-Delgado, J.J., Elert, A.M., Silbernagl, D., Balakshin, M., Sammalkorpi, M. and Osterberg, M. (2021) 'Experimental and Simulation Study of the Solvent Effects on the Intrinsic Properties of Spherical Lignin Nanoparticles', *J Phys Chem B*, 125(44), 12315-12328, available: http://dx.doi.org/10.1021/acs.jpcb.1c05319.

Appendix A – Statistical analysis of particle dispersions

As identified in section 5.1.2, there was an overlap in the distributions of two independently assembled CJM devices. To further assess the similarity, the intensity of particle distributions was correlated to assess statistical similarity,

Figure 73. A gradient of y = 1.10 x was observed, and R^2 value of 0.99.

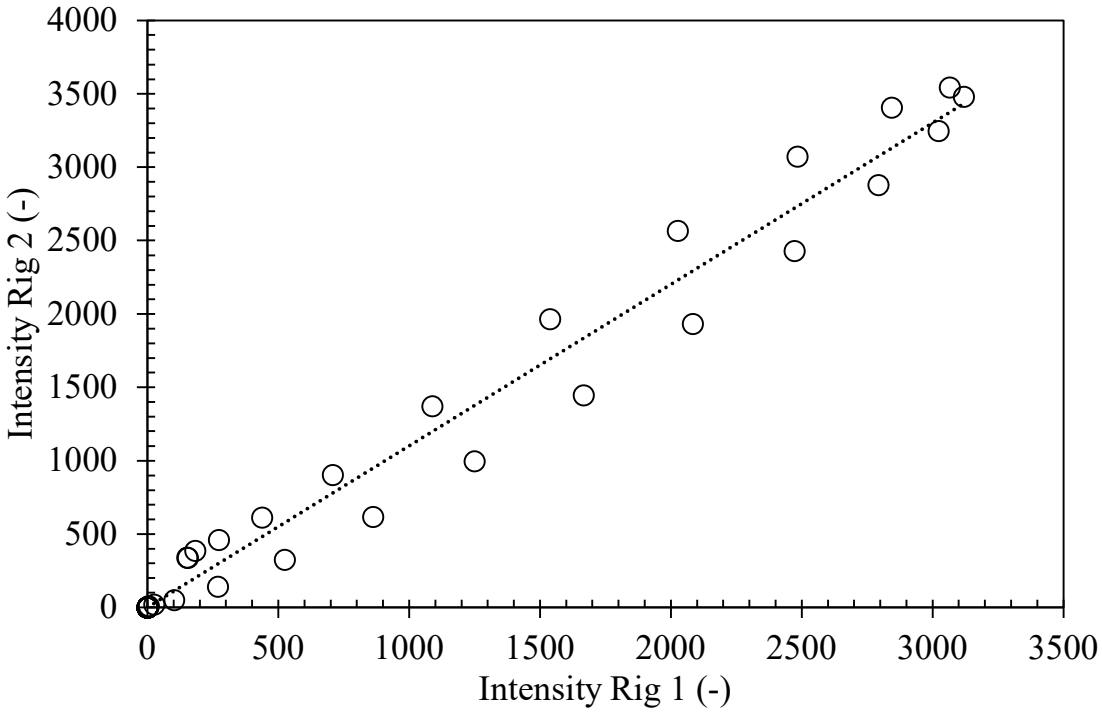


Figure 73: Linear regression analysis of the size-weighted intensities of particle dispersions formed in two CJM devices plotted as an x,y scatter. Trendline indicates the linear correlation between the two devices (y = 1.10x), R^2 0.99.

Similarly, the overlap observed between successive material extractions was assessed statistically, Figure 74. The recorded gradient and R^2 values of 1.10 and 0.99 respectively offer further evidence for the reproducibility of the device.

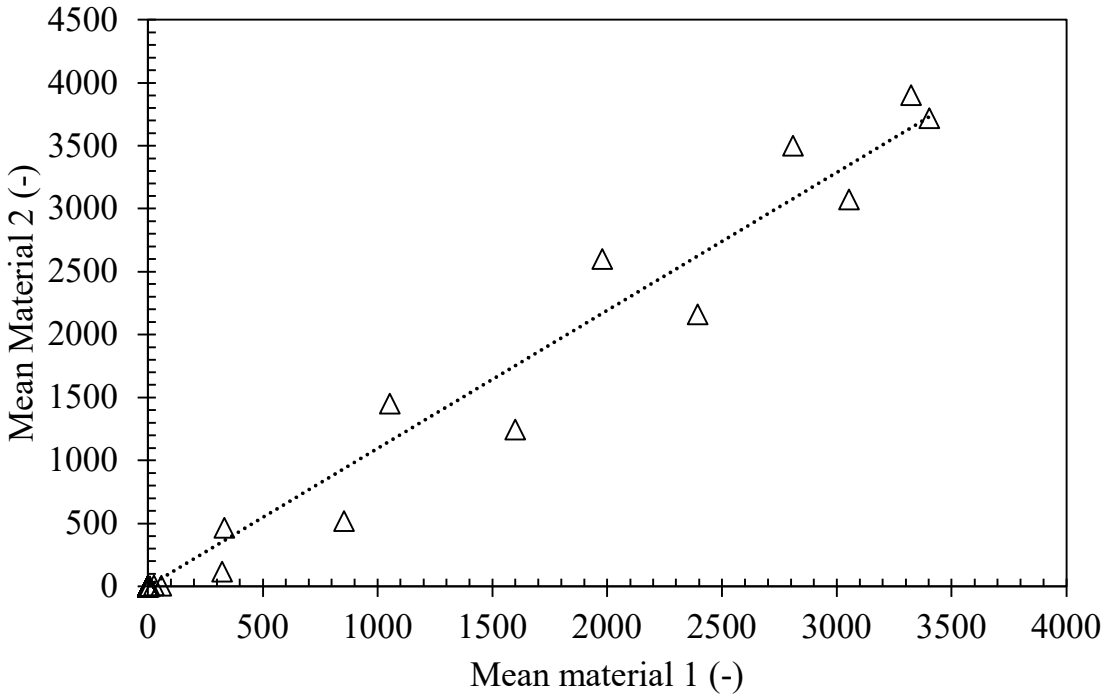


Figure 74: Linear regression analysis of the size-weighted intensities of particle dispersions formed in a CJM device from two separate material extractions, plotted as an x,y scatter. Trendline indicates the linear correlation between the two devices ($y = 1.10x$), R^2 0.98.

When comparing lipid containing and lipid removed systems, a difference in overlap of distributions was observed. This suggests that there is a statistically significant difference between the lipid-containing and lipid-removed datasets. This difference was quantified by correlating the intensities of an extract with lipid containing, and lipid removed, Figure 75.

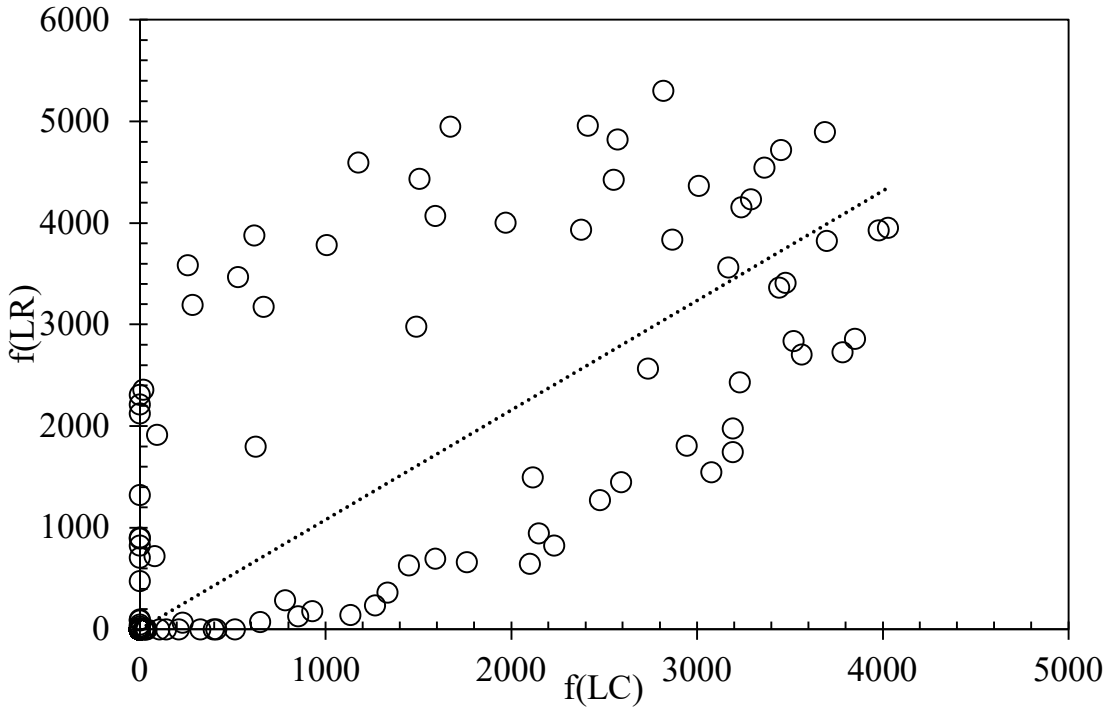


Figure 75: Linear regression analysis of the size-weighted intensities of particle dispersions formed in a CJM device from a material extraction containing lipid fraction (x) against a hexane washed lipid removed version (y), plotted as an x,y scatter. Trendline indicates no linear correlation between the two devices (y = 1.07x), R^2 0.70.

Assessing the reproducibility of two successive lipid removed extractions, there was an observed overlap between the two particle distributions. To quantify the similarity, the intensities of two independent distributions were correlated, Figure 76. An R^2 value of 0.95 was observed.

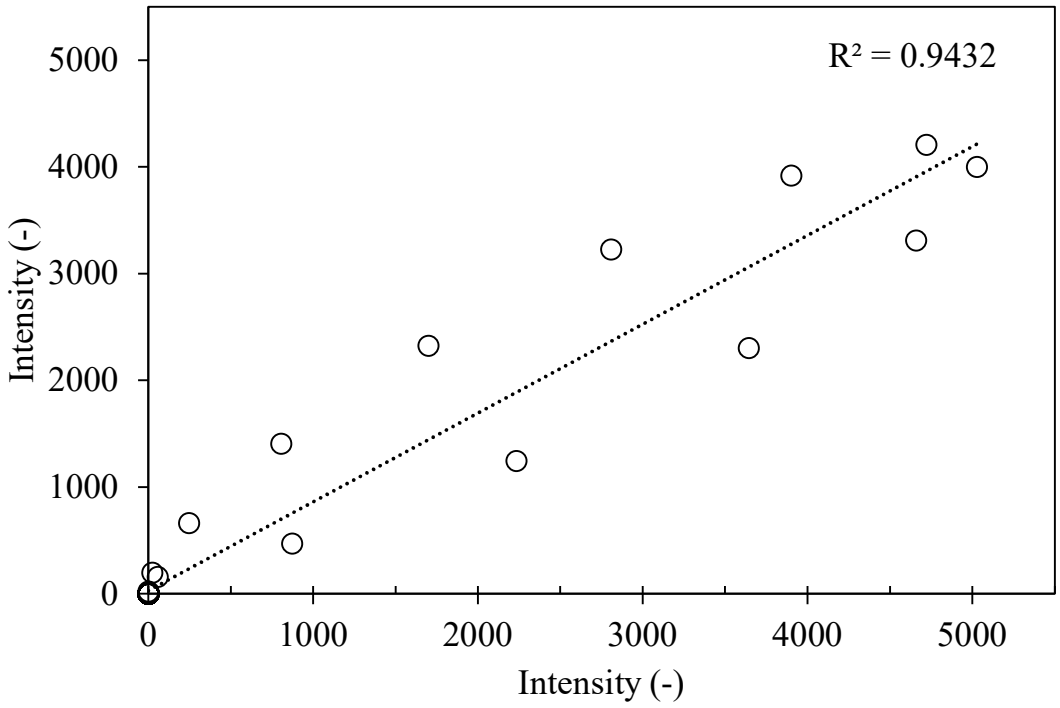


Figure 76: Linear regression analysis of the size-weighted intensities of particle dispersions formed in a CJM from two batches of lipid-removed lignin-rich cocoa bean extract. Trendline indicates the linear correlation between the two devices (y = 0.94 x).